



Searches for Supersymmetry and Dark Matter in final states with b -jets and E_T^{miss} utilising the higgs as a handle for new physics with the ATLAS detector

Thesis submitted in accordance with the requirements of the
University of Liverpool for the degree of Doctor in Philosophy by

Hamish Edward Teagle

September 2021

Abstract

The Standard Model (SM) is the most powerful and successful description of nature we have. Its predictions have stood up to decades of scrutiny and, since the discovery of the Higgs boson by the ATLAS and CMS collaborations in 2012, all the fundamental particles of the theory have been observed. However, we also know the theory to be incomplete. This thesis describes several searches for evidence of physics beyond the SM in proton-proton collision data collected by the ATLAS experiment at the Large Hadron Collider (LHC). The searches are motivated in two theoretical bases: WIMP dark matter scenarios which propose additional massive weakly-interacting particles aiming to explain astrophysical observations, and Supersymmetry (SUSY) which is a complete theoretical framework based upon symmetry extensions to the SM and predicts many additional massive particles that partner those of the SM and, under certain constraints, also provides a WIMP dark matter candidate.

In this work, the theoretical foundations of the SM and the relevant proposed extensions are briefly discussed. The methodology of the searches are then described along with their results. Firstly in chapter 8 two searches for Supersymmetric partners of the third generation quarks are outlined, targeting two decay chain scenarios. A dark matter model considering spin-0 mediators that expresses a similar experimental signature to the Supersymmetric signatures is also presented in this analysis. In chapter 9 a search for Supersymmetric partners to the electro-weak gauge bosons is presented taking two approaches: firstly a statistical analysis based on studying the shapes of key kinematic variables, and secondly a machine-learning (ML) based approach is targeting specific hard-to-reach areas of phase-space is presented. Lastly, in chapter 10 a search for pseudo-scalar mediated dark matter is presented motivated by the 2HDM+a model.

The commonality between the searches lies in the experimental signatures they produce. They are all characterised by the presence of b-quarks and weakly interacting particles that are evidenced in the detector as missing transverse energy, E_T^{miss} . In addition, two of the proposed models contain the higgs boson in their decays, this is utilised as a handle to identify the signatures.

In the appendix an evaluation of the construction methods and the material content to be used in the construction of the support structure for the silicon detector systems in the ATLAS inner detector upgrade is outlined and the comparison with the design specification is discussed. The upgrade will be implemented for the high luminosity run of the LHC.

Contents

I Theoretical Overview	1
1 The Standard Model	3
1.1 Symmetry in the Standard Model	3
1.2 Quantum Electrodynamics	4
1.3 Glashow's Model-Electroweak interactions	6
1.4 Electroweak Symmetry Breaking-The Higgs Mechanism	8
1.5 Quantum ChromoDynamics	11
1.6 The Strong Coupling and Asymptotic Freedom	12
1.7 Yukawa Couplings of Fermions	14
1.8 Phenomenology of the Standard Model	14
2 Beyond the Standard Model	17
2.1 Open questions in the Standard Model	17
2.2 Supersymmetry	25
2.3 Dark Matter	38
II The LHC and ATLAS detector	43
3 The LHC	45
3.1 Collider Physics	45
3.2 The CERN Accelerator Complex	48
4 The ATLAS detector	51
4.1 Detector Geometry	51
4.2 Magnet system	52
4.3 Inner Detector	52
4.4 Calorimeters	56
4.5 Muon Spectrometer	59
4.6 Trigger	60
5 Data and Monte-Carlo Simulation	63
5.1 ATLAS Data	63
5.2 Monte-Carlo Simulation	63

Contents

III Analysis Methods	69
6 Physics Objects	71
6.1 Track Reconstruction	71
6.2 Jets	72
6.3 Electrons	76
6.4 Photons	77
6.5 Muons	78
6.6 Taus	78
6.7 Missing Transverse Energy	78
6.8 Overlap Removal	80
6.9 Event Cleaning	80
6.10 Systematic Uncertainties	81
7 Analysis Techniques	83
7.1 Statistical Analysis	83
7.2 Discriminant Variables	87
7.3 Machine Learning Techniques	89
IV Searches for beyond the Standard Model physics in Run 2	95
8 Searches for third generation squarks	97
8.1 Phenomenology of Bottom Squarks	97
8.2 Bottom squark and dark matter signals with $b\bar{b} + E_T^{\text{miss}}$ final states	98
8.3 Bottom squark with multiple b-jets	121
8.4 Third generation SUSY limits	137
9 Searches for Electro-Weak SUSY	145
9.1 Signal Model	145
9.2 Selection-based Analysis	146
9.3 ML Analysis	151
9.4 Electro-Weak SUSY Limits	156
10 Searches for direct Dark Matter production	163
10.1 Signal model	163
10.2 Event Selection	164
10.3 Background Estimation	164
10.4 Systematic Uncertainties	165
10.5 Results	166
11 Conclusion	171

Appendix 175

A Understanding the Local Support Structures for the ATLAS High-Luminosity Upgrade	175
A.1 Introduction	175
A.2 Stave Production	179
A.3 Petal Production	186
A.4 Mass determination in the Stave Production	191
A.5 Conclusion: Comparing production mass measurements with prediction.	193

List of Figures

1.1	Neutral current interaction of electron and electron neutrino, mediated by the Z boson.	8
1.2	The shape of the Higgs potential from equation 1.26 which breaks the $SU(2)_L \times U(1)_Y$ symmetry. The wine bottle shape illustrates the global minima at non-zero values of ϕ . Oscillation quanta of the field transverse to the ring of minima are interpreted as the Higgs boson.	9
1.3	The virtual loops that cause the shielding/anti-shielding effects that cause the dependence of the QED and QCD coupling constants.	12
1.4	Illustration of the effective couplings of QCD and QED as a function of momentum transfer Q^2 .	13
1.5	Summary of the total production cross-section for a variety of processes measured in proton-proton collisions with centre-of-mass energies between 2.76 and 13 TeV. The measured values are compared with SM theoretical calculations at next-to,next-to leading order in the strong coupling or higher. All of the measurements made agree with the SM prediction to great accuracy.	16
2.1	1-loop fermion interaction with the Higgs boson.	18
2.2	Running of the couplings of the gauge interactions of the Standard Model.	19
2.3	The temperature power spectrum of the CMB using data collected from the Planck telescope [10], showing the fit of base- Λ CDM (cold dark matter) which parameterises the big bang model describing the evolution of the universe with expansion from dark energy and large-scale structure formation from dark matter.	21
2.4	Results of the BNL and FNAL g-2 μ measurements and their combined average, compared with the accepted theoretical value from the muon g-2 theory initiative [21].	23
2.5	Feynman diagrams for processes that contribute to the muon anomalous magnetic moment, including possible BSM contributions illustrated in 2.5(c).	24
2.6	1-loop scalar boson interaction with the Higgs boson.	29
2.7	Running of the couplings of the gauge interactions in the MSSM with proposed particles around the TeV scale.	30
2.8	Proton decay via intermediate scalar violating baryon number conservation.	30
2.9	Plots of possible mass spectra with the MSSM.	31
2.10	Typical spectrum of superpartner masses driven by naturalness in the Higgs mechanism.	33
2.11	SUSY sparticle production cross-sections as a function of sparticle mass calculated and next-next-to-leading order + next-next-to leading log for proton-proton collisions with centre of mass energy of 13 TeV.	34
2.13	Chargino-Neutralino production decaying via a W boson and the lightest neutralino, a Higgs and the lightest neutralino, with final state of 2 b-quarks and 1-lepton.	36

List of Figures

2.14 Feynman diagrams for Supersymmetric contributions to the muon anomalous magnetic moment.	36
2.15 From [28], illustration of the viable parameter space considering the maximum contribution to a_μ . The measurement from BNL and FNAL are in green and yellow respectively. The red lines show the contributions to a_μ for $\tan\beta = 40$	37
2.16 Processes for which collider searches achieve the highest sensitivity to chargino and neutralino masses.	37
2.17 Signatures from the single vector/axial vector mediator DM models	39
2.18 Signatures from the single scalar/pseudo-scalar mediator DM models in colour neutral mediator scenarios.	40
2.19 Signatures from the single scalar/pseudo-scalar mediator DM models in colour charged mediator scenarios.	40
2.20 Feynman diagrams that contribute to the DMtW 2.20(a) 2.20(b) and DMtt 2.20(c) channels of dark matter production in the 2HDM+a model.	42
 3.1 Acceleration of charged particles experiencing a voltage gradient from the oscillating electric field in an RF cavity. The formation of bunches based on the 'bucket' of viable accelerating region.	46
3.2 Mean number of interactions per bunch for the data taking periods including run 1 and run 2 data taking periods of the 13TeV LHC runs.	48
3.3 The accelerator complex at CERN.	49
 4.1 Illustration of the polar coordinate system used in the ATLAS detector.	51
4.2 Illustrations of (a) the ATLAS superconducting magnet arrangement providing the magnetic field for the detector volume and (b) the magnetic field shape inside the detector volume that the magnets produce.	53
4.3 Illustrations of the concentric layers of the inner detector subsystem in the ATLAS detector (cite: https://tracer.web.cern.ch/tracer/), with (a): the full inner detector, and (b),(c),(d) the concentric inner-most to outer-most detectors: Pixel, SCT,TRT.	54
4.4 Rejection of jets arising from the hadronisation of 4.4(a) light-flavour and 4.4(b) charm quark vs efficiency of identifying a b-jet in Run1 without the implementation of the IBL vs in Run 2 with the information from the IBL.	55
4.5 Geometry of the ATLAS Tile calorimeter	57
4.6 Illustration of the geometry of the cell construction for the LAr based EM calorimeter showing the bulk square cells and the front strip cells and their measurements in η [39].	58
4.7 Illustration of the muon spectrometer of the ATLAS detector, showing the barrel section of the MDTs and RPCs in blue and the end-cap sections containing the CSCs and TGCs in purple.	59
4.8 Illustration of the anode wire and cathode strip arrangement in the cathode strip chambers of the muon spectrometer, citeMuonSpecTDR.	60
4.9 Cross-sections of key SM processes, corrected for branching ratio of the decay channel [42].	61

List of Figures

5.1 Illustration of a MC simulated event, ttH production with the Sherpa [47] Monte Carlo generator. Colours indicate the different stages/areas of the hadron-hadron interaction: Hard process, Initial state parton shower, hadronisation and fragmentation, hadron decays, underlying event, beam remnants	67
6.1 Comparison between different jet clustering algorithms showing the area of the jets formed with calorimeter hits derived from parton level information of the hard scatter. The right plots also includes the addition of pile-up and underlying event contributions [Cacciari:2008gp]. The SISCone algorithm is a cone algorithm with split-merge steps, k_t and Cam/Aac are sequential recombination algorithms. The anti- k_t algorithm is shown to have the most consistent area and is independent of pile-up.	73
6.2 Comparison of the resolution of jets reconstructed using the PFlow method vs a standard algorithm using only topo clusters, measured in di-jet MC simulation showing in 6.2(a) the difference between reconstructed transverse momentum (p_T) and true p_T , 6.2(b) the resolution of angular components η and ϕ as a gaussian distribution between reconstructed true values. The angular resolution is improved in all regions, the p_T resolution is improved for low p_T jets though the improvement is reduced at higher p_T [71].	74
6.3 The (a) light flavour jet and (b) charm rejection for the different algorithms and sub-algorithms used in the flavour tagging as a function of the b-jet efficiency. In general, the DL1 algorithm performs the best, having the highest rejection and efficiency of all considered [73].	76
7.1 Illustration of the ideal arrangement of signal, control and validation regions as defined in the phase-space of two observables[86].	85
7.2 Illustration of the structure of a simple regression tree [91]	91
8.1 Illustration of the branching fraction of the $\tilde{\chi}_2^0$ to Higgs $\tilde{\chi}_1^0$ as a function of the bino fraction of the LSP. Many bino-like LSP scenarios have this as a large branching fraction.	98
8.2 Signals targeted in the bbMeT analysis.8.2(a) is a simplified SUSY model considering pair produced bottom squarks decaying symmetrically to a b-quark and $\tilde{\chi}_1^0$.8.2(b) is a simplified dark matter model in which the dark matter candidates are produced in pairs via a scalar or pseudo-scalar mediator particle which is generic.	99
8.3 Signal mass hypotheses points considered in the analysis for the bottom squark scenario.	99
8.4 Efficiency of the E_T^{miss} trigger for an example 2018 data period (the key features are the same for all data periods) as a function of the reconstructed E_T^{miss} and leading jet p_T . The events used are selected requiring one muon with $p_T > 30\text{GeV}$ and passing the muon trigger. The trigger-level information is then modified so that the muon momentum is removed to mimic the behaviour if the muon was lost to missing energy.	101
8.5 Distributions of the signal classification score comparing training and validation sets for the true-labeled background classes and the true-labeled signal class.	104

List of Figures

8.6 Distributions of signal classification score after the training preselection. Only statistical uncertainties are considered in the error band. (a) The lower panel shows the integrated significance assuming 20% background signal systematic uncertainties. The arrow indicates the lower bound of the SRB signal region bins. (b) Shows the data/MC comparison, blinded at high values, where signal contribution is significant.	105
8.7 Binning of the signal score in the exclusion signal region. The lower panel shows the integrated exclusion significance considering both signal and background statistical uncertainties but assuming a flat 20% systematic. Only statistical uncertainties are considered in the error band.	105
8.8 Summary of the post-fit relative systematic uncertainties of the various signal region yields, also split by component: Experimental (detector/reconstruction-based), theoretical (modeling), CR statistical (statistical uncertainty from the data yield in the control regions) and the MC statistics.	114
8.9 Post-fit distribution of (a) m_{CT} in SRA (b) w_{XGB} in SRB and $E_{\text{T}}^{\text{miss}}$ in (c) SRC-2b, (d) SRC-1b1v, (e) SRC-0b1v. Where relevant, the signal region selection is indicated by a black arrow. In each of (a)–(e) the lower plot shows the ratios of the observed yields to the post-fit predicted background yields, with a red arrow indicating when a ratio value is outside the displayed interval. The “Other” category includes contributions from diboson, and $t\bar{t} + W/Z/H$ production. The shaded band represents the total uncertainty of the background prediction. The last bin includes overflow events.	117
8.10 Post-fit distribution of (a) $w_{\text{D-low}}^Z$ and (c) $\cos \theta_{bb}^*$ in SRD-low and (b) $w_{\text{D-high}}^Z$ and (d) $\cos \theta_{bb}^*$ in SRD-high. Where relevant, the signal region selection is indicated by a black arrow. In each of (a)–(d) the lower plot shows the ratios of the observed yields to the post-fit predicted background yields. The “Other” category includes contributions from diboson and $t\bar{t} + W/Z/H$ production. The shaded band represents the total uncertainty of the background prediction.	118
8.11 Comparison between observed and background-only post-fit predicted background yields for the signal regions. The ratio plot represents the statistical significance of the discrepancy between the observed and predicted value. The “Other” category includes contributions from di-boson and $t\bar{t} + W/Z/H$ production. The shaded band represents the total uncertainty of the background prediction.	119
8.12 Bottom squark signature targeted in the multiple b-jets analysis.	121
8.13 The points generated for the two grids considered in the analysis for (a) the points with $\Delta m(\tilde{\chi}_2^0, \tilde{\chi}_1^0) = 130 \text{ GeV}$ and (b) the points with $m_{\tilde{\chi}_1^0} = 60 \text{ GeV}$	122
8.14 Turn-on curves for the $E_{\text{T}}^{\text{miss}}$ triggers as a function of offline $E_{\text{T}}^{\text{miss}}$ with respect to a fully efficient muon trigger. The muons in the event are treated as invisible by subtracting the muon transverse momentum from the $E_{\text{T}}^{\text{miss}}$. We observe that the triggers become fully efficient between 200 and 250 GeV.	123
8.15 Signal phenomenology targeted by the three signal region types.	124
8.16 The regions of the signal mass grids which are targeted by the three signal regions which have been developed. <i>Left:</i> The $\Delta m(\tilde{\chi}_2^0, \tilde{\chi}_1^0) = 130 \text{ GeV}$ grid includes a dedicated region, SRB, targeting the compressed regime along the diagonal. <i>Right:</i> the $m(\tilde{\chi}_1^0) = 60 \text{ GeV}$ grid including a dedicated region, SRC, targeting the compressed diagonal region. The SRA region is sensitive to the bulk regions of both grids.	125

8.17 Truth level distributions of the two ΔR variables used as the basis for the “MaxMin” algorithm. Left: Angular separation in ΔR of the two b-jets from the \tilde{b} decay, referred to as $\Delta R_{\max}(b, b)_{truth}$. Right: Angular separation of the two b-jets arising from the same Higgs, referred to as $\Delta R_{\max-\min}(b, b)_{truth}$.	126
8.18 Average mass of the b -jet pairings	128
8.19 Summary of the yields for all regions in the background-only fit. The lower panel shows the most relevant information concerning the deviation between observed data and predicted SM yields in each region.	137
8.20 95% confidence level exclusion contours for the M60 and DM130 signal hypothesis grids. In the regions where the sensitivity of the alternative signal regions, SRB and SRC, overlaps with SRA, the best expected (using SM MC prediction only) signal region is used to determine the CLs value for each point. Since the regions are not statistically independent, they cannot be combined.	138
8.21 Exclusion limits at 95% CL on the masses of the \tilde{b} and $\tilde{\chi}_1^0$ displayed in the (a) $(m_{\tilde{b}}, m_{\tilde{\chi}_1^0})$ and (b) $(m_{\tilde{b}}, \Delta m_{\tilde{b}, \tilde{\chi}_1^0})$ planes. The dashed line and the shaded band are the expected limit and its $\pm 1\sigma$ uncertainty, respectively. The thick solid line is the observed limit for the central value of the signal cross-section. Regions excluded by previous analyses [97] are shaded in light grey, while the region with $\Delta m_{\tilde{b}, \tilde{\chi}_1^0} < 5\text{GeV}$, not investigated in this analysis, is shaded in dark grey.	139
8.22 95% CL limits on the cross-section for the models of dark matter production mediated by a (a) scalar or (b) pseudoscalar mediator. The dashed line and the shaded band are the expected limit and its $\pm 1\sigma$ and $\pm 2\sigma$ uncertainties, respectively. The thick solid line is the observed limit for the central value of the signal cross-section. The grey line shows the limit from previous results [98]. The hatched red band shows the uncertainty of the model cross-section.	140
8.23 95% CL limits on bottom squark pair production considering several final state scenarios analysed from data collected with the ATLAS detector. The results presented in this thesis are shown for the analysis described in section 8.3 by the dark blue line which is combined with a complimentary analysis that targets final states where the higgs decays to hadronic τ leptons [99]. The analysis described in section 8.2 is shown by the green line. Additional contributing results are shown for the case where the bottom squark decays via a top quark [100] by the purple line and for the mono-jet analysis by the light blue line [101].	141
8.24 95% CL limits on bottom squark pair production analysed from data collected by the CMS detector. The grey and red lines show results for Run 1 [102] and Run 2 [103] analyses studying the m_{T2} variable and blue line shows the Run 2 result studying the E_T^{miss} [104] variable.	142
9.1 A diagram illustrating the signal scenario considered for the production of $\tilde{\chi}_1^\pm$ and a $\tilde{\chi}_2^0$ decaying via W and Higgs respectively.	146
9.2 Comparison of the observed and expected event yields in control, validation, exclusion, and discovery signal regions. The bottom panel shows the significance of the differences between the observed and expected yields.	150

List of Figures

9.3	Feature importance of each of the most impactful variables used in the BDT broken down by class. The impact is based on the SHAP score which evaluates the effect of the model incorporating a variable vs not incorporating the variable, relative to other variables used [108].	152
9.4	The pulls between the number of events observed and the total background expected after-fit in control, validation and signal regions. The lower panel shows the significance of the deviation. The data is not shown for the signal regions.	156
9.5	Model-dependent exclusion contour at 95% CLs. The observed limit is given by the solid line with the signal cross-section uncertainties shown by the dotted lines as indicated in the text. Expected limits are given by the dashed line.	157
9.6	The expected exclusion limit for signals in the Wh analysis at 95% CLs. The limit includes all experimental and theoretical systematic uncertainties. 9.6(b) shows the limit in an alternate view with the mass difference $\Delta m(\tilde{\chi}_2^0, \tilde{\chi}_1^0)$ on the y-axis. In red the 1st wave expected limit is shown for comparison.	158
9.7	95% CL limits on $\tilde{\chi}_1^\pm, \tilde{\chi}_2^0$ production decaying via a higgs, analysed from data collected by the ATLAS detector. The result from the analysis in section 9.2 is shown by the light blue. This result provides the strongest limit in the compressed region above $m_{\tilde{\chi}_1^\pm, \tilde{\chi}_2^0} = 250$ GeV. The previous run 1 result is shown by the blue line [109]. This is a selection-based approach with a simplified fit method compared with the run 2 analysis considering a shape fit in m_T . The public result that has the strongest limit in the compressed region is the analysis targeting higgs decays to photons, illustrating by the green line. The ML-based analyses described in section 9.3 will extend this sensitivity to higher $m_{\tilde{\chi}_1^\pm, \tilde{\chi}_2^0}$. The analysis targeting the all-hadronic final state, illustrated by the red line [] gives the strongest constraints towards high $m_{\tilde{\chi}_1^\pm, \tilde{\chi}_2^0}$	159
9.8	95% CL limits on $\tilde{\chi}_1^\pm, \tilde{\chi}_2^0$ production decaying via a higgs, analysed from data collected by the CMS detector. The limits in grey line and green line target the same 1-lepton 2 b -jets final state described in this work for the run 1 and run 2 datasets respectively [110],[111]. The coverage of the CMS reach to these models is comparable with ATLAS with only reduced sensitivity to compressed scenarios, which is due in part to the reduced E_T^{miss} resolution compared with ATLAS. As with the ATLAS results, the strongest limit towards high $m_{\tilde{\chi}_1^\pm, \tilde{\chi}_2^0}$ is given by the all-hadronic final state shown by the blue line.	160
10.1	Feynman diagrams that contribute to the tW channel of dark matter production via the pseudo-scalar mediator a in the extended 2HDM+a model.	164
10.2	Distributions of m_T , am_{T2} and E_T^{miss} from the background-only fit. The SR requirement is indicated by the arrow. The expected distributions for representative scenarios with different m_a , m_{H^\pm} , and $\tan\beta$ are shown. The lower panels show the ratio of data to the background prediction.	167

List of Figures

10.3 The expected and observed exclusion contours as a function of (m_a , m_{H^\pm}) (top) and (m_{H^\pm} , $\tan\beta$) (bottom), assuming only DMtW contributions, for the individual tW1L (purple line) and tW2L [112] (pink line) analysis channels, and for their statistical combination (green line). Experimental and theoretical systematic uncertainties, as described in Section 6, are applied to background and signal samples and illustrated by the ± 1 standard-deviation and ± 2 standard-deviation yellow bands and the green dotted contour lines, respectively, for the statistical combination.	170
A.1 Illustration of the internal structure of the local supports in staves and petals. Component materials are shown as a slice through the support.	177
A.2 Illustration of the differing geometries of the petal and stave support structures.	178
A.3 Images of the glue area taping and resultant glued area on the bottom face-sheet from step 1 of the procedure.	180
A.4 Images of the glue contact with the carbon foam blocks.	182
A.5 Image of the glue leaking from the c-channel-face-sheet contact after step 3.	184
A.7 Image of the excess honeycomb lying above the carbon fibre due to imprecision in the depth of the honeycomb manufacture.	185
A.8 Image of the bottom face-sheet after gluing c-channels and close-outs (stage 1).	187
A.10 Illustration of the mass contributions from sub-components within the stave at each stage.	192

List of Tables

1.1	Fermions of the Standard Model showing the charge and mass of each particle, all fermions have spin 1/2.	14
1.2	Bosons of the Standard Model showing the charge, spin and mass of each particle.	15
2.1	Chiral and Gauge supermultiplets of the MSSM.	26
2.2	New particles predicted in the MSSM and their gauge and mass eigenstates.	27
7.1	Description of some of the XGBoost model hyper-parameters and their functions.	93
8.1	Dark matter signal samples.	100
8.2	Definition of the pre-selection region used to select the inputs for the training of the SRB BDT.	103
8.3	Baseline signal points used for evaluating the BDT models.	103
8.4	Signal region selection for SRC regions.	107
8.5	E_T^{miss} binning for the SRC exclusion regions.	107
8.6	SRA signal, control and validation region definitions. Pink cells for the control and validation regions' columns indicate which selections ensure that the regions are orthogonal to the SR.	109
8.7	Multi-bin selections used for the definition of the SRA exclusion regions.	109
8.8	SRB signal, control and validation region definitions. Pink cells for the control and validation regions' columns indicate which selections ensure that the regions are orthogonal to the SR.	110
8.9	SRC signal and validation region definitions. Pink cells for the validation regions' columns indicate which selections ensure that they are orthogonal to the corresponding SR.	110
8.10	SRC control region definitions. Pink cells for the control regions' columns indicate which selections ensure that they are orthogonal to the corresponding SR.	111
8.11	SRD signal, control and validation region definitions. Pink cells for the control and validation regions' columns indicate which selections ensure that they are orthogonal to the corresponding SR.	111
8.12	sbot-AB control regions. Fit results for the CRs with an integrated luminosity of 139 fb^{-1} . The results are obtained from the control regions using the background-only fit. The errors shown are the statistical plus systematic uncertainties. Uncertainties on the fitted yields are symmetric by construction, where the negative error is truncated when reaching to zero event yield.	113

List of Tables

8.13 sbot-AB signal regions. The results for the m_{CT} binned SRA regions are grouped together. The background normalisations are obtained from the control regions using the background-only fit. The errors shown are the statistical plus systematic uncertainties. Uncertainties on the fitted yields are symmetric by construction, where the negative error is truncated when reaching to zero event yield.	113
8.14 Combined C-type control regions. Fit results with an integrated luminosity of 139 fb^{-1} . The results are obtained from the control regions using the background-only fit (see text for details). The errors shown are the statistical plus systematic uncertainties. Uncertainties on the fitted yields are symmetric by construction, where the negative error is truncated when reaching to zero event yield.	113
8.15 sbot-C Signal regions. Fit results for an integrated luminosity of 139 fb^{-1} . The results are obtained from the control regions using the background-only fit. The errors shown are the statistical plus systematic uncertainties. Uncertainties on the fitted yields are symmetric by construction, where the negative error is truncated when reaching to zero event yield.	115
8.16 All regions in DMB1. Fit results for one bin CR, VR and SR with an integrated luminosity of 139 fb^{-1} . The results are obtained from the control regions using the background-only fit (see text for details). Nominal MC expectations (normalised to MC cross-sections) are given for comparison. The errors shown are the statistical plus systematic uncertainties. Uncertainties on the fitted yields are symmetric by construction, where the negative error is truncated when reaching to zero event yield.	115
8.17 All regions in DMB2. Fit results for one bin CR, VR and SR with an integrated luminosity of 139 fb^{-1} . The results are obtained from the control regions using the background-only fit. The errors shown are the statistical plus systematic uncertainties. Uncertainties on the fitted yields are symmetric by construction, where the negative error is truncated when reaching to zero event yield.	116
8.18 Summary of the selection applied in order to study the E_T^{miss} trigger turn-on.	122
8.19 Definition of the three preselection regions.	124
8.20 Significance (Z_n) evolution for the algorithm discriminating cuts for the 'MaxMin' algorithm of SRA on a selection of benchmark signal models.	127
8.21 Signal region definitions for the inclusive A-type SR, alongside the three varying m_{Eff} binned regions. The letter appended to the SRA label corresponds to the low, medium or high m_{Eff} selection.	127
8.22 Selections for SRB.	129
8.23 Significance evolution for the main discriminating selections and the alternative algorithm of SRB on benchmark signal models.	129
8.24 Signal region selections for the C-type SRs.	130
8.25 Selections for CR strategy. The letter appended to the CR label corresponds to the low, medium and high m_{Eff} selection for CRA.	131
8.26 Selections for 0 Lepton VR strategy for the A and B-type regions. For the A-type regions, the letter appended to the CR label corresponds to the low, medium and high m_{Eff} selection.	133

8.27	Expected background event yields and dominant systematic uncertainties on background estimates in the A-type (inclusive), B-type and C-type (inclusive) regions. Individual uncertainties can be correlated, and do not necessarily add up quadratically to the total background uncertainty. The percentages show the size of the uncertainty relative to the total expected background.	134
8.28	Background-only fit results for the inclusive A and B-type CR performed using 140.5fb^{-1} , the post-fit uncertainty shows the total statistical and systematic uncertainty. The individual bins in m_{E_f} are also shown.	135
8.29	Background-only fit results for the A- and B-type regions (top table) and C-type regions (bottom table) performed using 139 fb^{-1} of data. The quoted uncertainties on the fitted SM background include both the statistical and systematic uncertainties.	136
8.30	From left to right, observed 95% CL upper limits on the visible cross sections σ_{vis} , the observed (S_{obs}^{95}) and expected (S_{exp}^{95}) 95% CL upper limits on the number of signal events with $\pm 1\sigma$ excursions of the expectation, the CL of the background-only hypothesis, CL_B , the discovery p -value (p_0), truncated at 0.5, and the associated significance (in parentheses).	143
8.31	Left to right: SM expectation from background-only fit for the model-independent regions, 95% CL upper limits on the visible cross-section ($\langle \epsilon \sigma \rangle_{\text{obs}}^{95}$), on the observed (S_{obs}^{95}) and expected (S_{exp}^{95}) number of signal events. The last two columns indicate the CL_B value, i.e. the confidence level observed for the background-only hypothesis, and the discovery p -value ($p(s = 0)$) capped at a value of 0.5.	143
9.1	Definition of 9 SRs, binned both in m_T and m_{CT} , resulting in a two-dimensional shape fit. The exclusion-specific selections for the model-dependent fit are denoted excl. The discovery region definitions are denoted disc.	147
9.2	Control region definitions. As preselections, 1 lepton, 2-3 jets and 2 b-jets are also required. The selection criteria that make the regions orthogonal are highlighted.	148
9.3	Background fit results for the exclusion SR regions. The errors shown are the statistical plus systematic uncertainties. Uncertainties in the fitted yields are symmetric by construction, except where the negative error is truncated at an event yield of zero.	149
9.4	Background fit results for the , TRM, TRH, WCR and STCR region(s), for an integrated luminosity of 140.5 fb^{-1} . The errors shown are the statistical plus systematic uncertainties. Uncertainties on the fitted yields are symmetric by construction, where the negative error is truncated when reaching to zero event yield.	150
9.5	Definition of the pre-selection that is applied in the ML-based analysis used to select MC samples for training the BDT.	153
9.6	The input variables for the XGBoost algorithm. Split into object-level and event-level variables.	153
9.7	Definition of the signal region targeting the $\tilde{\chi}_2^0 \tilde{\chi}_1^\pm \rightarrow Wh$ compressed signals	154
9.8	Definition of the control regions for estimating $t\bar{t}$, single-Top and W+jets dominant background processes. The selections in red highlight the selections that make the regions orthogonal to each other. The selections in blue highlight the selections that make the regions orthogonal to the control and signal regions.	155
9.9	Post-fit yields for the SM background processes in the control regions from the background-only fit.	155

List of Tables

9.10 Post-fit yields for the SM background processes in the signal regions from the background-only fit.	156
9.11 Breakdown of upper limits.	161
10.1 Summary of the signal region selections developed with the adaptive grid search algorithm and additional E_T^{miss} binning used in the model-dependent fit.	165
10.2 The selection cuts defining the control and validation regions. The red highlighted selections indicate those that ensure orthogonality with the signal region.	165
10.3 Results of the background only fit for the CRs. Statistical and experimental uncertainties are considered.	166
10.4 Background-only fit results for the tW_{1l} signal region. The backgrounds which contribute only a small amount (rare processes such as triboson, $t\bar{t} t\bar{t}$, $t\bar{t} WW$ and Higgs boson production processes, and non-prompt or misidentified leptons background) are grouped and labelled as ‘Others’. The quoted uncertainties of the fitted SM background include both the statistical and systematic uncertainties.	168
10.5 The 95% CL upper limits on the visible cross section ($\langle\epsilon\sigma\rangle_{\text{obs}}^{95}$) and on the number of signal events (S_{obs}^{95}) for all SRs and analysis channels as detailed in the text. The fourth column (S_{exp}^{95}) shows the 95% CL upper limit on the number of signal events, given the expected number (and $\pm 1\sigma$ exclusions of the expectation) of background events. The last two columns indicate the CL_B value, i.e. the confidence level observed for the background-only hypothesis, and the discovery p -value ($p(s = 0)$). The associated significance is provided in parentheses.	169
A.1 Measured glue contribution of the stave at each stage of production, by mass and as a percentage of the total stave mass.	191
A.2 The measured and predicted masses and radiation length percentages for the stave, calculations follow the aforementioned assumptions.	194

Part I

Theoretical Overview

1 The Standard Model

The Standard Model is a theoretical framework which describes the existence of elementary particles and the interactions between these particles via the known fundamental forces, with the exception of gravitation. The elementary particles are divided into those which make up the matter of the world around us, the leptons and quarks, and those which act to mediate the fundamental forces, known as bosons. The exception is the Higgs boson which does not mediate a fundamental force but plays a special role in setting the scale of natural world we see today and introducing masses to the other elementary particles 1.4. The predictions made by the SM are both precise and wide-ranging which has allowed it to become one of the most deeply probed theoretical models developed. It has been hugely successful in accurately describing nature at every trial.

1.1 Symmetry in the Standard Model

In 1918 Emmy Noether showed [1] that if, under a continuous translation of variables or coordinates, the equations of motion for a physical system remain of the same form (i.e. they are *covariant*), there must exist a corresponding conserved current within the system. Transformations with this feature are called *symmetry transformations*. Some examples of symmetries that are respected by physical systems are: symmetry under translations in time, linear coordinate translations, and rotational translations. The resultant conserved currents related to these symmetries infer the conservations of energy and linear and angular momentum respectively. This deep relationship between symmetries in the equations describing physical systems and the properties they infer forms the basis of the Standard Model's structure.

Symmetry translations of this type are generally described in terms of groups. The 3-dimensional geometric translations can be combined with relativistic space-time translations in Minkowski space i.e. Lorentz boosts (under which the Minkowski metric is invariant) to form the Poincaré group. Elementary particles can be defined as those particles whose intrinsic properties are invariant under transformations of the Poincaré group.

In addition, one can consider transformations that act on the space-time functions in the equations of motion and not on the coordinates or variables. An example is a phase transformation of the quantum mechanical wave function:

$$\psi \longmapsto \psi' = e^{i\alpha} \psi \tag{1.1}$$

1 The Standard Model

under which the Schrödinger equation is invariant:

$$H\psi = i\hbar\partial_t\psi \quad (1.2)$$

These transformations are known as *internal symmetry transformations* and also infer conserved currents.

The transformations described so far apply in the same way at every point in time and space - they are *global* transformations. However this notion can be extended to transformations which are dependent on the local coordinates i.e. transformations of the form:

$$\psi(x) \longmapsto \psi' = e^{i\alpha(x)}\psi(x) \quad (1.3)$$

Where $\alpha(x)$ denotes an arbitrary function of the space-time coordinate x . Theories which are invariant under transformations of this type are known as *locally gauge invariant*.

The SM is a Quantum Field Theory (QFT), an extension of classical field theory with quantisation in the fields. QFT is a Lagrangian formalism, encoding the equations of motion of the fields in Lagrangian densities \mathcal{L} , which can be extracted via the *principle of least action*, leading to the Euler-Lagrange equations. The concept from Noether's theorem of symmetries implying conserved quantities is easily applicable in this formalism by simply requiring that \mathcal{L} is invariant under a given symmetry transformation. In the QFT realm, the conserved quantities of internal symmetries are conserved currents which describe the interactions between particles. These concepts applied in this mathematical structure are the foundation of the SM.

1.2 Quantum Electrodynamics

Dirac expressed the behaviour of free, quantum mechanical particles in a relativistic way with his equation:

$$(i\gamma^\mu\partial_\mu - m)\psi = 0 \quad (1.4)$$

Requiring that it should be linear in space-time derivatives, ∂_μ . The Dirac Lagrangian for free particles is then:

$$\mathcal{L}_{Dirac} = \bar{\psi}(i\gamma^\mu\partial_\mu - m)\psi \quad (1.5)$$

where the particles fields, ψ , are 4-component Dirac spinors and γ^μ are 4x4 Dirac matrices. The Dirac Lagrangian is inherently invariant under global transformations (of the form in 1.1). However, it is clear that the invariance does not hold under local transformations of the form in 1.3. To ensure

1.2 Quantum Electrodynamics

invariance in this case requires replacing the normal space-time derivative, ∂_μ , with the covariant derivative D_μ such that $D_\mu\psi$ transforms identically to ψ :

$$D_\mu\psi(x) \mapsto D'_\mu\psi(x)' = e^{i\alpha(x)}(D_\mu\psi(x)) \quad (1.6)$$

The covariant derivative is defined as:

$$D_\mu\psi(x) = (\partial_\mu - ieA_\mu)\psi(x) \quad (1.7)$$

such that the transformation requirement from 1.6 is upheld:

$$D_\mu\psi(x) \mapsto D'_\mu\psi(x)' = e^{i\alpha(x)}(\partial_\mu\psi(x) + i\partial_\mu\alpha(x) - ieA'_\mu\psi(x)) \quad (1.8)$$

$$= e^{i\alpha(x)}(\partial_\mu\psi(x) - ieA_\mu\psi(x)) = e^{i\alpha(x)}D_\mu\psi(x) \quad (1.9)$$

The 4-vector gauge field A_μ is introduced which transforms as:

$$A_\mu \mapsto A'_\mu = A_\mu - \frac{1}{e}\partial_\mu\alpha(x) \quad (1.10)$$

The field equations for A_μ are:

$$\partial^2 A^\nu - \partial^\nu(\partial_\mu A^\mu) = J^\nu \quad (1.11)$$

J^ν is the conserved current predicted from Noether's theorem and leads to Maxwell's equations of electromagnetism.

The term $-\frac{1}{4}F_{\mu\nu}F^{\mu\nu}$ where $F_{\mu\nu} = \partial_\mu A_\nu - \partial_\nu A_\mu$, which is the Lagrangian of the free gauge field A_μ , is included in the Lagrangian along with the term describing the interaction between A_μ and the fermion fields, \mathcal{L}_{int} : $e\bar{\psi}\gamma^\mu\psi A_\mu$. The full locally gauge invariant lagrangian becomes:

$$\mathcal{L}_{QED} = \mathcal{L}_{em} + \mathcal{L}_{Dirac} + \mathcal{L}_{int} = -\frac{1}{4}F_{\mu\nu}^{\mu\nu} + \bar{\psi}(i\cancel{D} - m)\psi + e\bar{\psi}\gamma^\mu\psi A_\mu \quad (1.12)$$

The gauge field A_μ is the photon field which arises naturally from the requirement that the Lagrangian be invariant under the local symmetry transformation. Equation 1.12 describes all the electromagnetic interactions mediated by the photon field forming the basis of quantum electrodynamics (QED). The gauge introduced in equation 1.3 is an example of a continuous symmetry that is encapsulated by the Lie group U(1), that is the group of unitary 1×1 matrices describing transformations on the space-time manifold. The concept of requiring invariance of a Lagrangian under transformations encapsulated within Lie groups can be extended to Lie groups of higher dimension.

1 The Standard Model

1.3 Glashow's Model-Electroweak interactions

One can consider transformations of the form:

$$\psi(x) \mapsto \psi'(x) = e^{ig\frac{\vec{\tau}}{2} \cdot \alpha(x)} \psi(x) \quad (1.13)$$

where $\vec{\tau}$ are the 2×2 Pauli matrices which are the generators of the SU(2) gauge group, also known as isospin generators. The lepton and quark fermion fields, χ_L , form doublets under this SU(2) transformation, meaning that there are two components that transform differently and have different quantum numbers:

$$\chi_L = \begin{pmatrix} \nu_L \\ e_L \end{pmatrix}, \begin{pmatrix} u_L \\ d_L \end{pmatrix} \quad (1.14)$$

where the subscript L denotes that these fields have left-handed chirality and the quantum numbers of weak isospin T and T^3 are introduced. Both components of the doublets have $T = \frac{1}{2}$, the upper components having $T^3 = +\frac{1}{2}$ and the lower components having $T^3 = -\frac{1}{2}$. The specification that the fermion fields that form doublets under this symmetry are left-handed is special to the SU(2) symmetry of the SM since the weak interaction only couples to left-handed chiral fields, it is often denoted $SU(2)_L$, the right-handed fermion fields therefore form singlets under SU(2). From the introduction of the transformation in 1.13 a triplet of isospin conserved currents arises:

$$J_\mu^i = \bar{\chi}_L \gamma_\mu \frac{1}{2} \tau^i \chi_L \quad (i = 1, 2, 3) \quad (1.15)$$

The invariance of the Lagrangian under the SU(2) transformation group introduces a new interaction known as the weak interaction. The 3 Pauli matrices, $\vec{\tau}$, which are the generators of SU(2) are associated with 3 massless spin 1 gauge bosons, W^\pm , W^3 . The interaction is inferred by the conserved current, J_μ^i , and is mediated by the gauge bosons that arise.

The identification of left-handed fermions as weak isospin doublets has interesting consequences. The weak charged currents allow for quarks to transition from one flavour to another, from up-type to down-type by changing the quantum number T_3 . With reference to table 1.1 and the discussion in section 1.8, the weak interaction not only allows transitions between up and down-type but also between quark generations as described by the CKM (Cabibo - Kobayashi - Maskawa) matrix. The CKM matrix describes the probability for quark transitions between flavours via quark mixing and, notably, contains non-zero off diagonal elements allowing inter-generational transitions. The physical quark states are mixed due to the CKM matrix (equation 1.16).

$$\begin{pmatrix} d' \\ s' \\ b' \end{pmatrix} = \begin{pmatrix} |V_{ud}| & |V_{us}| & |V_{ub}| \\ |V_{cd}| & |V_{cs}| & |V_{cb}| \\ |V_{td}| & |V_{ts}| & |V_{tb}| \end{pmatrix} \begin{pmatrix} d \\ s \\ b \end{pmatrix} \quad (1.16)$$

1.3 Glashow's Model-Electroweak interactions

where d' , s' and b' are the weak isospin doublets for the down-type quarks and d , s and b are the mass eigenstates. The matrix in the middle containing V_{ij} components is the CKM matrix.

The behavior of the weak force to only act on left-handed fermions is an interesting feature, it is the only SM interaction that violates *parity* symmetry. Parity transformations are those in which the sign of the position coordinates are reversed. Parity is conserved in electromagnetic and strong interactions but is violated by the chiral nature of the weak interactions. Originally, parity was thought to be a conserved quantity in physical interactions but with the observations of weak processes, the symmetry considered was extended to include charge, charge-parity (CP). In fact, the weak interaction is also CP violating to a small extent via the CKM matrix. The CKM matrix is parameterised by 3 mixing angles and a complex phase term. The complex phase modifies the rates for some anti-particle processes with respect to their particle counterparts, thus violating CP. This violation has interesting consequences for the matter-antimatter asymmetry observed in the universe which is discussed in section 2.1.5.

The weak force was known to mediate charged current interactions from observations such as β -Decay and as a result the gauge bosons of the field were proposed to also carry electric charge and thus must couple to the photon field of QED. To reach a consistent theory where the fermions described under the weak $SU(2)$ interactions are the same fermions that interact through the electromagnetic $U(1)$ interactions Glashow, Salam and Weinberg proposed that the electromagnetic and weak interactions could be accurately described within a unified electro-weak theory by requiring invariance under transformations of the combined gauge group $SU(2) \times U(1)$. This requires that the electromagnetic current is also present in addition to the isospin triplet in equation 1.15:

$$J_\mu^{em} = (\bar{e}_L \gamma_\mu e_L + \bar{e}_R \gamma_\mu e_R) \quad (1.17)$$

The electromagnetic current 1.17 standing alone is not invariant under rotations of $SU(2)$. To ensure this, an additional current J_μ^Y is introduced which forms the electromagnetic current when added to J_μ^3 such that:

$$J_\mu^{em} = J_\mu^3 + \frac{1}{2} J_\mu^Y \quad (1.18)$$

J_μ^Y is the *weak hypercharge current*. The charges related to these currents can be interpreted as:

$$Q = T^3 + \frac{1}{2} Y \quad (1.19)$$

where T^3 and Y are the third weak isospin component and the weak hypercharge respectively, Q is the electromagnetic charge. The $U(1)$ group is associated with the weak hypercharge quantum number, and is often denoted $U(1)_Y$, and $SU(2)_L$ is associated with weak isospin.

The complete gauge transformations for left and right-handed fermions under $SU(2)_L$ and $U(1)_Y$ are:

$$\chi_L \mapsto \chi'_L = \exp[-ig \frac{\vec{\tau}}{2} \cdot \Delta(x) + ig' \frac{\Lambda(x)}{2}] \chi_L \quad (1.20)$$

1 The Standard Model

$$e_R \mapsto e'_R = \exp[ig'\Lambda(x)]e_R \quad (1.21)$$

The $SU(2)_L \times U(1)_Y$ combined symmetry is gauged by the introduction of a triplet of weak gauge bosons $W_\mu^i (i = 1, 2, 3)$ and hypercharge gauge boson B_μ , with the W_μ^1 and W_μ^2 being electrically charged and W_μ^3 and B_μ being neutral. The neutral vector fields are revealed physically as a mixture:

$$\begin{pmatrix} B_\mu \\ W_\mu^3 \end{pmatrix} = \begin{pmatrix} \cos \theta_W & \sin \theta_W \\ -\sin \theta_W & \cos \theta_W \end{pmatrix} \begin{pmatrix} \gamma \\ Z^0 \end{pmatrix} \quad (1.22)$$

Where θ_W is the weak mixing angle, which is not a predicted parameter of the theory but must be determined experimentally. The resulting phenomenology is that of 4 vector bosons, 2 charged and 2 neutral. The photon, γ , mediates the electromagnetic interactions and the three W^\pm, Z^0 bosons mediate the weak interactions. The formulation of the electroweak theory allows for neutral current interactions (figure 1.1) which were observed in 1973 in the Gargamelle bubble chamber at CERN [2].

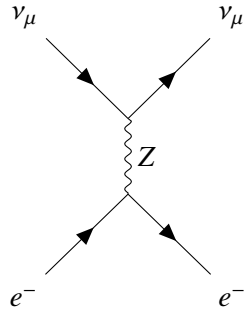


Figure 1.1: Neutral current interaction of electron and electron neutrino, mediated by the Z boson.

Requiring exact invariance under $SU(2)_L \times U(1)_Y$, however, imposes that the gauge bosons of the theory must be massless since the mass terms violate the symmetry, which is not observed in nature. Fermions are also required to be massless as their mass terms are not invariant under the introduced gauges, which is clearly not observed. The resolution of this problem comes with the introduction of *spontaneous symmetry breaking* with the Higgs mechanism which allows the symmetry breaking mass terms to arise.

1.4 Electroweak Symmetry Breaking-The Higgs Mechanism

In order to break the electro-weak symmetry of $SU(2)_Y \times U(1)_Y$, a complex scalar field is introduced of the form:

$$\Phi = \begin{pmatrix} \phi^+ \\ \phi^0 \end{pmatrix} \frac{1}{\sqrt{2}} \begin{pmatrix} \phi_1 + i\phi_2 \\ \phi_3 + i\phi_4 \end{pmatrix} \quad (1.23)$$

1.4 Electroweak Symmetry Breaking-The Higgs Mechanism

which transforms as a doublet under $SU(2)_L$. The Lagrangian of the field can be written as:

$$\mathcal{L}_\Phi = (\mathcal{D}_\mu \Phi)^\dagger \mathcal{D}^\mu \Phi - V(\Phi) \quad (1.24)$$

where

$$\mathcal{D}_\mu = \partial_\mu + \frac{i}{2} g \vec{\tau} \cdot \vec{W}_\mu + ig' \frac{Y}{2} B_\mu \quad (1.25)$$

is the covariant derivative of $SU(2)_L \times U(1)_Y$, g and g' are the couplings of the $SU(2)_L$ and $U(1)_Y$ gauge groups and the final term:

$$V(\Phi) = \mu^2 (\Phi^\dagger \Phi) - \lambda (\Phi^\dagger \Phi)^2 \quad (1.26)$$

is the potential of the Higgs field. μ^2 is the mass term of the scalar field and λ is the self coupling. To ensure that the vacuum is stable, λ is required to be less than zero. If μ^2 is less than zero the potential has a global minima which is not at $\Phi = 0$, leading to a non-zero value for Φ in the vacuum state as illustrated in figure 1.2.

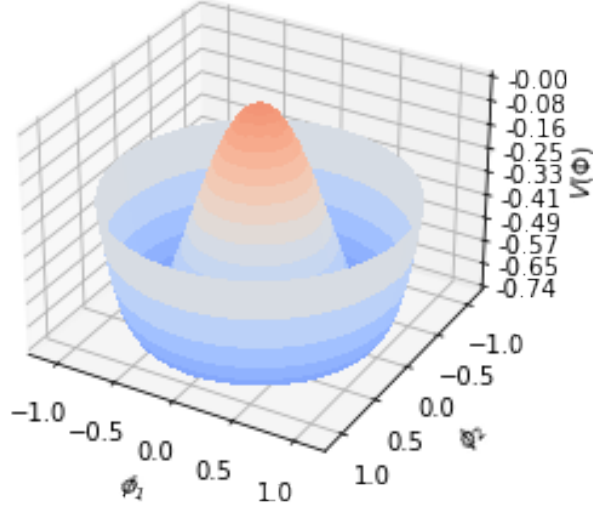


Figure 1.2: The shape of the Higgs potential from equation 1.26 which breaks the $SU(2)_L \times U(1)_Y$ symmetry. The wine bottle shape illustrates the global minima at non-zero values of ϕ . Oscillation quanta of the field transverse to the ring of minima are interpreted as the Higgs boson.

In terms of the real scalar fields, the vacuum expectation values can be shifted to unitary gauge such that:

$$\langle 0 | \phi_1 | 0 \rangle = \langle 0 | \phi_2 | 0 \rangle = \langle 0 | \phi_4 | 0 \rangle = 0 \quad (1.27)$$

1 The Standard Model

and keeping ϕ_3 as the non-zero component:

$$\langle 0 | \phi_3 | 0 \rangle^2 = v^2 = \frac{\mu^2}{\lambda} \quad (1.28)$$

such that the field doublet in this chosen vacuum is:

$$\Phi = \frac{1}{\sqrt{2}} \begin{pmatrix} 0 \\ v + H \end{pmatrix} \quad (1.29)$$

where H is the neutral scalar Higgs field. This enables the surviving current of the field in the vacuum to be neutral, which ensures that the electromagnetic part of the symmetry is unbroken:

$$SU(2)_L \times U(1)_Y \mapsto U(1)_{EM} \quad (1.30)$$

The feature of conserving the invariance of the lagrangian under the $U(1)_{EM}$ transformations means that the photon remains massless, whereas the breaking of the $SU(2)_L \times U(1)_Y$ symmetry gives mass terms to the weak bosons W^\pm and Z^0 as illustrated in the following.

With the introduction of the scalar field ϕ , the electroweak Lagrangian is:

$$\mathcal{L} = \frac{-1}{4} W_{\mu\nu}^a W_{\mu\nu}^a - \frac{1}{4} B_{\mu\nu} B_{\mu\nu} + (\mathcal{D}_\mu \Phi)^\dagger \mathcal{D}^\mu \Phi - \lambda (\Phi^\dagger \Phi - \frac{v^2}{2})^2 \quad (1.31)$$

where $W_{\mu\nu}^a$ and $B_{\mu\nu}$ are the field strength tensors for the three $SU(2)_L$ weak gauge fields W ($a=1,2,3$) and the $U(1)$ hypercharge gauge field B respectively. In the unitary gauge, the covariant derivative becomes (eq 1.32)

$$\mathcal{D}_\mu = \begin{pmatrix} \frac{-ig}{2\sqrt{2}} (W_\mu^1 - iW_\mu^2)(v + H) \\ \frac{-i}{2\sqrt{2}} (g'B_\mu - gW_\mu^3)(v + H) + \frac{1}{\sqrt{2}} \partial_\mu H \end{pmatrix} \quad (1.32)$$

using the substitutions for the vector fields

$$W_\mu^\pm = \frac{1}{\sqrt{2}} (W_\mu^1 \mp iW_\mu^2) \quad (1.33)$$

$$Z_\mu = \frac{1}{\sqrt{g^2 + g'^2}} (gW_\mu^1 - g'B_\mu) \quad (1.34)$$

$$A_\mu = \frac{1}{\sqrt{g^2 + g'^2}} (gB_\mu + g'W_\mu^3) \quad (1.35)$$

the quadratic term in the Lagrangian becomes

$$(\mathcal{D}_\mu \phi)^\dagger \mathcal{D}_\mu \phi = \frac{1}{2} (\partial_\mu H)^2 + \frac{g^2 v^2}{4} W_\mu^+ W_\mu^- + \frac{1}{2} \left(\frac{(g^2 + g'^2)v^2}{4} \right) Z_\mu Z_\mu \quad (1.36)$$

1.5 Quantum ChromoDynamics

Equation 1.36 introduces the mass terms for the W and Z bosons identified as $m_W = \frac{gv}{2}$, $m_Z = \frac{\sqrt{g^2 + g'^2}v}{2}$ with absent mass term for the photon field as expected. The full Lagrangian up to quadratic terms is

$$\mathcal{L} = -\frac{1}{2}W_{\mu\nu}^+W_{\mu\nu}^- + m_W^2 W_\mu^+ W_\mu^- - \frac{1}{4}F_{\mu\nu}F_{\mu\nu} - \frac{1}{4}Z_{\mu\nu}Z_{\mu\nu} + \frac{m_Z^2}{2} + \frac{1}{2}(\partial_\mu H)^2 - \lambda v^2 H^2 \quad (1.37)$$

With the introduction of the Higgs field the weak bosons are assigned masses within the theory with relationship between the masses relying on the weak mixing angle θ_W , $m_Z = \frac{m_W}{\cos \theta_W}$. This framework for the electroweak unification with the Higgs mechanism allowed for the precise prediction of the masses of the W and Z bosons which were subsequently observed in 1983 by the UA1 and UA2 experiments at CERN [3],[4]. The introduction of the Higgs field also allows the introduction of masses for the fermions via Yukawa interactions (section 1.7).

The final term in the lagrangian is the mass term for the scalar field-the Higgs boson, $m_H = \sqrt{2\lambda}v$. The Higgs can be interpreted as the non-zero excitations of the Higgs potential. Although the theory does not precisely predict the value of the Higgs mass, measurements of Electroweak couplings at the LEP collider at CERN indicated it to be 150 ± 36 GeV [5]. In 2012 the ATLAS and CMS experiments observed the Higgs boson at a mass of around 125 GeV [6] [7]. The observation was made using a statistical combination of channels with higgs decays to photons and Z bosons being the most sensitive channels. The discovery completed the puzzle of observing all fundamental particles of the SM experimentally.

1.5 Quantum ChromoDynamics

In the late 1950s and early 60s bubble chamber and spark chamber experiments at CERN and around the world made discoveries of many new hadrons. Due to the number of the new particles discovered, some in the physics community hypothesised that these were not fundamental particles but in fact had composite structure. This led to the quark structure model proposed by Gell-Mann and Zweig that the hadrons were composites of 3 quarks: up, down and strange as an SU(3) triplet. However with the discovery of the Ω^- baryon, comprising 3 strange quarks in the ground state, the quark model required extension in order to be consistent with the Pauli exclusion. To solve this, Gell-Mann and Fritzsch proposed that quarks had an additional, exact SU(3) symmetry and carried a new conserved quantum number called *colour*, giving quantum chromodynamics (QCD) its name. Quarks are triplets in the fundamental representation of SU(3), with colour charge red, green or blue:

$$\psi(x) = \begin{pmatrix} \psi_R(x) \\ \psi_G(x) \\ \psi_B(x) \end{pmatrix} \quad (1.38)$$

In addition to solving the statistical problems with composite baryons, the interactions of the strong force are also encapsulated in the SU(3) gauge group, whose generators are $t_a = \lambda_a/2$ where λ_a are

1 The Standard Model

the 8 Gell-Mann matrices ($a=1,2\dots,8$). Introduced as a gauge symmetry, the Dirac lagrangian can be made invariant under transformations of the form:

$$\psi(x) \mapsto \psi'(x) = e^{iT^a\alpha_a(x)}\psi(x) \quad (1.39)$$

$G_{\mu\nu}^a$ are the 8 vector boson fields which mediate the strong interactions, known as gluons, and α are the 8 angles that, multiplied with the Gell-Mann matrices, give the transformation. The field strength tensor of QCD is:

$$G_{\mu\nu}^a = \partial_\mu G_\nu - \partial_\nu G_\mu + g_s f^{abc} G_\mu^b G_\nu^c \quad (1.40)$$

The field strength tensor in equation 1.40 is similar in form to that of QED apart from the extra term $g_s f^{abc} G_\mu^b G_\nu^c$ which, due to the non-abelian nature of SU(3), contains non-zero structure constants f^{abc} which give rise to 3 and 4-point self-interactions of the gluons. The covariant derivative is given by:

$$\partial_\mu \mapsto D_{\mu i} = \partial^\mu \delta_{ij} - ig_s t_{ij}^a G^{a\mu} \quad (1.41)$$

The subtle non-abelian nature of SU(3) has important the phenomenology of quarks and for how the strong force behaves at different energies. The next section, section 1.6, outlines these consequences in more detail.

1.6 The Strong Coupling and Asymptotic Freedom

In quantum field theories such as the SM, the vacuum state is not empty but can be considered as a sea of filled negative energy states. Fluctuations in the vacuum induce the creation of pairs of virtual particles, the fluctuations can be prompted by the available energy phase-space of a passing particle such as a photon in QED and as a result the vacuum fluctuations depend upon the momentum transfer of the particle. The effect of the virtual particles is that the charges they act to modify the charge of the incident particle as observed by other particles playing a role in the interaction. This effect is known as shielding. As a result, the coupling of the electromagnetic and strong interactions becomes dependent on the momentum transfer μ .

The diagrams in figure 1.3 show the cause of this effect.

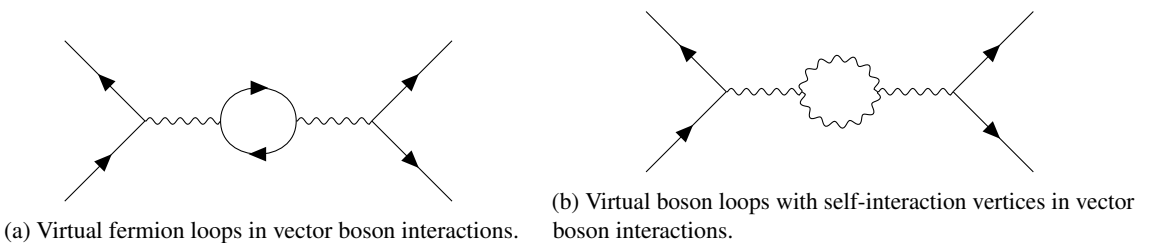


Figure 1.3: The virtual loops that cause the shielding/anti-shielding effects that cause the dependence of the QED and QCD coupling constants.

1.6 The Strong Coupling and Asymptotic Freedom

The effect of the left diagram is to reduce the effective coupling as the momentum transfer decreases. Conversely, the effect of the boson self-interaction in the right diagram has the effect of increasing the effective coupling. The QED Lagrangian contains no self-interaction terms for the photon fields and thus the diagram in 1.3(b) does not enter into matrix element calculations, whereas the self-interaction of the gluons in QCD allows for these interactions. The QCD and QED coupling constants thus depend on the momentum transfer with mirrored features, as illustrated in figure 1.4. In QCD the coupling strength as a function of momentum transfer Q^2 has the form:

$$\alpha_s(Q^2) = \frac{2\pi}{\beta_0 \ln(Q^2/\Lambda_{QCD})} \quad (1.42)$$

where $\beta_0 = 11 - \frac{2}{3}n_f$ and n_f is the number of quark flavours. As Q^2 increases the coupling strength decreases. The fact that quarks and gluons become asymptotically free in the large momentum transfer regime allows the accurate treatment of quarks and gluons as free particles when $Q^2 > \Lambda_{QCD}$ and a perturbative treatment is appropriate. Λ_{QCD} is known as the strong interaction scale and is the point at which the momentum transfer is small enough that the coupling constant is too large to be treated perturbatively. Phenomenologically, the feature that α_s tends to infinity as the momentum transfer decreases (increasing distance) is apparent as quarks and gluons are never observed as free particles, this is known as colour confinement. In nature only colour-neutral bound quark states known as hadrons (groups of 3 or more quarks) and mesons (quark anti-quark pairs) are observed.

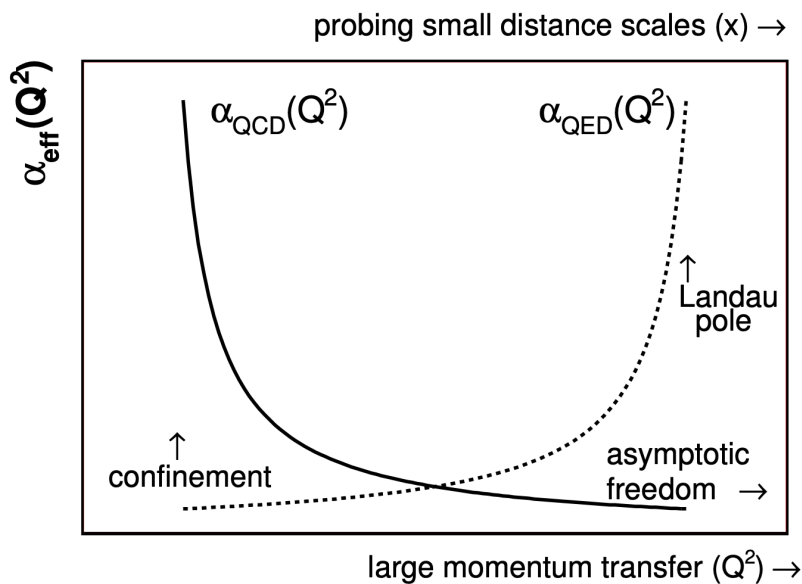


Figure 1.4: Illustration of the effective couplings of QCD and QED as a function of momentum transfer Q^2 .

1 The Standard Model

1.7 Yukawa Couplings of Fermions

The Higgs mechanism allows the introduction of mass terms for the leptons and quarks in a gauge invariant way via Yukawa interactions with the Higgs field. These take the form of additional terms in the lagrangian:

$$\mathcal{L}_Y(l) = -G_f[\bar{\chi}_L \Phi f_R + \bar{f}_R \Phi^\dagger \chi_L] \quad (1.43)$$

which becomes (in unitary gauge):

$$\mathcal{L}_Y(l) = \frac{-G_f v}{\sqrt{2}} (\bar{f} l) - \frac{-G_f}{\sqrt{2}} (\bar{f} f H) \quad (1.44)$$

and the mass term for the fermion, f , is $m_l = \frac{-G_f v}{\sqrt{2}}$ and it couples to the Higgs field with $\frac{-G_f}{\sqrt{2}} = \frac{m_f}{v}$ where G_f is the Yukawa coupling. These relationships show that particles with greater mass have a stronger coupling to the Higgs. This feature has important impact on phenomenology of physics including the Higgs boson. When calculating radiative corrections the heavier fermions that couple to the Higgs, namely the top and bottom quarks in the SM, have the largest impact on e.g. corrections to the Higgs vacuum expectation value. If we are to take the SM particle content as complete, calculations of the radiative corrections to the Higgs mass from particles that interact with the Higgs field appear to require very unnatural fine tuning to bring the Higgs mass down to the electroweak scale observed in nature. This is known as the Hierarchy Problem, it is discussed in [2.1.1](#) and has important consequences for possible phenomenology of massive particles in extensions beyond the Standard Model.

1.8 Phenomenology of the Standard Model

The fermion and gauge boson content of the Standard Model is summarised in tables [1.1](#) and [1.2](#) where we can classify the particles by their spin, electric charge and mass.

Gen	Quarks			Leptons		
		Charge (e)	Mass		Charge (e)	Mass
I	Up u	+2/3	2.16 MeV	Electron e	-1	0.511 MeV
	Down d	-1/3	4.67 MeV	e -neutrino ν_e	0	<1.1 eV
II	Charm c	+2/3	127 MeV	Muon μ	-1	105.7 MeV
	Strange s	-1/3	93 MeV	μ -neutrino ν_μ	0	<0.19 MeV
III	Top t	+2/3	172.8 GeV	Tau τ	-1	1.78 GeV
	Bottom b	-1/3	4.18 GeV	τ -neutrino ν_τ	0	<18.2 MeV

Table 1.1: Fermions of the Standard Model showing the charge and mass of each particle, all fermions have spin 1/2.

1.8 Phenomenology of the Standard Model

The fermion content is composed of the up and down-type quark fields and the lepton fields. The quarks carry both electric and colour charge and interact with the strong, weak and electromagnetic forces. These come in 3 generations which mirror each other in all but their masses - subsequent generations have increasing mass. The leptons, which are comprised of the left and right-handed charged components and the left-handed neutral neutrinos, also come in 3 generations with the same feature of increasing masses. The leptons do not carry colour charge so do not interact via the strong force. The neutrinos of the SM carry no electric charge so only interact via the weak force.

The boson content comprises the vector bosons which mediate the fundamental forces: the neutral photon mediator of electromagnetism, neutral Z and charged W^\pm mediators of the weak interactions, and the 8 gluons which mediate the strong interaction between quarks. In addition there is also the higgs boson which is special, being a scalar particle, it is the Goldstone Boson of the Higgs field.

SM Bosons		Charge (e)	Spin	Mass
Z	Z	0	1	91.2 GeV
W	W^\pm	± 1	1	80.4 GeV
Photon	γ	0	1	0
Gluon	g	0	1	0
Higgs Boson	h	0	0	125.1 GeV

Table 1.2: Bosons of the Standard Model showing the charge, spin and mass of each particle.

The Standard Model is the most successful theory of nature developed. Its predictions have agreed with almost every experiment designed to scrutinise it and it provides a precise and wide-ranging view of nature. It is, however, clear that it cannot be the full story.

1 The Standard Model

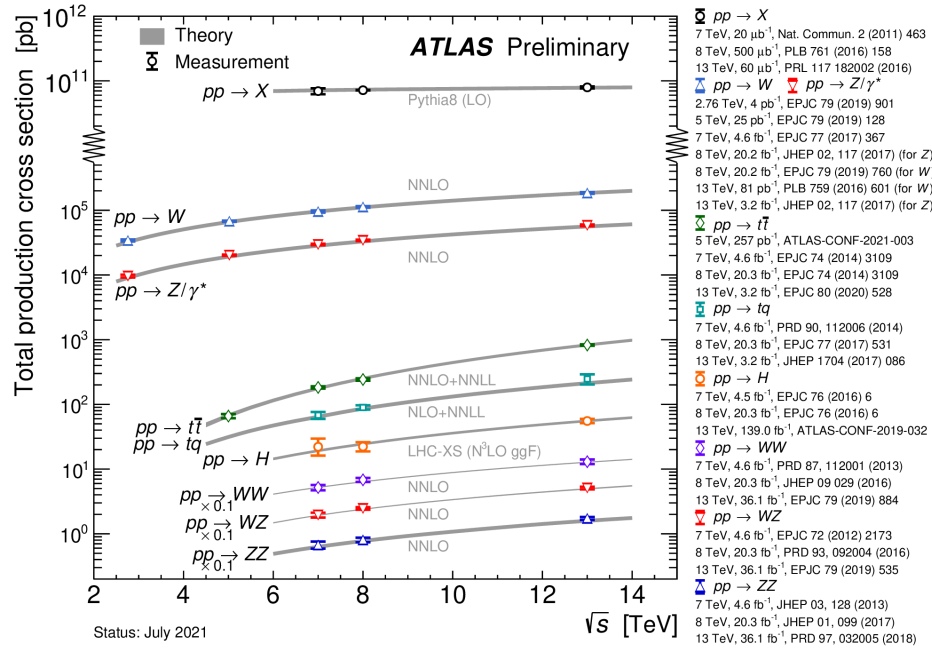


Figure 1.5: Summary of the total production cross-section for a variety of processes measured in proton-proton collisions with centre-of-mass energies between 2.76 and 13 TeV. The measured values are compared with SM theoretical calculations at next-to,next-to leading order in the strong coupling or higher. All of the measurements made agree with the SM prediction to great accuracy.

2 Beyond the Standard Model

Although the Standard Model provides our current best description of the sub-atomic world, there are many observations of nature that it does not describe. The clearest insufficiency is that it provides no description of the remaining fundamental force: gravity. In addition, some features of the theory contain inconsistencies or require unnatural modification in order for it to be accurate. The SM also gives no explanation for the presence or nature of dark matter and dark energy which are indicated by cosmological observations and thought to make up around 95% of the mass-energy content of the universe. These observations motivate the pursuit of an extension beyond the SM in its current formulation.

The space for extensions to the SM is vast, including additional symmetries, new particle and gauge fields and additional dimensions. Sections 2.2 and 2.3 introduce some of the most well-motivated and studied of these extensions to the SM which address some of the SM's outstanding issues.

2.1 Open questions in the Standard Model

This section will discuss briefly some of the key areas in which the SM falters: the Hierarchy Problem, which relates to the unexplained gap between the energy scale of electroweak symmetry breaking and the Plank scale; Gauge unification, which is required in order to have a complete theory which unifies the gauge interactions in the early universe; the origin of neutrino masses, which must arise to be in accordance with observations of neutrino mixing; and Matter-Antimatter asymmetry, the question of why there is so much matter remaining in the universe and seemingly no anti-matter. These outstanding issues are the main source of inspiration when constructing extensions beyond the SM. A development beyond the SM should aim to solve some of these issues and produce a better theory than the current one.

2.1.1 The Hierarchy Problem

The Higgs mass that is observed in nature and sets the scale for the electroweak sector of the Standard model is given by the bare mass attributed to the particle plus quantum corrections arising from particles that interact with it:

$$m_h^2 = m_{h-\text{bare}}^2 + \Delta m_h^2 \quad (2.1)$$

2 Beyond the Standard Model

where Δm_h^2 is the term containing the quantum corrections. The SM fermions that couple to the Higgs field with the term $-\lambda_f H \bar{f} f$ give 1-loop corrections illustrated in figure 2.1.

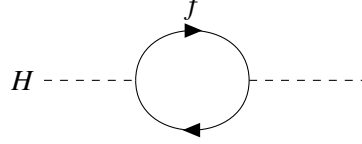


Figure 2.1: 1-loop fermion interaction with the Higgs boson.

The corrections to the squared Higgs mass take the form:

$$\Delta m_H^2 = \frac{-|\lambda_f|^2}{8\pi^2} \Lambda_{UV}^2 + \dots \quad (2.2)$$

In equation 2.2 the correction has a quadratic dependance on Λ_{UV} , the ultraviolet cut-off scale which should be greater than or equal to the energy at which the theory is affected by physics of higher energies. This cut-off is generally placed close to the Plank scale: $M_P \sim 10^{18}\text{GeV}$ and as a result corrections coming from these kind of interactions are of order greater than 10^{30}GeV . Since the measured value of m_h is $\approx 125\text{GeV}$ the bare mass, $m_{h-\text{bare}}$, must cancel the quantum corrections to such astounding precision that it is considered unnatural. Rather than accept this cancellation as pure fluke, it is likely that this is an indication of some underlying theory that prescribes that the electroweak scale is where it is observed to be. BSM theories are often based around solving the Hierarchy problem via additional gauge bosons and fermion-boson symmetries as discussed in section 2.2.

2.1.2 Gauge Unification

Higher order calculations of the SM gauge interactions show that the couplings of the strong, weak and electromagnetic interactions all vary with increasing energy scale of interactions, as illustrated in figure 2.2.

In the SM the coupling strengths approach similar values at a very high energy, the strengths of the 3 interactions become close but are not predicted to precisely unify exactly at a given energy. If the trajectory of the couplings were to be modified slightly by interactions beyond the Standard Model then the coupling strengths could unify at high energy. This gives an indication that fundamental gauge forces of the SM could be unified into a single force above this energy, and in principle with gravity above the Planck scale.

The concept of aligning the fundamental forces under one unified force at very high energy is coherent with the chronology of the universe within the Big Bang theory. In the very early moments, known as the Planck epoch (less than 10^{-43}s after the Big Bang), all the forces were unified as a single force. Then, as the universe expanded and the energy of interactions lowered, gravity separated from the nuclear and electromagnetic forces. At 10^{-36}s the strong and electro-weak forces separated, the

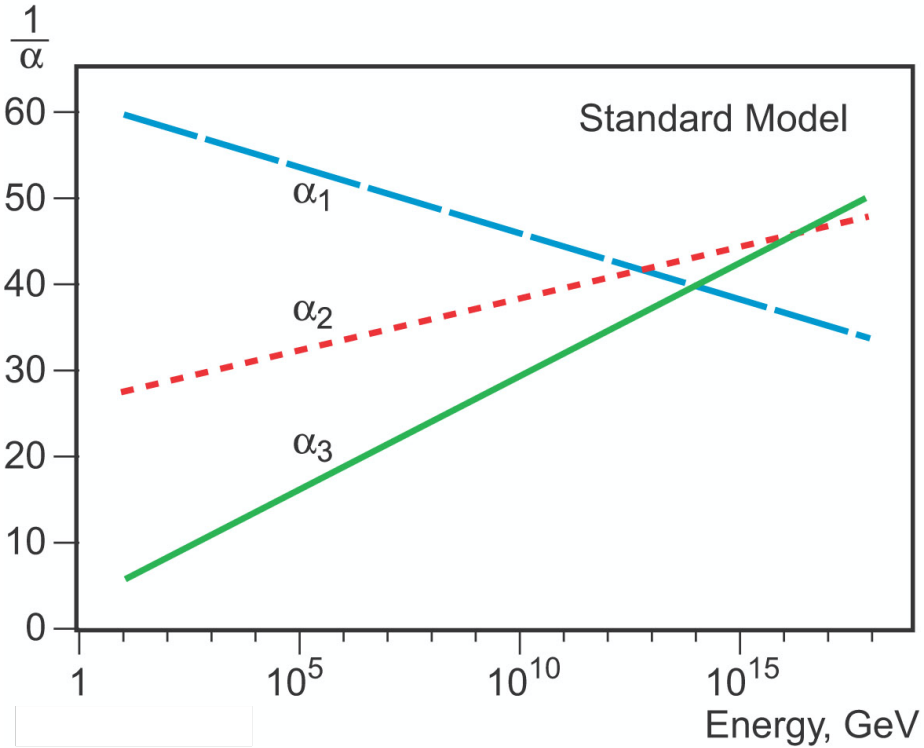


Figure 2.2: Running of the couplings of the gauge interactions of the Standard Model.

separation is thought to be responsible for the period of rapid inflation of the universe which is required to explain cosmological observations of uniformity [8] [9]. At 10^{-11} s, the electromagnetic and weak forces separated and we arrive at the 4 fundamental forces that we observe today. Unification of the couplings is desirable in Grand Unified Theories (GUTs) within which the SM is the low energy representation of the theory. The motivation is that a GUT encompasses the symmetries of the lower energy representations under one unified symmetry group.

Supersymmetry (section 2.2) is one such extension to the SM which allows the modification of the gauge couplings such that they unify. This is one of the key motivations for the searches discussed in this work (sections 8, 9).

2.1.3 Dark Matter

In the early 20th century observations of the velocities of stars orbiting galaxies and the motions of galaxy clusters indicated that the cumulative mass of gravitationally interacting matter in these systems was far more than could be accounted for by the observed matter of stars and gases. These observations indicate that an unobserved form of matter exists within galaxies that interacts gravitationally but has no electromagnetic or strong interactions and whose abundance far outweighs that of ordinary matter in the universe. Further astronomical studies show the impact of dark matter in the early universe in

2 Beyond the Standard Model

the cosmic microwave background (CMB). By studying local fluctuations in the temperature of the CMB through the CMB power spectrum, the densities of overall matter and baryonic matter can be extracted. Figure 2.3 shows the temperature variation at points in the measured regions as a function of the multipole moment - a measure of the angular resolution (inversely proportional to the size of the angle considered).

The Plank experiment in 2018 measured the baryonic density as $\Omega_b = 0.02233 \pm 0.00015$ but overall mass density as $\Omega_m = 0.1428 \pm 0.0011$. This leads to the conclusion that the dark matter relic density is $\Omega_c h^2 = 0.120 \pm 0.001$ [10]. Many of the explanations put forward for this type of matter describe the existence of additional, stable, weakly interacting massive particles (WIMPs) that would mediate the necessary gravitation but be unobserved with traditional methods. Some known forms of matter within the SM do have these properties, namely neutrinos. Neutrinos are known to have a small mass, the strongest limit on the neutrino mass scale from studies of Beta decay in tritium, place an upper limit of $\lesssim 1.1$ eV [11]. However, their abundance and masses are far too small to account for the gravitational effects observed, the upper bound for neutrino relic density is $\Omega_\nu h^2 < 0.003$. In addition, since neutrinos obey Fermi-Dirac statistics, the density that neutrinos can have is limited - this limit prescribes that the neutrino density is lower than that of observed regions of high dark matter density in irregular galaxies.

The dark matter candidates discussed in this work, both within SUSY (section 8 and 9) and explicit dark matter models (10), have WIMP attributes and the model parameters are motivated by constraints from the observed dark matter relic density from the Planck experiment and others.

A multitude of non-WIMP dark matter theories exist. Axions arose as a solution to the strong CP problem [12] where an additional, spontaneously broken $U(1)_{PQ}$ is introduced, the Goldstone boson of the symmetry breaking is the axion which would be long-lived with small couplings to other SM particles and massive. Sterile neutrinos, discussed in 2.1.4, are right-handed partners to the SM neutrinos, that could explain neutrino masses and mass eigenstate mixing and in addition could be heavy, stable and weakly interacting. Non-particle explanations for the dark matter observations do exist such as modified Newtonian dynamics and primordial black holes though these proposals tend to have significant drawbacks in explaining the array of DM cosmological phenomena simultaneously.

2.1.4 Neutrino Masses

Within the Standard Model, only left-handed neutrinos and right-handed anti-neutrinos exist. They are considered to be Dirac fermions and therefore must have left-handed and right-handed components in order to receive a Dirac mass term of the form:

$$m_\nu \bar{\nu}_R \nu_L \quad (2.3)$$

The SM forbids neutrino mass terms since they are either not invariant under weak isospin or violate fermion number conservation. If the neutrinos are considered to be massless then their flavour states and mass eigenstates are identical and processes such as $\nu_\mu \rightarrow \nu_e$ are forbidden. However, in the late

2.1 Open questions in the Standard Model

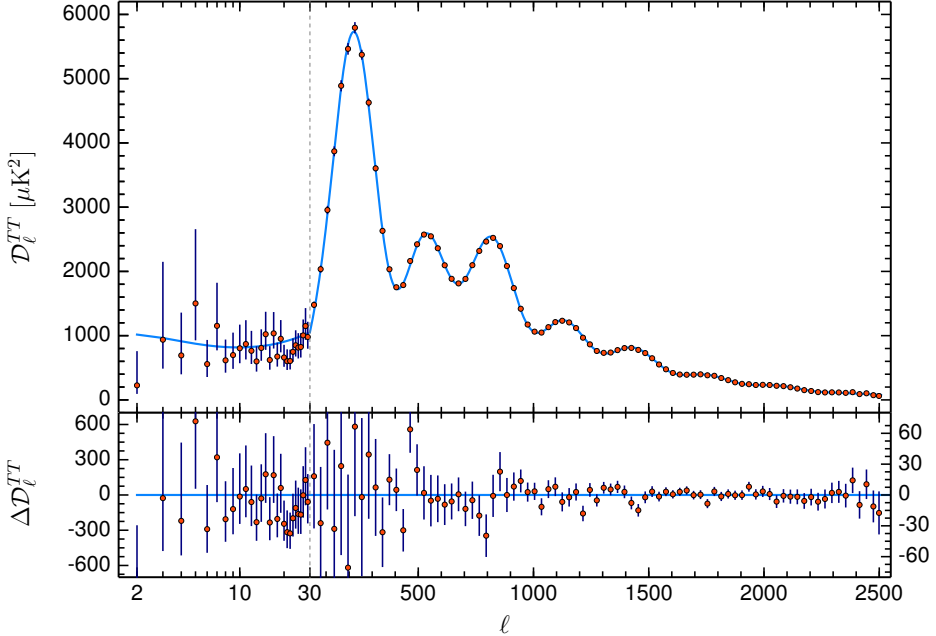


Figure 2.3: The temperature power spectrum of the CMB using data collected from the Planck telescope [10], showing the fit of base- Λ CDM (cold dark matter) which parameterises the big bang model describing the evolution of the universe with expansion from dark energy and large-scale structure formation from dark matter.

20th century experiments studying the neutrino flux coming from solar nuclear interactions found under-fluctuations of the expected neutrino rates, and surprisingly, different experiments observed different fluctuations dependent on the processes used to identify the neutrino. In the 1990's results from the Kamiokande and Super-Kamiokande experiments and Sudbury Neutrino Observatory (SNO) [13–15] showed the same phenomenon in atmospheric neutrinos - they measured ν_e rates to be as predicted but a large under-fluctuations in ν_μ rates which depended strongly on the distance that the neutrino travelled before being detected. This was the experimental indication of neutrino oscillations and the 'missing' muon neutrinos were found to be represented in increased ν_τ rates. The oscillation $\nu_\mu \rightarrow \nu_\tau$ is allowed if the neutrino eigenstate is a mass eigenstate constituting a mixture of neutrino flavours and thus the neutrinos must have a small but non-zero mass.

There are many proposed extensions to the SM that introduce neutrino masses such as the introduction of effective Higgs couplings to the neutrinos, yielding very small masses through suppression at some very high mass scale in which new physics is introduced. A prominent model for extending the SM picture is with the introduction of a right-handed neutrino field and the requirement that neutrinos are Majorana fermions (they are their own anti-particles with the difference being the spin). With these assumptions in place the neutrinos receive two mass terms-Dirac and Majorana.

$$\mathcal{L}_{\nu\text{-mass}} = m_\nu \nu_L \nu_R + \frac{1}{2} M_\nu \nu_R \nu_R \quad (2.4)$$

where m_ν is the Dirac term and M is the Majorana mass term. If the left and right-handed states then

2 Beyond the Standard Model

mix upon interaction with the Higgs field the mass eigenstates can be observed as a pair of a very light and a very heavy neutrino, which is known as the 'see-saw' mechanism of type I :

$$\nu_{light} \approx \nu_L + \left(\frac{m_\nu}{M_\nu}\right)\nu_R \approx \nu_L \quad (2.5)$$

$$\nu_{heavy} \approx \nu_R - \left(\frac{m_\nu}{M_\nu}\right)\nu_L \approx \nu_R \quad (2.6)$$

The heavier neutrinos would be 'sterile' having no charges under the SM gauge groups. If heavy sterile neutrinos exist they could be observed in collider experiments searching for evidence of heavy neutral fermions, though, in these models sterile neutrino masses are allowed up the GUT scale and so could be out of the reach of collider experiments. Evidence for sterile neutrinos can also be sought by observing lepton number violating processes such as neutrinoless double beta decay, which would indicate that neutrinos have Majorana masses.

2.1.5 Matter-Antimatter asymmetry

In the known universe we observe only stable matter in our local surroundings, though from the Dirac equation we would expect that matter and antimatter were produced in equal proportions in the early universe and that the evolution of the universe would result in all matter and antimatter annihilating after the temperature of the universe cooled enough that photons could escape the immediate interactions with particles. We would expect to be left with a universe composed entirely of radiation.

In order to arrive at the matter prevalence we see today, matter and antimatter must interact slightly differently in order for baryogenesis to occur. The conditions which we need for this to happen are known as the Sakharov conditions [16]:

1. violation of Baryon number;
2. charge and Charge-Parity (CP) violation;
3. interactions occur outside thermal equilibrium.

No observations of interactions that violate baryon number conservation have been observed. The Standard Model is known to allow Charge-Parity violating interactions in the weak sector contained within the CKM matrix. It is thought that this violation at low energies holds for the much higher energies of the early universe. The CP-violation of the CKM matrix contributes to baryon asymmetry at 3-loop level and is not enough to account for the matter dominance we see.

2.1.6 Muon anomalous magnetic moment ($g-2$)

To date, precision measurements of the SM predictions have not yielded any deviation with significance greater than the 5σ mark commonly accepted as required to claim discovery. However there have been long-standing precision measurements of lepton properties that are in tension with the predictions of the SM to lesser extent. Notable are the lepton universality anomalies measured in ratios of b-meson decays to electrons and muons with the LHCb experiment [17][18]. The most interesting for BSM scenarios is the measurement of the muon anomalous magnetic moment which was measured to be greater than the SM prediction by the Brookhaven National Lab (BNL) in 2011 at significance of 3.7σ [19]. 10 years later the measurement has been repeated with the E989 experiment [20] in a new experimental setup at the Fermi National Laboratory and confirmed the BNL result increasing the significance to 4.2σ (figure 2.4).

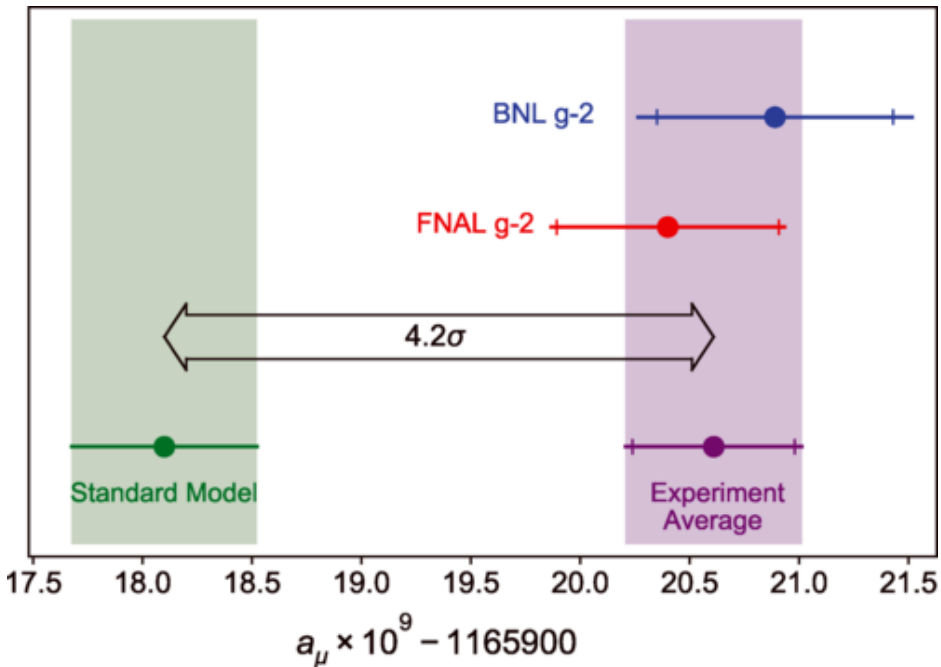


Figure 2.4: Results of the BNL and FNAL $g-2 \mu$ measurements and their combined average, compared with the accepted theoretical value from the muon $g-2$ theory initiative [21].

BSM theories involving new particles and interactions often impact the leptonic anomalous magnetic moment through additional virtual interactions which modify the way the muon interacts with the electromagnetic field. The change in the anomalous magnetic moment due to the influence of BSM particles is denoted Δa_μ . The muon is particularly sensitive to these due to its high mass relative to the electron. The Feynman diagrams for new particle interactions that affect the magnetic moment of the muon are shown in figure 2.5.

Proposed BSM scenarios are strongly motivated if they can provide explanation for the deviation from the SM. Conversely, if a more complete extension to the SM does not explain the anomaly, then this

2 Beyond the Standard Model

can be considered less well motivated as this itself would require additional extension.

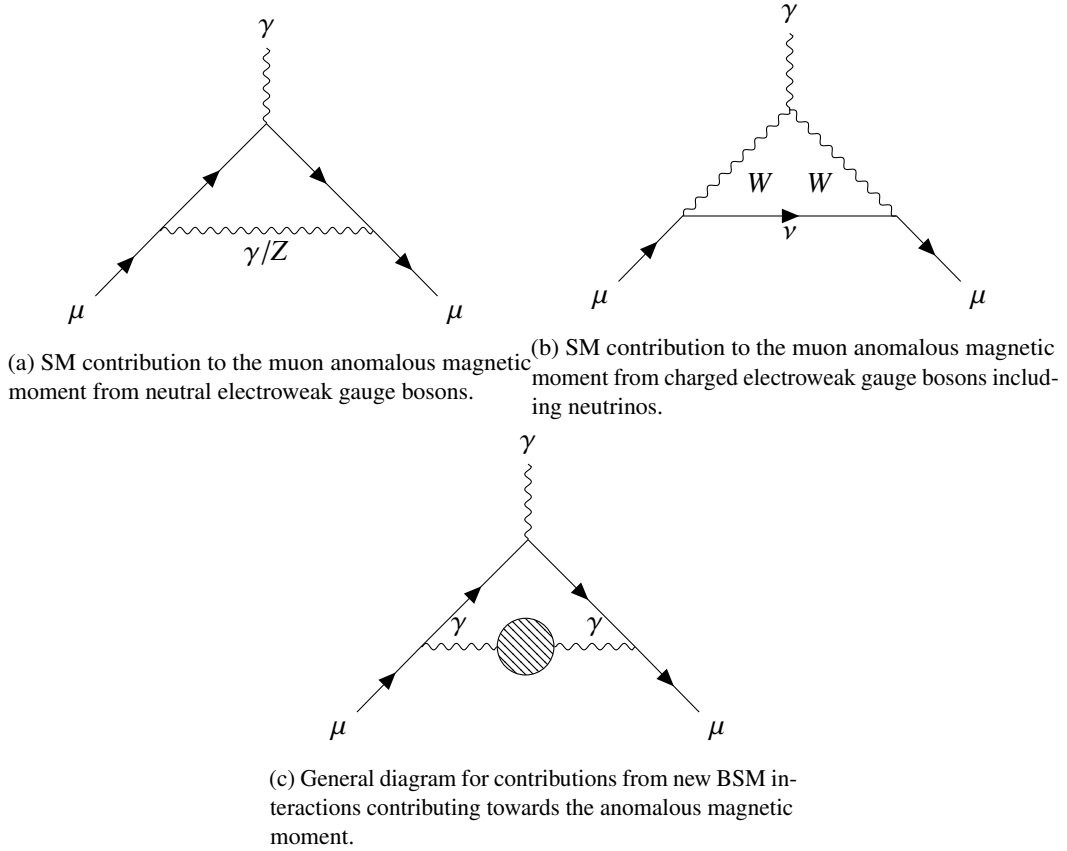


Figure 2.5: Feynman diagrams for processes that contribute to the muon anomalous magnetic moment, including possible BSM contributions illustrated in 2.5(c).

2.1.7 Further Open Questions and BSM Theories

There are many further questions about the properties of the particle content of nature that the SM does not answer: why do we only observe 3 fermion generations and not more and why are the relative masses of the fermions so vastly different between generations? Other missing pieces seem further out of the reach of current theories and experimental tests: how is gravity quantised and how to incorporate general relativity, what is the origin of Dark Energy - which is thought to cause the expansion of the universe.

In the following section a complete BSM extension which is able to address many of these open questions is introduced - Supersymmetry. More targeted BSM scenarios, using a bottom-up approach to explain dark matter are introduced in section 2.3.

2.2 Supersymmetry

The main theoretical basis for building extensions to the Standard Model is the introduction of additional symmetries which also encapsulate or at least allow for the $SU(3)_c \times SU(2)_L \times U(1)_Y$ symmetry group of the SM. In supersymmetric theories an additional space-time symmetry is introduced which relates spin states. The symmetry can be expressed as a unitary operator, Q , that converts fermionic states into bosonic states and vice-versa:

$$Q|fermion\rangle = |boson\rangle, \quad Q|boson\rangle = |fermion\rangle \quad (2.7)$$

The specific nature of viable symmetry extensions to the SM is heavily constrained by the Coleman-Mandula theorem [22] and its extensions [23] which state that a non-trivial symmetry cannot be constructed from a combination of space-time and internal symmetries under a standard Lie algebra. This appears to forbid new symmetries like that shown in eq 2.7 but, however, the theorem can be circumvented if the symmetry is constructed as a Lie *superalgebra* rather than a Lie algebra as in the SM. This is the formulation that supersymmetry takes. The operator Q and its hermitian conjugate Q^\dagger are fermionic and have commutations:

$$\{Q, Q^\dagger\} = P^\mu \quad (2.8)$$

$$\{Q, Q\} = \{Q^\dagger, Q^\dagger\} = 0 \quad (2.9)$$

$$[P^\mu, Q] = [P^\mu, Q^\dagger] = 0 \quad (2.10)$$

where P^μ are the generators of space-time translations and rotations. The particles under a supersymmetric theory are composed of pairs of boson and fermion states in the fundamental representation, known as *supermultiplets*. The operators commute with the generators P^μ allowing the theory to be relativistically viable. The same is true for the generators of the SM gauge symmetries, thus the superpartners have the same SM gauge quantum numbers. The phenomenological basis for SUSY as an extension to the SM is that the known SM particles are one side of the supermultiplets and thus a complete set of so-far unobserved superpartners exist with a difference in spin of 1/2 with respect to their SM counterparts.

The simplest supersymmetric extension to the SM which is consistent with the SM phenomenology is the minimal supersymmetric Standard Model (MSSM). The phenomenology of the MSSM is as follows: the SM fermions are proposed to exist in chiral supermultiplets with each helicity state being paired with a scalar superpartner. The Standard Model gauge bosons are part of a gauge supermultiplet with the vector bosons being paired with a spin 1/2 Weyl fermion with 2 helicity states. The nomenclature given to the superpartners is to prepend an 's' (scalar) to the name of the SM partner if the SM particle is a fermion and to append 'ino' if the SM particle is a boson.

2 Beyond the Standard Model

The Higgs component of a supersymmetric extension to the SM requires some further development. In order to avoid gauge anomalies with the introduction of fermion superpartners to the Higgs and to allow the necessary Yukawa couplings to up and down-type quarks, an additional $SU(2)_L$ doublet field must be introduced. The two doublet fields are referred to as H_u and H_d . H_u contains a positively charged and a neutral component whereas H_d contains a neutral and a negatively charged component. The particle content of the MSSM is summarised in table 2.1.

Chiral supermultiplets	spin 0	spin 1/2	$SU(3)_c \times SU(2)_L \times U(1)_Y$
squarks, quarks	Q	$(\tilde{u}_L, \tilde{d}_L)$	$(\mathbf{3}, \mathbf{2}, \frac{1}{6})$
	\bar{u}	\tilde{u}_R^*	$(\bar{\mathbf{3}}, \mathbf{1}, \frac{-2}{3})$
	\bar{d}	\tilde{d}_R^*	$(\bar{\mathbf{3}}, \mathbf{1}, \frac{1}{3})$
sleptons, leptons	L	$(\tilde{v}e_L)$	$(\bar{\mathbf{1}}, \mathbf{2}, \frac{-1}{2})$
	\bar{e}	\tilde{e}_R^*	$(\bar{\mathbf{1}}, \mathbf{2}, 1)$
Higgs, Higgsinos	H_u	$(H_u^+ H_u^0)$	$(\bar{\mathbf{1}}, \mathbf{2}, \frac{+1}{2})$
	H_d	$(H_d^0 H_d^-)$	$(\bar{\mathbf{1}}, \mathbf{2}, \frac{-1}{2})$
Gauge supermultiplets	spin 1/2	spin 1	
gluino, gluon wino, W bosons bino, B boson	\tilde{g}	g	$(\mathbf{8}, \mathbf{1}, 0)$
	$\tilde{W}^\pm \tilde{W}^0$	$W^\pm W^0$	$(\mathbf{1}, \mathbf{3}, 0)$
	\tilde{B}^0	B^0	$(\mathbf{1}, \mathbf{1}, 0)$

Table 2.1: Chiral and Gauge supermultiplets of the MSSM.

Since the supersymmetric operators Q and Q^\dagger commute with the 4-momentum operator P^2 , if supersymmetry were a perfect symmetry in nature, the superpartners would have the same mass as their SM counterparts. Since we do not observe the superpartners at the same mass as the SM particles with spin difference 1/2, we must conclude that SUSY is broken in some way and that the superpartner masses are above the scale of the SM. This symmetry breaking, along with electroweak symmetry breaking of the SM, allows mixing of gauge eigenstates of the supermultiplets. The phenomenology of mass eigenstates that results is illustrated in table 2.2.

The SUSY mass eigenstates shown in table 2.2 for the weak sector are different to the SUSY multiplets in table 2.1. The multiplets \tilde{W}^0 and \tilde{W}^\pm , so-called *winos*, are the partners to the $SU(2)_L$ gauge bosons and \tilde{B}^0 , the *bino*, is the partner to the $U(1)_Y$ gauge boson before electroweak symmetry breaking. The mass eigenstates that are realised are a mixture of these with the Higgsinos, which are discussed in more detail in section 2.2.1.

Sector	Gauge eigenstates	Sparticle mass eigenstates
Quark Sector	$\tilde{u}_L \tilde{u}_R, \tilde{d}_L \tilde{d}_R$	$\tilde{u}_1 \tilde{u}_2, \tilde{d}_1 \tilde{d}_2$
	$\tilde{c}_L \tilde{c}_R, \tilde{s}_L \tilde{s}_R$	$\tilde{c}_1 \tilde{c}_2, \tilde{s}_1 \tilde{s}_2$
	$\tilde{t}_L \tilde{t}_R, \tilde{b}_L \tilde{b}_R$	$\tilde{t}_1 \tilde{t}_2, \tilde{b}_1 \tilde{b}_2$
Lepton Sector	$\tilde{e}_L \tilde{e}_R, \tilde{\nu}_{e_L}$	$\tilde{e}_L \tilde{e}_R, \tilde{\nu}_{e_L}$
	$\tilde{\mu}_L \tilde{\mu}_R, \tilde{\nu}_{\mu_L}$	$\tilde{\mu}_L \tilde{\mu}_R, \tilde{\nu}_{\mu_L}$
	$\tilde{\tau}_L \tilde{\tau}_R, \tilde{\nu}_{\tau_L}$	$\tilde{\tau}_L \tilde{\tau}_R, \tilde{\nu}_{\tau_L}$
Higgs and Electro-weak sector	$H_u^0 H_u^+ H_d^0 H_d^-$	$h_0 H^0 A^0 H^\pm$
	$\tilde{W}^0 \tilde{B}^0 \tilde{H}_u^0 \tilde{H}_d^0$	$\tilde{\chi}_4^0 \tilde{\chi}_3^0 \tilde{\chi}_2^0 \tilde{\chi}_1^0$
	$\tilde{H}_u^+ \tilde{W}^\pm \tilde{H}_d^-$	$\tilde{\chi}_2^\pm \tilde{\chi}_1^\pm$
Strong sector	\tilde{g}	\tilde{g}

Table 2.2: New particles predicted in the MSSM and their gauge and mass eigenstates.

Despite the 'minimal' nomenclature, the MSSM still has over 100 free parameters. To reduce the set of free parameters the MSSM is often constrained into various subsets by further constraining theoretical assumptions. The phenomenological MSSM (pMSSM) is a well motivated and widely used model often used to evaluate sensitivity from experiments to realistic scenarios. The free parameter number of the MSSM is reduced to 19 by the following assumptions:

- The first and second generations quarks are mass degenerate
- R-parity is conserved
- The lightest supersymmetric particle is the lightest neutralino

In the following section the background of supersymmetry breaking will be briefly discussed. The following sections give descriptions of how SUSY can solve some of the outstanding problems in the SM: the hierarchy problem 2.2.2, gauge unification 2.2.3 and conditions required for a supersymmetric theory to provide a dark matter candidate 2.2.4.

2.2.1 SUSY Breaking

Since we do not observe the superpartners at the same mass as the known SM particles, we must conclude that SUSY is not a perfect symmetry, that is somehow broken, and that the superpartners have masses greater than their SM counterparts.

In general we expect that Supersymmetry is broken spontaneously, such that the lagrangian of the theory is itself invariant under supersymmetric transformations and that the benefits of the symmetry

2 Beyond the Standard Model

are preserved but that an additional field exists with a non-zero vacuum expectation that is not invariant. This is similar to the case of spontaneous electroweak symmetry breaking via the Higgs mechanism described in section 1.4. An effective lagrangian can be written:

$$\mathcal{L} = \mathcal{L}_{SUSY} + \mathcal{L}_{soft} \quad (2.11)$$

such that \mathcal{L}_{SUSY} is the invariant part of the effective lagrangian and \mathcal{L}_{soft} is the non-invariant part derived from spontaneous symmetry breaking at some higher energy scale. \mathcal{L}_{soft} must contain only mass terms and positive-mass coupling parameters in order to avoid the introduction of additional quadratic divergences that ruin the structure which provides the SUSY solution to the hierarchy problem.

With reference to table 2.2, after electroweak symmetry breaking superpartners of the electroweak sector and the Higgs sector mix to form the mass eigenstates. The resulting phenomenology is five Higgs particles, two charged and three neutral, where h_0 is the lowest mass and is thought to be the SM Higgs boson. The neutral Higgs fields also mix with the neutral electroweak gauge fields to produce 4 electrically neutral fermion sparticles: $\tilde{\chi}_i^0, i = 1, 2, 3, 4$, the *neutralinos*. The charged Higgs fields also mix with the charged electroweak gauge fields to produce charged mass eigenstates, the *charginos* $\tilde{\chi}_i^\pm, i = 1, 2$.

For the quark and lepton sectors, in principle all up-type/down-type squarks/leptons can mix (including across generations though this mixing is expected to be very small). The first two generations of squarks and sleptons have small Yukawa and soft couplings and as a result their mixing is small, the mass eigenstates of the left and right-handed pairs are unmixed and have similar masses. For third generation superpartners, which have large Yukawa couplings, the left and right-handed fields mix substantially. This substantial mixing has the effect of reducing the mass of the lighter of the pairings. Therefore in most models we would expect that the lighter top squark is the lightest squark and that the bottom squark and tau slepton are the lightest of the down-type squarks and the sleptons.

2.2.2 Supersymmetric solution to the Hierarchy problem

Having a natural resolution to the hierarchy problem is a strong motivation for SUSY. The notion that explanations of the world should be natural and elegant has lead to many breakthroughs in our scientific understanding [24]. Though an argument based on naturalness may seem subjective, we can consider the likelihood that the extremely precise choice of parameters in the Higgs VEV are chosen by nature compared with the likelihood that an underlying theory exists that enforces, in a natural way, that the electroweak scale is where we observe it. Cancellation of the terms in the radiative corrections to the Higgs mass imply explanation by an underlying symmetry. Naturalness arguments will also be used in section 2.2.5 as a guiding principle for motivating the details of SUSY phenomenology.

2.2 Supersymmetry

Equation 2.2 shows the corrections relating to fermion interactions with the Higgs at the order of Λ_{UV}^2 . A similar correction is expected for scalar particle's interactions:

$$\Delta m_H^2 = \frac{\lambda_S}{16\pi^2} \Lambda_{UV}^2 + \dots \quad (2.12)$$

The scalar terms have opposite sign to the fermionic corrections in equation 2.2. The proposition of a symmetry wherein the SM quarks and leptons have 2 scalar partners introduces the same number of positively and negatively signed contributions to Δm_H and if the couplings are related by $\Lambda_S = |\Lambda_f|^2$ then the contributing terms would cancel and the fine tuning is alleviated. This symmetry is precisely the one on which supersymmetry is based and the result is a strong motivation for the theory, which was not originally developed to solve the Hierarchy Problem.

This motivation of a natural solution to the Hierarchy Problem somewhat constrains the theory. On the other hand we know that SUSY must be broken in some way such that the superpartners differ in mass to their SM counterparts, but that 2-loop corrections to Δm_H contain terms related to the mass of the particles so for the naturalness argument to hold, the newly introduced particles must not have masses much above the TeV scale. This proposition is also a key motivation towards searching for supersymmetric particles in current collider experiments.

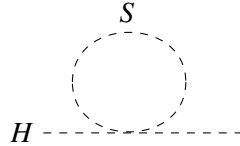


Figure 2.6: 1-loop scalar boson interaction with the Higgs boson.

2.2.3 Gauge Unification in Supersymmetry

Within the SM, the running of the gauge couplings $g_1 = \sqrt{\frac{5}{3}}g'$, $g_2 = g$, $g_3 = g_s$ with energy scale μ are governed by the renormalisation group equations:

$$\frac{dg_i}{dt} = \frac{g_i}{16\pi^2} [b_i g_i^2 + \frac{1}{16\pi^2} (\sum_{j=1}^3 b_{ij} g_i^2 g_j^2 - \sum_{j=1}^3 a_{ij} g_i^2 \lambda_j^2)] \quad (2.13)$$

where $t = \ln \mu / M_G$ and M_G is the scale of grand unification (GUT scale), λ_i are the Yukawa couplings of the particles and a_{ij} , b_{ij} and b_j are the coefficients that control the running. a_{ij} , b_{ij} and b_j depend on the particle content of the theory with masses less than μ . In the SM, there is no additional particle content between the weak scale ($\sim m_Z$) and M_G and thus the coefficients are constant. This results in the running illustrated in figure 2.2 where the interaction strengths nearly, but not quite, converge.

2 Beyond the Standard Model

As discussed in section 2.1.2, this is thought to be a shortcoming of the SM. If, however, we introduce the particle content of the MSSM at a scale of ~ 1 TeV, then the running is modified for scales above 1 TeV which can result in the unification of the gauge couplings at some high energy scale $\sim 10^{15}$ GeV as shown in figure 2.7. This resolution of gauge unification is an important motivating feature of SUSY when considered as part of a viable GUT.

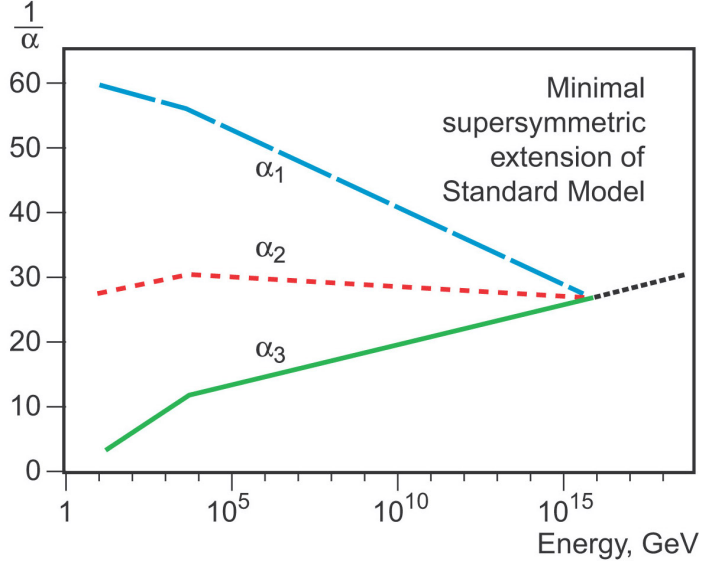


Figure 2.7: Running of the couplings of the gauge interactions in the MSSM with proposed particles around the TeV scale.

2.2.4 R-Parity

Supersymmetric lagrangians allow for terms that introduce violation of lepton and baryon conservation that is inbuilt in the SM. No observations have been made of baryon and lepton number violating processes and, in addition, the terms (if not heavily suppressed by some mechanism) would allow for un-reasonably short proton lifetimes where the proton can decay via channels such as shown in figure 2.8.

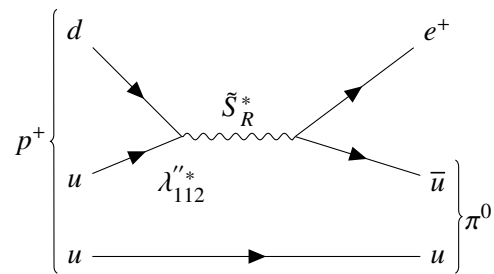


Figure 2.8: Proton decay via intermediate scalar violating baryon number conservation.

2.2 Supersymmetry

In order to impose that these vertices are forbidden, a symmetry is introduced that requires the conservation of a quantity known as R-parity, which is defined as:

$$P_R = (-1)^{3(B-L)+2s} \quad (2.14)$$

where B and L are the baryon and lepton numbers and s is the spin of the particle. From this definition the quark and lepton supermultiplets have $P_R = -1$ and the gauge supermultiplets have $P_R = +1$. The symmetry requires that terms in the lagrangian have total R-parity of +1. In order to preserve R-parity, each decay of a sparticle produces a SM particle and another sparticle. In R-parity respecting SUSY models, heavy SUSY particles tend to decay promptly to final states containing the lightest supersymmetric particle (LSP) which is often considered to be the lightest neutralino, $\tilde{\chi}_1^0$. The introduction of R-parity also imposes that the LSP is stable. This is an additional motivation for introducing conservation of the property as it simultaneously solves the issue of lepton and baryon number violation and enforces that the LSP is stable making it a good dark matter candidate.

The suppression of baryon and lepton number violating processes can be achieved in other ways where the vertices are allowed in the lagrangian but heavily suppressed. Such R-parity violating models lead to interesting signatures of superpartners with long lifetimes.

2.2.5 The SUSY mass spectrum and the Naturalness Guidance

In general, SUSY theories do not a-priori prescribe specific mass values for the superpartners introduced. This is clearly a problem when we consider how one would design methods for finding evidence for the particles, particularly when looking for direct evidence for their production in collider experiments. Two example mass spectra for the superpartners including the lightest Higgs boson (considered to be SM-like) are give in figure 2.9.

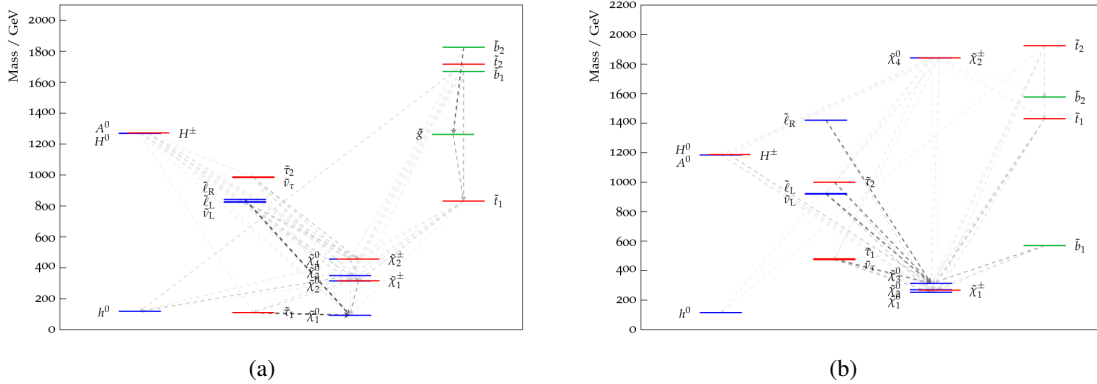


Figure 2.9: Plots of possible mass spectra with the MSSM.

In order identify sparticle mass spectra that are theoretically well motivated, we can re-visit one of the motivations for the introduction of SUSY - its elegant solution to the Hierarchy Problem, which is based on naturalness. A naturalness condition in the context of electroweak symmetry breaking can be loosely defined as requiring that the corrections to the quadratic terms in the Higgs potential are around

2 Beyond the Standard Model

the order of the electroweak scale. The condition can be summarised at tree level in the MSSM as [25]:

$$-\frac{m_Z^2}{2} = |\mu|^2 + m_H^2 \quad (2.15)$$

The first conclusion that can be gained is that the higgsinos should not be too heavy, since their mass is driven by the parameter μ - the supersymmetric equivalent of the Higgs mass in the SM. The second is that the particles that give the largest corrections to the Higgs mass cannot be too massive. The largest 1-loop correction to the Higgs mass is from the top squark via its Yukawa interaction [25] (at 1-loop LL):

$$\delta m_{H_u^2}|_{stop} = \frac{-3}{8\pi^2} y_t^2 (m_{Q_3}^2 + m_{u_3}^2 + |A_t|^2) \log(\frac{\Lambda}{\text{TeV}}) \quad (2.16)$$

Where $m_{Q_3}^2$ is the left-handed top squark mass and $m_{u_3}^2$ is the right handed top squark mass, y_t is the top Yukawa coupling and Λ is the scale at which SUSY soft symmetry breaking is introduced.

The gluino produces large 1-loop radiative corrections to the top squark mass and thus to the Higgs mass at 2-loop order and so must also not be too massive (2-loop LL):

$$\delta m_{H_u^2}|_{gluino} = \frac{-2}{\pi^2} y_t^2 (\frac{\alpha_s}{\pi}) |M_3|^2 \log^2(\frac{\Lambda}{\text{TeV}}) \quad (2.17)$$

where α_s is the strong coupling constant and M_3 is the gluino mass. From these equations and the naturalness definition 2.15, we observe that to ensure natural SUSY the top squark and gluino masses are constrained by the Higgs mass, m_H . The constraint on the top squark mass also implies a constraint on the bottom squark mass. If we require a light top squark, we in turn require that the left handed bottom squark is also not too massive, in order to preserve weak isospin symmetry.

Since the discovery in 2012 of a SM-like Higgs boson with a mass of around 125GeV there are additional constraints on SUSY phenomenology. Though the 3rd generation squarks are required by naturalness to be not too heavy, their masses are also bounded from below to ensure that the corrections to m_h (which is less than m_Z at tree level) are large enough to raise m_h to the observed Higgs mass of 125GeV. The radiative contributions from lighter squarks are far smaller than from the top and bottom squarks and as a result they can be considered to have large masses and be decoupled from the lighter parts of the spectrum . If the SM Higgs is the lightest Higgs in MSSM scenarios then in the limit of decoupling its mass is given by [26]:

$$m_h^2 = M_Z^2 \cos^2 2\beta + \delta_t^2 \quad (2.18)$$

where $\tan \beta$ is the ratio of the electroweak VEVs in the model and δ_t is the radiative correction coming from interactions with tops and top squarks. In order to have δ_t large enough to raise m_h to its observed value, either substantial mixing of top squarks, putting $m_{\tilde{t}} \sim 360\text{-}600\text{GeV}$ with maximal mixing, or very heavy top squarks $m_{\tilde{t}} > 3\text{TeV}$ and minimal mixing are required. This requirement of heavy top squarks can however be alleviated in the next to minimal supersymmetric Standard Model (NMSSM)

2.2 Supersymmetry

for example, where the Higgs mass parameter is instead a gauge singlet superfield [27].

The superpartners mass constraints proposed by naturalness can be summarised as [25]:

- the two top squarks and the left-handed bottom squark being around the TeV scale due to their corrections to m_h^2 ,
- two neutralinos and one chargino below around 200-250GeV due to higgsino masses driven by μ ,
- a gluino with mass below 900 GeV-1.5 TeV due to 2-loop corrections to m_h^2 .

Having proposed masses in these ranges gives good motivation to search for these particles in current hadron colliders such as the LHC, where the collision energy is high enough to produce these particles. A typical spectrum of naturalness motivated superpartner masses is given in figure 2.10, not that in this illustration the gluino masses are below those of the third generation squarks, however, in the analyses their masses are considered to be much greater and decoupled from the spectrum. The constraints on gluino masses are stronger than any other sparticles.

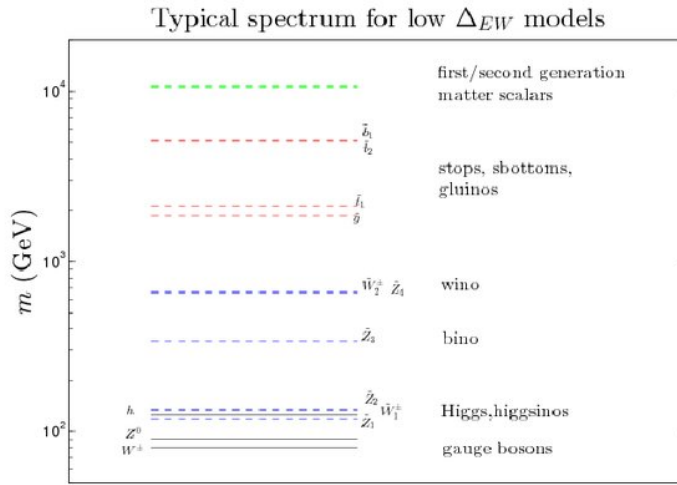


Figure 2.10: Typical spectrum of superpartner masses driven by naturalness in the Higgs mechanism.

2 Beyond the Standard Model

2.2.6 SUSY signatures

When considering the viability of discovering SUSY at colliders the production cross-section of the relevant sparticles must be considered. Production cross-sections can be calculated, making some relevant assumptions, as a function of the sparticle mass. Examples of production cross-sections for gluinos, 3rd generations squarks and electroweakinos are given in figure 2.11.

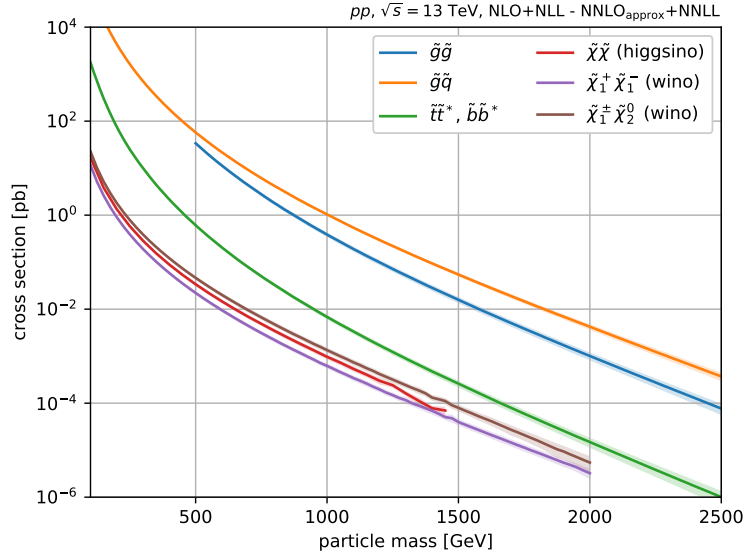


Figure 2.11: SUSY sparticle production cross-sections as a function of sparticle mass calculated and next-next-to-leading order + next-next-to leading log for proton-proton collisions with centre of mass energy of 13 TeV.

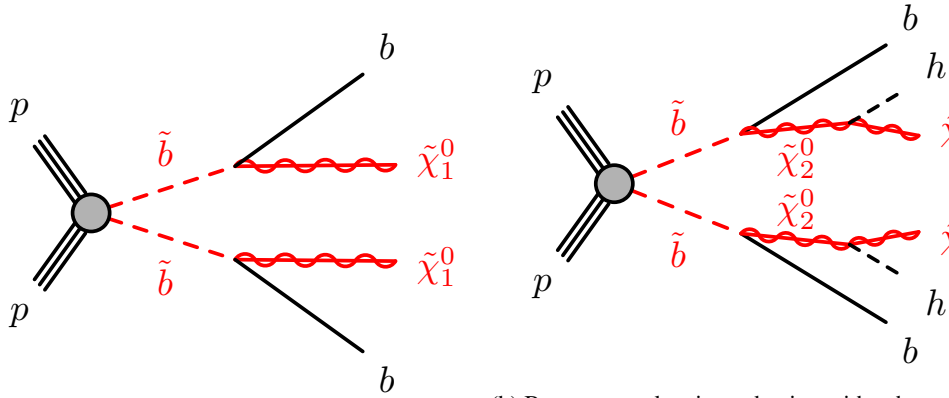
The processes with highest cross-section are gluino-gluino and gluino-squark production. The second highest are production of the 3rd generation squarks. Electroweakino production has a much lower cross-section. Since electroweakinos are more strongly motivated at lower masses the search for them is only becoming promising with the increasing dataset sizes such as those collected at the LHC.

The branching ratios of sparticle decays will depend on the sparticle mass eigenstate in question and its mixing. In so-called 'direct' decay models the sparticles are pair produced and decay directly to the LSP and another SM particle. The branching ratio of 3rd generation quarks often favours decays containing 3rd generation quarks. If heavier neutralinos are produced, their decay chains tend to involve SM electroweak bosons resulting in final states including the LSP.

The prevalence of different SM electroweak bosons in the decay chains is determined by the mixing of the electroweakino eigenstates and the SUSY mass parameters. For example, when $|\mu| \ll |M_1||M_2|$ the mass splittings between the lighter electroweakinos are small and the decays of $\tilde{\chi}_1^\pm$ and $\tilde{\chi}_2^0$ are dominated by off-shell W^* and Z^* . However, in scenarios where $|M_1| \leq |\mu|$ and $|M_2| > |M_1|$, the mass splitting is larger. Here the $\tilde{\chi}_1^0$ has a large Bino contribution, the higgs coupling $h\tilde{\chi}_2^0\tilde{\chi}_1^0$ is larger than

$Z \tilde{\chi}_2^0 \tilde{\chi}_1^0$ and $\tilde{\chi}_2^0 \rightarrow h \tilde{\chi}_1^0$ is the dominant decay. These scenarios have become especially interesting recently since the discovery of the Higgs and knowledge of its mass allows its presence to act as a handle for identifying these signatures. Two processes involving pair production of bottom squarks and a process with chargino-neutralino production are considered in the analysis sections:

- Pair produced bottom squarks, \tilde{b} , decaying symmetrically to a bottom quark and the lightest neutralino, $\tilde{\chi}_1^0$, illustrated in figure 2.12(a). This signature is studied in section 8.2.
- Pair produced bottom squarks, \tilde{b} , decaying symmetrically to a bottom quark and the second-lightest neutralino, $\tilde{\chi}_2^0$, which then subsequently decays to a higgs boson and the lightest neutralino, $\tilde{\chi}_1^0$, illustrated in figure 2.12(b). This signature is studied in section 8.3.
- The lightest chargino, $\tilde{\chi}_1^\pm$, is produced alongside the second-lightest neutralino, $\tilde{\chi}_2^0$. The chargino decays into a W and the lightest neutralino, whilst the second-lightest neutralino decays into a higgs boson and the lightest neutralino, $\tilde{\chi}_1^0$, illustrated in figure 2.13. Searches for this signature are described in chapter 9.



(a) Bottom squark pair production with subsequent decay to b-quarks and the second-lightest neutralino which decay to b-quarks and the lightest neutralino.
 (b) Bottom squark pair production with subsequent decay to b-quarks and the second-lightest neutralino which decays to the lightest neutralino and a Higgs.

2.2.7 SuperSymmetry and the g-2 anomaly

With reference to the g-2 discussion in section 2.1.6, the BSM framework that is most accommodating of the anomaly is the MSSM. Here, positive contributions to Δa_μ arise from interactions of the muon with the electric field via new fermions and scalars in the loops. These additional interactions are mediated via sleptons and electroweakinos, the diagrams are given in figure 2.14.

Considering the introduction of new particle interactions in the MSSM as the sole explanation to the muon g-2 provides additional guidance on the viable model parameters. All contributions from MSSM interactions to a_μ are related linearly to the ratio of the Higgs VEVs, $\tan\beta = v_u/v_d$. At 1-loop level, considering $M_{SUSY} >> M_Z$, the dominant contributing parameters, alongside $\tan\beta$, are the electroweakino mass parameters: M_1, M_2 and μ , and the smuon masses: $m_{\tilde{\mu}_{L/R}}$. The viable parameter

2 Beyond the Standard Model

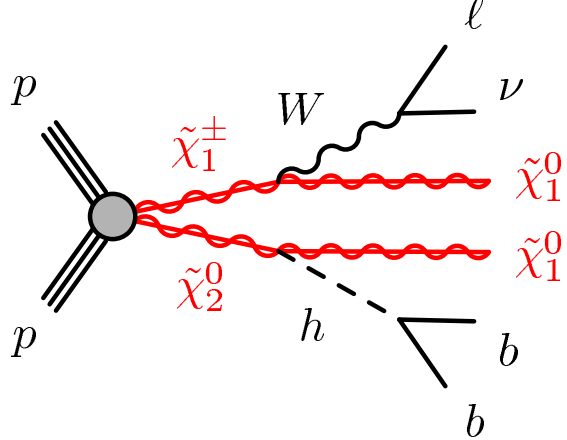


Figure 2.13: Chargino-Neutralino production decaying via a W boson and the lightest neutralino, a Higgs and the lightest neutralino, with final state of 2 b -quarks and 1-lepton.

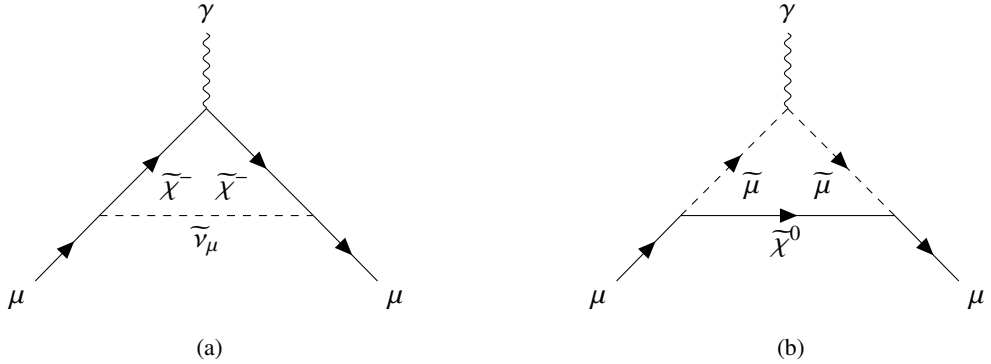


Figure 2.14: Feynman diagrams for Supersymmetric contributions to the muon anomalous magnetic moment.

space can be spanned by the masses of the heaviest chargino and lightest smuon. Figure 2.15 is taken from [28] and illustrates the areas where the maximised SUSY contribution is consistent with the g-2 anomaly.

The processes to which collider searches are most sensitive, having the largest reach in terms of chargino and neutralino mass, are pair production and decays via sleptons to final states with three leptons, a neutrino and two LSPs (figure 2.16a). If this process is either suppressed or kinematically non-viable due to slepton masses higher than chargino/neutralino masses then the decay via a Higgs (figure 2.16(b)) targeted in this thesis is most sensitive.

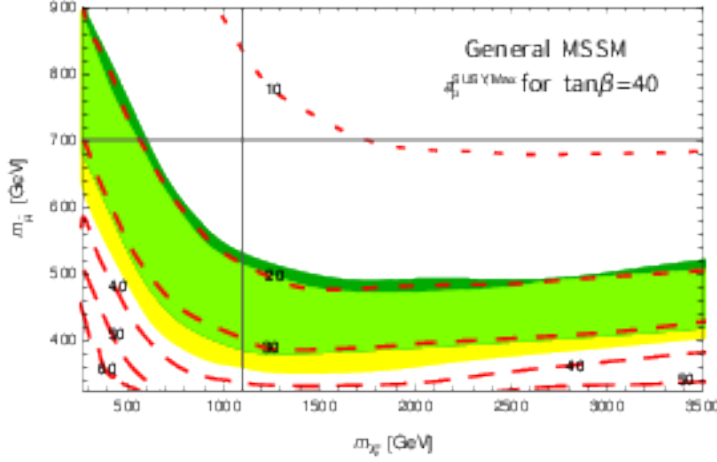


Figure 2.15: From [28], illustration of the viable parameter space considering the maximum contribution to a_μ . The measurement from BNL and FNAL are in green and yellow respectively. The red lines show the contributions to a_μ for $\tan\beta = 40$.

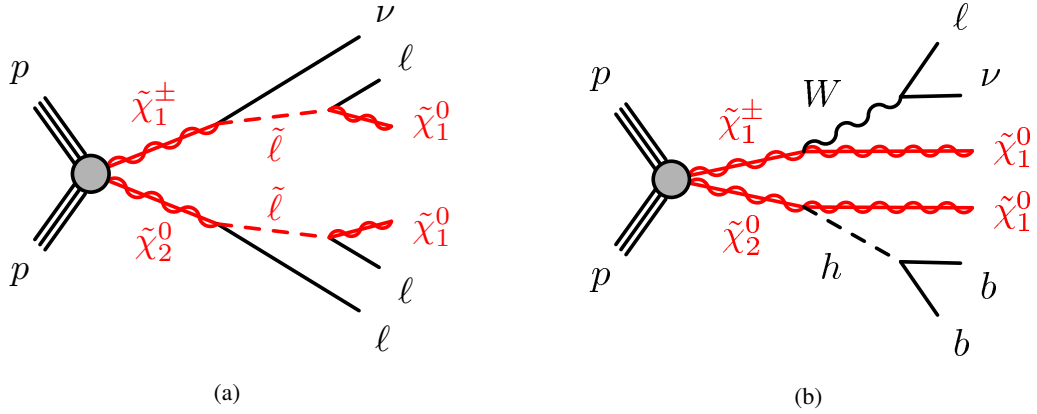


Figure 2.16: Processes for which collider searches achieve the highest sensitivity to chargino and neutralino masses.

The MSSM provides many viable scenarios for explaining Δa_μ , taking into consideration that the LSP is stable and its abundance does not exceed dark matter relic density constrains the MSSM viable scenarios, some of which are interesting for current and future collider searches:

- Bino-like LSP with mass close to slepton masses, with heavy Wino-like neutralino and $\mu > 1 \text{ TeV}$.
- Higgsino-like or Wino-like LSP with $m_{LSP} \sim m_{\tilde{t}}$
- Higgsino-like or Wino-like LSP with m_{LSP} lighter than $m_{\tilde{t}}$

2 Beyond the Standard Model

The above features are interesting since they tend to evade older, more simplified MSSM signatures by having compressed SUSY spectra. These types of signatures are difficult to access with colliders searches and are particularly focussed upon in this thesis.

2.3 Dark Matter

Whilst SUSY provides a viable dark matter candidate in R-parity conserving models, other extensions to the SM can introduce new particles with properties that make them viable dark matter candidates. In the simplest terms, proposed dark matter particles must have the following properties: they are stable, massive and at most weakly interacting with the SM.

Since our requirements on the properties of dark matter only put an upper bound on the strength of the interaction with the SM, we may even consider that dark matter is simply de-coupled from the SM or interacts so weakly that we would never observe it. However, there is motivation that this is not the case. It is proposed that in the early universe dark matter and ordinary matter were in a thermal equilibrium of production and annihilation processes. The density of dark matter that remains in the universe today would then be set when the temperature of the universe became low enough that the equilibrium became unsustained. From observations of the relic density of dark matter we can extrapolate back to the point of release from equilibrium. From this point the mass and couplings of the dark matter to the Standard Model particles can be determined to lie within some well defined bounds and it turns out that these bounds allow for the production of dark matter particles to have reasonable cross-sections in modern day collider experiments [29].

Direct searches for dark matter aim to observe the recoil of dark matter particles off ordinary matter. This experimental approach means that the DM signatures are relatively independent of the underlying model (though interaction cross-sections are a key piece in placing limits). Indirect searches target observations of dark matter particles annihilating with one another to produce Standard Model particles. In collider searches, as considered in this work, the inverse process is sought after: to observe collisions of Standard Model particles producing dark matter in the final state. Searches for these processes do depend on the details of the interactions between dark matter and the SM in order to identify signatures that would be present in the detector. The following sub-sections discuss some of the models used in this thesis.

2.3.1 Simplified Dark Matter Mediator Models

Simplified models tend to focus on signatures with specific final states, making few assumptions in order to reduce the number of parameters inherent in the models [30]. Collider searches predominantly focus on models in which a new mediator sector is introduced that provides the interaction between the DM and SM sectors. These mediator models can be considered in two types: Models where a single new mediator is introduced, which is either spin 1 or spin 0, and models where the mediator is

introduced as part of an extended Higgs sector.

For the case of models with a single mediator where the mediator is spin 1, a new gauge symmetry is introduced, the mediator is either vector or axial vector. A wide ranging phenomenology of signatures can be realised dependent on the properties of the mediator. It can either be neutral under the SM gauge groups, or charged under baryon number or flavour. The flavour charged scenario is particularly interesting for high energy colliders as this permits interaction of the DM candidate with the top quark and also predicts flavour changing neutral currents. Signatures of these models are shown in figure 2.17.

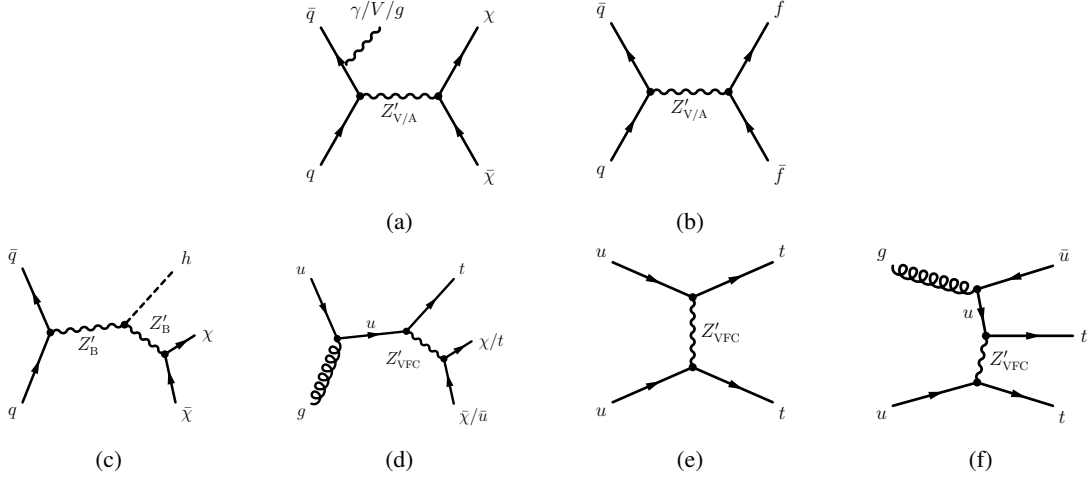


Figure 2.17: Signatures from the single vector/axial vector mediator DM models

In the second case with scalar/pseudo-scalar mediator, the mediator couples to SM fermions with strength proportional to the SM Yukawa coupling and can either be colour neutral or charged. The colour neutral scenario, which is also known as 'minimal flavour violating', can produce signatures with two or more top quarks in the final state making the Yukawa related nature of the interaction open to investigation. Additionally interesting from a phenomenological perspective is that the coupling to up and down-type quarks is not constrained in the model so final states with bottom quarks could have dominant sensitivity in cases where the coupling to up-type quarks is suppressed [31].

The colour charged models produce very similar phenomenology to that of the MSSM if the SUSY dark matter candidate is proposed to be the lightest neutralino. The phenomenology changes if specific assumptions are made about the mediator couplings to specific quarks. Scenarios can be considered where the mediator either couples only to the bottom quark, couples to the left-handed quarks of the first and second generations, or couples to the right-handed quarks. The signatures from these types of models are shown in figure 2.18 for colour neutral and 2.19 for colour charged.

Though simplified models give a good way of providing dark matter benchmarks which are relatively model independent, they can also result in theoretical incompleteness or inconsistency with the SM, violating unitarity and gauge invariance. Recent work has pushed towards addressing these issues with

2 Beyond the Standard Model

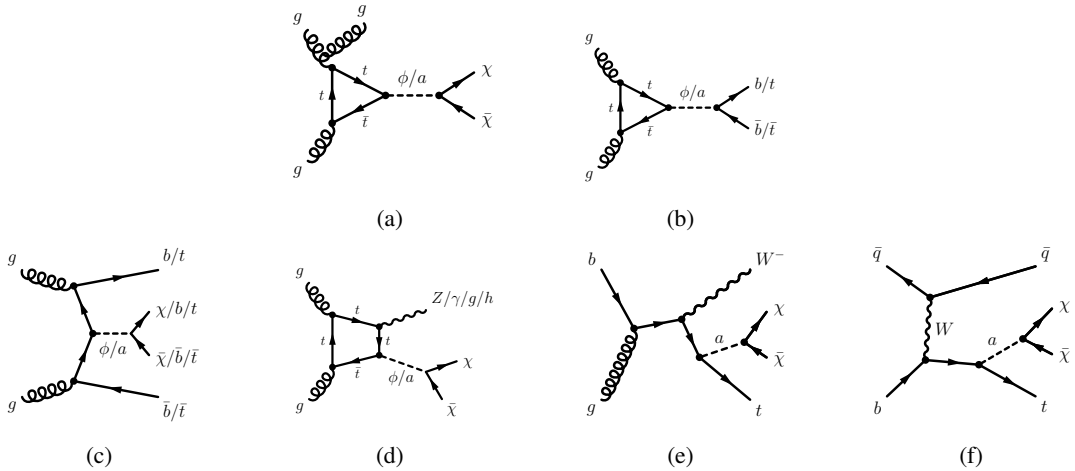


Figure 2.18: Signatures from the single scalar/pseudo-scalar mediator DM models in colour neutral mediator scenarios.

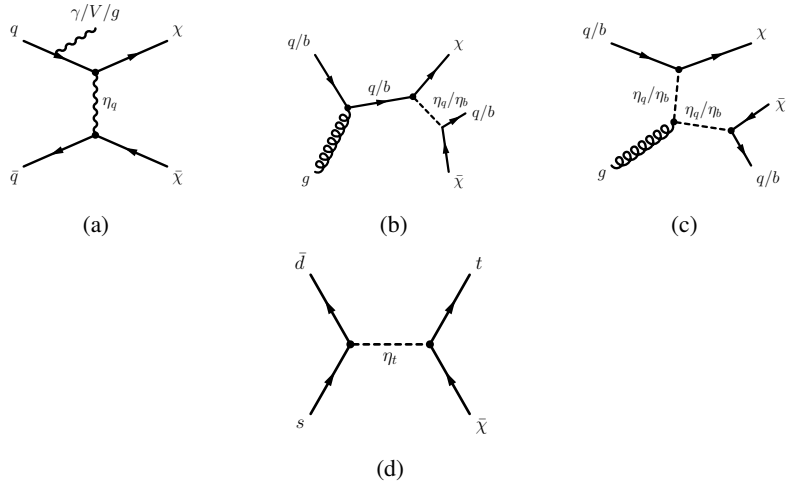


Figure 2.19: Signatures from the single scalar/pseudo-scalar mediator DM models in colour charged mediator scenarios.

the development of simple models that, however, are based in a self-consistent theoretical framework and are also consistent with the SM. This work has lead to a group of models which have formed the basis for the most recent dark matter searches at the LHC, one of the most prominent are the two higgs doublet models.

2.3.2 Two Higgs doublet + a models

The 2HDM models are the simplest way to build dark matter models that are both Lorentz invariant and consistent with the SM framework i.e. that they are invariant under the SM gauge groups, are ultraviolet complete and are fully renormalisable. The models require a mediator to connect the

2.3 Dark Matter

visible and dark sectors, scalar mediator models tend to have stronger constraints from direct detection experiments so in order to probe more unexplored areas available to colliders a pseudo-scalar is chosen, this class of models are called 2HDM+a models [32].

The dark matter candidate particle in these models is a Dirac fermion, denoted by χ , which is a singlet under the SM gauge groups. The Higgs doublet that is introduced in the model is the same doublet that is included in the MSSM. The mass eigenstates of the BSM particle content of the model are aligned with the CP eigenstates: there is a light and a heavy scalar, h and H (where h is proposed to be SM-like) and two charged scalars H^\pm . The pseudoscalar state from the higgs doublet mixes with the pseudoscalar mediator producing two mass eigenstates a and A . The mediator to the dark sector fermions is a . The parameter space of the model is spanned by three mixing angles α, θ, β which capture the mixing between the CP-even and CP-odd states and the ratio of the vacuum expectation values respectively, three quartic couplings $\lambda_3, \lambda_{P1}, \lambda_{P2}$ which are the couplings between the higgs doublets and the masses of all new eigenstates.

Interestingly in the context of this thesis, one of the few scenarios that can incorporate the g-2 deviation discussed in section 2.1.6 without the introduction of additional vector bosons are the 2HDM models [33]. The most favoured of these is the flavour aligned model allowing the widest phase-space of scenarios where contributions to Δa_μ are positive and of the level of the observed deviation. If the additional neutral Higgs in the model has large Yukawa couplings to muons and is not too heavy, then the deviation can be incorporated. Allowed masses of A that can explain the anomaly reach up to ~ 100 GeV.

A large variety of final states can arise from processes in this model. One promising and unexplored process is DM production in association with a top quark and a W, so called 'DMtW' channel. In addition, sensitivity to the associated production of two top quarks, DMtt can be explored using a similar strategy. Both processes have been shown to have promising sensitivity to the 2HDM+a model scenario [34]. The DMtW process specific diagrams are given in figures 2.20(a) and 2.20(b) along with the DMtt diagram in 2.20(c).

2 Beyond the Standard Model

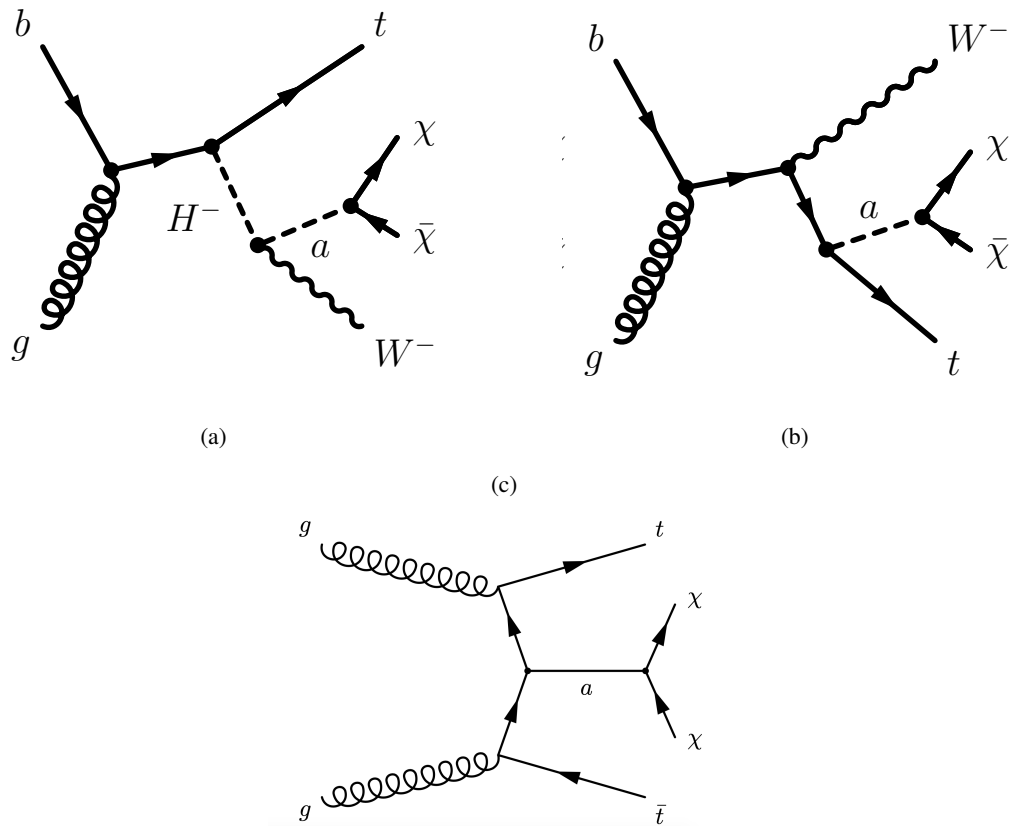


Figure 2.20: Feynman diagrams that contribute to the DMtW 2.20(a) 2.20(b) and DMtt 2.20(c) channels of dark matter production in the 2HDM+a model.

Part II

The LHC and ATLAS detector

3 The LHC

The Large Hadron Collider (LHC), based at CERN (Conseil Européen pour la Recherche Nucléaire), is the world's largest and most powerful hadron collider. It is situated 100m underground spanning the Franco-Swiss border near Geneva. The LHC collides hadrons at 4 interaction points, at which detectors are placed to study the physics of the collisions. ATLAS (A Toroidal Lhc ApparatuS) is the largest of these detectors. Data collected from proton-proton collisions with the ATLAS detector form the basis of this thesis. In this chapter a brief description of accelerator physics, the LHC accelerator and the ATLAS detector is given.

3.1 Collider Physics

3.1.1 Particle Acceleration

Modern day particle accelerators use radio-frequency (RF) cavities to accelerate charged particles in a vacuum. An RF cavity is an evacuated chamber, within which, an oscillating electric field is applied. The oscillation frequency is tuned such that incoming charged particles experience a voltage gradient from the field and thus are accelerated in one direction. The frequency is set so that incoming particles traveling at an ideal speed arrive in phase with the accelerating gradient of the field and experience acceleration in their direction of travel, as illustrated in figure 3.1.

In addition to providing acceleration, the RF cavities also act to normalise the proton kinetic energies. A particle traveling slightly faster than the ideal specified by the oscillation frequency will experience a deceleration due to the RF electric field acting with a potential in the opposite direction to the particle's direction of travel. Conversely, a particle traveling slightly slower than the ideal will receive a stronger acceleration due to the sharper gradient in the direction of travel. In this way the particles form bunches, as illustrated in figure 3.1, with relatively uniform energy.

3 The LHC

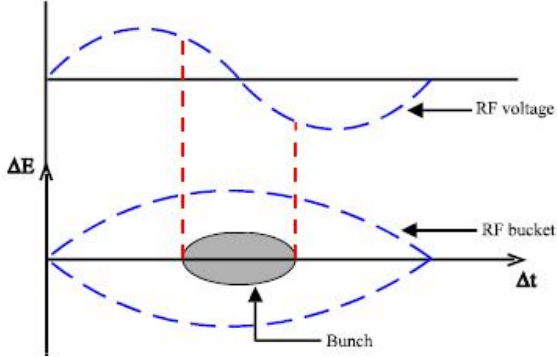


Figure 3.1: Acceleration of charged particles experiencing a voltage gradient from the oscillating electric field in an RF cavity. The formation of bunches based on the 'bucket' of viable accelerating region.

3.1.2 Synchrotron Radiation

In the long history of particle physics research progression in the experimental field has been made by studying the physics at increasingly high energies. From Einstein's famous $E = mc^2$, with increasing energy of interactions comes the ability to produce higher mass particles. The latest and furthest progression is the LHC which achieves centre-of-mass (CoM) energy proton-proton collisions at 13TeV - the highest ever achieved - and this is expected to be increased to 14TeV.

The LHC is a circular collider, bunches of hadrons are accelerated in opposing directions within the synchrotron, gaining energy as they pass through RF cavities, until the bunches are focussed together at the interaction points where collisions occur. By colliding beams of particles in opposing directions circular colliders can reach higher CoM collision energies for the same beam energy compared with fixed target experiments. In addition, since only a fraction of the incoming particles interact when the beams cross, the energy of particles that haven't interacted is conserved as the beams continue to circulate.

The circular collider design, however, comes with a trade-off. When charged particles circulate at high speed they emit synchrotron radiation which reduces the beam energy by an amount, ΔE , given by 3.1 every rotation:

$$\lim_{v \rightarrow c} \Delta E = \frac{4\pi}{3} \frac{q^2}{R} \left(\frac{E}{mc^2} \right)^4 \quad (3.1)$$

Here E is the beam energy, q is the charge of the accelerated particles, R is the radius of the synchrotron, and m is the particle mass. Equation 3.1 illustrates the motivation behind developing the LHC as a hadron collider rather than an electron-positron collider like its predecessor, LEP. Though e^+e^- collisions are clean and gain from the additional energy of annihilation from the rest mass, equivalent

to $2m_e$, the CoM collisions are much lower in energy due to the quartic effect of the mass in equation 3.1. The ratio of energy lost due to synchrotron radiation by a proton vs an electron is given by:

$$\frac{\Delta E_{electron}}{\Delta E_{proton}} = \left(\frac{m_{proton}}{m_{electron}} \right)^4 \approx 10^{13} \quad (3.2)$$

By colliding protons rather than electron-positron pairs, far higher energies can be achieved.

3.1.3 Luminosity and Pile-Up

When colliding particles at the interaction points we are interested in the rate at which different interaction processes occur which are being studied. Since quantum interactions are by their nature probabilistic, increasing the rate of these processes gains the necessarily high number of recorded observations required to study them using statistical techniques. The rate of a process occurring in a collider experiment is dependent on the *instantaneous luminosity* (\mathcal{L}) of the combined beams and is given by [35]:

$$\frac{dR}{dt} = \mathcal{L} \prod \sigma_p \quad (3.3)$$

where σ_p is the cross-section of the process and the instantaneous luminosity is defined as:

$$\mathcal{L} = f_{rev} \frac{N_p^2 n_b}{4\pi \sigma_x \sigma_y} F \quad (3.4)$$

where f_{rev} is the frequency of revolution of the beams, N_p is the number of protons per bunch, n_b is the number of bunches per beam, σ_x and σ_y are the sizes of the bunches at the interaction point in directions perpendicular to travel and F is a factor accounting for the angle that the beams cross at. The interaction region, also known as the luminous region, is approximately gaussian in beam overlap. At the LHC this region measures between 8-15 microns in the transverse direction and the gaussian width, σ_y is 35-50 microns.

When the proton bunches collide, typically multiple interactions occur. These additional overlapping inelastic collisions are known as pile-up. In a single bunch crossing the hits in the detector can come from any of these multiple interactions. For this reason the tracking of particles emerging from the interaction point is used to identify the multiple vertices in the beam crossing. Within ATLAS the vertex with the highest sum of transverse momenta of particles attributed to it is considered most interesting and is recorded, it is referred to as the *primary vertex*. Conditions required for achieving high instantaneous luminosity such as increased bunch crossing rate and increased beam overlap also increase the number of interactions per bunch crossing.

This will have a growing impact as the LHC moves to the high-luminosity LHC phase. The profile of collisions per bunch crossing is quantified by the mean number of interactions per bunch crossing,

3 The LHC

$\langle \mu \rangle$. This is defined as the instantaneous luminosity multiplied by the inelastic cross section divided by the revolution frequency:

$$\mu = L_{inst}\sigma_{inel}/f_r \quad (3.5)$$

For data-taking periods thus far at the LHC as recorded by the ATLAS detector the profile of $\langle \mu \rangle$ is given in figure 3.2.

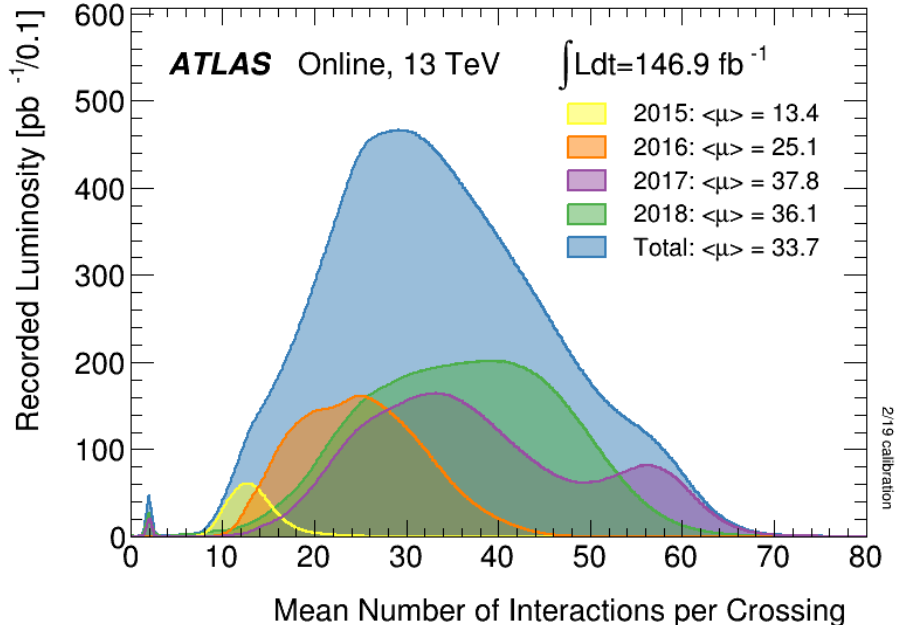


Figure 3.2: Mean number of interactions per bunch for the data taking periods including run 1 and run 2 data taking periods of the 13TeV LHC runs.

3.2 The CERN Accelerator Complex

The accelerator complex at CERN is illustrated in figure 3.3. The process of accelerating protons to very high energies in the LHC begins with several stages of acceleration from smaller systems of the complex. These are the Linac2 linear accelerator, the Proton Synchrotron (PS), the Proton Synchrotron Booster (PSB) and the Super Proton Synchrotron (SPS). Firstly hydrogen gas is injected into the first stage accelerator, here the electrons are stripped from the protons by an applied electric field. The remaining protons are then passed along the chain of sub-accelerators in bunches, increasing their energy at each stage via acceleration in the RF cavities until they are finally injected into the LHC ring. The LHC ring is contained in circular tunnel 100m underground with a circumference of 26.7 kilometers. The collider tunnel contains two parallel beam pipes in which the proton bunches travel in opposing directions.

3.2 The CERN Accelerator Complex

The beam pipes contain a total of 1232 superconducting dipole magnets generating 8.3 Tesla fields which bend the proton trajectories to follow the curve of the ring. Additional quadrupole magnets focus the beam, compressing the proton bunches in the plane perpendicular to their direction of travel, near to interaction points where the opposing bunches collide. The proton bunches circulate in opposing directions whilst their energy is increased to energies of 6.5TeV producing a CoM energy of 13TeV. The LHC primarily collides protons but can additionally collide lead ions in either proton-lead or lead-lead scenarios.

Throughout the complex there are 7 detectors positioned around the ring designed to study a large array of phenomena from the beam. The 4 main detectors placed at the interaction points are ATLAS and CMS (general purpose detectors), LHCb(forward detector specialising in b-physics) and ALICE (specialising in heavy ion physics).

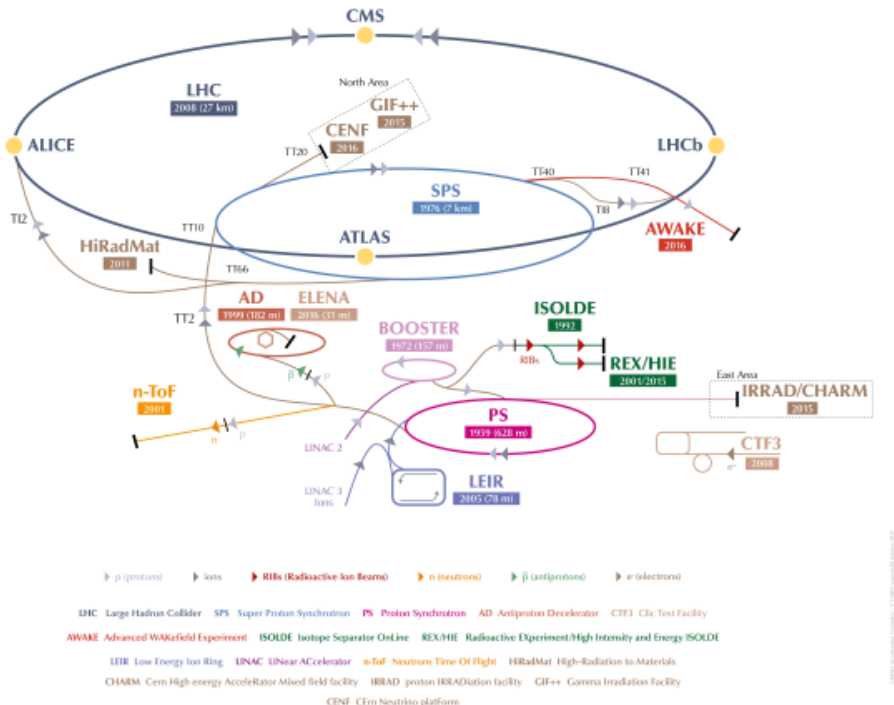


Figure 3.3: The accelerator complex at CERN.

4 The ATLAS detector

The ATLAS detector is a general purpose particle detector situated 100m underground at one of the 4 collision points on the LHC ring. The detector is cylindrically shaped, 46m long with a 25m diameter, it surrounds the LHC beam pipe and is symmetrical around the collision point. The arrangement gives detection coverage of almost 2π in azimuthal angle. The detector consists of 6 subsystems which will be summarised here. the 4 detector subsystems are the inner detector (ID), electromagnetic calorimeter (ECAL), hadronic calorimeter (HCAL) and the muon spectrometer (MS). The remaining two are the magnet and trigger subsystems.

4.1 Detector Geometry

The geometry of ATLAS can be generalised as cylindrical and it is useful to define a polar coordinate system to work with. Though a cartesian system is also used in some cases, the polar system will be used throughout this work. This reference frame is particularly useful since many features of data analysis and object reconstruction utilise the rotational symmetry about the beam axis and often important variables are defined in the plane transverse to the beam direction. The coordinate system is illustrated in figure 4.1.

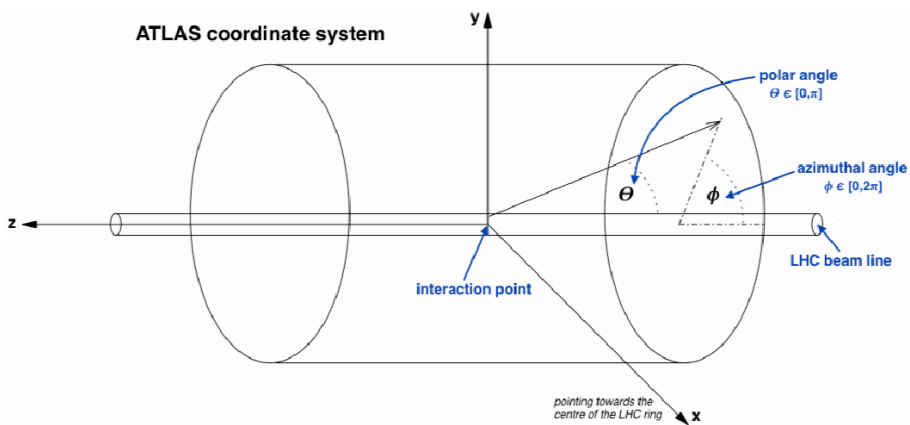


Figure 4.1: Illustration of the polar coordinate system used in the ATLAS detector.

Usually pseudo-rapidity, η defined in equation 4.1, is used in place of the polar angle θ , it is related to the rapidity and is Lorentz invariant for massless particles or in the limit $\frac{m}{|\vec{p}|} \rightarrow 0$ where \vec{p} is the

4 The ATLAS detector

particle's 3-momentum. In the limit the particle energy is approximately its momentum $E \approx |\vec{p}|$ and the pseudo-rapidity and rapidity (y) are the same quantity.

$$\eta = -\ln(\tan \frac{\theta}{2}) = \frac{1}{2} \ln(\frac{|\vec{p}| + p_z}{|\vec{p}| - p_z}) \quad (4.1)$$

$$y = \frac{1}{2} \ln(\frac{E + p_z}{E - p_z}) \quad (4.2)$$

where p_z is the z-component of the particle's momentum.

4.2 Magnet system

The magnet system is comprised of 4 parts: a thin central solenoid and 3 larger toroidal solenoids. The central solenoid surrounds the inner detector and provides a 2T field at the interaction point, along the axis of the beam line. The outer toroids have 1 central barrel component and 2 end-cap components, each having 8 separate coils. These provide the magnetic field for the outer detector muon spectrometer with a 4T field strength on the superconductor.

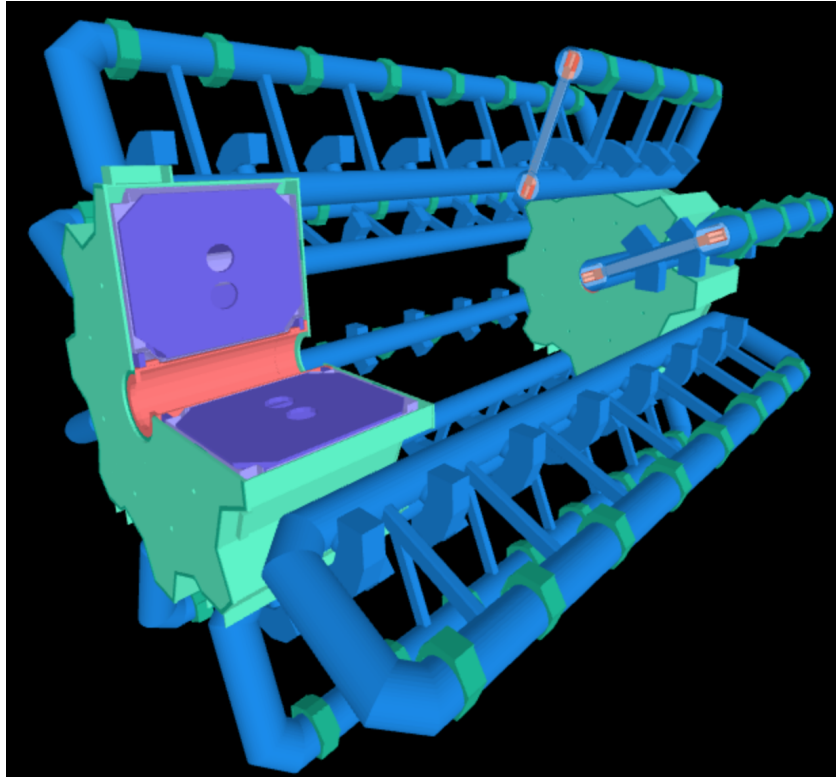
The magnet system in the ATLAS detector provides a strong magnetic field throughout the areas of the detector through which particles pass. As charged particles move through the magnetic field their trajectory is deflected due to the the Lorentz force . Tracking detectors determine the trajectory of the charged particle and from the curvature the momentum of the particle can be deduced.

The magnetic field at different points in the detector is modified by detector components in the vicinity and the distance from the solenoids. A precise knowledge of the field strength throughout the detector is important to reduce both uncertainty on particle identification in the inner detector region and on momentum resolution, the latter more profoundly in the muon spectrometer. Figures 4.2(a) and 4.2(b) illustrate the arrangement of the solenoids in the detector and how the magnetic field strength changes within the detector region.

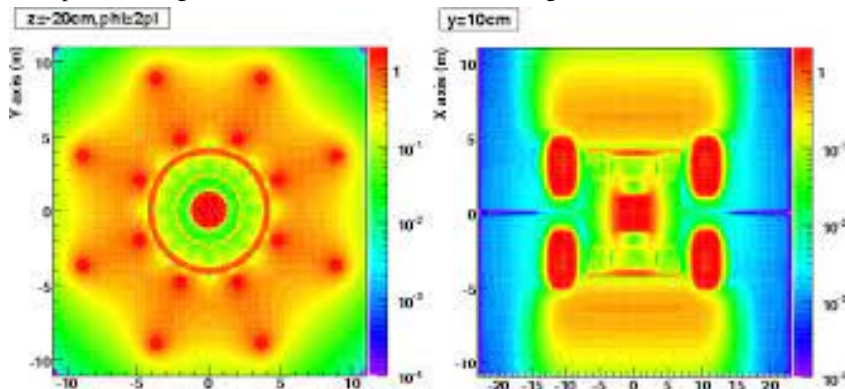
4.3 Inner Detector

The Inner detector (ID) provides information of hits as charged particles pass through the detector, from this tracking of the particle trajectory is established. Tracking information is used for identification and determination of the particle momenta. The inner detector is composed of 4 separate sub-detectors arranged concentrically around the beam pipe, from inner-most to outer-most these are the insertable B-layer, Pixel detector (PD), Semiconductor Tracker (SCT), and Transition Radiation Tracker (TRT). An illustration of the full inner detector is given in figure 4.3(a) and its subsystems in figures 4.3(b) 4.3(c) 4.3(d).

4.3 Inner Detector



(a) Illustration of the ATLAS toroidal magnet arrangement, showing the barrel toroids in blue and the end-cap toroids in green. A cross-section is taken showing the inner structure



(b) Illustration of the magnetic field shape within the detector region.

Figure 4.2: Illustrations of (a) the ATLAS superconducting magnet arrangement providing the magnetic field for the detector volume and (b) the magnetic field shape inside the detector volume that the magnets produce.

4.3.1 Insertable B-layer

The insertable B-layer (IBL) was implemented inside the original Pixel detector arrangement during long shutdown 1 in 2014 in preparation for the LHC Run 2. Sitting at a radius of 31-40mm from the interaction point, it provides a high resolution hit close to the event, which increased the azimuthal

4 The ATLAS detector

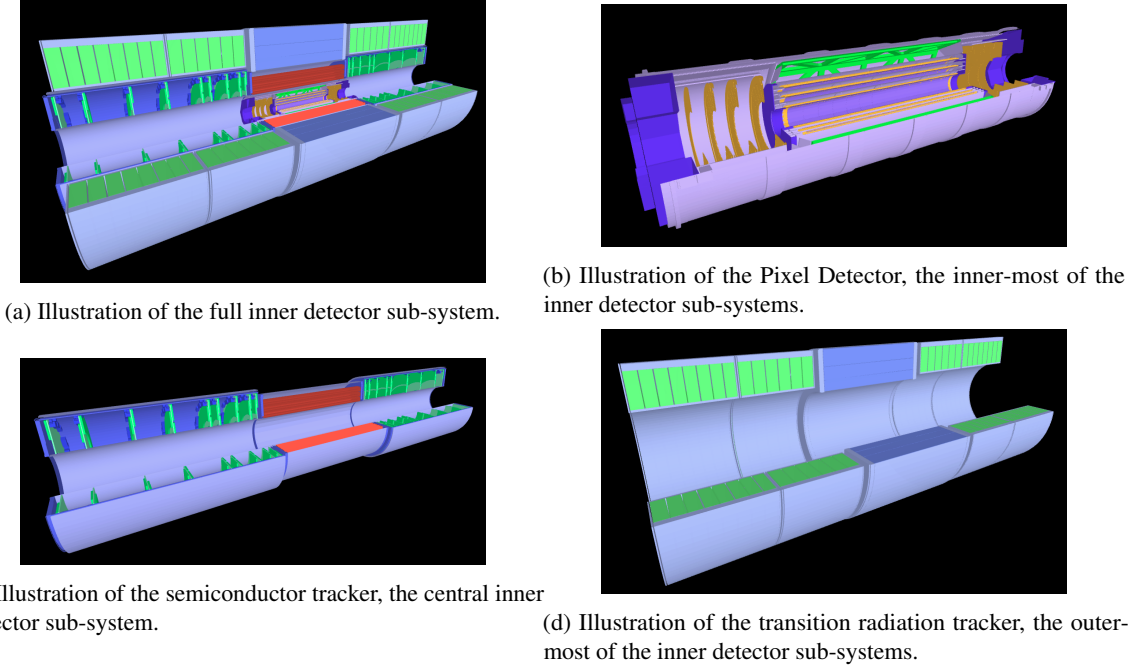


Figure 4.3: Illustrations of the concentric layers of the inner detector subsystem in the ATLAS detector (cite:<https://tracer.web.cern.ch/tracer/>), with (a): the full inner detector, and (b),(c),(d) the concentric inner-most to outer-most detectors: Pixel, SCT,TRT.

and longitudinal resolution of the detector by a factor of 2 for low energy charged particles (transverse momentum $\sim 1\text{ GeV}$). This is particularly important for identification of heavy flavour quarks produced in the interaction. The additional hit information and improved resolution in turn improves the identification of primary and secondary vertices. Heavy flavour quarks in the event are identified by the presence of a secondary decay vertex within the hadronisation that form jet structures in the detector. Details on the identification of jets from b and c-quarks are given in 6.2.2. The improvement in the rejection of light-flavour and charm quark initiated jets due to the b-layer information is illustrated in figure 4.4.

4.3.2 Pixel Detector

The pixel detector is composed of 4 layers of pixel modules in the barrel region, at radii of 50.5, 88.5 and 112.5 mm, and 3 circular disks of modules in each end-cap. The PD allows for tracking in a pseudo-rapidity (η) up to $|\eta| = 2.5$.

4.3.3 Semi-Conductor Tracker

The SCT is comprised of 4 barrel layers coving the central region around the interaction point, and 18 rings that cover the end-cap regions at greater distance along the beam-pipe direction. The sensors in the detector are *p-in-n* microstrip sensors [36]. Strips of *p*-type semiconductor material (material

4.3 Inner Detector

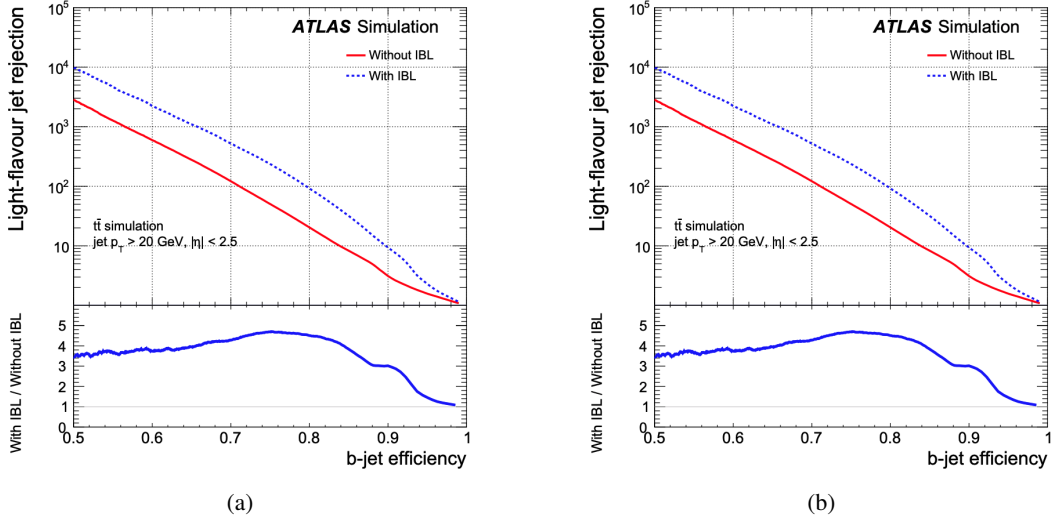


Figure 4.4: Rejection of jets arising from the hadronisation of 4.4(a) light-flavour and 4.4(b) charm quark vs efficiency of identifying a b-jet in Run1 without the implementation of the IBL vs in Run 2 with the information from the IBL.

over-abundant in electron holes) are embedded in an n -type bulk material (over-abundant in electrons) with a negative electric potential bias applied between the two. As charged particles move through the sensor active volume, electron-hole pairs are liberated from the material and move towards the respective materials, the electrical signal is collected and a hit is recorded. The sensors have an intrinsic resolution of $23\mu\text{m}$ and space resolution of $\sim 16\ \mu\text{m}$ in $R - \phi$ and $\sim 580\ \mu\text{m}$ in Z. The SCT is comprised of a carbon-fibre composite structure which has a concentric barrel-shape in the central region and is comprised of disks in the forward end-cap regions. The sensor modules then sit on the support structure, a module is comprised of four silicon sensors glued to base board, two on each side arranged with a small stereo angle (± 20 mrad).

4.3.4 Transition Radiation Tracker

The TRT is an detector with gaseous active medium which provides tracking in the radius of 560 to 1080 mm in the barrel region and 617 to 1106 mm in the end-cap region [37], covering the area up to the inner solenoid. The detector contains $\sim 300,000$ thin Kapton tubes with a $31\mu\text{m}$ gold-plated tungsten wire at the centre. The tubes are filled with either Xenon or Argon-based gaseous mixture which constitutes the active medium which is ionised when charged particles pass through. The charge then drifts towards the anode wall of the tube or the cathode central wire where the electrical signal is collected. Around 30 hit points are collected with a precision of 0.1-0.13 mm, dependent on the region of detector, for each charged particle track passing through.

The TRT also provides additional particle identification information for discerning electrons from charged pions. The discerning factor comes from the fraction of hits in a track that pass an adjustable high-threshold for charged deposited in the hit. The amount of energy deposited from transition

4 The ATLAS detector

radiation as an ultra-relativistic particle passes between mediums grows with the Lorentz γ -factor, how fast the particle is traveling. An electron with the same momentum as a pion will deposit more transition radiation in a hit, and so can be distinguished from a pion.

4.4 Calorimeters

The calorimeter systems in ATLAS measure the energy of particles and their decay products as they pass through the detector. As particles interact with the detector materials, they release energy through various methods: charged particles and photons radiate via Bremsstrahlung and electron-positron pair creation which produces particle showers with only photons and electron-positron pairs. Hadrons passing through detector material also radiate via strong interactions. Hadronic showers can contain additionally produced hadrons and subsequent secondary EM showers. The resultant particles produce a cone within in the detector emanating from the interaction. These signatures are known as jets, their identification is discussed in detail in section 6.2.

The sub-detectors can be split into those designed for measuring electromagnetic activity: electromagnetic showers from particles passing through the detector and electromagnetic components of hadronic showers, known as the ECAL (electromagnetic calorimeter), and those measuring hadronic components of the hadronic showers, known as the HCAL (hadronic calorimeter). ATLAS uses two types of calorimeter: Liquid Argon based (LAr) and steel + scintillator (Tile). Both are sampling calorimeters with a structure of layers with absorber material and active medium for sampling energy.

Liquid Argon Calorimeters The LAr calorimeters provide the electromagnetic calorimetry for the barrel region (EMB, $|\eta| < 1.475$) and the end-cap regions (EMEC, $1.375 < |\eta| < 3.2$), the hadronic calorimetry for the end-cap regions (HEC) with $1.5 < |\eta| < 3.2$ and the calorimetry furthest from the interaction point along the beam line (FCAL) with $3.1 < |\eta| < 4.9$. The calorimeter is composed of sections containing LAr which is ionised by charged particles passing through. A strong potential difference is applied between electrodes placed into the LAr. The charge is collected at the electrodes which is converted to signal. The charge collected is related to the energy of the particle(s) that initiated the ionisation, thus allowing extrapolation of the particle energy. The sections of LAr are interspersed with absorber: lead in the EMEC and HEC and copper and tungsten in the FCAL.

Tile Calorimeters The tile calorimeters provide calorimetry for hadronic particles in the barrel region, $|\eta| < 1.7$, split into a central barrel section with two outer barrel rings. They are composed of low-carbon steel as the absorber sandwiching plastic scintillator plates which are aligned with the radius of the detector from the interaction point 4.5. As the charged particles pass through the scintillator, light is emitted, which is collected by fibers and passed to Photo multiplier tubes (PMT) which convert the light into electrical signal.

The resolution of an energy measurement, E , of a calorimeter can be parameterised as ([38]):

$$\frac{\sigma(E)}{E} = \frac{a}{\sqrt{E}} \oplus \frac{b}{E} \oplus c \quad (4.3)$$

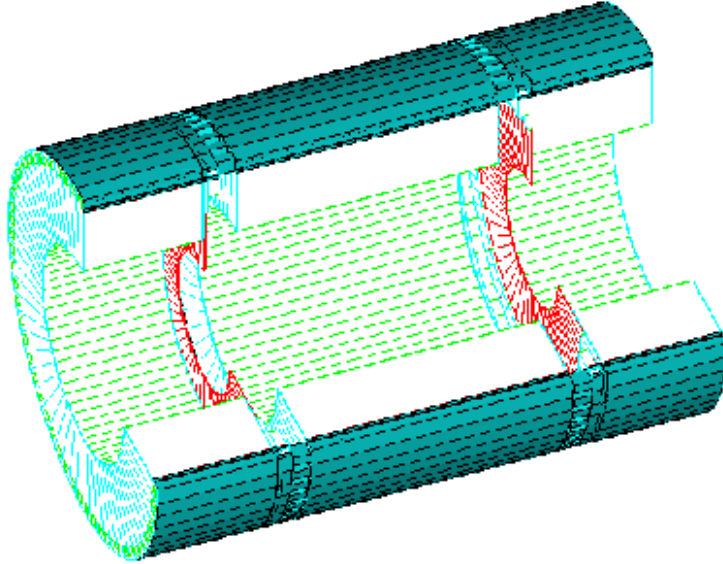


Figure 4.5: Geometry of the ATLAS Tile calorimeter

where \oplus indicates a sum in quadrature. a is the stochastic term which accounts for statistical fluctuations in the track lengths of the charged particles in the shower. In homogenous calorimeters the stochastic effect is small, though in sampling calorimeters it affects the number of charged particles that cross the active layers and thus has a larger impact. b is a term accounting for electric noise in the detector system, such as the amplification of charge in charge collection detectors. c is a constant term that accounts for effects independent of the particle energy such as non-uniformity in the detector material.

4.4.1 Electromagnetic Calorimeters

The EM calorimeter structure (ECal) has an accordion shape with the layers of LAr scintillator interspersed between the absorber materials. The cells are square in shape for the bulk of the calorimeter, with strip shaped cells in the first layer, as illustrated in figure 4.6. The coverage reaches up to $|\eta|=3.2$, the central cells have a granularity of size $\eta \times \theta=0.025 \times 0.0245$ whilst the first layer strip cells have an η resolution of $\eta=0.0031$.

The design specification parameterising the resolution of the LAr ECal is given in equation 4.4 [40]. As the ECal is a sampling calorimeter, the stochastic term is significant.

$$\frac{\sigma(E)}{E} = \frac{10\%}{\sqrt{E}} \oplus \frac{170\text{MeV}}{E} \oplus 0.7\% \quad (4.4)$$

4 The ATLAS detector

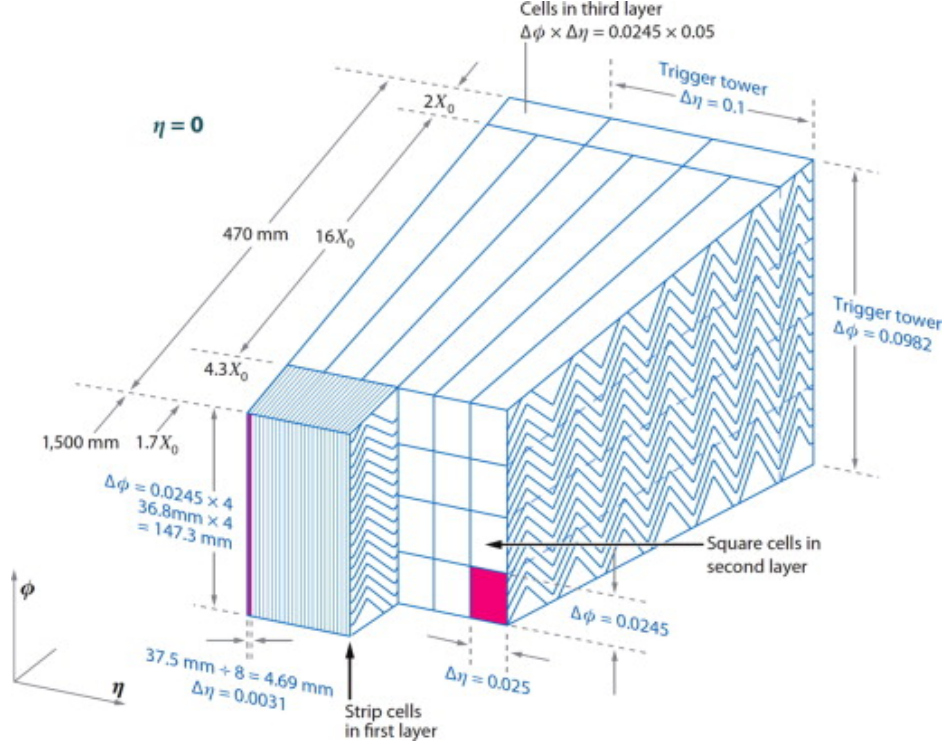


Figure 4.6: Illustration of the geometry of the cell construction for the LAr based EM calorimeter showing the bulk square cells and the front strip cells and their measurements in η [39].

4.4.2 Hadronic Calorimeters

The hadronic calorimeter comprises steel and plastic scintillator tiles in the barrel region up to $|\eta|=1.7$, with the end-cap region being LAr and copper, in addition the FCal tungsten and LAr reaches up to $|\eta|=5$. The tile-based calorimetry has less precise resolution compared with the LAr-based. Its design parameterisation is given in equation 4.5. The stochastic term is dominant here and the constant term relating to the electronic noise is negligible.

$$\frac{\sigma(E)}{E} = \frac{52.9\%}{\sqrt{E}} \oplus 5.7\% \quad (4.5)$$

The calorimeters give full azimuthal coverage such that the component of particle energies transverse to the beam direction can be reconstructed. This is an essential part of the detector design as it allows for the measurement of energy imbalance in the transverse plane such as that carried away by non-interacting particles, this is known as *missing energy* (E_T^{miss}). The capability of the detector to measure this to high precision is essential for searching for new physics. More detail is given about measuring this imbalance in section 6.7.

4.5 Muon Spectrometer

Muons with high transverse energy arising from collisions are a particularly interesting feature of high-energy physics processes. High energy muons tend to pass through the inner detector and the calorimeters without interaction, thus the muon spectrometer at greater radial distance and is designed to identify muons whilst measuring their momentum. Muons passing through the outer radial regions of the detector are deflected by magnetic fields of the barrel and end-cap toroids that sit outside the hadronic calorimeter. The spectrometer also provides triggering capability on identification of muon events. The subsystems can be split into precision tracking and triggering systems.

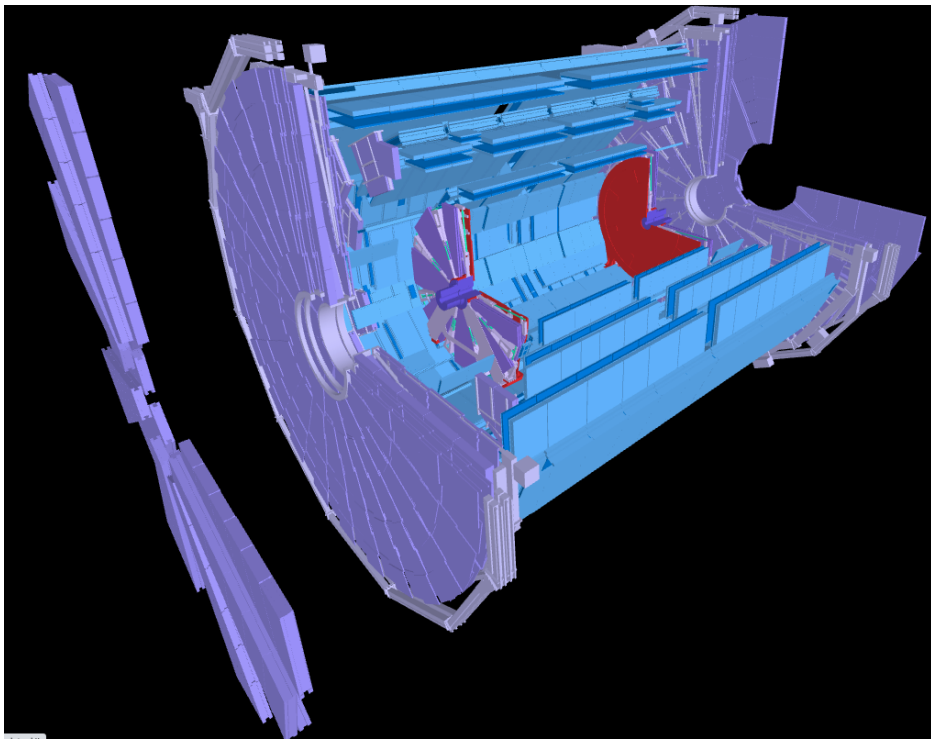


Figure 4.7: Illustration of the muon spectrometer of the ATLAS detector, showing the barrel section of the MDTs and RPCs in blue and the end-cap sections containing the CSCs and TGCs in purple.

4.5.1 Tracking

The muon tracking is arranged into 3 concentric layers of tracking detectors. The majority of the muon tracking is covered by monitored drift tubes (MDTs). These are 30mm diameter aluminum tubes containing a tungsten-rhenium wire with $50\mu\text{m}$ diameter, the void filled with an Argon-Methane-Nitrogen mixture. The MDTs provide an average resolution of $80\mu\text{m}$ [41] per tube.

4 The ATLAS detector

At high $|\eta|$ cathode strip chambers (CSCs) are used in place of MDTs to provide higher granularity. These are multi-wire proportional chambers, meaning they contain many anode wires in layers separated by adjacent strips of cathodes that provide read-out of signal 4.8. The wires have a diameter of $30\mu\text{m}$ and are tungsten-rhenium as in the MDTs, and the cathodes are copper. The gas in the volume is again argon-based ($\text{Ar} - \text{CO}_2 - \text{CF}_4$). The CSCs have a resolution of $60\mu\text{m}$.

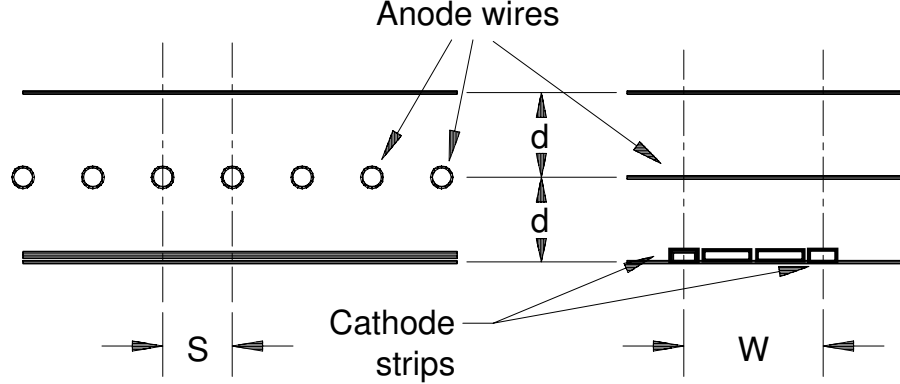


Figure 4.8: Illustration of the anode wire and cathode strip arrangement in the cathode strip chambers of the muon spectrometer, citeMuonSpecTDR.

4.5.2 Triggering

The muon triggering system is comprised of resistive plate capacitors (RPCs) in the barrel region and thin gap chambers (TGCs) in the end-cap regions. As well as providing triggering on muon identification, the RPCs and TGCs give spatial information of a secondary hit, which is used to extend track precision. The RPCs are constructed from 2 resistive plates, 2mm thick, which sandwich the active gas in a thin gap, also 2mm wide. The signal is read out by two sets of orthogonal strips, which provide the position information orthogonal to the direction of the tracking (MDTs) measurement and trigger information. The RPCs have relatively low spatial resolution of 1cm but high resolution in time of 1ns. The gas used is a mixture of $\text{C}_2\text{H}_2\text{F}_4$ and C_4H_10 .

The TGCs are constructed as two cathodes separated by a gas gap of 2.8mm of a mixture of CO_2 and C_5H_12 containing anode wires of diameter $50\mu\text{m}$, similarly to the CSCs. The cathode wires are orthogonal to the anode wires of the MDTs and the signal from these provides the spatial information of the secondary hit.

4.6 Trigger

The LHC is designed to collide proton bunches at a rate of 40MHz. At every collision information is gathered by the detector and were all this information to be stored for every collision this would mean producing data at a rate of ~ 60 million MBps, far too high for any current data acquisition system to handle. In addition, not all collisions are of great interest when considering the physics goals of the

4.6 Trigger

experiment. With reference to figure 4.9, by far the highest cross-section process is inelastic scattering, then multi-jet production, with processes producing heavier SM particles orders of magnitude lower. The ATLAS trigger system is designed to select collision data at a reduced rate identifying events that contain more interesting physics.

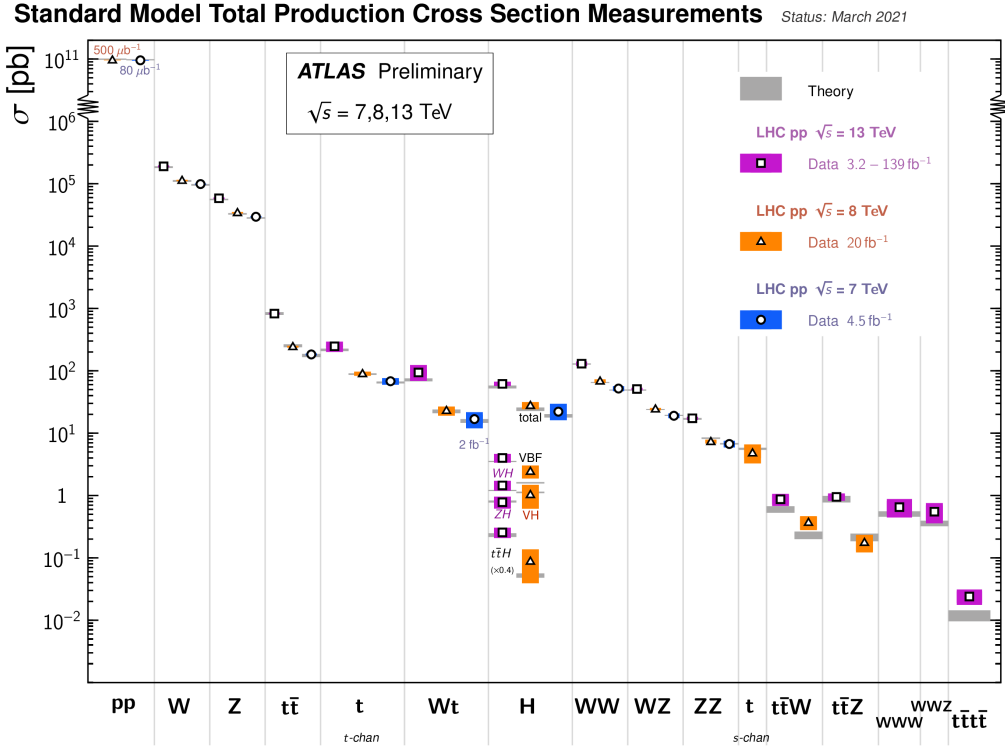


Figure 4.9: Cross-sections of key SM processes, corrected for branching ratio of the decay channel [42].

In Run 2 of the LHC, triggering in ATLAS has two stages: a fast first stage of hardware based decisions called Level 1 (L1), and a second slower software based stage called High Level Trigger (HLT).

4.6.1 L1 Trigger System

The L1 trigger takes information predominantly from the muon spectrometer (L1muon) and the calorimeters (L1calo). It uses dedicated electronics to combine information from sub-detectors to identify regions of interest (ROIs) within angular space of the detector. The L1 trigger in Run 2 also includes dedicated programmable hardware, known as Field Programmable Gate Arrays (FPGAs), which encode algorithms that act on the information coming from L1calo and L1muon. This information enables the identification of global features of the event which are physics specific such as energy imbalances in the event, total energy from the event or specific kinematic relationships between trigger objects. The L1 subsystem has an array of candidate trigger objects: Total Energy

4 The ATLAS detector

(TE), Missing Energy (XE), Muons (MU), electromagnetic clusters (EM), Jets (JET) and taus (TAU). L1 hardware has a latency of $2.5\mu\text{s}$ and reduces the event data rate from 40MHz to 100kHz.

4.6.2 High Level Trigger

The HLT is software based using a farm of 40,000 processors to apply algorithms based on the regions of interest and candidate trigger objects indicated by the L1 subsystem. Decisions are made here whether to discard or write the event to disk in several data streams: physics analysis, trigger analysis or detector monitoring/calibration. The HLT reduces the final event data rate to around 1.5kHz.

Of specific interest in this work are the triggers for electrons, muons and $E_{\text{T}}^{\text{miss}}$. Two key algorithms are used in the $E_{\text{T}}^{\text{miss}}$ trigger, the 'mht' algorithm simply takes the negative sum of the transverse momenta of candidate jets objects identified by the HLT. The 'pufit' algorithm uses clusters of energy identified in the calorimeters (topo clusters), calculating the momentum by assuming the particles incident on the calorimeter are massless and in addition applies a subtraction of energy coming from pile-up occupancy. The pile-up subtraction is done by measuring the average energy in regions of pseudo-rapidity in the detector, excluding those that exceed the average by 2σ , and removing this average from the topo-clusters.

Electron triggers are seeded by regions of interest identified in the EM calorimeter, where clustering algorithms are applied. For identification of electrons for triggering, a likelihood is calculated based on information from the tracks of the inner detector, the TRT and EM calorimeter clustering. Muon triggers are based on the dedicated triggering

5 Data and Monte-Carlo Simulation

The work presented in this thesis uses proton-proton-proton collision data and simulated events. In this chapter, the details of these data are outlined. In particular the methods used to generate simulation that mimics real collision data are reported. This includes a description of typical Monte-Carlo (MC) generators which form the foundation of the simulation.

5.1 ATLAS Data

The data used in the physics analysis sections of this thesis, 8, 9 and 10, were gathered during the LHC Run 2 operating period (2015-2018) of proton-proton collisions at centre-of-mass energy of 13TeV. The total integrated luminosity collected by ATLAS during this run is $\sim 150 \text{ fb}^{-1}$. The recorded data is selected based upon the trigger from which the events were recorded, dependent on the prominent features of the analysis. Data is used according to the 'Good Run List' which identifies runs of satisfactory detector operation. Data collected in periods in which detector issues were present are removed. Around 93% of the collected data is suitable for physics analysis giving an integrated luminosity of 139 fb^{-1} . The pile-up profile of proton-proton interactions per bunch-crossing is given in figure 3.2, for Run 2 the average, $\langle \mu \rangle$, was ~ 40 .

5.2 Monte-Carlo Simulation

In high energy physics analysis, the modeling of physics processes being studied is a cornerstone of the work. Detailed simulation based on theoretical calculation of the underlying physics are used in almost all areas. In ATLAS, studies of SM processes often use simulation with certain parameters of interest being studied having different variations within the simulation. An example is mass measurements such as the W mass [43] where the W pole mass is varied. In searches for BSM physics the simulation has 2 main use cases: firstly to understand the characteristic features and rate of SM processes that contribute in the regions investigated in order to provide a background estimation (where the BSM process is considered the signal). Secondly the simulation provides an understanding of the characteristic features and rate of the BSM scenarios which allow a detailed development of the analysis strategy which maximises the sensitivity of the search. The simulation for the SM backgrounds is developed based on the current best knowledge of the SM theory and parameters. Often measurements of the SM are used to tune and improve these models. The BSM simulation is of course based on the theoretical extension being studied, multiple hypotheses/parameters of the

5 Data and Monte-Carlo Simulation

extension can be investigated in one search.

Monte-Carlo (MC) methods form the basis for the simulations. They allow the modeling of processes which have an inherent probabilistic nature by (pseudo-)random sampling from an underlying probability distribution. This is the case for all physics at the quantum scale. The MC simulation in ATLAS is comprised of 5 parts:

- Parton Distribution Functions
- Hard Scatter
- Modeling the parton shower
- Hadronisation
- Underlying Event
- Detector Response

5.2.1 Parton Distribution Functions (PDFs)

As protons are not fundamental particles but are composites containing fundamental particles bound together, the interactions are between the fundamental particles that comprise the proton, known as partons. The partons are the 3 quarks (2 up and 1 down) from which the proton gets its quantum numbers - *valence quarks*, *sea quarks* which are quark anti-quark pairs created within the fluctuating fields of the proton and the gluons. To correctly model proton-proton collisions the kinematics of the partons must be understood. Parton Distribution Functions are sets of probability densities for a parton to have a momentum fraction, x , of the proton momentum. These fractions vary with the energy scale Q^2 of the interaction, for example the fraction carried by the gluons increases with Q^2 . The rate of change of parton densities within the proton with Q^2 can be described in perturbative QCD by the DGLAP equations [44][45][46]. The momentum fractions x carried by the partons are extracted from data by studying cross-sections for different processes at varied Q^2 and deep inelastic scattering (DIS).

5.2.2 Hard Scatter

The hard scatter of a given process is the highest energy interaction between partons from the colliding hadrons. The Matrix Element (ME) is the probability amplitude of the hard scatter process. The programs that perform these calculations are known as *Event Generators*. They start with an inclusive production cross section for the given process which is given by:

$$\sigma_{h_1, h_2 \rightarrow X} = \int dx_a \int dx_b f_a^{h_1}(x_a, \mu_F^2) f_b^{h_2}(x_b, \mu_F^2) \int d\phi_{a,b \rightarrow X} \frac{d\hat{\sigma}_{ab}(\phi_{a,b \rightarrow X}, \mu_F^2)}{d\phi_{ab \rightarrow X}} \quad (5.1)$$

5.2 Monte-Carlo Simulation

This equation for the inclusive production of particle X from incoming hadrons, h_1, h_2 , can be split. The left two integrals integrate over the possible momenta of the two interacting partons, a and b , having momenta x_a and x_b where the probability for these parton momenta are defined by the parton density functions f_a and f_b at the factorisation scale μ_F . The right integral integrates the differential cross-section $d\hat{\sigma}_{ab}/d\phi_{ab \rightarrow X}$ (Matrix Element squared) over the final state phase-space element $d\phi_{a,b \rightarrow X}$. This splitting of the cross-section calculation is allowed by virtue of the factorisation theorem. The right integral is a precise calculation using perturbative QCD (pQCD) to a fixed order in α_s . In order to use pQCD, α_s must be small in the energy regime considered, this is true for the hard scatter for parton energies above μ_F (short distance regime). However, below μ_F (long distance regime), perturbative treatment cannot be used and the physics is modeled not by direct calculation in QDC but by characteristics extracted from data.

ME calculations at Leading order (LO) in α_s have been automated for all processes and most event generation is done at next-to (NLO) or next-to-next-to leading order (NNLO). This means the calculation for Feynman diagrams with up to 6 strong interaction vertices. An event hard scatter is built by randomly generating the initial 4-momenta of the incoming particles from the PDFs (section 5.2.1) which then proceed to the final state particles of the hard interaction. The next step is modeling the parton shower.

5.2.3 Parton Shower

In event generators the final state particles from the hard scatter proceed via the introduction of Markov processes to evolve the final state particles into a shower of further partons. DGLAP equations are used to model the production of new final state parton at scale μ_F from the parent parton at scale $\mu_F + d\mu_F$. The new parton is balanced by an additional new parton by the generator, such that a parton decays to two new partons, in order to preserve unitarity. The process is repeated down to an energy scale close to Λ_{QCD} where the partons become colour confined, the hadronisation scale. For ME generators of order > LO, final state radiation can be produced either from the ME or the PS and can be a source of double-counting. In this case matching and merging algorithms are applied to avoid this.

5.2.4 Hadronisation

At the end of the parton shower, many partons are available with decreasing energy (long distances), they reach the colour confinement regime. The confinement of the partons into colourless states is modeled in a few ways, employed in different MC programs:

- **The Lund string model:** At long distances the QCD potential is approximately linear in the distance between the partons. The confining potential of two quarks is modeled as a string, on which gluons are transverse excitations. As a parton travels in direction opposing the confinement potential it transfers kinetic energy to the string and at some point is confined by the string and the quark begins to travel in the opposite direction, this is the yo-yo model of mesons. The string of an initial quark-antiquark pair will break into further hadrons with

5 Data and Monte-Carlo Simulation

breaking probability proportional to the light-cone area of the string between the quark-pair and gluons on the string. At a string break, hadrons are produced and they carry away momentum from the system.

- **The Cluster model:** Gluon splitting to quark-antiquark pairs is forced at a low bound energy Q_0 . A colour flow is followed through the parton shower and colour singlet pairs are close in phase-space and are confined into heavy meson resonances which then decay to lighter hadrons.

5.2.5 Underlying Event

Since hadrons are composed of multiple partons, sea and valance quarks and gluons, when hadrons collide there may be multiple parton-parton interactions (MPI) in one hadron-hadron collision. Activity outside the hardest (highest energy) parton-parton interaction is called the underlying event (UE) and mainly comes from additional gluon exchange. The UE contributes to the hadron content of the final state and the level of activity in the UE is heavily dependent on the impact parameter of the collision.

The UE is modeled in MC generators as additional perturbative contributions to the hard interaction. These additional contributions follow poisson statistics and are constrained by a colour screen parameter, this parameter comes from the fact that a parton with momentum p has a wavelength $\propto 1/p$ and if the wavelength is larger than the distance between two coloured states then the colour will be screened and the parton will not interact via the strong force. The colour screening parameter is tuned in the MC models.

5.2.6 Detector Response

The ATLAS detector is modeled using the GEANT4 program [48], a specialised simulation software framework for modeling particle behaviour in materials and detector response. The full detector geometry is modeled including the active detector volume and material content of the supporting structures. The geometry of the detector is measured to high precision at intervals during the running of the experiment and the model is updated in a time-dependent fashion to account for mis-alignments. Particles trajectories through the model are identified as a series of hits with materials in the line of flight. A parameterisation of the detector component responses has been developed using test-beam setups and is applied to simulate the behaviour upon interaction with the particles. The digitisation of the detector output is also parameterised such that the output of the program is of the same format as the real detector.

The full simulation of the behaviour of large numbers of particles in the detector is incredibly computationally expensive. To counter this, a fast implementation of the simulation is applied to MC processes where their study is relatively agnostic to finer details of the detector response. Particular improvement is made by using approximations in the modeling of the calorimetry. This faster approach is referred to as *fast sim*.

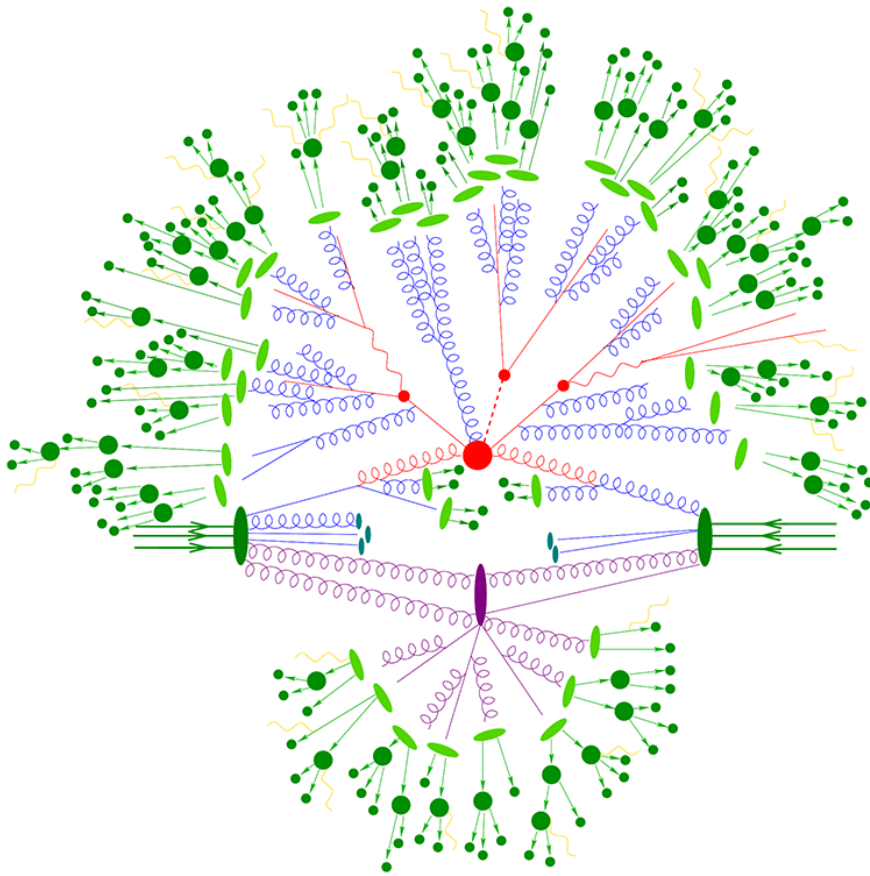


Figure 5.1: Illustration of a MC simulated event, ttH production with the Sherpa [47] Monte Carlo generator. Colours indicate the different stages/areas of the hadron-hadron interaction: Hard process, Initial state parton shower,hadronisation and fragmentation, hadron decays, underlying event, beam remnants.

The generation of the simulated event samples includes the effect of multiple proton-proton interactions per bunch crossing (pile-up 3.1.3). These are modeled by overlaying the hard-scatter event with simulated inelastic proton-proton events generated by the Pythia MC generator. The MC events are weighted to reproduce the distribution of the average number of interactions per bunch crossing observed in the data.

5.2.7 Monte-Carlo Generators

A variety of MC generator softwares, that implement the components described above in slightly different ways, are used in this work to simulate SM and BSM processes. Those are: PowhegBox, SHERPA, Madgraph5_amc@NLO, Pythia and Herwig. The latter two generators can also be applied as parton shower MC generators and provide sophisticated PS functionality that interface to other ME generators.

5 Data and Monte-Carlo Simulation

- **SHERPA**[2.2.1] [49] is a generator using next-to-leading-order (NLO) matrix elements (ME) for up to two partons, and leading-order (LO) matrix elements for up to four partons calculated with the Comix [50] and OPENLOOPs [51–53] libraries. The ME calculations are matched with the SHERPA parton shower [54] using the MEPSatNLO prescription [55–58] using the set of tuned parameters developed by the SHERPA authors. SHERPA is used to simulate electroweak boson processes: $W/Z + jets$, di-boson and tri-boson samples.
- **Pythia**[8] [59] is a software program for modeling hadronisation, parton shower and underlying event of the simulation. It interfaces with programs producing the hard-process to develop complex hadronic final states. The parameters used follow the A14 tune [60] and using the NNPDF2.3-LO set of PDFs [61]. It is used in the production of $t\bar{t}$, single-top processes and tH .
- **PowhegBox**[v2] [62–65] is a generator used to provide matrix elements at NLO in the strong coupling constant α_s . It uses the NNPDF3.0-NLO [66] PDF. PowhegBox is interfaced with PYTHIA[8.230] [59] for the parton shower and hadronisation, using the A14 set of tuned parameters [60] and the NNPDF2.3-LO set of PDFs [61]. This combination is referred to as Powheg+Pythia8, it is used to simulate the $t\bar{t}$, single-top processes and tH .
- **Madgraph5_amc@NLO**[2.3.3] [67] is a generator which provides matrix elements at NLO in the strong coupling constant α_s with the NNPDF3.0-NLO [66] parton distribution function (PDF). It is interfaced with PYTHIA[8.210] [59] for the parton shower and hadronisation, using the A14 set of tuned parameters [60] and the NNPDF2.3LO [66] PDF set. This arrangement was used to simulate all BSM processes and also tV .
- **HERWIG**[7] is a generator able to provide NLO ME calculations, and provides matching algorithms compatible with both Madgraph5_amc@NLO and PowhegBox. In this work is implemented using the H7UE set of tuned parameters [68] and the MMHT-LO PDF set [69]. It is predominantly implemented for PS and hadronisation alternatives for top processes.

Part III

Analysis Methods

6 Physics Objects

As discussed in chapter 4, the information collected by the detector subsystems during a bunch-crossing is extensive. On top of data collected from all detector systems from the primary event, the information stored includes noise, pile-up and underlying event contributions. The particles that reach the detector and initiate the signals that we measure are the remnants of the interaction(s) that occurred. They are comprised of decay products of unstable particles produced in the interaction that decay before reaching the inner detector and products of hadronisation of quarks from the interaction. The resulting signature observed from these particles are often showers of particles (known as jets) from complex decay and hadronisation chains. The properties of the parent particle(s) from which they originated must be determined.

The aim of event reconstruction is to try understand as much about the final state of an interaction as possible from the detector information. In general this is done by grouping energy deposits in the detector into physics objects relating to the event which can be either event-level objects, relating to the primary event as a whole such as the missing transverse energy or sum of momenta attributed to the primary vertex (PV, section 6.9), or sub-event level objects like signatures of final-state particles, electrons, muons, jets passing through the detector. This chapter provides descriptions of the physics objects defined and used in the data analysis of later sections.

Physics objects in this work are categorised at two levels referred to as *baseline* and *signal*. Baseline objects refer to a looser object definition which is more inclusive and is often used as a definition for applying object vetos. Signal refers to tighter requirements on the object identification and have increased purity.

6.1 Track Reconstruction

The ID silicon detectors reconstruct the trajectory of charged particles through the detector [70]. Interactions of charged particles with the silicon pixels and strips are identified by deposits of charge that exceed the threshold for the given sensor. The charge deposits are identified as *space-points*, denoting the position of the deposit. Track finding algorithms are applied using the information from the space-points to reconstruct particle trajectories.

The procedure takes a combinatorial approach, beginning with *track seeds* which are sets of three space-points, a combinatorial Kalman filter is then applied to incorporate additional space-points to the seeds that are consistent with charged particle trajectory, these combinations of space-points

6 Physics Objects

form the track candidates. The charge clusters may be assigned to more than one track candidate, in these instances the most suitable track is determined by considering the number of clusters associated, the number of missing clusters that would be expected to form a full trajectory (holes) and a χ^2 fit of the track points. After overlapping cluster associations are resolved, minimum requirements are placed on the remaining tracks considering the number of clusters, the number of holes and the track momentum is required to be >400 GeV. In addition impact parameters are defined: d_0^{BL} ; the minimum distance of the track from the beam-line in the $R - \phi$ plane and z_0^{BL} ; the distance of the track from the primary vertex (6.9)) in the direction of the beam-line. The requirements are $|d_0^{BL}| < 2.0\text{mm}$ and $|z_0^{BL} \sin \theta| < 3.0\text{mm}$ where θ is the polar angle of the track. Once these requirements are passed the tracks are considered 'good' tracks and are used for further object reconstruction or directly in analysis.

6.2 Jets

Jets are objects built to identify the collimated sprays of particles that arise when coloured partons of the final state initiate a parton shower, radiate additional particles through Bremsstrahlung and hadronise. Unstable hadrons then decay further adding complexity to the structure in the detector. The construction of jets starts from the identification of topological clusters of energy attributed to particles in the calorimeters, known as *topo-clusters*. Firstly a calorimeter seed cell is identified where the energy deposition measured in the cell is >4 standard deviations above the average cell noise for the detector conditions, the cluster is built by iteratively adding adjacent cells whose energy exceeds 2 standard deviations above the noise average until there are none left. Finally, cells adjacent to the cluster are added once, irrespective of their energy.

The jets are formed by combining topo-clusters using clustering algorithms. The prominent algorithm used in ATLAS is the anti- k_t algorithm [Cacciari:2008gp], which is infra-red and collinear (IRC) safe. IRC safety enforces that the jets identified by an algorithm are independent of additional collinear particle splitting and soft QCD emissions. These conditions are important as they prevent divergences in fixed order pQCD calculations.

The basis of the anti- k_t algorithm is the definition of distances between two particles i, j (identified by topo-clusters) δ_{ij} which are sub-components of the jet, and the distance between a particle and the beam, δ_{iB} .

$$\delta_{ij} = \min(k_{ti}^{-2}, k_{tj}^{-2}) \frac{\Delta_{ij}^2}{R^2} \quad (6.1)$$

$$\delta_{iB} = k_{ti}^{-2} \quad (6.2)$$

where k_{ti} is the transverse momentum of particle i , $\Delta_{ij}^2 = (y_i - y_j)^2 + (\phi_i - \phi_j)^2$ where y_i is the rapidity and ϕ_i is the azimuthal angle of particle i . R is a pre-defined radius controlling Δ_{ij} which is can be adjusted according to the requirements of the user, in ATLAS for most purposes it is set to 0.4.

6.2 Jets

The algorithm proceeds by looking at all the distances δ_{ij} and δ_{iB} looking for the smallest. If the smallest is between two particles, then the two particles are combined into a *pseudo-jet* which is then considered as a singlet particle in further iterations. If the smallest is between a particle and the beam, then it is considered a jet and removed from further iterations. The algorithm relies heavily on the transverse momenta of the particles. This has the benefit that the jet features, such as area and shape, are largely unaffected by low-momentum additional contributions such as pile-up or activity from the underlying event. This can be seen in figure 6.1. The consistency in area, jet shape and resilience to pile-up are essential for maintaining the jet energy resolution.

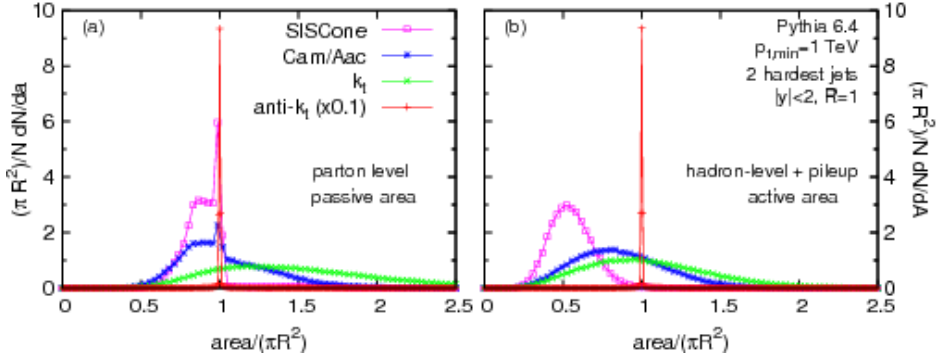


Figure 6.1: Comparison between different jet clustering algorithms showing the area of the jets formed with calorimeter hits derived from parton level information of the hard scatter. The right plots also includes the addition of pile-up and underlying event contributions [Cacciari:2008gp]. The SISCone algorithm is a cone algorithm with split-merge steps, k_t and Cam/Aac are sequential recombination algorithms. The anti- k_t algorithm is shown to have the most consistent area and is independent of pile-up.

6.2.1 PFlow Jets

During Run1 of the LHC a technique was developed to improve the energy and angular resolution of hadronic jets using additional information from tracking in combination with the calorimeter information [71], the technique is referred to as *particle-flow*. Tracks are selected based on strict requirements of at least 9 hits in the ID with no missing hits in tracking layers, with transverse momentum in the range [0.5,50]GeV (excluding those tracks which are associated to a candidate electron or muon). Selected tracks are then associated to topo-clusters by requiring $E^{cluster}/p^{trk} > 0.1$ where $E^{cluster}$ is the calibrated energy of the cluster and p^{trk} is the momentum of the track. The p_T -ordered tracks are then matched to their nearest cluster using the metric:

$$\Delta R' = \sqrt{\left(\frac{\Delta\phi}{\sigma_\phi}\right)^2 + \left(\frac{\Delta\eta}{\sigma_\eta}\right)^2} \quad (6.3)$$

where σ_ϕ and σ_η are the widths of the topo-cluster in ϕ and η . If a track has no topo cluster within $\Delta R' < 1.64$ then it is not included in the correction.

The tracks are assumed to have been left by particles with charged pion mass, so that an assumption can be made about the amount of energy they should deposit. When the tracks are matched to clusters,

6 Physics Objects

if the energy expected to be deposited by the particle from its track momentum (calculated as an average measured in pion simulation) is greater than the energy contained within the cluster, the topo cluster is subtracted from the jet algorithms. If the energy is less than expected, then the energy of cells in the cluster are removed iteratively by weighting those close to the trajectory of the track. The result of this subtraction is employed in the anti- k_t algorithm which is then applied considering the tracks that are attributed to the primary vertex (PV) (requiring $|z_0 \sin \theta| < 2\text{ mm}$) and the remaining topo clusters. This additional information improves the energy and angular resolutions of the reconstructed jets at lower transverse momentum as well as the angular resolution (figure 6.2) when compared with the same jet algorithm using only calorimeter information (LC+JES). In addition, hadronic activity with energy below the threshold value for a topo-cluster can be considered which is an important contribution for improving the resolution of global event metrics such as the missing transverse energy.

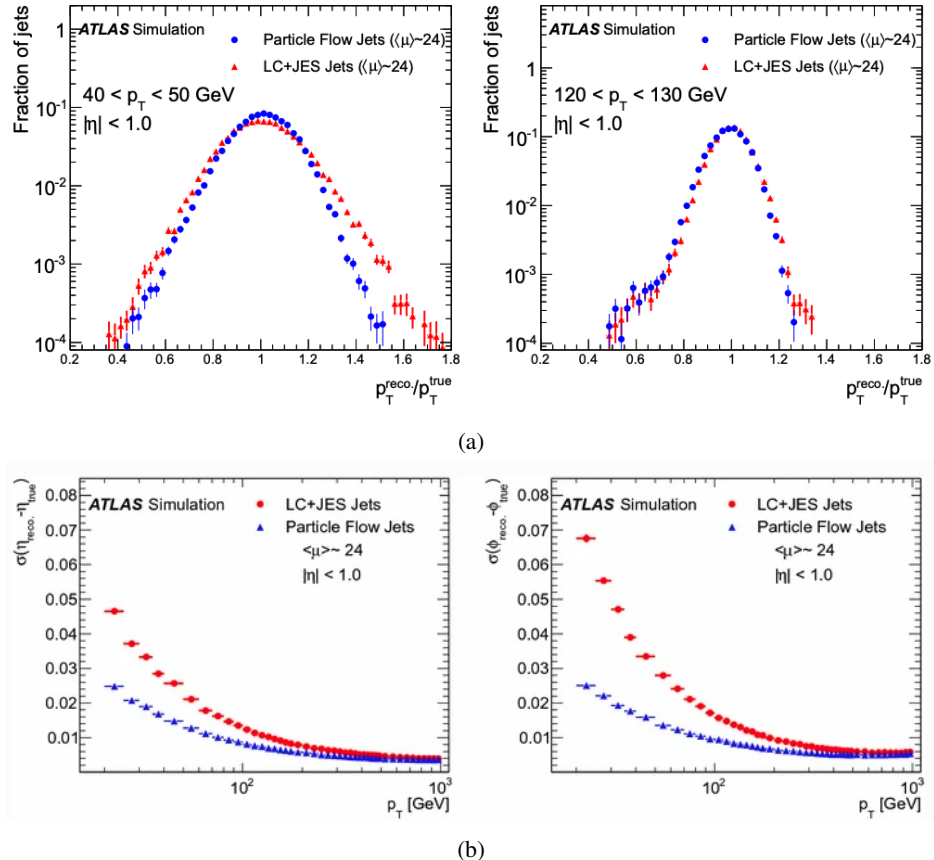


Figure 6.2: Comparison of the resolution of jets reconstructed using the PFlow method vs a standard algorithm using only topo clusters, measured in di-jet MC simulation showing in 6.2(a) the difference between reconstructed transverse momentum (p_T) and true p_T , 6.2(b) the resolution of angular components η and ϕ as a gaussian distribution between reconstructed true values. The angular resolution is improved in all regions, the p_T resolution is improved for low p_T jets though the improvement is reduced at higher p_T [71].

6.2.2 Jet Flavour Tagging

In interactions that result in final states involving quarks, the signature within the detector depends on the lifetime of the quarks produced. The heavier flavours have shorter lifetimes, top quarks decay before they hadronise, bottom and charm quarks form heavy hadrons with lifetimes long enough that they often decay inside the detector within the particle shower that is forming. It is possible, using detector information, to identify whether a jet initiated from a heavy-flavour quark: bottom or charm quark rather than light flavours: up, down, strange. The heavy flavour charm and bottom jets have features such as a secondary vertex from the decay of the hadron that formed inside the jet cone that make them distinguishable from light flavour jets. Within ATLAS, the identification is done by combining ‘low-level’ information with ‘high-level’ information in multi-variate algorithms based on features measured in MC simulation. In this context, low-level information relates to components of substructure of the jet whilst high-level information relates to features of the jet itself such as its transverse momentum and direction. For standard jets the tagging algorithms consider the separation into b-quark, c-quark and light (u,d,s) quark categories. As top quarks decay before they can hadronise and form jets, they may be reconstructed as a large radius jets if the decay products are collinear for boosted top quarks. Boosted top jets are identified with dedicated jets reconstruction algorithms that have a larger radius, the details are outside the scope of this work.

The low-level information is constructed from dedicated algorithms that identify the features of the jet associated with heavy-flavour decay. This includes a consideration of the impact parameters, transverse, z_0 , and longitudinal, d_0 , of the tracks associated to a jet. Tracks with $p_T > 1$ GeV passing quality requirements on the number of hits are used to calculate a log likelihood ratio of the flavour of the jet (b/c/light) based on the number of tracks and the impact parameters using a template probability distributions derived from MC. An alternative method for deriving information from the track impact parameters make use of a recurrent neural network to consider information from many tracks associated to the jet in sequence which provides a flavour tag probability (derived from MC) as output.

Track information is also used to identify the presence of one or more secondary vertices (SVs) within the boundaries of the jet constructed with the anti- k_t clustering algorithm. The secondary vertex finder [72] is used to find a single SV by looking at pairs of tracks that form a vertex but are inconsistent with features of other long-lived particle decays (k_s, Λ). The JetFitter algorithm attempts to reconstruct the topology of decays within the jet boundary.

Muon information is gathered with the soft-muon tagger to compliment the jet-structure information in the case where the heavy-flavour hadron decay includes a muon. The branching fraction for b and c-hadrons to muons is greater than for other hadrons and thus the presence can provide an additional handle for discrimination. If a muon is detected having a trajectory that falls within $\Delta R < 0.4$ of the jet axis it is attributed to the jet. Features of the muon such as track reconstruction quality, impact parameter d_0 , angular separation from the jet axis ΔR and its transverse momentum relative to the jet are used as input to a boosted decision tree (BDT) which discriminates b,c and light-flavour sources

6 Physics Objects

and outputs a probability for each. The BDT is trained using MC simulated samples.

To make the final tagging discrimination of the jet flavour, the information from the low-level is combined with high-level information and input to a multi-variate algorithm (MVA) which gives an output score for either b,c or light-flavour tag. The MVA is again trained using MC simulated events. When used in analysis, the output score is discretised in relation to the efficiency of tagging the jet. This is used so that a calibration to data can be performed, resulting MC-to-data scale factors are derived in η and p_T bins.

In this work, two MVAs are used: the first, denoted MV2c10 [73], is a BDT algorithm that combines the low-level impact parameter, secondary vertex information and soft-muon BDT output with the p_T and η of the jet. The second is denoted DL1 [73] and is a Deep Neural Network (DNN) algorithm that combines low-level impact parameter, secondary vertex and soft-muon tagging information (inputs used in the SMT BDT). Both algorithms provide output scores for either b-tag, c-tag or light-tag classifications which are then calibrated to data.

Figure 6.3 shows the performance of the algorithms comparing the secondary vertex finder, jet fitter and impact parameter components separately against the MVA algorithms MV2 and DL1.

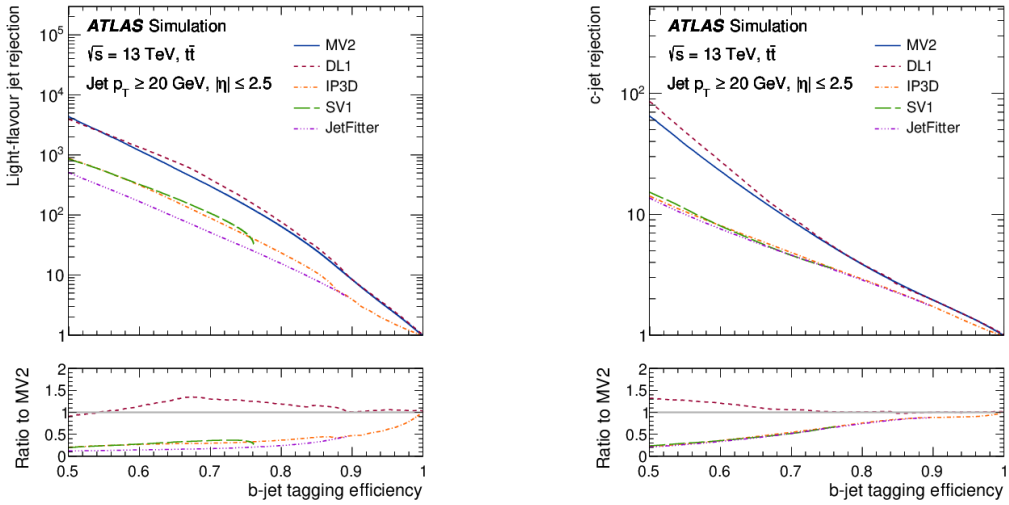


Figure 6.3: The (a) light flavour jet and (b) charm rejection for the different algorithms and sub-algorithms used in the flavour tagging as a function of the b-jet efficiency. In general, the DL1 algorithm performs the best, having the highest rejection and efficiency of all considered [73].

6.3 Electrons

As high energy electrons produced in the final state pass through material they dissipate energy through Bremsstrahlung and other subsequent processes producing showers of electron-positron pairs

and photons collectively referred to as EM showers. The showers can form in the EM calorimeter or in earlier material parts of the ID. The identification and reconstruction of electrons is based on identifying topo-clusters of energy (as with jet reconstruction) in the calorimeters [74] with associated track in the ID. The clusters are grouped into super-clusters, which have variable size. The energy associated with an electron is taken from the EM calorimeter part of the topo-cluster only, identification requires that the fraction of the energy deposited in the EM is greater than the energy deposited in the hadronic calorimeter for a cluster. EM clusters formed by photons and electrons are very similar, the distinction between the two objects is made by the association of a track of the charged electron to the cluster. Tracks are matched to EM clusters if the difference in psuedo-rapidity, $|\Delta\eta| < 0.05$ and requiring $-0.10 < q \prod(\phi_{track} - \phi_{cluster}) < 0.05$, where q is the charge of the track determined by the direction of bend in the magnetic field.

Electron object identification is conducted using information from track quality, TRT, information on the longitudinal and lateral shape of the EM cluster and is derived using a likelihood discriminant based on probability density functions smoothed with a kernel density estimator. The probability density functions are derived from data using $Z \rightarrow e^+e^-$ and $j/\psi \rightarrow e^+e^-$ processes where the electrons are identified using the tag and probe method [75].

An identified electron will have some overlap in its calorimeter and track signatures from other particles in the detector and noise. Hence we are required to isolate the signature associated with the electron. The calorimeter isolation is performed by selecting positive energy calorimeter clusters within an angular range of $\Delta\eta \times \Delta\phi = 5 \times 7$ cell units (the cells of the EM calorimeter granularity). The electron track is isolated by forming a cone around the electron track with cone size dependent on the p_T of the track, given by:

$$\Delta R = \min\left(\frac{10}{p_T[\text{GeV}], \Delta R_{max}}\right) \quad (6.4)$$

where ΔR is a pre-defined maximum cone size.

6.4 Photons

Photons are identified from super-clusters in the EM calorimeters which do not have an associated track in the inner detector but instead, in the case of a converted photon, will have an associated photon conversion vertex or, in the unconverted case, be associated to neither track or conversion vertex. The photon conversion vertex is reconstructed from tracks in the inner detector, both from the SCT and TRT, that are loosely associated to an EM cluster. They are identified as either two oppositely charged tracks that have a common vertex with properties consistent with coming from a massless particle or single tracks that have no hits in the first layers of the inner detector [74].

Within this work, photons are not explicitly used as physics objects in the analysis but their identification is used as input when calculating the E_T^{miss} as described in section 6.7.

6 Physics Objects

6.5 Muons

Muons are identified using information from several different detector subsystems. They can be identified by combinations of charged particle tracks in the ID matched with tracks or segments of tracks (few hits) in the muon spectrometer, tracks that are only in the muon spectrometer that are extrapolated to the PV at the beam-line or combination of ID tracks matched to minimum ionising energy deposits in the calorimeters. The identification of muons is based on defining several working points, the definition of the physics object then is subject to the requirements of the analysis. The requirements are dependent on the sub-detectors in which the muon signal is identified, they include requirements on the number of hits in the tracks, goodness of fit of the track matching between sub-detectors. Impact parameter requirements are also applied to distinguish prompt muons from muons arising from heavy flavour hadron decays. The working points are *Loose*, *Medium*, and *Tight* [76] with increasing purity respectively.

Isolation of muons is used to further suppress contributions from heavy flavour hadron decays, again several working points are defined. The isolation used can be either track-based, calorimeter-based or combined particle-flow based. The track-based isolation is developed by measuring the sum of the transverse momenta of tracks from the primary vertex in an angular cone around the muon track. Similarly, for the calorimeter-based isolation an angular cone is measured around the calorimeter cluster associated to the muon. The particle-flow isolation matches contributions from the tracks and calorimeters in order to remove double-counting, resulting in better prompt muon efficiency [76].

6.6 Taus

In this work a loose tau definition is used in order to apply an inclusive veto on their presence. Tau candidates are defined as jet candidates that have $|\eta| < 2.5$ and less than four associated tracks with $p_T \geq 500$ MeV in the inner detector and with angular separation from the E_T^{miss} direction of $\Delta\phi(\vec{E}_T^{\text{miss}}, \tau_{\text{cand}}) < \frac{\pi}{3}$.

6.7 Missing Transverse Energy

Due to the composite nature of protons, in proton-proton collisions the component of momentum in the beam-line direction of the interacting partons is not known, however, the initial momentum of the partons perpendicular to the beam-line will always be (approximately) zero. Hence, the vectorial sum of the transverse momenta of final state particles will be zero. The E_T^{miss} is a key observable for inferring the presence of particles carrying energy from an event without being detected, that can be identified as an imbalance in the final state transverse momentum when summing the transverse momenta of the final state particles. This is crucial for BSM searches for signals with weakly interacting final-state particles that do not interact with the detector. E_T^{miss} is defined as the negative

6.7 Missing Transverse Energy

sum of transverse momenta of all calibrated final state objects associated to the primary vertex, plus a soft term accounting for particles not identified as objects [77]:

$$E_T^{\text{miss}} = |\vec{p}_T^{\text{miss}}| \quad (6.5)$$

where

$$\vec{p}_T^{\text{miss}} = - \sum \vec{p}_T^u - \sum \vec{p}_T^e - \sum \vec{p}_T^\gamma - \sum \vec{p}_T^e - \sum \vec{p}_T^\tau - \sum \vec{p}_T^{\text{jets}} - \sum \vec{p}_T^{\text{soft}} \quad (6.6)$$

The vector quantity is often useful, the direction is quoted in the azimuthal angle ϕ . The term $\sum \vec{p}_T^{\text{soft}}$ accounts for energy not attributed to a reconstructed object. In Run 2, ATLAS analyses use the track-based soft term (TST). This is the sum of all track transverse momenta passing quality requirements and attributed to the primary vertex that are not associated with a reconstructed object. The other terms sum the transverse momenta of objects in the event using the calibrated p_T of the object. The reason for summing objects rather than just tracks and calorimeter hits associated to the PV is that the objects, once identified can be calibrated, giving better energy resolution.

6.7.1 Object-Based E_T^{miss} significance

The measurement of E_T^{miss} relies on the precise determination of the p_T of reconstructed objects, thus mis-measurement of objects (particularly high p_T jets) will produce events with spurious surplus E_T^{miss} . All objects measured in the detector have imperfect resolutions and reconstruction efficiencies. In order to take into account resolution effects, a new variable has been developed which includes momentum resolution of the reconstructed objects to give a measure of the p-value of the measured E_T^{miss} being real from the hypothesis of a zero E_T^{miss} event [ATLAS-CONF-2018-38].

The significance is defined based on a ratio of likelihoods,

$$\mathcal{L}$$

, considering the hypotheses of the measured E_T^{miss} being correct and it being spurious due to mis-measurement of the objects:

$$\mathcal{S}^2 = 2 \log\left(\frac{\mathcal{L}(\vec{p}_T^{\text{miss}}|\vec{p}_T^{\text{miss}})}{\mathcal{L}(\vec{p}_T^{\text{miss}}|0)}\right) = (\vec{p}_T^{\text{miss}})^T \left(\sum_i \mathbf{V}^i\right)^{-1} (\vec{p}_T^{\text{miss}}) \quad (6.7)$$

where \mathbf{V}^i is a correlation matrix describing the resolution of the i th object included in the E_T^{miss} calculation. The object momentum resolutions can be decomposed into two components: parallel and perpendicular to the direction of \vec{p}_T^{miss} , the resolutions are assumed to be gaussian around the true value and uncorrelated such that \mathbf{V}^i takes the form:

$$\mathbf{V}^i = \begin{pmatrix} \sigma_{p_T^i}^2 & 0 \\ 0 & p_T^i \sigma_{p_T^i}^2 \end{pmatrix} \quad (6.8)$$

6 Physics Objects

The object-based E_T^{miss} significance is found to significantly outperform standard E_T^{miss} in separating of events containing real E_T^{miss} from those with E_T^{miss} coming from mis-measurement in events with at least one jet.

6.8 Overlap Removal

Occasionally, multiple physics objects can be reconstructed from the same or overlapping signals in the detector. In these cases it is important to make a decision about which object to keep to avoid double-counting. An algorithm of preferred objects is established:

- Two electrons are identified from the same track in the ID, lower p_T electron is removed.
- A muon and electron sharing the same ID track, the electron is removed.
- Electrons within angular distance, $\Delta R < \min(0.4, 0.04 + 10\text{GeV}/p_T)$ of a jet are removed.
- Jets with axes within $\Delta R < 0.2$ of a muon. If the tracks from the MS pass through the jet, the jet is removed, otherwise the muon is removed.

Objects remaining after the overlap removal form the final analysis objects.

6.9 Event Cleaning

In order to maintain the quality of data used certain conditions are required to pass relating to the detector performance at the time it was recorded. These requirements can be applied to physics objects, events or regions of data. They are described in the following.

A primary vertex must be defined for an event to be considered. The requirement for identification of a PV is the presence of at least two tracks associated to the same vertex where the tracks are required to have a transverse momentum of $p_T > 500 \text{ MeV}$ and be in the central region, $|\eta| < 2.5$. They must also satisfy a minimum number of hits and be below a maximum number of missing hits (holes) in the pixel and SCT tracking layers. The hit and hole requirements vary depending on the centrality of the track.

Detector subsystems such as the calorimeters and the SCT can experience noise bursts, either due to electronic interference or high occupancy from previous events. The subsystems often require resetting to alleviate these issues. Events which are recorded during these resets are excluded from the analysis dataset.

In Run 2 of the LHC the run periods are split into one minute periods known as luminosity blocks. If a luminosity block has problems with beam stability, magnet conditions or issues with the experiment sub-detectors then it can be classed as 'bad'. Bad luminosity blocks are excluded from physics

analysis.

In addition to removing events not considered satisfactory, physics events that cause the HLT system to time-out are recorded in a separate debug data stream which can then be considered for analysis, even though the events did not strictly pass trigger requirements.

6.10 Systematic Uncertainties

Systematic uncertainties are introduced in the statistical analysis to parameterise uncertainty in two areas: uncertainties on experimental measurements and Monte-Carlo modeling uncertainties. The experimental uncertainties are estimated using information from simulation and measurements of well-known processes in data comparing known values with reconstructed values in the detector. Modeling uncertainties come from assumptions made in the simulation of the physics processes, these can be uncertainties on physical constants used, QCD-related scale and matching between the hard-scatter and parton-shower elements of MC simulation or others specific to the process such as interference treatment.

The uncertainties are applied in the calibration of individual object parameters, global event variables such as E_T^{miss} and general detector conditions such as pile-up and luminosity. The systematic uncertainties are provided as nuisance parameters to the likelihood fit of the analysis and their probability distribution functions are assumed to be Gaussian and are assigned as $\pm 1\sigma$ variations.

6.10.1 Jets

In calibrating the jet energy, the jet energy scale (JES) and jet energy resolution (JER) uncertainties are determined through a combination of measurement of balanced jet events in both data and MC simulation as described in [78][79]. These include calibration uncertainties on the processes used to conduct calibration (electron, muon and photon energy and identification), uncertainties in the samples used for the calibration (e.g. statistical uncertainty and different generators), impacts from the pile-up, quark flavour-specific composition within the jet and the associated response difference based on flavour. The flavour tagging uncertainties come from statistical uncertainties on the samples used to derive the data/MC scale factors. All jet uncertainties are parameterised according to the jet kinematics.

6.10.2 Electrons and Muons

Uncertainties for light leptons are attributed to the energy calibration, the (mis-)identification and isolation parameters requirements. Analyses in this work use lepton triggers for data selection which require an associated scale-factor to correct the MC response to replicate the behaviour in data.

6 Physics Objects

Uncertainties are attributed accounting for effects on data selection for the tag and probe method and MC samples used to produce the scale factors [80],[76].

6.10.3 Missing Transverse Energy

The uncertainties on the reconstructed object values used to calculate each term in 6.6 and an uncertainty attributed to the scale for the soft-term are propagated to the final E_T^{miss} term [81].

6.10.4 Luminosity Uncertainty

An uncertainty is assigned to the value of the total integrated luminosity used for calculating expected MC event numbers from the process cross-section. The luminosity is determined during the running of the detector through a combination of dedicated detectors (LUCID [82], ATLAS BCM [83]) and detector information such as the number of tracks reconstructed. The luminosity is calibrated using van Der Meer scans and an uncertainty of 1.7% [84] was assigned for the full 139 fb^{-1} Run 2 dataset.

6.10.5 Pile-Up Uncertainty

Due to the heavy computational load required for MC simulation, most is done prior to or during the period of data taking. Thus, the pile-up conditions are not known exactly. Events are instead simulated with a range of additional pile-up events. As mentioned in section 5.2.6, to produce an accurate pile-up profile replicating the data conditions, a weighting scheme is used to increase the importance of MC events that have the required pile-up for a given run. The associated uncertainty is introduced applying $\pm 1\sigma$ of the pile-up value measured.

6.10.6 Modeling Uncertainties

Modeling uncertainties can be split into two types: those that are based on comparing different Monte-Carlo generation programs for either the matrix element calculation or the showering program. These are generally applied as 2-point systematics where a nominal program is chosen and the variation from a different generator is taken as the uncertainty, this is sometimes symmetrised. The other type of modeling uncertainty comes from the choice of theoretical values for the QCD scale or approach for dealing with interfering processes, diagram subtraction vs diagram reduction. The dominant modeling uncertainties contributing in each analysis are discussed in more detail in the analysis sections.

7 Analysis Techniques

In order to analyse the collected data and search for new phenomena in a quantitative way, statistical methods must be employed. This chapter describes the statistical techniques used to quantify the results and the process of designing the analysis strategy in section 7.1.1. The analysis design relies on the identification of key variables of the observed physics in its construction. More traditional variables which aim to generalise the discrimination between different processes are summarised in section 7.2. The use of more advanced techniques based on machine-learning methods are also employed in this work, the details of these are described in section 7.3.

7.1 Statistical Analysis

7.1.1 Analysis Design

Due to the probabilistic nature of quantum interactions and the composite nature of protons collisions, in most cases the proton-proton interactions are not investigated individually but instead measurements are made of distributions in the data and statistical analysis is used to draw conclusions about the underlying processes producing the distributions. In searching for new physics, particularly physics with low cross-sections, the core tenet of the analysis is to use selections on the properties of events to define regions of phase-space where events coming from the process of interest are expected to contribute significantly such that their presence can be determined against the expected background. These are known as *Signal Regions* (SRs).

The measurement made is a counting experiment upon which the different hypotheses can be tested. The null hypothesis is that only Standard Model processes contribute and additional hypotheses for the presence of BSM processes in the data can be tested for. In addition, in the event of confirming the null hypothesis, the measurement can be used to establish limits on the maximum cross-sections of specific hypothesised BSM process.

This approach means that the most sensitive signal regions are those where the expected signal contribution is high with respect to the background SM processes and where the uncertainty on the signal and background contributions is as low as possible. When designing the analysis, MC simulation is used to define optimally sensitive signal regions. To estimate the sensitivity of a signal region using MC, an approximate significance can be defined and used as a metric to be maximised in

7 Analysis Techniques

the region optimisation. For a region with predicted total events, n , summing the expected signal and background contributions from MC $n = s + b$ with uncertainty σ the significance is given by [85]:

$$Z = \sqrt{2(n \ln\left[\frac{n(b + \sigma^2)}{b^2 + n\sigma^2}\right] - \frac{b^2}{\sigma^2} \ln\left[1 + \frac{\sigma^2(n - b)}{b(b + \sigma^2)}\right])} \quad (7.1)$$

σ includes both statistical uncertainties from the MC and a flat uncertainty used to approximate the systematic uncertainty which is usually estimated from previous measurements and knowledge of uncertainties in the backgrounds for this phase-space. Maximising this significance gives an approximation of the region most sensitive for signal discovery without the computational impact of producing a full fit.

Equation 7.1 is used in the later sections to optimise signal region design. Throughout this thesis this optimisation is done by taking a small number of signal hypotheses, defined by the model BSM process and the proposed masses of the new particles, and optimising the selections on discriminant variables maximising Z. In addition, one can define multiple signal regions which, if they are statistically independent, can be fit simultaneously to provide increased sensitivity. Multiple signal regions are often defined splitting powerful discriminant distributions into separate bins. In the context of significance, the sensitivity of multiple simultaneously fit SRs is approximated by summing their Z values in quadrature. In later sections the optimisation is done by a grid search, where powerful, largely uncorrelated discriminant variables are identified and a set of resonable binning and selection combinations is tested to maximise the cumulative Z value.

Once the SRs are defined, the background SM processes that contribute in the SRs can be estimated from MC. The background estimation for processes can either be taken directly from the MC prediction or data measurements can be used to derive the estimate. The later are referred to as *data driven* estimates. In this work a semi data-driven approach is taken for the dominant SM processes through the construction of addition dedicated regions used to measure the rates of the SM processes, known as *Control Regions* (CRs). CRs are designed to be statistically independent of the SRs, having a high purity of the targeted SM processes, but also occupying a similar phase-space to that of the SRs. The rates for given processes are then measured in the CRs and these rates are extrapolated to the SRs.

When designing control regions, the background measurement made must be extrapolated over certain discriminant variables to the signal regions, validation regions are designed to validate that the extrapolation is accurate. These are typically defined somewhere between the CRs and VRs in one or more of the discriminants (but orthogonal to both) in order ensure that the extrapolation produces good agreement between the MC prediction and data yield. This concept of region organisation in the parameter space being extrapolated over is illustrated in figure 7.1.

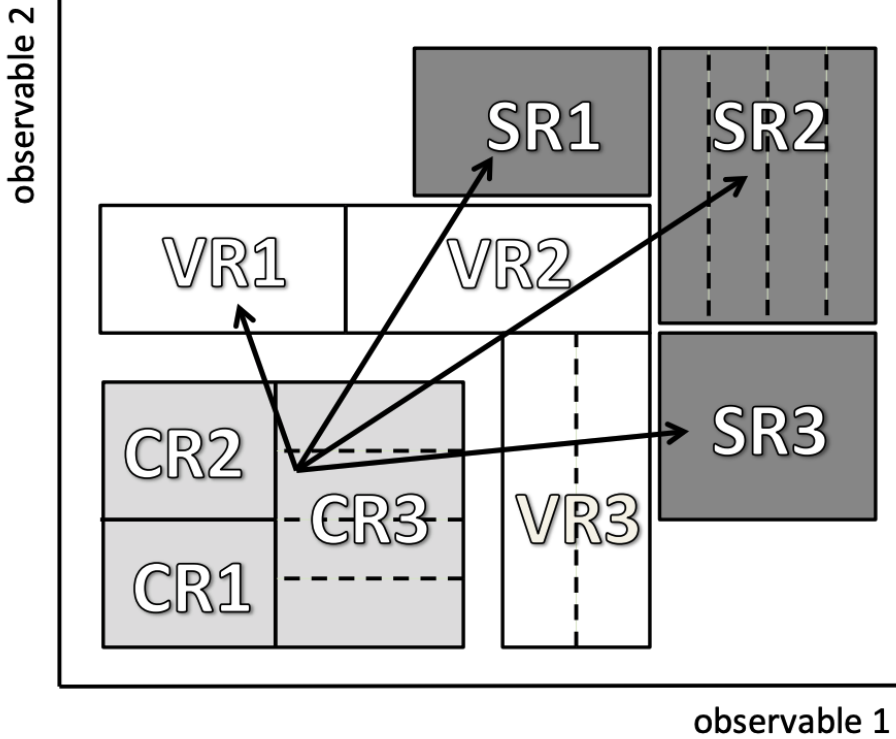


Figure 7.1: Illustration of the ideal arrangement of signal, control and validation regions as defined in the phase-space of two observables[86].

7.1.2 Statistical Analysis

The software package used for the statistical analysis in this work is HistFitter [Baak:2014wma]. Within HistFitter, the regions are defined and histograms of data and MC yields are built from the definitions, in turn a parametric model is built containing the parameter of interest (often the signal rate), transfer factors for backgrounds normalised to control regions and statistical uncertainties which are defined as nuisance parameters. A Likelihood function is then built from the parameterised models as the product of Poisson distributions describing the number of events in the regions defined:

$$L(n, \theta^0 | \mu_{sig}, \vec{\mu}_p, \vec{\theta}) = \mathcal{P}_{SR} \times \mathcal{P}_{CR} \times C_{syst} \quad (7.2)$$

$$= \prod_{i \in SR} P(n_i | \lambda_i(\mu_{sig}, \vec{\mu}_p, \vec{\theta})) \times \prod_{i \in CR} P(n_i | \lambda_i(\mu_{sig}, \vec{\mu}_p, \vec{\theta})) \times C_{syst}(\vec{\theta}^0, \vec{\theta}) \quad (7.3)$$

where P is the Poisson distribution of region i with n_i observed events, $\vec{\mu}_p$ are the normalisation factors for the backgrounds determined with data-driven estimates from the CRs, $\vec{\theta}$ is the vector of nuisance parameters describing the MC statistical and systematic uncertainties. The systematic uncertainties are modeled as gaussians which interpolate between the central (nominal) probability density function

7 Analysis Techniques

(PDF) and the PDF of the systematic variation where $\pm\theta_i$ is one standard deviation in the uncertainty, θ^0 are the central values. C_{syst} is the PDF introducing the nuisance parameters.

The likelihood in 7.2 is used for hypothesis testing, the profile log likelihood ratio [87] is calculated as a test statistic for a given signal contribution μ_{sig} considering:

$$q_{\mu_{sig}} = -2\log(L(\mu_{sig}, \hat{\theta})) \quad (7.4)$$

from this the p-value for the hypothesis test can be computed as:

$$p_{\mu_{sig}} = \int_{q_{\mu_{sig},obs}}^{\infty} f(q_{\mu_{sig}}|\mu_{sig}) dq_{\mu_{sig}} \quad (7.5)$$

where $f(q_{\mu_{sig}}|\mu_{sig})$ is the PDF of $q_{\mu_{sig}}$ for signal contribution μ_{sig} . $f(q_{\mu_{sig}}|\mu_{sig})$ is approximated by a non-central χ^2 distribution if there is only 1 parameter of interest. The rejection of the hypothesis test is set at some p-value agreed within the field. The p-value as a metric of confidence in a hypothesis has problems when considering a signal hypothesis in cases where the MC over-predicts the data. Instead the CLs method [88] is used. CLs is a modified p-value, also referred to as normalised, which takes into account the p-value for rejecting the probability of accepting a background-only hypothesis as well as rejecting the signal+background hypothesis:

$$CLs = \frac{p_{s+b}}{1 - p_b} \quad (7.6)$$

Where p_{s+b} is the p-value for signal+background and p_b for background only. This is a conservative approach that protects against falsely excluding signals in instances with: low cross-sections, where the PDFs for signal+background and background-only overlap heavily, and in the case of a downward fluctuation in the data.

When the fit is conducted, the normalisation of MC processes measured in the CRs is translated to the SRs through transfer factors, μ_p , for background process p using the ratios of CR and SR MC estimations and scaling to the data measured in the CR. By taking ratio between MC predictions in the SR and CR many of the systematic uncertainties cancel to a large degree if they are correlated between the two regions.

Three fit types are used for the analyses presented here:

- **Background-Only Fit:** Here only the CRs are used in the fit and no BSM signal is included. This fit provides an estimate for the background contributions in the SRs and VRs which are extrapolated from the fit in the CRs.
- **Model-Independent Fit:** In this fit, both the CRs and a single SR is included in the fit, but no signal is included. This single SR may also be referred to as the discovery signal region. With binned distributions it is often taken as the most sensitive bin inclusive of bins at higher values of the variable. The purpose of this fit is to perform the null (background-only) hypothesis test and set upper limits on the number of possible signal events.

- **Model-Dependent Fit:** This fit includes both CRs and all SRs and includes a specific signal contribution. A hypothesis test is performed on the presence of the signal in the data. The CLs for the given signal hypothesis is derived from this fit.

7.2 Discriminant Variables

In searches for BSM physics, particularly when considering new physics interactions with low cross-sections, event-level features are used to distinguish events coming from the signal process (the BSM process being targeted) from background processes (SM processes or detector/experimental backgrounds). The greater the ability of the discriminant variable to distinguish signal from backgrounds, the greater the statistical power of the analysis.

A large number of variables are used in the work presented. This section aims to outline and define the more complex variables that require detailed explanation, whereas more straightforward common variables will be defined in the relevant analysis sections.

7.2.1 Mass Scale Variables

In many BSM scenarios, particularly including dark matter and SUSY, the masses of the new particles introduced are above the scale of the heaviest SM particles. From this difference in scale, discriminants can be constructed based on the reconstructed invariant mass of final state objects, referred to as mass-scale variables.

m_T

The *transverse mass*, denoted m_T is defined as:

$$m_T = \sqrt{2p_T(\alpha)E_T^{\text{miss}}(1 - \cos\Delta\phi(\vec{p}_T(\alpha), \vec{p}_T^{\text{miss}}))} \quad (7.7)$$

where α is a visible final state object, usually either electron or muon in the 1-lepton final states. m_T aims to reconstruct the invariant mass of semi-invisibly decaying particles, such as leptonic W-decays. The distribution has an end-point around the mass of the decaying particle. Semi-decaying BSM particles that are heavier than SM particles or that have increased E_T^{miss} will have an extended distribution tail.

7.2.2 m_{CT} and m_{T2}

These variables are constructed based on the assumption of a pair of identical particles produced in the interaction which decay symmetrically semi-invisibly producing two chains of particles each having

7 Analysis Techniques

one invisible final state particle. m_{T2} [89] is an extension of m_T and defines the minimum mass of the pair-produced parent particles consistent with the kinematics of the event. It is defined as:

$$m_{T2}^2 = \min[\max(m_T^2(\alpha, p), m_T^2(\beta, q))] \quad (7.8)$$

where α and β are the momenta of the visible parts of the two decay branches, p and q are the proposed transverse momenta of the invisible particles in the branches. The minimisation is conducted by selecting values for p and q such that $p + q = \vec{p}_T^{miss}$. This minimisation implies that the more massive the parent particles, the higher the value of m_{T2} thus distinguishing high-mass BSM parents from SM parents in similar decay chains.

m_{T2} can also be extended to address signatures where the legs decay with asymmetric masses of the invisible particles, $m(p) \neq m(q)$, denoted am_{T2} .

The variable m_{CT} has similar properties to m_{T2} and is defined as:

$$m_{CT}^2 = (E_T(\alpha) + E_T(\beta))^2 - (\alpha_T - \beta_T)^2 \quad (7.9)$$

Where α and β are the momenta of the visible particles coming from the first leg decay. Both variables have end-points that only depend on the masses of the particles in the decay chain, however m_{T2} requires an assumption to be made on the mass of the invisible particles.

H_T

This is defined as the scalar sum of all jet transverse momenta associated to the primary vertex. It gives a measure of the energy content of the hadronic components of the event which is often greater in BSM signals than SM processes in cases where heavy BSM particles decay to quarks producing a final state with many high p_T jets.

m_{Eff}

Also known as the effective mass, this variable is defined as $H_T + E_T^{miss}$ of the event, where both are scalar quantities. This is useful in distinguishing signals with high jet-multiplicity and large missing energy.

Angular variables

In many cases the topology of events can be used as a discriminant characteristic. This based measures of the angular distance between objects in the detector. The main measures used are $\Delta\phi$ - the azimuthal angle between two objects, $\Delta\eta$ - the difference in pseudo-rapidity between two objects and ΔR which combines both and is defined as:

$$\Delta R = \sqrt{\Delta\phi^2 + \Delta\eta^2} \quad (7.10)$$

7.3 Machine Learning Techniques

Machine Learning (ML) is a term used to describe a group of techniques where algorithms for specific tasks are derived using the observation of some dataset to derive the algorithm parameters. Common methods are: *Regression*, where a continuous function is developed which describes the relationship between one or more input variable(s) and predicts a continuous output, and *Classification*, where a (continuous or discrete) algorithm/function is developed which predicts whether a set of input observables describe one or more underlying classes. Classification is used in this work.

The 'learning' part of the title describes the statistical methods that allow the algorithm or function in development to be adjusted and improved based on observation of some data. In the case of *supervised* learning the data shown contains both the input observables and the true (correct) output which the model aims to predict in general, known as a labelled dataset. In the case of classification, this is the true class the observables of an instance are associated with.

7.3.1 Gradient Boosted Decision Trees

The approach taken with the ML methods in this work is to target signal hypotheses that are in regions of phase-space which are not accessible by using cuts and fits in the major discriminating variables. Though the key discriminating variables are not sensitive enough to discriminate these signal hypotheses independently, the signal is still expected to be kinematically discernible from background process through subtleties of the variable combinations and correlations. Therefore machine-learning techniques are introduced in order to exploit more complex differences that can distinguish the signal. The ML algorithms used in this work are gradient boosted decision trees (gBDTs). gBSTs are constructed by developing sets of regression tree functions which are then combined into one full ensemble by adding consecutively, taking notation from [90], for K total functions:

$$\hat{y}_i = \sum_k^K f_k(\vec{x}_i), \quad f_k \in \mathcal{F}$$

where \mathcal{F} is the space of regression trees. Regression trees differ from decision trees in that each leaf represents an output score(s) relating to the class being predicted. The gradient boosting mechanism defines the way in which the trees are constructed. Each new split or 'learner' is added to the tree by optimising the learner split according to a given objective function (whose form and gradients are pre-defined). The objective function constructed from a loss function along with a regularisation term which constrains the model complexity. The purpose of the loss function is to give a measure of the goodness of the model, the training procedure aims to minimise this function based on the data

7 Analysis Techniques

in the training set or subset. The loss function used in XGBoost models in this work is always the categorical cross-entropy (equation 7.11).

$$\mathcal{L}_{cross-entropy} = - \sum_{i=1}^N y_i \cdot \ln(\hat{y}_i) \quad (7.11)$$

where N is the number of output categories, y_i is the output of the model for category i and \hat{y}_i is the target class (the base truth category). The cross-entropy is effective at measuring the distinguishing power between discrete probability distributions and so is ideal for kinematic distributions of different quantum processes.

The objective function is a combination of the first and second order derivatives of a chosen loss-function, $l(y_i, \hat{y}_i^{(t)})$, which acts on the predicted and true outputs y_i and \hat{y}_i for the i th class, and a regularisation term, $\Omega(f_t)$ which punishes complexity in the model to avoid over-fitting. The objective at step t in tree building is:

$$obj^{(t)} = \sum_{i=1}^n [g_i f_t(x_i) + \frac{1}{2} h_i f_t^2(x_i)] + \Omega(f_t) \quad (7.12)$$

where n is number of classes of the model. The first and second order derivatives (gradient and hessian) of the loss function are given by:

$$g_i = \partial_{\hat{y}_i^{(t-1)}} l(y_i, \hat{y}_i^{(t-1)}) \quad (7.13)$$

$$h_i = \partial_{\hat{y}_i^{(t-1)}}^2 l(y_i, \hat{y}_i^{(t-1)}) \quad (7.14)$$

The tree can be defined as the a combination of weights, w_i , that prescribe the scores on the leaves and function, q , that maps the input variables to a leaf. T is the total number of leaves:

$$f_t(x) = w_{q(x)} q : R^d \rightarrow \{1, 2, \dots, T\} \quad (7.15)$$

The regularisation term for tree f is defined as:

$$\Omega(f) = \gamma T + \frac{1}{2} \lambda \sum_{j=1}^T w_j^2 \quad (7.16)$$

The objective can then be written for the t^{th} tree:

$$obj^{(t)} = \sum_{j=1}^T [G_j w_j + \frac{1}{2} (H_j + \lambda) w_j^2] + \lambda T \quad (7.17)$$

7.3 Machine Learning Techniques

where G_j and H_j are sums of the gradient and hessians for the data points, I_j , that are mapped to the leaf, j :

$$G_j = \sum_{i \in I_j} g_i, H_j = \sum_{i \in I_j} h_i \quad (7.18)$$

i.e. the summed gradients for leaf, j , calculated for a given batch of data. The optimal weights that minimise the objective function are:

$$w_j^* = -\frac{G_j}{H_j + \lambda} \quad (7.19)$$

The objective reduction is given by:

$$obj^* = -\frac{1}{2} \sum_{j=1}^T \frac{G_j^2}{H_j + \lambda} + \gamma T \quad (7.20)$$

which gives a measure of how good the tree structure is at minimising the objective function. In the learning process, equation 7.20 is used to progress the tree structure by considering splitting leaves dependent on the input variables. If the new split reduces 7.20 then it is added to the tree. Figure 7.2 shows a simple illustration of a regression tree structure.

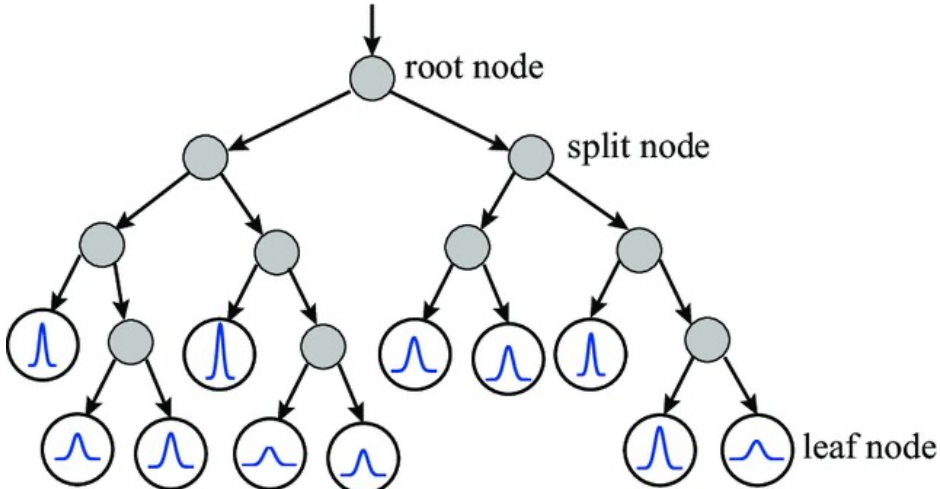


Figure 7.2: Illustration of the structure of a simple regression tree [91]

Weights

Throughout this work the ML methods are developed using MC simulation. In MC simulation weights are applied to specific events to indicate their true prevalence if it is different to the prevalence in simulation. This is taken into account in the training procedure by calculating the total weight of a given event (multiplication of scale factors, tag and trigger weights and generator weights) normalised

7 Analysis Techniques

to luminosity. The weights are then introduced with the event as *instance weights*. The weights are introduced for each data point, they multiply the gradient and hessian. For instance weight W_i equation 7.18 becomes:

$$G_j = \sum_{i \in I_j} g_i W_i, H_j = \sum_{i \in I_j} h_i W_i \quad (7.21)$$

The input data for training is generally imbalanced, meaning that the training statistics are higher for some classes than others. This can be re-balanced by the use of class-based weights which modify W_i dependent on the class, however when these were explored they were found not to improve the model performance. Another feature of MC samples used at the LHC is the use of *sliced* samples. These are processes where the production of events are restricted to some phase-space at parton level in order to increase statistics in that specific region of phase-space (usually high E_T^{miss} regions). For the background samples both high-statistics sliced samples (weighted) and lower statistics nominal samples were explored. It was found that the reduced statistics nominal samples with the inherent correct distributions performed better where they were applicable.

Optimisation

When constructing gBDTs a number of hyper-parameters can be modified that control the way in which the training proceeds and also the structure of the algorithm itself. The key hyper-parameters are summarised in table 7.1. The model hyper-parameters are optimised using a grid search cross-validation. Since the size of the training samples is large and the grid-search is extremely computationally intensive the distributed analysis framework DASK [92] is used overcome memory and compute constraints by utilising many computing nodes synchronously.

The key hyper-parameters of the XGBoost package are defined in table 7.1

Overfitting Checks

The training procedure in supervised learning relies on an observed dataset for training the model-the training set, which is then paired with a separate dataset used for evaluating the model performance -the validation set. The validation dataset is not used in the model development. The purpose of the validation set is two-fold: during training it is used to limit the training procedure when the loss-function on the validation set stops decreasing, secondly after training it is used to ensure that the model generalises well to the instances that were not used in the training - avoiding overfitting. Overfitting is determined by comparing distributions of the class output scores for a completed model for the training and validation subsets separately with their truth labels. Here the truth labels are simplified into background class (grouping the separate backgrounds into one) and signal class. This is a representative illustration of the trained model since the classification is conducted in a 'one vs

7.3 Machine Learning Techniques

Hyper-parameter	Description	Impact
η	Amount by which the feature weights are reduced after each step.	Increasing leads to more conservative model
γ	Minimum reduction in loss required to make a further partition.	Increasing leads to more conservative model
Max tree depth	Max depth of each tree	Increasing leads to more complex model
Min child weight	Minimum sum of weights in an instance for tree partitioning to progress	Increasing leads to more conservative model
λ	L2 regularisation: Penalises the sum of the weights (BDT equivalent)	Reduces model complexity by penalising individual large weights and promoting many small weights
α	L1 regularisation: Penalises the squared sum of weights (BDT equivalent)	Reduces model complexity by penalising individual large weights and promoting many small weights

Table 7.1: Description of some of the XGBoost model hyper-parameters and their functions.

all' approach for each of the classifications. In order to quantify the difference between the train and validation responses for the output scores a Kolmogorov-Smirnov (KS) [93] test is conducted on the (normalised) output distributions. A high KS score indicates consistency between two distributions, lower bounds of 0.9 and 0.75 are established for the background and signal categories respectively since the signal category has reduced statistics.

Part IV

Searches for beyond the Standard Model physics in Run 2

8 Searches for third generation squarks

8.1 Phenomenology of Bottom Squarks

The third generation SUSY searches in this work target the pair production of bottom squarks in R-parity conserving models. The bottom squarks (along with the top squarks) are well motivated to have masses around the TeV scale through naturalness arguments, as discussed in section 2.2.5, making them within reach of the LHC. The models considered are simplified models with the following assumptions: the branching ratios of all SUSY particles are assumed to be 100%, the SUSY particles in the interaction are the only sparticles produced at the LHC and all other sparticles are de-coupled. The free parameters of the models are just the sparticle masses. The produced sparticles are all considered to decay promptly and symmetrically, with the decay chains ending in the LSP which is stable and massive and therefore a WIMP dark matter candidate. Simplified models are considered in order to allow the analysis to be designed with reduced specificity towards the exact theoretical assumptions. This allows the scope of the result to be greater and it can be used in a wider theoretical context to constrain specific scenarios.

Two bottom squark scenarios are considered here. The models differ in their decay chains: in the first the bottom squarks decay directly to a b-quark and the LSP which is the lightest neutralino, $\tilde{\chi}_1^0$. This is referred to as the direct decay scenario and is illustrated in figure 8.2(a). In the second case the decay is more complex, the bottom squarks decay to a b-quark and an intermediate $\tilde{\chi}_2^0$ which then decays into the higgs (which is considered SM-like) and the lightest neutralino, $\tilde{\chi}_1^0$, in a two-step decay illustrated in figure 8.12. As discussed in 2.2.6 this decay chain can become dominant in SUSY models where the \tilde{b} is heavier than the $\tilde{\chi}_2^0$ and the $\tilde{\chi}_1^0$ has a large Bino component. This is illustrated in figure 8.1 which shows the branching fraction of the $\tilde{\chi}_2^0$ to higgs as a function of the $\tilde{\chi}_1^0$ Bino component for a set of models from the pMSSM (section 2.2). The resulting final states for these models contain only jets, b-jets and E_T^{miss} .

The analysis targeting the direct decay scenario is described in section 8.2, along with the analysis of a similar final state model of direct dark matter production. The analysis targeting the two-step decay is described in section 8.3. The direct decay analysis shares a final state with many other BSM processes so in addition to the bottom squark model a simplified dark matter model is also studied. The dark matter model based on the recommendations of the ATLAS and CMS collaboration DM forum. The model considers s-channel production of a spin 0 mediator, which is either scalar (ϕ) or pseudo-scalar (a) which decays to dark matter (χ). The model assumes Yukawa-like couplings between the mediator and the SM fermions so the model considers associated production with b-quarks, which complements similar searches with top-quarks.

8 Searches for third generation squarks

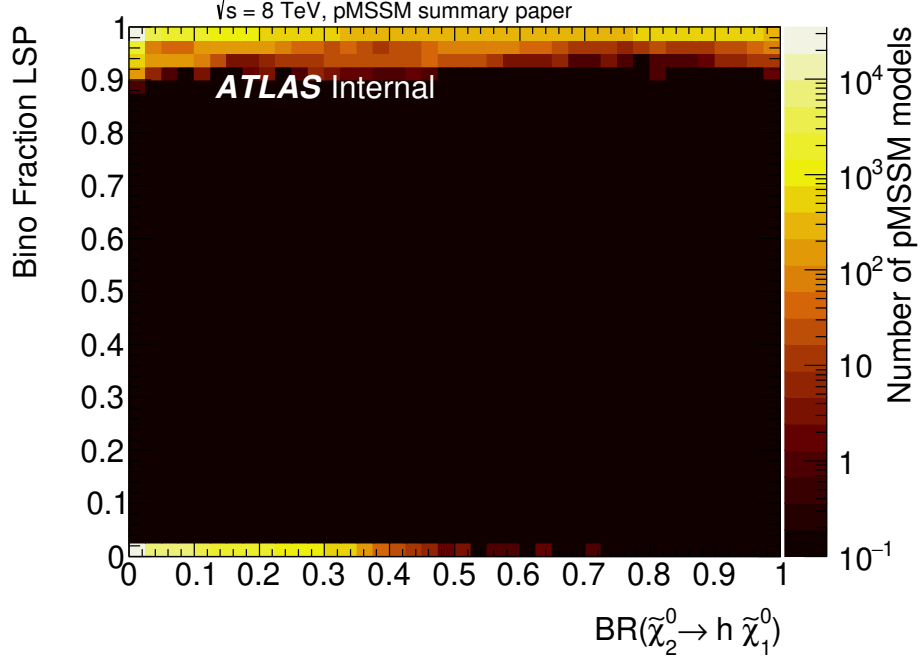


Figure 8.1: Illustration of the branching fraction of the $\tilde{\chi}_2^0$ to Higgs $\tilde{\chi}_1^0$ as a function of the bino fraction of the LSP. Many bino-like LSP scenarios have this as a large branching fraction.

8.2 Bottom squark and dark matter signals with $b\bar{b} + E_T^{\text{miss}}$ final states

This analysis targets BSM scenarios that produce final states with two b-jets and large missing transverse energy, referred to as $b\bar{b}Met$. Final states of this nature can be realised in many BSM theories, in this work there are two main scenarios, their Feynman graphs are shown in figure 8.2.

The phase-space of the bottom squark signals is spanned by the masses of the \tilde{b} and $\tilde{\chi}_1^0$, the signal points considered are summarised in figure 8.3.

For the dark matter model, there are 4 free parameters, the mediator mass, $m_{\phi,a}$, the dark matter mass, m_χ , and the couplings of the mediator to DM and the SM, g_χ, g_v . In this analysis the additional assumption is made that $g_\chi = g_v = 1$, since the couplings determine the production cross-section this becomes the parameter which is studied in the limit. The phase space of the DM signals is spanned by the mediator mass. The signal points considered for the scalar and pseudo-scalar cases are summarised in table 8.1.

Personal contributions to this analysis include: development of the software, training and deployment for the ML methods and design of the combined AB region fit, performing the statistical analyses for the AB combined design and development and maintenance of the software for the statistical analysis.

8.2 Bottom squark and dark matter signals with $b\bar{b} + E_T^{\text{miss}}$ final states

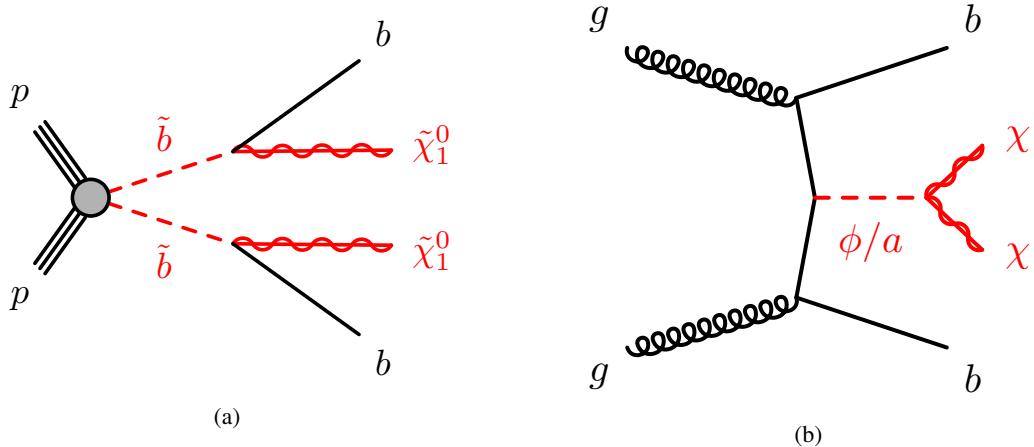


Figure 8.2: Signals targeted in the bbMeT analysis. 8.2(a) is a simplified SUSY model considering pair produced bottom squarks decaying symmetrically to a b-quark and $\tilde{\chi}_1^0$. 8.2(b) is a simplified dark matter model in which the dark matter candidates are produced in pairs via a scalar or pseudo-scalar mediator particle which is generic.

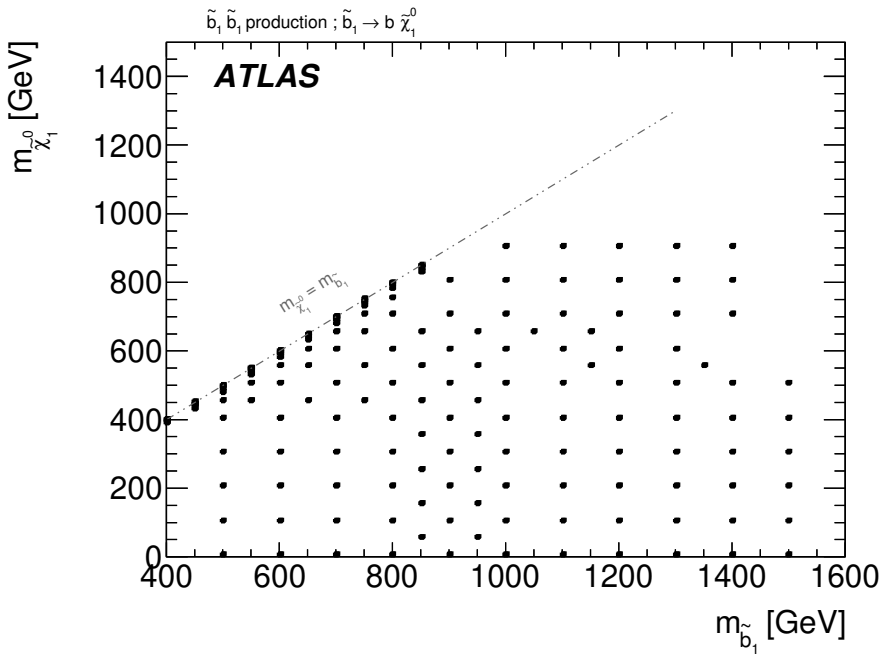


Figure 8.3: Signal mass hypotheses points considered in the analysis for the bottom squark scenario.

8.2.1 Event Selection

The common signature in this analysis is a final state with two jets arising from b-quarks, zero leptons and large missing transverse energy, generally there is also a requirement of low additional jet multiplicity. In general, for the bottom squark 0-lepton regions E_T^{miss} triggers are used over b-jet triggers due to their higher efficiency. However, for dark matter signals the requirement on the offline

8 Searches for third generation squarks

Table 8.1: Dark matter signal samples.

Coupling	ϕ mass [GeV]	x-section [pb]	x-section uncertainty [pb]
scalar	10	4.0935	± 0.410
scalar	20	2.9800	± 0.255
scalar	50	1.3633	± 0.168
scalar	100	4.3620E-01	± 0.0891
scalar	200	5.5780E-02	± 0.0167
scalar	300	8.7483E-03	± 0.00367
scalar	500	4.2020E-04	± 0.000249
pseudoscalar	10	4.0916	± 0.410
pseudoscalar	20	2.9794	± 0.263
pseudoscalar	50	1.3631	± 0.173
pseudoscalar	100	4.3605E-01	± 0.0886
pseudoscalar	200	5.5779E-02	± 0.0165
pseudoscalar	300	8.7372E-03	± 0.00367
pseudoscalar	500	3.1625E-04	± 0.000192

E_T^{miss} enforced for the triggers to be fully efficient placed at 250 GeV heavily impacts the acceptance for low $m_{\phi,a}$ scenarios. For this reason, the E_T^{miss} trigger efficiency was studied considering both the E_T^{miss} and the leading jet p_T which also impacts the efficiency of the E_T^{miss} trigger. A plateau condition-equation 8.1 is instead used as the offline requirement designed in order to reduce the offline E_T^{miss} requirement so that lower values of E_T^{miss} can be used in events with high leading jet p_T . For background control there are single and di-lepton regions where single-lepton triggers are used instead. Several signal regions are designed in order to maximise sensitivity to different signal mass hypotheses. SRA, SRB, and SRC target the bottom squark signals in different areas of sparticle mass phase-space and SRD1 and SRD2 target the dark matter signals for different mediator masses.

$$\frac{p_T^{j_1} - 20}{5000} (E_T^{\text{miss}} - 160) > 1 \quad (8.1)$$

The effectiveness of the requirement outlined in equation 8.1 is illustrated in figure 8.4 showing the efficiency of the E_T^{miss} trigger as a function of E_T^{miss} and leading jet p_T .

Signal Region A

Signal Region A aims to gain sensitivity to bottom squark signals with large mass difference, $\Delta m(\tilde{b}, \tilde{\chi}_1^0)$, between the bottom squark and the neutralino. These signals feature high p_T b-jets and large missing energy making the SUSY mass-scale discriminants powerful. The selection requires zero leptons and 2-4 jets. The two jets with highest p_T have lower bounds placed on their p_T and are required to be b-tagged, whilst the remaining jets have upper bounds on their transverse momenta and are not b-tagged. Loose requirements on the invariant mass of the b-tagged jets and the ratio of the E_T^{miss} to the m_{Eff} are also applied. These selections form the basis of the region design and are referred to as *baseline* selections.

8.2 Bottom squark and dark matter signals with $b\bar{b} + E_T^{\text{miss}}$ final states

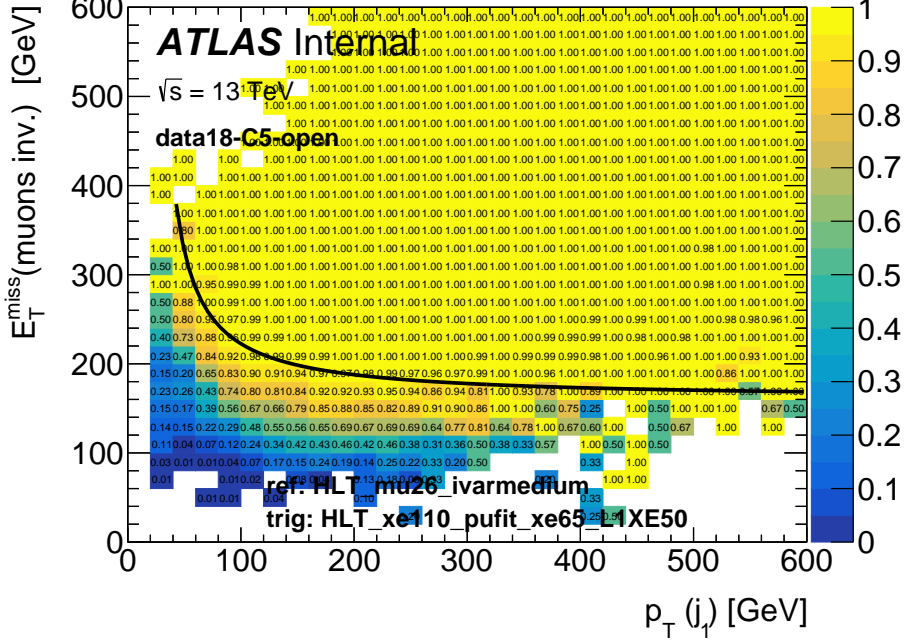


Figure 8.4: Efficiency of the E_T^{miss} trigger for an example 2018 data period (the key features are the same for all data periods) as a function of the reconstructed E_T^{miss} and leading jet p_T . The events used are selected requiring one muon with $p_T > 30 \text{ GeV}$ and passing the muon trigger. The trigger-level information is then modified so that the muon momentum is removed to mimic the behaviour if the muon was lost to missing energy.

To maximise sensitivity the mass-scale variables, namely $m_{E_{\text{eff}}}$ and m_{CT} , are exploited in a binned fit. Throughout this analysis the m_{CT} is calculated using the b-jets as the inputs to the calculation (α and β in equation 7.9). The kinematic end-point for the m_{CT} distribution for a bottom squark signal is given by:

$$m_{\text{CT}}^{\text{end}} \approx \frac{m_b^2 - m_{\chi_1^0}^2}{m_b^2} \quad (8.2)$$

and thus will differ dependent on the mass hypothesis. For this reason m_{CT} is binned over a large range to maximise sensitivity to a large area of mass phase-space. When the m_{CT} selection is applied, additional requirements on $m_{E_{\text{eff}}}$ gains additional discriminating power, therefore a combined binning in $m_{E_{\text{eff}}}$ and m_{CT} is used. This is referred to as 2-dimensional fit. The baseline selections for SRA are given in the first column in table 8.6 and the binning selections are given in table 8.7. For the model-independent fit, instead of binning in $m_{E_{\text{eff}}}$ as in table 8.6, the lower bound of the first bin is used as the selection and the region is inclusive in $m_{E_{\text{eff}}}$ from this lower bound.

8 Searches for third generation squarks

Signal Region B

The bottom squark SRB signal region focuses on signal samples with mass differences in the range $\Delta m(\tilde{b}, \tilde{\chi}_1^0) \sim 50 - 100$ GeV. These signals, due to their lower mass splitting, have softer decay products than signals in the bulk region. As a result the key discriminants that are used in SRA to discriminate from the SM backgrounds have a similar shape in the signal to the background processes for these semi-compressed hypotheses and do not give good sensitivity. However, in comparison with the fully compressed mass hypotheses signals ($\Delta m(\tilde{b}, \tilde{\chi}_1^0) < 20$ GeV) the b-quarks have higher p_T and the decay products are not soft enough to warrant the use of soft b-tagging as described in section 8.2.2. Therefore a separate strategy is required to gain sensitivity to these signal points. Machine learning methods are employed which exploit differences between background SM and signal processes in multiple variables and the correlations between these variables.

The machine learning framework used is XGBoost [90]. One output score per category is calculated containing the predicted probability of an event being the category. The training is conducted using MC samples in five categories: three main backgrounds $t\bar{t}$, $Z + jets$, $W + jets$ production (other smaller backgrounds are grouped into a separate category) and semi-compressed signal samples ($\Delta M(\tilde{b}, \tilde{\chi}_1^0) \leq 200$ GeV). Splitting the background processes into multiple categories is motivated by the option that their output scores could be used to develop control or validation regions with high purity and, in addition, a better signal/background discrimination was observed using this arrangement. This is thought to be due to the different SM processes having rather different features that are complex to group into a single background category.

In a pre-processing step the azimuthal angles of the (b)jets and the E_T^{miss} in the event are rotated such that the E_T^{miss} has $\phi=0$. This reduces the number of symmetries which the BDT must learn. These are denoted by ϕ^{rotated} . Low-level variables, such as jet 4-vector (polar) components and high-level variables such as $m_{E\ell f\ell}$, $S_{obj-based}$ and m_{bb} are all used in the training.

The training samples are skimmed with a targeted pre-selection, summarised in table 8.2. The pre-selection is based on features of the signal that are somewhat trivial and known a-priori. This reduces the complexity of the model having to learn these simple features. Before training, the modeling of the input variables are verified by comparing the input variable distributions of the SM backgrounds with data distributions and also comparing the linear correlations (defined in equation 8.3) between the most important 6 variables used in the BDT in SM backgrounds and data.

$$Lin_{Corr} = \frac{(x - \hat{x}) \cdot (y - \hat{y})}{RMS_x \cdot RMS_y} \quad (8.3)$$

for variables x and y with mean values \hat{x}, \hat{y} where:

$$RMS_x = \sqrt{\frac{\sum_{i=1}^n (\hat{x} - x_i)^2}{n}} \quad (8.4)$$

8.2 Bottom squark and dark matter signals with $b\bar{b} + E_T^{\text{miss}}$ final states

Table 8.2: Definition of the pre-selection region used to select the inputs for the training of the SRB BDT.

Lowest unprescaled trigger	E_T^{miss}
Event Cleaning	✓
E_T^{miss} [GeV]	>250
Number of <i>baseline</i> leptons	0
N_{jets}	$\in [2,4]$
$N_{b\text{-jets}}$	≥ 2
$\min[\Delta\phi(\text{jet}_{1-4}, E_T^{\text{miss}})]$	> 0.4
mCT	< 250

The full MC dataset is split in 80:20 proportion into training and validation sets. In order to ensure that the model has enough complexity to maximise sensitivity based on the given training statistics, the model hyper-parameters are tuned such that the model just begins to overfit the training data. The minimum tree depth that provides enough model complexity to overfit was found to be six. The regularisation parameters were then introduced and increased until the overfitting was reduced to an acceptable level. An acceptable level is determined by measuring the difference between the test and validation responses using the KS measure described in section 7.3.1. Once this was achieved, the final optimisation procedure comprised scanning over variations of the parameters shown in table 7.1 (excluding max tree depth), within reasonable ranges.

This of course results in many trained models. To select the most effective of these models, the precision-recall (PR) curves were inspected. The models that showed the best performance in the PR curves were then applied to the full MC dataset. Of these trainings the optimally performing model is selected by scanning along the signal classification score and calculating the maximum average significance (equation 7.1) for a range of baseline signal points (table 8.3) for each trained model using the complete, weighted Monte-Carlo dataset. The overfitting test described in 7.3.1 is employed and the resulting plot for the trained model is shown in figure 8.5.

$m(\tilde{b})$ GeV	$m(\tilde{\chi}_1^0)$ GeV
750	700
800	600
800	700
900	700

Table 8.3: Baseline signal points used for evaluating the BDT models.

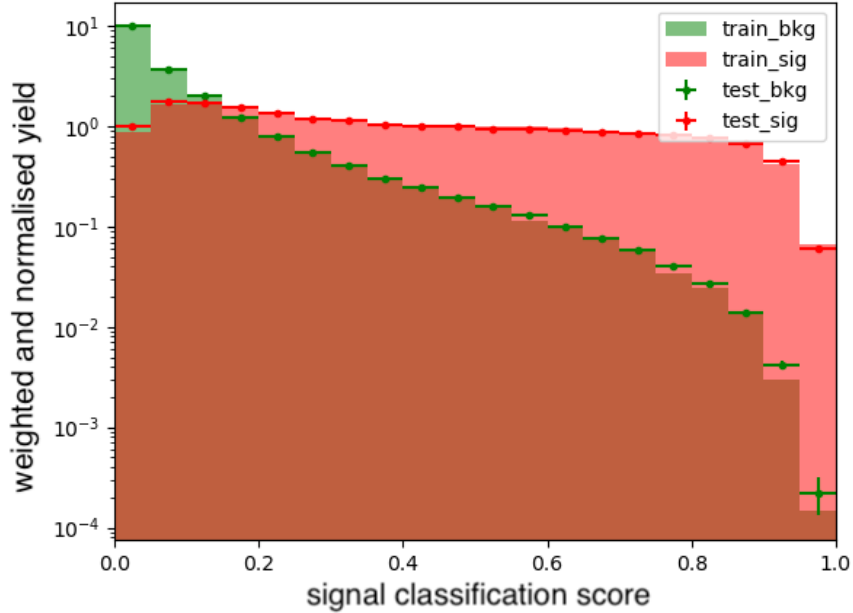


Figure 8.5: Distributions of the signal classification score comparing training and validation sets for the true-labeled background classes and the true-labeled signal class.

Machine Learning Signal Region Optimisation The signal regions are defined using the XG-Boost signal classification score as the final discriminating variable. The discovery signal region is defined by placing a cut on the signal class output score at a high value, which maximises the discovery significance for the baseline points, optimised considering statistical uncertainty in the signal and the background and a 20% flat approximate systematic uncertainty. The final exclusion signal region is binned in 4 orthogonal bins of the signal output score, shown in figure 8.7. The exclusion and discovery regions are designed for the model-dependent and model-independent fits respectively, these are formalised in Table 8.8.

8.2 Bottom squark and dark matter signals with $b\bar{b} + E_T^{\text{miss}}$ final states

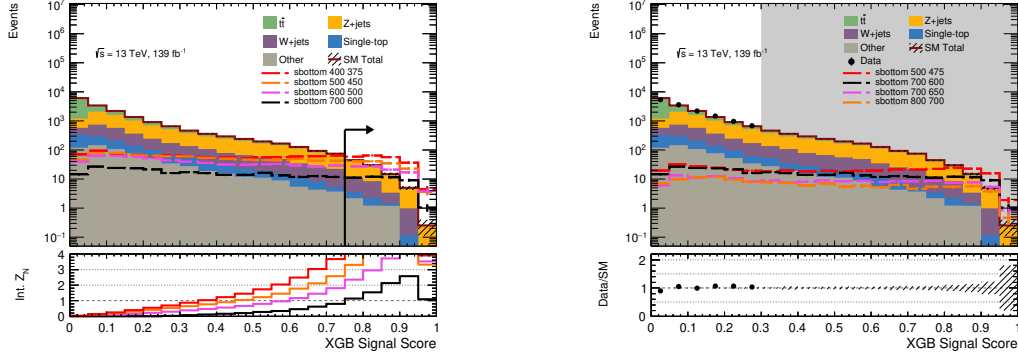


Figure 8.6: Distributions of signal classification score after the training preselection. Only statistical uncertainties are considered in the error band. (a) The lower panel shows the integrated significance assuming 20% background signal systematic uncertainties. The arrow indicates the lower bound of the SRB signal region bins. (b) Shows the data/MC comparison, blinded at high values, where signal contribution is significant.

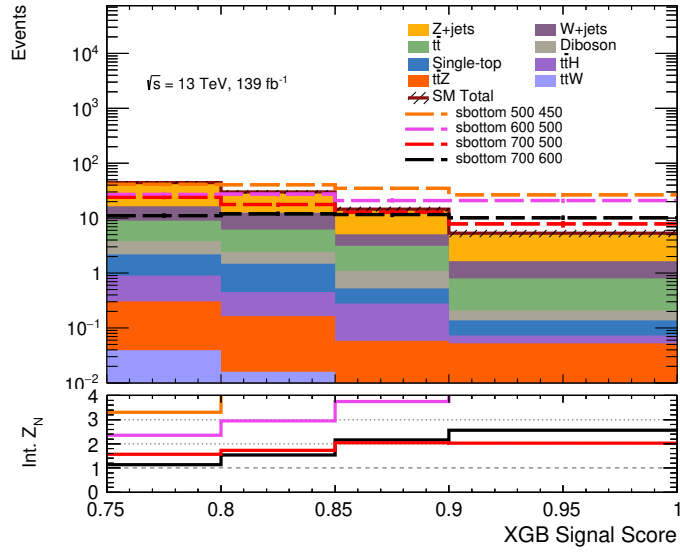


Figure 8.7: Binning of the signal score in the exclusion signal region. The lower panel shows the integrated exclusion significance considering both signal and background statistical uncertainties but assuming a flat 20% systematic. Only statistical uncertainties are considered in the error band.

8 Searches for third generation squarks

8.2.2 Signal Region C

SRC is designed to gain sensitivity to scenarios where the mass difference $\Delta m(\tilde{b}, \tilde{\chi}_1^0)$ is extremely compressed, $\lesssim 50$ GeV. In this case the b-quarks from the bottom squark decay have low p_T and thus are reconstructed as b-jets with very low efficiency using the standard flavour tagging methods and may not even be reconstructed as a jet. To counter this, a different approach is taken wherein the presence of the b-quarks is determined by identifying secondary vertices. The technique is referred to as *track-cluster based low p_T vertex tagging* (TC-LVT) [94], it clusters tracks with relatively high momenta that are not associated to a jet and then uses the secondary vertex finder algorithm (described in 6.2.2) with these tracks to identify vertices.

The SR design combines three regions which are complimentary, distinguished by the number of (DL1) b-tagged jets present. These are: SRC2b requiring exactly two b-jets, SRC1b1v requiring exactly one b-jet and at least one secondary vertex and SRC0b1v with zero b-jets and at least one secondary vertex. All regions additionally require the presence of a non-btagged, high p_T jet which aims to identify the presence of initial state radiation (ISR). The presence of the ISR jet is also identified by the development of the variable \mathcal{A} . The transverse momentum of the ISR jet is expected to be significantly higher than the other jets in the event: the variable is constructed from the p_T of the leading and sub-leading (p_T -ordered) jets:

$$\mathcal{A} = \frac{p_T^{j1} - p_T^{j2}}{p_T^{j1} + p_T^{j2}} \quad (8.5)$$

Additional variables used are based on the angular separation between b-jets, expected to be large in signal events, and requiring low hadronic activity using an upper bound on H_T . The secondary vertices can be mistakenly reconstructed from 'fake' sources such as c-hadron decays so requirements on the vertex p_T and mass are used to restrict this. The signal regions are summarised in table 8.4.

The signal regions are statistically independent to each other so they are constrained simultaneously in the fit. The regions in table 8.4 are used for the model-independent limit fit. The exclusion regions used in the model-dependent fit are additionally binned in E_T^{miss} .

8.2 Bottom squark and dark matter signals with $b\bar{b} + E_T^{\text{miss}}$ final states

Table 8.4: Signal region selection for SRC regions.

Selection	sbot-SRC-2b0v	sbot-SRC-1b1v	sbot-SRC-0b1v
Is j_1 b -tagged?	0	0	0
p_T^{j1} (GeV)	> 500	> 400	> 400
E_T^{miss} (GeV)	> 500	> 400	> 400
H_T^3	–	< 80	< 80
\mathcal{A}	> 0.80	> 0.86	–
m_{jj} (GeV)	> 250	> 250	–
$N_{b\text{-jets}}$	≥ 2	= 1	= 0
$\Delta\phi(j_1, b_1)$	–	> 2.2	–
N_{vtx}	≥ 0	≥ 1	≥ 1
m_{vtx} (GeV)	–	> 0.6	> 1.5
p_T^{vtx} (GeV)	–	> 3	> 5
$\Delta\phi(j_1, \text{vtx})$	–	–	> 2.2
$ \eta_{\text{vtx}} $	–	< 1.2	< 1.2

Table 8.5: E_T^{miss} binning for the SRC exclusion regions.

Selection	sbot-SRC-2b0v	sbot-SRC-1b1v	sbot-SRC-0b1v
$2 E_T^{\text{miss}}$ bins in range [GeV]	[500,650],>650	[400,600],>600	[400,600],>600

8.2.3 Signal Region D

SRD is the region designed for sensitivity to the dark matter scenarios. The region is further split into SRD-low targeting mediator masses in the range $m_{\phi/a} \in [10 - 100]$ GeV and SRD-high targeting $m_{\phi/a} \in [200 - 500]$ GeV. The two follow the same strategy, a common, loose pre-selection is applied requiring zero leptons, two b -jets and that the plateau from equation 8.1 is satisfied. After this pre-selection the signal samples are grouped into low and high mediator masses and a BDT is trained to distinguish between either signal group and a single SM background for each of the 3 dominant SM backgrounds: top pair production, Z+jets, W+jets resulting in 6 separate BDTs. The signal regions are then defined by selections on the output for each of the BDTs which can be tuned to reduce specific contributions from the dominant backgrounds. Additional specific variables relating to the event jet topology: δ^+ , δ^- and $\cos\theta_{bb}^*$ are used. These are defined as follows:

$$\delta^+ = \min[\Delta\phi(jet_{1-3}, \vec{p}_T^{\text{miss}})] - \Delta\phi_{bb} \quad (8.6)$$

$$\delta^+ = \min[\Delta\phi(jet_{1-3}, \vec{p}_T^{\text{miss}})] + \Delta\phi_{bb} - \pi \quad (8.7)$$

$$\cos\theta_{bb}^* = |\tanh\frac{\Delta\eta(b_1, b_2)}{2}| \quad (8.8)$$

8 Searches for third generation squarks

The inclusive signal regions are defined in table 8.11. The exclusive regions are designed binning the full $\cos \theta_{bb}^*$ distributions in 5 bins between 0 and 1. The input variables considered for the BDT are those that do not correlate strongly with $\cos \theta_{bb}^*$ so that the $\cos \theta_{bb}^*$ distribution does not become sculpted by the BDT selections, they are:

- The number of b-jets and jets and their p_T .
- Mass scale and missing energy variables: E_T^{miss} , $S_{\text{obj-based}}$, H_T , $m_{CT}^{j_1 j_2}$, $m_{CT}^{b_1 b_2}$, m_{Eff} , p_T^{j1}/H_T
- Angular variables: $\min[\Delta\phi(\text{jet}_{1-3}, E_T^{\text{miss}})]$, $\Delta\phi_{bb}$, δ^+ , δ^-

The discovery signal regions are defined as a single bin requiring high signal $\cos \theta_{bb}^*$ as opposed to binning the distribution as with the exclusive regions.

8.2.4 Background Estimation

For signal regions A, B and D the dominant expected SM background is Z+jets where the Z decays to neutrinos, resulting in large E_T^{miss} , and the jets are b-tagged. However, for SRC there are also significant contributions from W+jets and top processes. The CRs are designed to constrain these SM contributions.

A common approach is taken for the Z+jets control regions: events are selected with kinematics as similar to the signal regions as possible but requiring two same flavour, opposite sign (SFOS) leptons whose invariant mass is close to the Z-peak. The leptons are then treated as invisible for all further consideration and the E_T^{miss} is adapted by vectorially adding the momenta of the leptons to the E_T^{miss} , this is denoted $\tilde{E}_T^{\text{miss}}$ and mimics the $Z \rightarrow \nu\bar{\nu}$ signature. The contribution from di-leptonic $t\bar{t}$ to the Z CRs is reduced by requiring low E_T^{miss} . Single lepton triggers are used. In the two lepton Z CR/VR contexts, the BDTs scores from the B and D-type regions are re-calculated replacing E_T^{miss} with $\tilde{E}_T^{\text{miss}}$ in all regions. Two Z control regions are designed for SRD-high and SRD-low in this context. The B-type control regions are placed at low signal score with respect to the signal region with the additional requirement that the leading jet is not b-tagged (this reflects the signal region features) and the extrapolation to higher signal score is validated using a validation region at high signal score.

For the C-type signal regions there are three associated Z Control regions, one for each of the b-jet multiplicities used in the signal region definition, following a similar methodology to that of the A, B and D Z control regions. In addition, the W and top CRs are built with single-lepton selections. Two W+jets CRs are designed one with one b-jet and at least one TC-LVT vertex, and the other with zero b-jets and at least one TC-LVT vertex. The top control region is designed with a two b-jets and zero TC-LVT vertices and is used to normalise $t\bar{t}$ and single-top processes simultaneously.

The validation regions are generally designed to be kinematically closer to the signal regions than the CRs. In the A-type regions, VRs are designed to validate the extrapolation over the m_{bb} and m_{CT} variables but are zero lepton regions, they are also split into low and high m_{Eff} .

8.2 Bottom squark and dark matter signals with $b\bar{b} + E_T^{\text{miss}}$ final states

The B-type VR is a two lepton SFOS region that is designed to validate the extrapolation from the CR which is placed at lower values of the signal output score to the higher values of the signal region. The signal score selection of the two lepton VR is loosened with respect to the SR due the lower efficiency for reconstructing two leptons and reduced branching fraction. Three validation regions for the C-type are designed: two b -jets one b -jet plus one vertex and zero b -jets plus one vertex selections are used, mimicking those of the SRs.

The selections for all regions are summarised in table 8.6 through 8.11.

Table 8.6: SRA signal, control and validation region definitions. Pink cells for the control and validation regions' columns indicate which selections ensure that the regions are orthogonal to the SR.

Variable		SRA	CRZA	VRA- m_{CT} -low m_{Eff}	VRAB- m_{bb} -low m_{Eff}	VRAm _{CT} -high m_{Eff}	VRAD- m_{bb} -high m_{Eff}
Number of baseline leptons		0	2			0	
Number of high-purity leptons		–	2 SFOS			–	
$p_T(\ell_1)$	[GeV]	–	> 27			–	
$p_T(\ell_2)$	[GeV]	–	> 20			–	
$m_{T}(\mathbf{p}_T^{\ell_1}, \mathbf{p}_T^{\ell_2})$	[GeV]	–	> 20			–	
$m_{\ell\ell}$	[GeV]	–	[81, 101]			–	
Number of jets				$\in [2, 4]$			
Number of b -tagged jets				2			
j_1 and j_2 b -tagged				✓			
$p_T(j_1)$	[GeV]				> 150		
$p_T(j_2)$	[GeV]				> 50		
$p_T(j_4)$	[GeV]				< 50		
$\min[\Delta\phi(\text{jet}_{1-4}, E_T^{\text{miss}})]4$	[rad]				> 0.4		
E_T^{miss}	[GeV]	> 250	< 100			> 250	
$\tilde{E}_T^{\text{miss}}$	[GeV]	–	> 250			–	
$E_T^{\text{miss}}/m_{Eff}$		> 0.25	–			–	
$\tilde{E}_T^{\text{miss}}/m_{Eff}$		–	> 0.25			–	
m_{bb}	[GeV]	> 200		< 200	> 200	< 200	> 200
m_{CT}	[GeV]	> 250		> 250	[150, 250]	> 250	[150, 250]
m_{Eff}	[GeV]	> 500		[500, 1500]			> 1500

Table 8.7: Multi-bin selections used for the definition of the SRA exclusion regions.

Variable	Selection		
SRA preselection (as in Table 8.6)	\checkmark		
m_{CT} bin	[250, 350]	[350, 450]	[450, 550]
m_{Eff} binning	5 bins $\in [500, 1500]$	2 bins $\in [500, 1500]$	2 bins $\in [1000, 2000]$
Variable	Selection		
SRA preselection (as in Table 8.6)	\checkmark		
m_{CT} bin	[550, 650]	> 650	
m_{Eff} binning	$> 1000 \text{ GeV}$	$> 1500 \text{ GeV}$	

8 Searches for third generation squarks

Table 8.8: SRB signal, control and validation region definitions. Pink cells for the control and validation regions' columns indicate which selections ensure that the regions are orthogonal to the SR.

Variable		SRB	CRZB	VRB
Number of baseline leptons		0	2	
Number of high-purity leptons		–	2 SFOS	
$p_T(\ell_1)$	[GeV]	–	> 27	
$p_T(\ell_2)$	[GeV]	–	> 20	
$m_{\ell\ell}$	[GeV]	–	[76, 106]	
$m_T(\mathbf{p}_T^\ell, \mathbf{p}_T^{\text{miss}})$	[GeV]	–	> 20	
Number of jets			$\in [2, 4]$	
Number of b -tagged jets			2	
$p_T(j_1)$	[GeV]		> 100	
$p_T(j_2)$	[GeV]		> 50	
$\min[\Delta\phi(\text{jet}_{1-4}, E_T^{\text{miss}})]/4$	[rad]		> 0.4	
j_1 not b -tagged		–	✓	–
E_T^{miss}	[GeV]	> 250	< 100	
$\tilde{E}_T^{\text{miss}}$	[GeV]	–	> 250	
m_{CT}	[GeV]		< 250	
w_{XGB}			> 0.85	[0.3, 0.63] > 0.63

Table 8.9: SRC signal and validation region definitions. Pink cells for the validation regions' columns indicate which selections ensure that they are orthogonal to the corresponding SR.

Variable		SRC-2b	SRC-1b1v	SRC-0b1v	VRC-2b	VRC-1b1v	VRC-0b1v
Number of jets				$\in [2, 5]$			
j_1 not b -tagged				✓			
Number of baseline leptons				0			
Number of b -tagged jets		≥ 2	1	0	≥ 2	1	0
N_{vtx}		≥ 0	≥ 1	≥ 1	≥ 0	≥ 1	≥ 1
m_{vtx}	[GeV]	–	> 0.6	> 1.5	–	> 0.6	> 1.5
p_T^{vtx}	[GeV]	–	> 3	> 5	–	> 3	> 5
$p_T(j_1)$	[GeV]	> 500	> 400	> 400	< 500	> 400	> 400
E_T^{miss}	[GeV]	> 500	> 400	> 400	< 500	> 400	> 400
$H_{\text{T};3}$	[GeV]	–	< 80	< 80	–	< 80	< 80
\mathcal{A}		> 0.80	> 0.86	–	[0.8, 0.9]	> 0.86	–
m_{jj}	[GeV]	> 250	> 250	–	[150, 250]	> 250	–
$\Delta\phi(j_1, b_1)$	[rad]	–	> 2.2	–	–	< 2.2	–
$\Delta\phi(j_1, \text{vtx})$	[rad]	–	–	> 2.2	–	–	< 2.2
$ \eta_{\text{vtx}} $		–	< 1.2	< 1.2	–	> 1.2	> 1.2

8.2 Bottom squark and dark matter signals with $b\bar{b} + E_T^{\text{miss}}$ final states

Table 8.10: SRC control region definitions. Pink cells for the control regions' columns indicate which selections ensure that they are orthogonal to the corresponding SR.

Variable		CRCT	CRCW-1b1v	CRCW-0b1v	CRCZ-2b	CRCZ-1b1v	CRCZ-0b1v
j_1 not b -tagged					✓		
Number of high-purity leptons			1			2 SFOS	
$H_{T,3}$	[GeV]			< 80			
$p_T(j_1)$	[GeV]		> 400		> 300		> 400
$m_T(\mathbf{p}_T^\ell, \mathbf{p}_T^{\text{miss}})$	[GeV]		[20, 120]				–
$m_{\ell\ell}$	[GeV]		–			[81, 101]	
E_T^{miss}	[GeV]		> 400			< 100	
$\tilde{E}_T^{\text{miss}}$	[GeV]		–		> 250		> 400
\mathcal{A}		> 0.5	> 0.8	–	> 0.5	> 0.8	–
m_{jj}	[GeV]	> 250	> 250	–	–	> 250	–
$N_{b\text{-jets}}$		≥ 2	1	0	≥ 2	1	0
N_{vtx}		–	≥ 1	≥ 1	–	≥ 1	≥ 1
m_{vtx}	[GeV]	–	> 0.6	> 1.5	–	> 0.6	> 1.5
p_T^{vtx}	[GeV]	–	> 3	> 5	–	> 3	> 5

Table 8.11: SRD signal, control and validation region definitions. Pink cells for the control and validation regions' columns indicate which selections ensure that they are orthogonal to the corresponding SR.

Variable		SRD-low	SRD-high	CRZD-low	CRZD-high	VRZD-low	VRZD-high
Trigger plateau				$(p_T(j_1) - 20 \text{ GeV})(E_T^{\text{miss}} - 160 \text{ GeV}) > 5000 \text{ GeV}^2$			
N_{jets}				2–3			
$N_{b\text{-jets}}$				≥ 2			
$p_T(j_1)$	[GeV]			> 100			
$p_T(j_2)$	[GeV]			> 50			
$\min[\Delta\phi(\text{jet}_{1-4}, E_T^{\text{miss}})]/3$	[rad]			> 0.4			
$S_{obj\text{-based}}$				> 7			
$p_T(j_1)/H_T$				> 0.7			
Number of baseline leptons		0		2		0	
Number of high-purity leptons		–		2 SFOS		–	
$p_T(\ell_1)$	[GeV]	–		> 27		–	
$p_T(\ell_2)$	[GeV]	–		> 20		–	
$m_T(\mathbf{p}_T^\ell, \mathbf{p}_T^{\text{miss}})$	[GeV]	–		> 20		–	
$m_{\ell\ell}$	[GeV]	–		[81, 101]		–	
$\tilde{E}_T^{\text{miss}}$	[GeV]	–		> 180		–	
E_T^{miss}	[GeV]	> 180		< 100		> 180	
w_D^{ll} D-low		> 0	–	–	> 0	–	
w_D^{ll} D-low		> 0	–	> 0	–	[-0.2, 0]	–
w_D^W D-low		> 0	–	–	> 0	–	
w_D^{ll} D-low		–	> 0	–	–	> 0	
w_D^{ll} D-high		–	> -0.1	–	> -0.1	–	[-0.3, -0.1]
w_D^Z D-high		–	> -0.05	–	–	–	> -0.05
w_D^W D-high		–					

8.2.5 Systematic Uncertainties

Detector-based, modeling and statistical uncertainties are all considered in the fit. Lepton uncertainties are considered for the control and validation regions to which they apply but are found to have negligible impact. Dedicated systematics are used to parameterise the uncertainty on the TC-LVT reconstruction efficiency and fake rate which are around 6% and 30% respectively. The development of the control regions allow the systematics to cancel to a large extent for the dominant Z+jets background process in all regions and the W+jets and top processes in SRC. Figure 8.8 illustrates the impact of the systematics in the different signal regions split by the binning.

The top production processes are assigned generator variation uncertainties, parton shower and hadronisation variation uncertainties from different MC alternative generators. For the Z+jets and W+jets modeling, seven -point variations of the renormalisation and factorisation scales as well as matching scale uncertainties between the matrix element and parton shower components and resummation scale are considered. An additional Z+jets uncertainty is prescribed to account for known mis-modeling [95] in particular kinematics of Z+ $b\bar{b}$ affecting the $\cos \theta_{bb}^*$ distribution using the generator aMC@NLO + Pythia.

The impact varies between regions but generally the modeling of Z+jets dominates, particularly in SRD. The dominant detector-related uncertainties come from the Jet energy scale which are large in some bins of SRB and SRC.

8.2.6 Results

The fit strategy for this analysis comprises 4 separate fits, the A and B-type regions are all mutually orthogonal and as a result they can be combined in a single fit - the AB fit. The C-type fit is conducted separately as it is not strictly orthogonal to the other bottom squark regions. For the dark matter regions, the SRD-low and SRD-high regions are not mutually orthogonal so they are fit separately, denoted fits D1 and D2.

Background-only Fit

The background-only, model-dependent and model-independent fits were performed and their results are summarised here. The yields in the control and signal regions for the background-only are given in tables 8.12 through 8.15.

Figures 8.9 and 8.10 show the post-fit distributions of the signal regions in the 'N-1' format, meaning that for the variable shown, the selection on said variable is removed and indicated with an arrow.

Figures 8.9, 8.10 and tables 8.12 8.17 show very good agreement is seen between the post-fit SM-only MC prediction and the measured data. No significant trends in disagreement between the MC and the data are observed in the important distributions illustrated.

Figure 8.11 summarises the yields in all signal regions comparing the predicted yield from the background-only fit showing the process components with the measured data yield.

8.2 Bottom squark and dark matter signals with $b\bar{b} + E_T^{\text{miss}}$ final states

table.results.yields channel	CRZA	CRZB
Observed events	101	89
Fitted bkg events	100.68 ± 8.43	89.35 ± 7.35
Fitted Z events	99.32 ± 8.42	80.65 ± 7.12
Fitted W events	0.00 ± 0.00	0.00 ± 0.00
Fitted ttbar events	$0.12^{+0.15}_{-0.12}$	4.51 ± 2.20
Fitted st events	0.00 ± 0.00	0.00 ± 0.00
Fitted group_ttW_ttZ_ttH_diboson events	1.23 ± 0.15	4.18 ± 0.31

Table 8.12: sbot-AB control regions. Fit results for the CRs with an integrated luminosity of 139 fb^{-1} . The results are obtained from the control regions using the background-only fit. The errors shown are the statistical plus systematic uncertainties. Uncertainties on the fitted yields are symmetric by construction, where the negative error is truncated when reaching to zero event yield.

table.results.yields channel	SRAmct250_meff	SRAmct350_meff	SRAmct450_meff	SRAmct550	SRAmct650	sbotB_XGB_bin0	sbotB_XGB_bin1	sbotB_XGB_bin2	sbotB_XGB_bin3
Observed events	552	104	23	7	8	62	36	19	3
Fitted bkg events	555.40 ± 75.02	119.90 ± 15.90	27.08 ± 3.85	10.44 ± 1.72	5.60 ± 1.35	50.41 ± 9.40	32.75 ± 6.84	14.97 ± 3.13	5.66 ± 1.53
Fitted Z events	473.06 ± 75.94	100.84 ± 16.04	22.61 ± 3.76	8.73 ± 1.60	4.54 ± 1.23	36.19 ± 8.38	22.03 ± 5.33	9.82 ± 2.64	4.09 ± 1.27
Fitted W events	56.32 ± 12.90	14.46 ± 3.22	3.46 ± 0.74	1.29 ± 0.36	0.61 ± 0.16	6.26 ± 2.37	5.49 ± 2.22	2.13 ± 0.99	0.83 ± 0.39
Fitted ttbar events	8.57 ± 3.94	1.38 ± 0.82	$0.15^{+0.17}_{-0.15}$	$0.05^{+0.13}_{-0.05}$	$0.00^{+0.01}_{-0.00}$	5.17 ± 1.47	3.69 ± 1.89	1.99 ± 0.77	0.57 ± 0.22
Fitted st events	$3.60^{+0.10}_{-0.10}$	$0.43^{+0.28}_{-0.13}$	$0.05^{+0.14}_{-0.05}$	0.00 ± 0.00	0.00 ± 0.00	$0.34^{+0.05}_{-0.04}$	$0.23^{+0.04}_{-0.03}$	$0.18^{+0.13}_{-0.18}$	$0.04^{+0.10}_{-0.04}$
Fitted group_ttW_ttZ_ttH_diboson events	13.86 ± 1.68	2.81 ± 1.46	0.81 ± 0.09	0.38 ± 0.06	0.45 ± 0.09	2.44 ± 0.77	1.31 ± 0.56	0.84 ± 0.17	$0.14^{+0.04}_{-0.14}$

Table 8.13: sbot-AB signal regions. The results for the m_{CT} binned SRA regions are grouped together. The background normalisations are obtained from the control regions using the background-only fit. The errors shown are the statistical plus systematic uncertainties. Uncertainties on the fitted yields are symmetric by construction, where the negative error is truncated when reaching to zero event yield.

table.results.yields channel	CRC_Top	CRC_W0b1v	CRC_W1b1v	CRC_Z0b1v	CRC_Z1b1v	CRC_Z2b0v
Observed events	145	287	106	72	95	81
Fitted bkg events	145.08 ± 12.02	287.04 ± 16.94	105.93 ± 10.28	72.03 ± 8.48	95.07 ± 9.75	80.99 ± 8.99
Fitted group_Z0b_Z1b_Z2b events	0.31 ± 0.13	1.16 ± 0.29	0.57 ± 0.18	69.43 ± 8.49	92.02 ± 9.76	71.19 ± 9.31
Fitted group_W0b_W1b events	49.14 ± 18.57	237.41 ± 21.24	79.36 ± 13.72	0.00 ± 0.00	0.00 ± 0.00	0.00 ± 0.00
Fitted ttbar events	78.22 ± 20.72	32.33 ± 11.67	18.41 ± 5.45	0.00 ± 0.00	$0.08^{+0.25}_{-0.08}$	5.17 ± 2.46
Fitted st events	10.07 ± 2.67	6.45 ± 2.13	3.79 ± 1.19	0.00 ± 0.00	0.00 ± 0.00	0.36 ± 0.32
Fitted group_ttW_ttZ_ttH_diboson events	7.33 ± 1.07	9.68 ± 1.95	3.80 ± 0.65	2.60 ± 0.21	2.96 ± 0.50	4.27 ± 0.41

Table 8.14: Combined C-type control regions. Fit results with an integrated luminosity of 139 fb^{-1} . The results are obtained from the control regions using the background-only fit (see text for details). The errors shown are the statistical plus systematic uncertainties. Uncertainties on the fitted yields are symmetric by construction, where the negative error is truncated when reaching to zero event yield.

8 Searches for third generation squarks

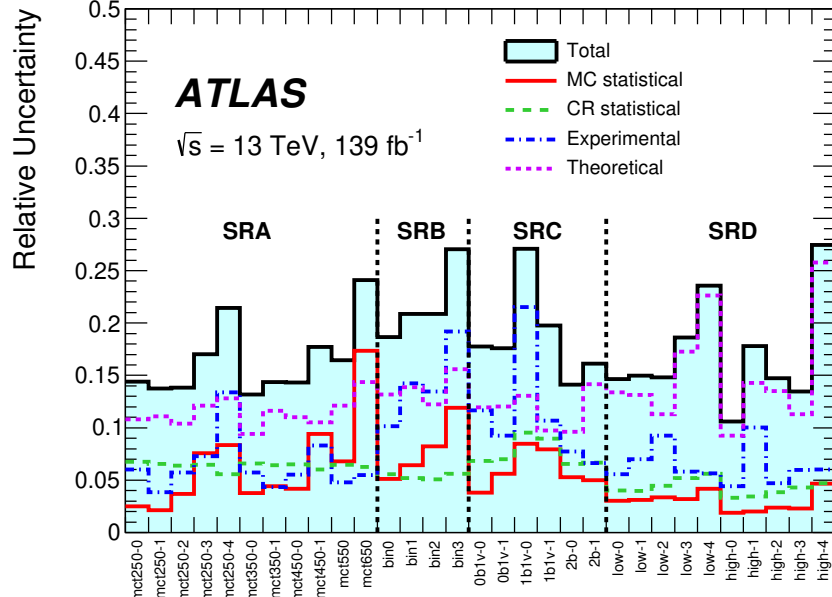


Figure 8.8: Summary of the post-fit relative systematic uncertainties of the various signal region yields, also split by component: Experimental (detector/reconstruction-based), theoretical (modeling), CR statistical (statistical uncertainty from the data yield in the control regions) and the MC statistics.

Figure 8.11 shows the good agreement in yields between the data and SM prediction for all signal regions used in the fit. Generally the SRA bins show excellent agreement with the prediction with the largest deviation being a 1σ under fluctuation in one of the m_{CT} bins. All data yields of SRB are in agreement with the prediction to within 1σ , small excesses are seen in the first 3 bins with a small under fluctuation in the final bin. In the SRC bins, very good data/MC agreement is observed in the 1b1v and 0b1v regions whereas both bins of the 2b region have small excesses around 1σ . In the dark matter regions, the low-mass region bins show a consistent small excess around 1σ , whereas the high-mass region bins show very good agreement until the final bins where there is a small excess of data.

8.2 Bottom squark and dark matter signals with $b\bar{b} + E_T^{\text{miss}}$ final states

table.results.yields channel	SRC_0b1v_eT_miss	SRC_1b1v_eT_miss	SRC_2b_eT_miss
Observed events	151	43	58
Fitted bkg events	147.92 ± 24.87	50.57 ± 10.07	44.47 ± 5.76
Fitted group_Z0b_Z1b_Z2b events	73.87 ± 18.73	20.10 ± 5.13	16.61 ± 4.01
Fitted group_W0b_W1b events	60.51 ± 11.18	26.07 ± 8.33	14.96 ± 3.68
Fitted ttbar events	7.04 ± 2.22	1.90 ± 0.96	8.92 ± 3.82
Fitted st events	1.40 ± 0.48	0.42 ± 0.41	1.25 ± 0.49
Fitted group_ttW_ttZ_ttH_diboson events	5.11 ± 1.23	2.07 ± 0.30	2.73 ± 0.58

Table 8.15: sbot-C Signal regions. Fit results for an integrated luminosity of 139 fb^{-1} . The results are obtained from the control regions using the background-only fit. The errors shown are the statistical plus systematic uncertainties. Uncertainties on the fitted yields are symmetric by construction, where the negative error is truncated when reaching to zero event yield.

table.results.yields channel	DMCRZB1	DMSRB1_cosbb	DMSRB1_Disc
Observed events	234	1256	497
Fitted bkg events	234.15 ± 15.30	1065.44 ± 134.95	381.54 ± 75.83
Fitted Z events	221.49 ± 15.75	688.17 ± 102.89	288.25 ± 71.40
Fitted W events	0.00 ± 0.00	138.39 ± 42.98	32.63 ± 12.96
Fitted ttbar events	8.12 ± 3.54	181.83 ± 70.78	47.25 ± 25.32
Fitted st events	1.92 ± 0.79	45.92 ± 30.47	10.71 ± 8.57
Fitted ttW events	$0.02^{+0.02}_{-0.02}$	0.07 ± 0.02	$0.00^{+0.01}_{-0.00}$
Fitted ttZ events	0.20 ± 0.03	0.42 ± 0.13	0.08 ± 0.07
Fitted ttH events	0.01 ± 0.00	0.94 ± 0.24	0.24 ± 0.04
Fitted diboson events	2.39 ± 0.32	9.70 ± 2.11	2.38 ± 0.92

Table 8.16: All regions in DMB1. Fit results for one bin CR, VR and SR with an integrated luminosity of 139 fb^{-1} . The results are obtained from the control regions using the background-only fit (see text for details). Nominal MC expectations (normalised to MC cross-sections) are given for comparison. The errors shown are the statistical plus systematic uncertainties. Uncertainties on the fitted yields are symmetric by construction, where the negative error is truncated when reaching to zero event yield.

8 Searches for third generation squarks

table.results.yields channel	DMCRZB2	DMSRB2_cosbb	DMSRB2_Disc
Observed events	423	1882	320
Fitted bkg events	423.02 ± 20.56	1853.10 ± 219.53	242.29 ± 66.47
Fitted Z events	398.06 ± 20.86	1351.84 ± 186.81	216.79 ± 64.63
Fitted W events	0.00 ± 0.00	222.60 ± 80.73	$8.71^{+11.21}_{-8.71}$
Fitted ttbar events	8.05 ± 2.91	162.24 ± 57.44	11.08 ± 6.13
Fitted st events	2.91 ± 0.74	45.92 ± 27.54	3.58 ± 2.04
Fitted ttW events	0.02 ± 0.01	0.13 ± 0.02	0.00 ± 0.00
Fitted ttZ events	0.30 ± 0.06	0.77 ± 0.23	0.07 ± 0.03
Fitted ttH events	0.00 ± 0.00	2.14 ± 0.30	0.15 ± 0.06
Fitted diboson events	13.68 ± 1.04	67.47 ± 5.27	1.91 ± 0.68

Table 8.17: All regions in DMB2. Fit results for one bin CR, VR and SR with an integrated luminosity of 139 fb^{-1} . The results are obtained from the control regions using the background-only fit. The errors shown are the statistical plus systematic uncertainties. Uncertainties on the fitted yields are symmetric by construction, where the negative error is truncated when reaching to zero event yield.

8.2 Bottom squark and dark matter signals with $b\bar{b} + E_T^{\text{miss}}$ final states

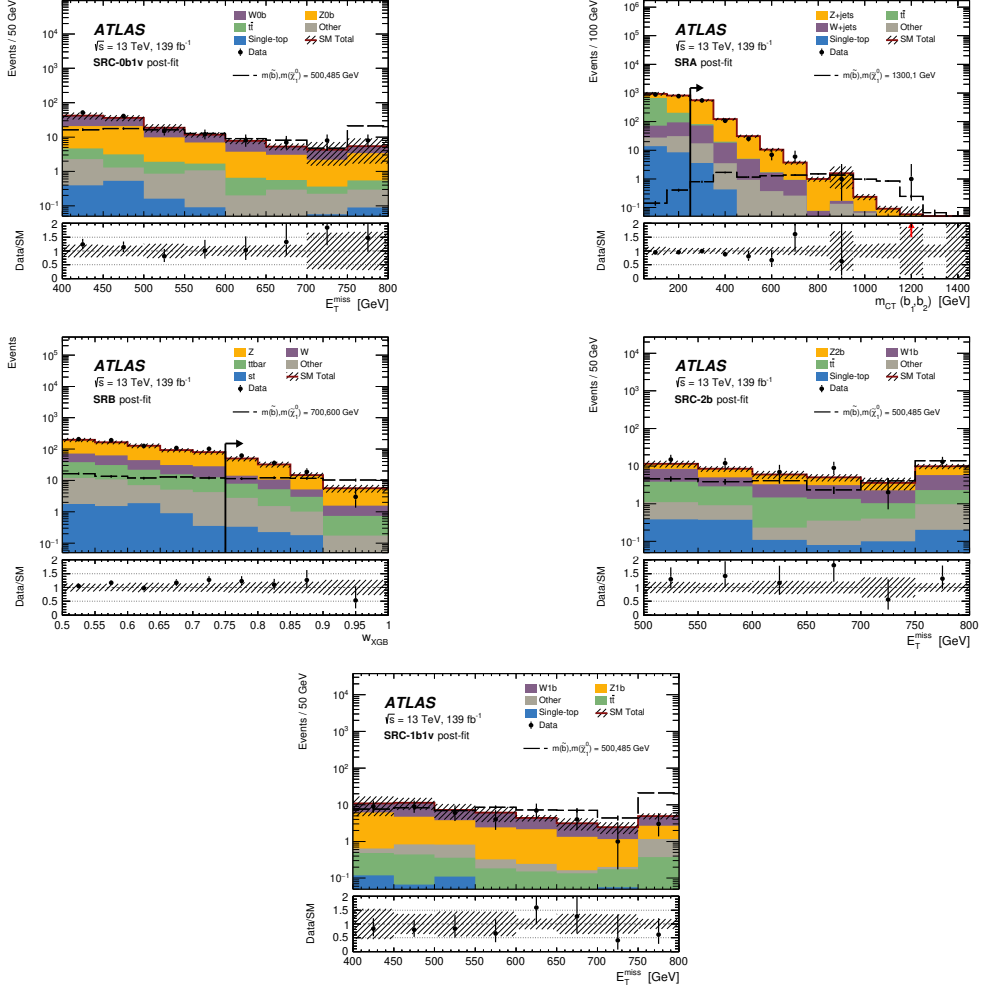


Figure 8.9: Post-fit distribution of (a) m_{CT} in SRA (b) w_{XGB} in SRB and E_T^{miss} in (c) SRC-2b, (d) SRC-1b1v, (e) SRC-0b1v. Where relevant, the signal region selection is indicated by a black arrow. In each of (a)–(e) the lower plot shows the ratios of the observed yields to the post-fit predicted background yields, with a red arrow indicating when a ratio value is outside the displayed interval. The “Other” category includes contributions from diboson, and $t\bar{t} + W/Z/H$ production. The shaded band represents the total uncertainty of the background prediction. The last bin includes overflow events.

8 Searches for third generation squarks

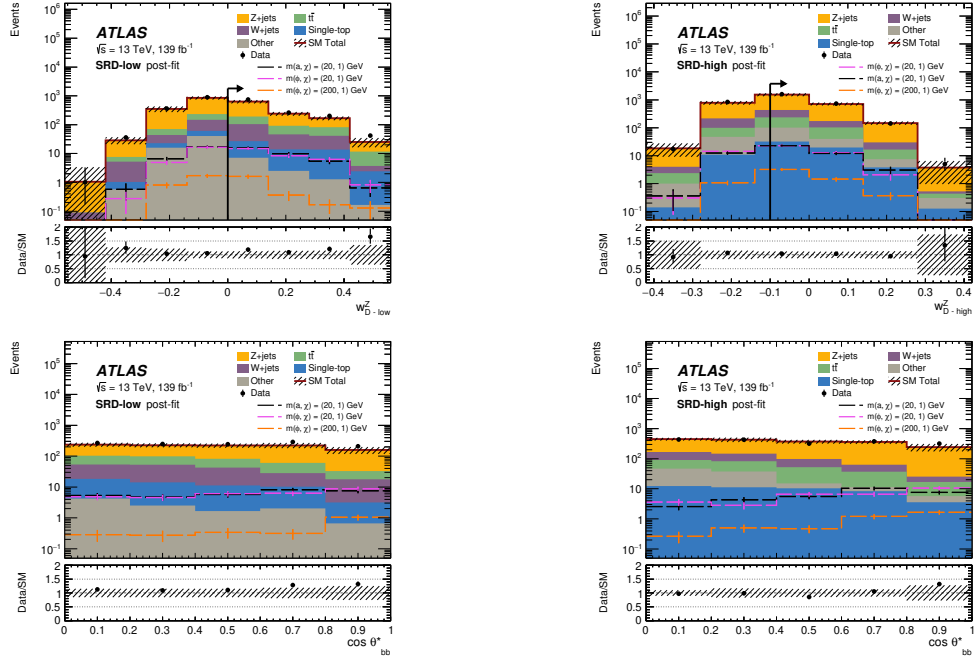


Figure 8.10: Post-fit distribution of (a) $w_{D\text{-low}}^Z$ and (c) $\cos \theta_{bb}^*$ in SRD-low and (b) $w_{D\text{-high}}^Z$ and (d) $\cos \theta_{bb}^*$ in SRD-high. Where relevant, the signal region selection is indicated by a black arrow. In each of (a)–(d) the lower plot shows the ratios of the observed yields to the post-fit predicted background yields. The “Other” category includes contributions from diboson and $t\bar{t} + W/Z/H$ production. The shaded band represents the total uncertainty of the background prediction.

8.2 Bottom squark and dark matter signals with $b\bar{b} + E_T^{\text{miss}}$ final states

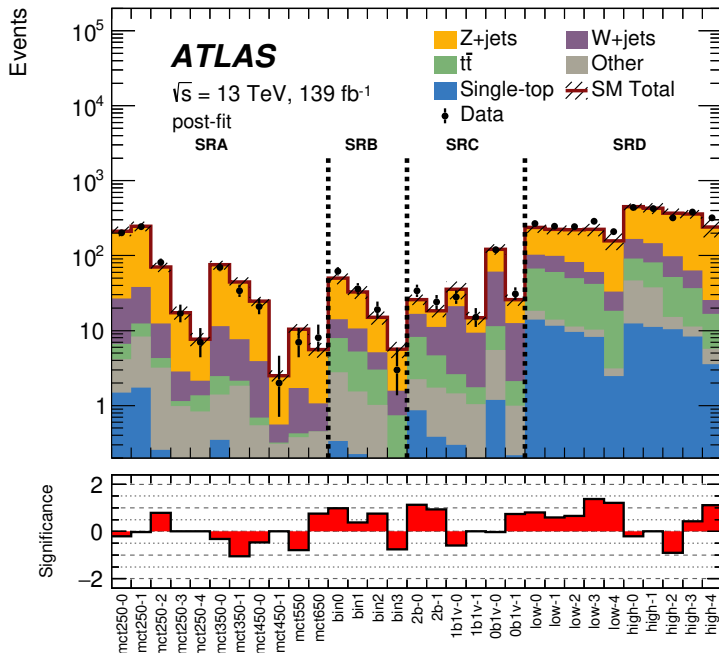


Figure 8.11: Comparison between observed and background-only post-fit predicted background yields for the signal regions. The ratio plot represents the statistical significance of the discrepancy between the observed and predicted value. The “Other” category includes contributions from di-boson and $t\bar{t} + W/Z/H$ production. The shaded band represents the total uncertainty of the background prediction.

8 Searches for third generation squarks

Overall the SM prediction describes the data well and no significant deviation from the SM expectation was observed, therefore limits on the specific signal hypotheses and possible BSM contribution are calculated, these are summarised in section [8.4](#).

8.3 Bottom squark with multiple b-jets

There are 3 free parameters to this model - the masses of the 3 sparticles. As a result, the 3-dimensional phase-space available is too large to be covered by one analysis so instead one degree of freedom is constrained in a theoretically motivated way.

Two choices are made for this constraint: in one case we consider the $\tilde{\chi}_1^0$ mass to be fixed at 60GeV. This is motivated if the $\tilde{\chi}_1^0$ is a WIMP dark matter candidate. Bino-like LSP models tend to produce more dark matter than is observed in the relic density [96], however the $\tilde{\chi}_1^0$ annihilation is enhanced if its mass lies at $m_{\tilde{\chi}_1^0} \sim m_h/2$ (the Higgs funnel). We know the SM Higgs mass is $m_h \sim 125$ GeV. This is referred to as the M60 grid and the space is spanned by $m_{\tilde{b}}$ and $m_{\tilde{\chi}_2^0}$ masses that are kinematically viable.

The second constraint is the requirement that $\Delta m(\tilde{\chi}_2^0, \tilde{\chi}_1^0) = 130$ GeV which is the compressed limit that allows the process to be kinematically viable, the phase space is then spanned by $m_{\tilde{b}}$ and $m_{\tilde{\chi}_2^0}$ and referred to as the DM130 grid. The mass hypotheses generated for investigation are shown in figure 8.13. The resulting final state is relatively unique with 6 b-quarks and large missing transverse energy.

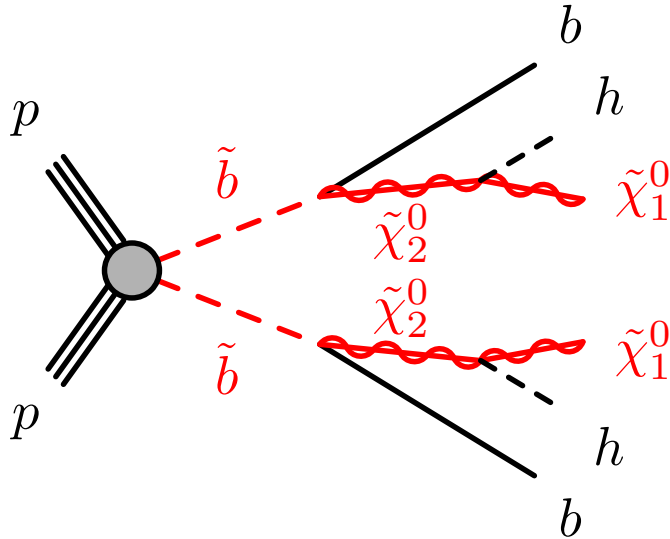


Figure 8.12: Bottom squark signature targeted in the multiple b-jets analysis.

Personal contributions to this analysis include: development of the two higgs reconstruction algorithms which form the basis of the approach for the bulk regions of both signal grids and the compressed region of the $\Delta m(\tilde{\chi}_2^0, \tilde{\chi}_1^0)=130$ GeV grid, described in sections 8.3.2 and 8.3.3. Region design for the B-type regions described in 8.3.3 and the associated background estimation described in 8.3.5.

8 Searches for third generation squarks

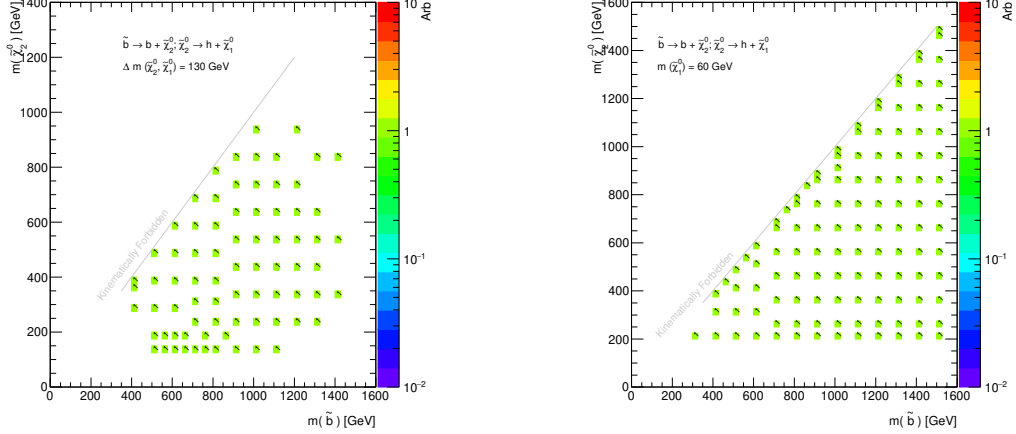


Figure 8.13: The points generated for the two grids considered in the analysis for (a) the points with $\Delta m(\tilde{\chi}_2^0, \tilde{\chi}_1^0) = 130\text{ GeV}$ and (b) the points with $m_{\tilde{\chi}_1^0} = 60\text{ GeV}$.

8.3.1 Event Selection

Data is selected using the E_T^{miss} triggers. As mentioned in the previous section, E_T^{miss} triggers in ATLAS are known not to be fully efficient at lower values of E_T^{miss} , therefore a selection is made on the reconstructed E_T^{miss} in order to be fully efficient. This selection is identified by studying the E_T^{miss} trigger efficiency with respect to another trigger, here muon triggers are used. Table 8.18 shows the selections used for the study. Since the E_T^{miss} triggers only use track and calorimeter information, the muon in the event can be treated as invisible in the E_T^{miss} trigger calculation in order to mimic the E_T^{miss} trigger response if it were not present. Figure 8.14 shows the ratio of efficiencies for the two triggers in both data and using a $t\bar{t}$ MC sample. Based on this study, an offline E_T^{miss} requirement of $> 250\text{ GeV}$ is used for all selections that use E_T^{miss} triggers throughout this analysis and similar arguments are made in the following analyses.

Table 8.18: Summary of the selection applied in order to study the E_T^{miss} trigger turn-on.

Reference	Selection		
Lowest unprescaled trigger	Muon	Muon &&	$\$E_T^{\text{miss}}\$$
Event Cleaning		✓	
Number of signal muons		1	
Number of baseline muons		1	
p_T (muon)		$\geq 27\text{ GeV}$	
Number of signal jets		≥ 4	
Number of signal b-jets		≥ 3	

E_T^{miss} triggers are used in all regions requiring zero leptons in this analysis. Regions with one or two leptons are also used for background estimation. The single lepton regions use the E_T^{miss} triggers as with the zero lepton regions, however the two lepton regions use single lepton triggers (electron or

8.3 Bottom squark with multiple b-jets

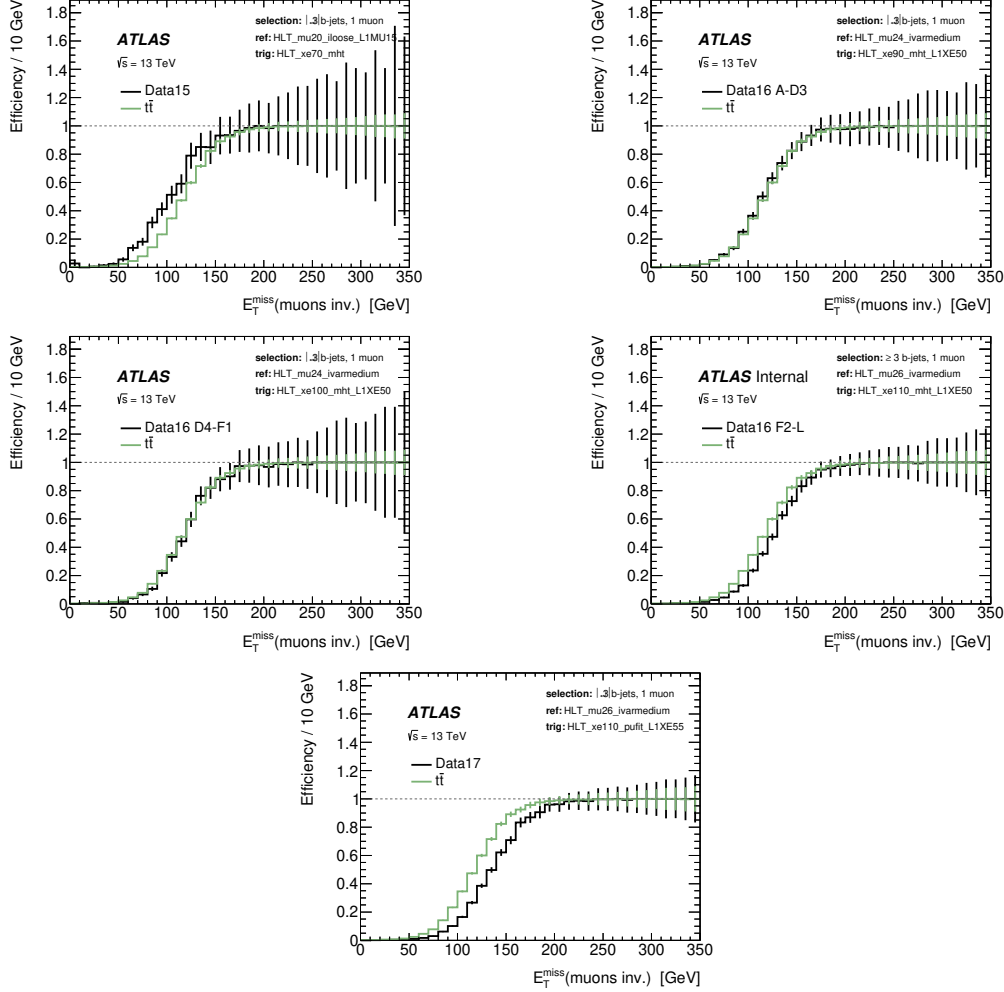


Figure 8.14: Turn-on curves for the E_T^{miss} triggers as a function of offline E_T^{miss} with respect to a fully efficient muon trigger. The muons in the event are treated as invisible by subtracting the muon transverse momentum from the E_T^{miss} . We observe that the triggers become fully efficient between 200 and 250 GeV.

muon). A set of so-called *preselection* regions are defined to enable the study and optimisation of the regions. These are summarised in table 8.19

8.3.2 Signal Regions

As the signal mass hypotheses considered in this analysis cover a large phase-space, the topology of the final state varies wildly between points. For this reason three approaches are developed that target areas of phase-space with similar features. The first is referred to as *SRA*. This aims to provide a general strategy to provide sensitivity the bulk regions of both the M60 and DM130 grids utilising features that are common to both. The other regions are referred to as *SRB* and *SRC* which are specifically targeted towards regions to which SRA loses sensitivity. These were found to be the

8 Searches for third generation squarks

Table 8.19: Definition of the three preselection regions.

Criterion	0-Lepton	1-Lepton	2-lepton (SF)
Lowest unprescaled trigger	E_T^{miss}	E_T^{miss}	Muon Electron
Event Cleaning	✓	✓	✓
Number of <i>baseline</i> leptons	0	1	2
Number of <i>signal</i> leptons	-	1	2 (SF, OS)
Number of <i>signal</i> jets			≥ 4
Number of b-tagged jets	≥ 2		≥ 3
$\min[\Delta\phi(\text{jet}_{1-4}, E_T^{\text{miss}})]$	> 0.4		-
$p_T l_1$	-	$> 20 \text{ GeV}$	$> 27 \text{ GeV}$
$p_T l_2$	-	-	$> 20 \text{ GeV}$
m_T	-	$> 20 \text{ GeV}$	-

'compressed' regions of both grids, meaning regions where the mass difference $\Delta m(\tilde{b}, \tilde{\chi}_2^0)$ is small, these are illustrated in figure 8.16. The specific features of the signals in these regions and how they're exploited are described in the relevant sections. The kinematics of the signal in these regions are highlighted in figure 8.15.

In addition to event-level characteristics of the signal, the presence of Higgs decays in the final state can be used as a handle to identify the process and discriminate from SM backgrounds. However with the presence of many b-jets in the final state the reconstruction of the Higgs reduces to a combinatorical problem. In SRA and SRB dedicated algorithms are employed based on event topology to reconstruct the mass of Higgs candidate(s). It is worth noting that due to the inefficiency associated with identifying b-jets, we do not aim to reconstruct the 6 b-jets that are expected in the final state.

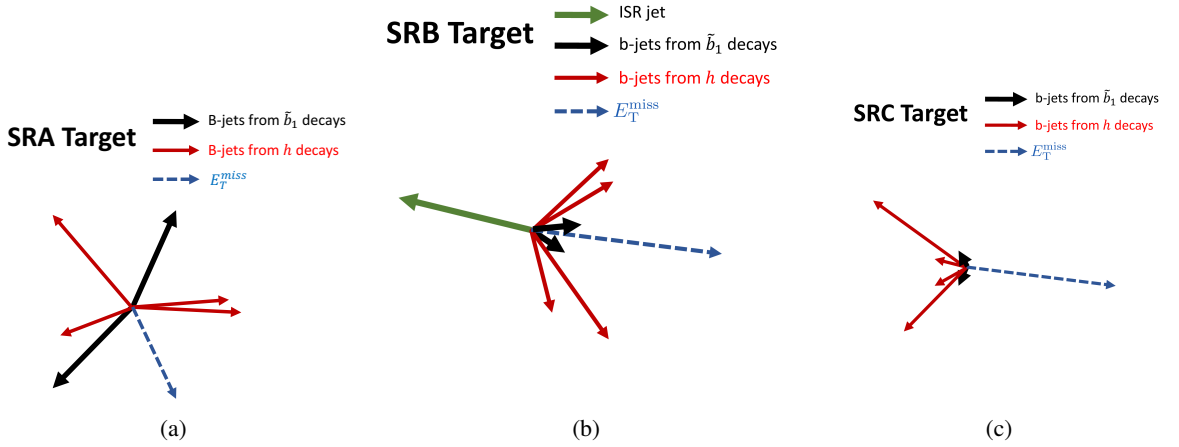


Figure 8.15: Signal phenomenology targeted by the three signal region types.

8.3 Bottom squark with multiple b-jets

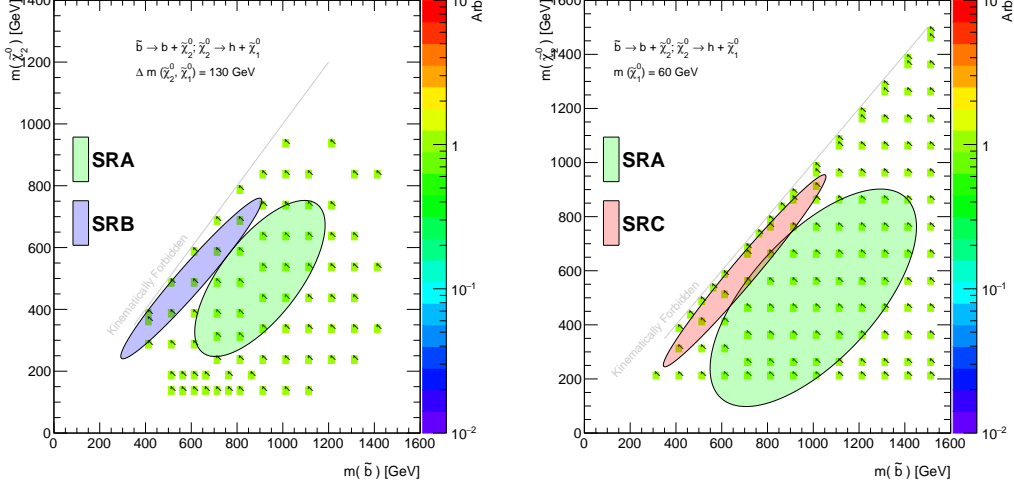


Figure 8.16: The regions of the signal mass grids which are targeted by the three signal regions which have been developed. *Left:* The $\Delta m(\tilde{\chi}_2^0, \tilde{\chi}_1^0) = 130$ GeV grid includes a dedicated region, SRB, targeting the compressed regime along the diagonal. *Right:* the $m(\tilde{\chi}_1^0) = 60$ GeV grid including a dedicated region, SRC, targeting the compressed diagonal region. The SRA region is sensitive to the bulk regions of both grids.

Signal Region A

SRA targets points for which the mass difference between the bottom squark and second-lightest neutralino is large. The b -quarks from the decay of the bottom squark have high p_T and the b -quarks from the Higgs decays also have relatively high p_T . Thus final states with many high p_T jets, many of which are b -tagged, are targeted. In combination with high E_T^{miss} , this gives a signature with high $m_{E_{\text{miss}}}$. Kinematic variables are developed in a reconstruction algorithm referred to as the *Max-Min* algorithm which aims to reconstruct a single Higgs candidate from b -jets.

Max-Min Algorithm

To reconstruct the Higgs candidate and its mass, the expected signal topology is used to identify b -jet pairs associated with one of the Higgs bosons in the decay chain, and to differentiate these from the b -jets arising from the \tilde{b} decays. In general, two b -jets with large separation in the detector come from the \tilde{b} decay while the remaining b -jets come from the decay of the Higgs bosons. Seeking to exploit such a topology in order to reconstruct the Higgs mass is the aim of the 'MaxMin' algorithm. This algorithm provides a few key variables which provide the basis for the definition of the signal region.

- $\Delta R_{\max}(b, b)$: Identifies the two b -jets with the largest angular separation which are most likely to originate from the initial decay of the \tilde{b} .
- $\Delta R_{\max-\min}(b, b)$: Identifies the two b -jets with the minimum angular separation from the remaining candidates which are most likely to originate from the same Higgs decay.

8 Searches for third generation squarks

- $m(h_{\text{cand}})$: The invariant mass of the two b-jets from $\Delta R_{\max-\min}(b, b)$ are used to reconstruct the Higgs mass.

For the SRA region, the algorithm is developed for events where there are four or more b-jets identified. The first stage of the algorithm selects the pair of b-jets with largest angular separation, defined by the metric; $\Delta R = \sqrt{\Delta\phi^2 + \Delta\eta^2}$, as seen in 8.17 (left). A selection of $\Delta R_{\max}(b, b) \geq 2$ is imposed for the two b-jets with the largest separation. This b-jet pair is subsequently no longer considered further in the algorithm calculation. Using the remaining b-jets, the pair with smallest angular separation is calculated. The two b-jets with the smallest ΔR (referred to as $\Delta R_{\max-\min}(b, b)$) is assumed to arise from the same parent Higgs boson, this distribution can be seen in 8.17 (right).

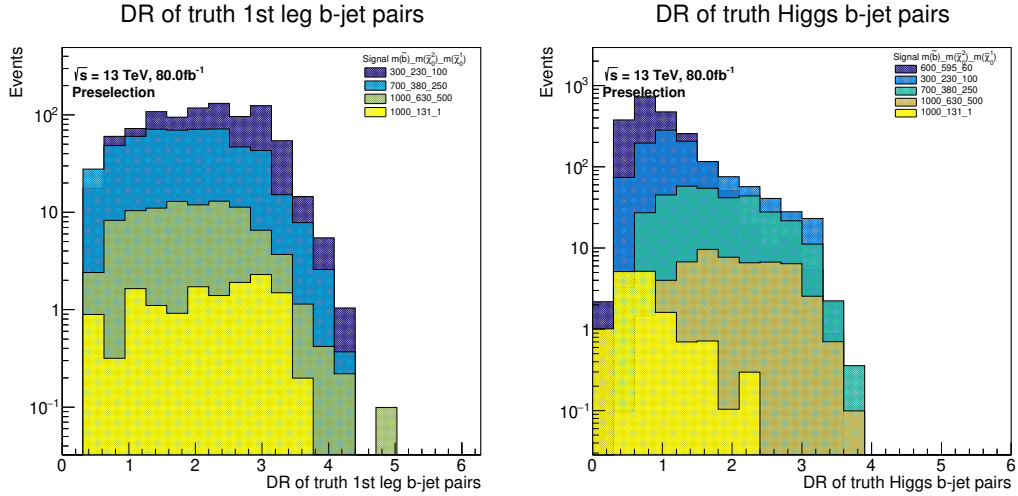


Figure 8.17: Truth level distributions of the two ΔR variables used as the basis for the “MaxMin” algorithm. Left: Angular separation in ΔR of the two b-jets from the \bar{b} decay, referred to as $\Delta R_{\max}(b, b)_{\text{truth}}$. Right: Angular separation of the two b-jets arising from the same Higgs, referred to as $\Delta R_{\max-\min}(b, b)_{\text{truth}}$.

In this approach the invariant mass of only the closest (in ΔR) pair of b-jets associated with a Higgs decay is calculated and used for signal discrimination. The efficiency in tagging 6 b-jets, from which two Higgs candidates should be reconstructed, is low and there are limited statistics for this to be a viable approach. Whilst the algorithm was developed for events with at least 4 b-jets, additional SR optimisation studies lead to tighter selections placed on the two ΔR variables to provide additional sensitivity to the signals under investigation. The evolution of the sensitivity by sequentially applying the algorithm selection on top of the pre-selection is presented in 8.20, all selections defining SRA from table 8.21 are applied as *baseline cuts* while the $m_{E_{\text{ff}}}$ and the algorithmic selection are added sequentially.

The SRA definition is summarised in table 8.21. After the $E_{\text{T}}^{\text{miss}}$ trigger selections is based on the jet requirements, veto on light leptons and a veto on tau jet candidates (as described in section 6.6), selections from the variables defined in with the max-min algorithm, a dedicated selection designed to remove background from QCD multijet events with substantial jet mis-measurement ($\min[\Delta\phi(\text{jet}_{1-4}, E_{\text{T}}^{\text{miss}})]$) and then selection on the effective mass ($m_{E_{\text{ff}}}$). The QCD rejection variable is designed to reject events where the jets are close in angular distance to the $E_{\text{T}}^{\text{miss}}$. An inclusive

8.3 Bottom squark with multiple b-jets

Table 8.20: Significance (Z_n) evolution for the algorithm discriminating cuts for the 'MaxMin' algorithm of SRA on a selection of benchmark signal models.

Signal Point ($m(\tilde{b})_m(\tilde{\chi}_2^0)_m(\tilde{\chi}_1^0)$)	1300_850_60	900_300_200	1100_330_200
Baseline cuts + $m_{Eff} > 1000 \text{ GeV}$	0.95	2.78	1.28
Baseline cuts + $m_{Eff} > 1000 \text{ GeV}$ + $\Delta R_{\max}(b, b) > 2.5$	0.88	2.85	1.31
Baseline cuts + $m_{Eff} > 1000 \text{ GeV}$ + $\Delta R_{\max}(b, b) > 2.5 + \Delta R_{\max-\min}(b, b) < 2.5$	1.06	3.10	1.45
Baseline cuts + $m_{Eff} > 1000 \text{ GeV}$ + $\Delta R_{\max}(b, b) > 2.5 + \Delta R_{\max-\min}(b, b) < 2.5$ + $m(h_{\text{cand}}) > 80 \text{ GeV}$	1.16	3.12	1.51

discovery region is designed with $m_{Eff} > 1000 \text{ GeV}$ and to increase the exclusion power m_{Eff} is also split into 3 bins: low (L), medium (M) and high (H).

Table 8.21: Signal region definitions for the inclusive A-type SR, alongside the three varying m_{Eff} binned regions. The letter appended to the SRA label corresponds to the low, medium or high m_{Eff} selection.

Variable	Units	SRA	SRA-L	SRA-M	SRA-H
Event Cleaning			✓		
E_T^{miss} Trigger			✓		
N_{leptons} (baseline)			0		
N_{jets}			≥ 6		
N_b -jets			≥ 4		
τ -veto			✓		
$\Delta R_{\max}(b, b)$			> 2.5		
$\Delta R_{\max-\min}(b, b)$			< 2.5		
$m(h_{\text{cand}})$	[GeV]		> 80		
E_T^{miss}	[GeV]		> 350		
$p_T(b_1)$	[GeV]		> 200		
$\min[\Delta\phi(\text{jet}_{1-4}, E_T^{\text{miss}})]$	[rad]		> 0.4		
m_{Eff}	[TeV]	> 1.0	$\in [1.0, 1.5]$	$\in [1.5, 2]$	> 2

8.3.3 Signal Region B

SRB is designed to compliment SRA for signals with compressed topologies as illustrated in figure 8.15(b). When the mass difference between the \tilde{b} and $\tilde{\chi}_2^0$ is low, then the bottom squark decay produces b-quarks with low p_T . Jets from low p_T quarks are inefficiently reconstructed in the detector and in addition the b-tagging efficiency is reduced, meaning they are unlikely to be reconstructed. Also since the mass difference between the $\tilde{\chi}_2^0$ and $\tilde{\chi}_1^0$ is just enough to produce an on-shell Higgs, both the Higgs and the $\tilde{\chi}_1^0$ are produced almost at rest, resulting in relatively low E_T^{miss} . In order to recover

8 Searches for third generation squarks

in these events the selection is based on identifying events with a strong jet from initial state radiation (ISR) which boosts the decay chain into a co-linear direction and the E_T^{miss} is recovered. With these topologies the max-min algorithm is not applicable since the b-jets from the first leg of the decay are largely un-reconstructed. Instead an alternate algorithm was developed and is described below, this differs in concept from the original algorithm in that it is intended to reconstruct two Higgs decays.

Alternative 'MaxMin' Algorithm

The two b -jets coming from the same Higgs decay are expected to have a relatively large angular separation, due to the Higgs being produced with low momentum. The algorithm proceeds by the following: the ΔR of all of the b -jet pairings are calculated, and the pair of b -jets which have the largest value of ΔR are assumed to come from the decay of the same Higgs boson. This pairing is removed from the consideration and the remaining b -jets are then looped over, the two remaining b -jets that give the largest ΔR are subsequently paired together, with the assumption that they arise from the second Higgs. The invariant masses of the two sets of b -jet pairs are calculated, and then the average value of the two invariant masses is taken and is expected to be around the Higgs mass. Figure 8.18 presents the average invariant mass of the two b -jet pairings, showing a clear peak at the expected value of the Higgs mass.

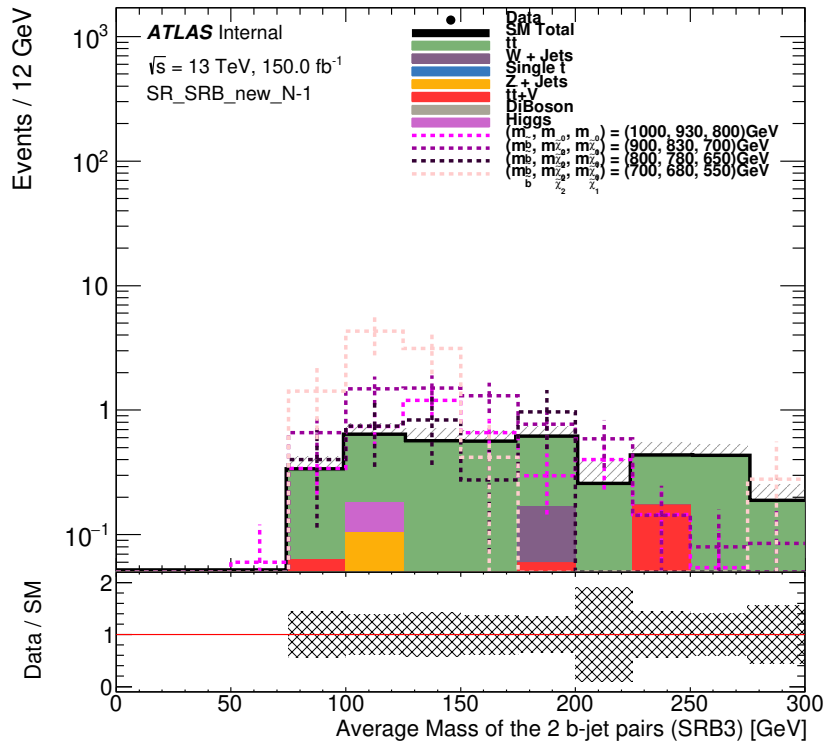


Figure 8.18: Average mass of the b -jet pairings

8.3 Bottom squark with multiple b-jets

From the average mass of the two b -jet pairings a selection is placed in a window around the Higgs mass. Additional selections are also placed on the p_T of the leading jet and also on the m_{Eff} of the event. Investigating the p_T of the leading jet in the event, it is found that for signal events this is predominantly coming from initial state radiation (ISR) as such a veto is placed on events where the leading jet is b-tagged as the ISR jet is likely due to gluon emission. To further select ISR-like events a selection on the $\Delta\phi$ between the missing transverse momentum and the leading jet direction, $\Delta\phi j_1 - E_T^{\text{miss}}$, is required to be large. The signal region selections are given in table 8.22. To verify the effectiveness of the main selections and the alternative algorithm, the significance increase from each selection is calculated and shown in table 8.23 for few benchmark signal models.

Table 8.22: Selections for SRB.

Variable	SRB
Event Cleaning	✓
E_T^{miss} Trigger	✓
N_{leptons} (baseline)	0
E_T^{miss}	> 350 GeV
N_{jets}	≥ 4
$N_{b-\text{jets}}$	≥ 4
non-b leading jet	✓
$p_T(j_1)$	> 350 GeV
m_{Eff}	> 1000 GeV
τ veto	✓
$\min[\Delta\phi(\text{jet}_{1-4}, E_T^{\text{miss}})]$	> 0.4
$ \Delta\phi(j_1, E_T^{\text{miss}}) $	> 2.8
$m(h_{\text{cand1}}, h_{\text{cand2}})_{\text{avg}}$	[75, 175] GeV

Table 8.23: Significance evolution for the main discriminating selections and the alternative algorithm of SRB on benchmark signal models.

Signal Point ($m(\tilde{b})$)_m($\tilde{\chi}_2^0$)_m($\tilde{\chi}_1^0$) GeV	1000_930_800	900_830_700	700_680_550
Baseline selections	0.06	0.64	0.97
Baseline selections + E_T^{miss}	0.48	1.01	1.59
Baseline selections + E_T^{miss} + $p_T(j_1)$	0.69	1.31	1.96
Baseline selections + E_T^{miss} + $p_T(j_1)$ + Algorithm	0.87	1.55	2.26

8.3.4 Signal Region C

SRC aims to compliment SRA in the compressed regions of the M60 grid. In this case, the masses of the \tilde{b} and the $\tilde{\chi}_2^0$ are similar and much greater than the 60 GeV $\tilde{\chi}_1^0$. This means that the Higgs and the $\tilde{\chi}_1^0$ are produced with large momenta and the E_T^{miss} is large. In this topology the Higgs reconstruction algorithms are not very effective but the signature of very high momenta with multiple b -jets is a

8 Searches for third generation squarks

powerful discriminator. The object-based E_T^{miss} significance is used as the key discriminating variable as it is powerful in distinguishing real missing energy from fake missing energy arising from jet mis-measurement. Similar baseline selections are applied regarding the E_T^{miss} selection and jet and b-jet multiplicities as with SRA and SRB. The $\mathcal{S}_{\text{obj-based}}$ selection begins at 22 and 4 bins of the variable are used to give strong exclusion. The SRC definition is summarised in table 8.24.

Table 8.24: Signal region selections for the C-type SRs.

Variable	Units	SRC	SRC22	SRC24	SRC26	SRC28
Event Cleaning				✓		
E_T^{miss} Trigger				✓		
E_T^{miss}	GeV			> 250		
N_{leptons} (baseline)				0		
$\min[\Delta\phi(\text{jet}_{1-4}, E_T^{\text{miss}})]$				> 0.4		
N_{jets}				≥ 4		
$N_{b-\text{jets}}$				≥ 3		
$\mathcal{S}_{\text{obj-based}}$		> 22	$\in [22, 24]$	$\in [24, 26]$	$\in [26, 28]$	> 28

8.3.5 Background Estimation

Due to the differing signal region definitions and the differences in the expected SM background composition and kinematics, dedicated control regions are built for each of the signal regions. Signal regions A and B are both dominated by $t\bar{t}$ from Monte-Carlo studies, contributing 73% and 68% of the SM expectation respectively. Due to the dominance of $t\bar{t}$ in these regions it is not necessary to develop control regions for the sub-leading backgrounds. The regions developed for $t\bar{t}$ control for SRA and SRB follow similar methodology, they are single-lepton regions with a selection on $m_T > 20$ GeV to remove background from multi-jet events with jets mis-identified as electrons. The regions aim to reflect as much as possible the kinematic selections of the signal regions. They are referred to as CRA_{1l} and CRB_{1l} . CRA is additionally subdivided into bins in m_{Eff} that reflect the m_{Eff} binning in SRA.

The expected SM contributions in SRC are more complex with 3 processes having significant contributions. Dominant is Z production in association with jets (Z+jets) where large missing energy results from the $Z \rightarrow \nu\bar{\nu}$ branching fraction ($\sim 42\%$). Sub-leading $t\bar{t}$ and single top contribute ~ 17 and 16% respectively. The strategy employed is to control the Z+jets in a 2-lepton SFOS control region ($CRC_{2l} - Z$) which exploits the $Z \rightarrow l\bar{l}$ decay where the leptons can be treated as invisible for event-level objects such as E_T^{miss} (denoted $\tilde{E}_T^{\text{miss}}$). A single-lepton control region is used to normalise both $t\bar{t}$ and single-top processes (CRC_{1l}). Additionally for the Z+jets control regions, binning is applied in $\mathcal{S}_{\text{obj-based}}$ to reflect the binning that is used in SRC.

All of the control region selections are summarised in table 8.25.

8.3 Bottom squark with multiple b-jets

Table 8.25: Selections for CR strategy. The letter appended to the CR label corresponds to the low, medium and high $m_{E_{miss}}$ selection for CRA.

Variable	Units	CRA_{1l}	CRA_{1l-L}	CRA_{1l-M}	CRA_{1l-H}	CRB_{1l}	CRC_{1l-top}	CRC_{2l-Z}
Event Cleaning						✓	✓	
$E_{T\text{miss}}$ trigger passed						-	-	
lepton trigger passed		-				✓		
$N_{\text{leptons}} (e, \mu)$ (baseline & signal)							2 (SFOS)	
N_{jets}								
$N_{b\text{-jets}}$								
m_T	[GeV]							
$E_{T\text{miss}}$	[GeV]							
$E_{T\text{l}}$	[GeV]							
$p_T(b_1)$	[TeV]							
$m_{E_{miss}}$								
leading jet non-b								
$ \Delta\phi(j_1 - E_{T\text{miss}}) $								
$\min[\Delta\phi(\text{jet}_{1-4}, E_{T\text{miss}})]$								
$\tilde{E}_{T\text{miss}}$	[rad]							
$m_{\ell\ell}$	[GeV]							
$S_{obj-based}$	[GeV]							

8.3.6 Validation of background estimation

For the A and B-type control regions, validation regions are designed with a 0-lepton selection to validate the extrapolation from 1 to 0-lepton requirements of the signal regions. They are kept orthogonal to the signal regions by requiring a different b-jet multiplicity. For the C-type validation, a similar approach is taken where 0-lepton validation regions are introduced. Orthogonality between the signal regions and the top validation region is achieved by inverting the SR selections on $S_{obj-based}$ and $\min[\Delta\phi(jet_{1-4}, E_T^{\text{miss}})]$. For the Z validation region, selections on the b-jet multiplicity and inverted $S_{obj-based}$ requirement with respect to the signal region ensure orthogonality and additional requirements on m_{CT} and $\min[\Delta\phi(jet_{1-4}, E_T^{\text{miss}})]$ increase the Z+jets purity in the region. The full selections of validation regions A and B and C are shown in table 8.26.

Table 8.26: Selections for 0 Lepton VR strategy for the A and B-type regions. For the A-type regions, the letter appended to the CR label corresponds to the low, medium and high m_{Eff} selection.

Variable	Units	$VR A_{0l}$	$VR A_{0l} - L$	$VR A_{0l} - M$	$VR A_{0l} - H$	$ VR B_{0l} $	$ VR C_{0l} - T $	$ VR C_{0l} - Z $	$ VR C_{0l} - Z - alt $
Event Cleaning			✓			✓			✓
E_T^{miss} trigger passed			✓			✓			✓
$N_{\text{leptons}}(e, \mu)$ (baseline & signal)		0		0		0		0	
N_{jets}		≥ 6		≥ 6		≥ 4		≥ 4	
$N_{b\text{-jets}}$		3	✓			✓		2	2
τ veto									
$\min[\Delta\phi(j_{\text{et}_1\text{-}4}, E_T^{\text{miss}})]$	[rad]								
leading jet non- b			-						
E_T^{miss}	[GeV]								
$S_{obj-based}$									
$p_T(j_1)$	[GeV]								
$p_T(b_1)$	[GeV]								
$ \Delta\phi(j_1 - E_T^{\text{miss}}) $	[rad]								
m_{Eff}	[TeV]	> 1	$\in [1, 1.5]$	$\in [1, 1.5]$	$\in [1.5, 2.0]$	> 2.0	$ > 1.0$	-	> 200
m_{CR}	[GeV]								-

8.3 Bottom squark with multiple b-jets

8 Searches for third generation squarks

8.3.7 Systematic Uncertainties

Detector-based, modeling and statistical uncertainties are all considered in the fit. Due to the close kinematic relationships between the background control regions and the signal regions, many of the systematics cancel significantly and are constrained for the dominant backgrounds. For the A and B-type signal regions, the theoretical uncertainties have the largest impact on the result, whereas in SRC, the impact of detector and modeling uncertainties are equal. In SRA and SRB the dominant detector effects are due to uncertainties in the b-tagging efficiency and mis-tag rate, and then sub-dominant is the jet energy scale and resolution effects. The largest modeling uncertainties are from $t\bar{t}$ parton shower and final state radiation (FSR) effects. In SRC, the dominant modeling uncertainties are the Z+jets (merging, factorisation and resummation scales) and sub-dominant $t\bar{t}$ and single-top (parton shower and FSR). The contributions are summarised in table 8.27.

Table 8.27: Expected background event yields and dominant systematic uncertainties on background estimates in the A-type (inclusive), B-type and C-type (inclusive) regions. Individual uncertainties can be correlated, and do not necessarily add up quadratically to the total background uncertainty. The percentages show the size of the uncertainty relative to the total expected background.

Region	SRA		SRB		SRC	
Total background expectation	17.1		3.3		37.9	
Total background uncertainty	2.8	(16%)	0.9	(27%)	6.2	(16%)
Systematic, experimental	1.4	(8%)	0.3	(10%)	3.0	(8%)
Systematic, theoretical	2.3	(13%)	0.6	(18%)	3.2	(8%)
Statistical, MC samples	0.7	(4%)	0.4	(12%)	2.0	(5%)

8.3.8 Results

Background-only Fit

The background-only, model-dependent and model-independent fits were performed and their results are summarised here. The yields in the control and signal regions for the background-only, null hypothesis test, in tables 8.28 and 8.29. In the signal regions, the expected yields of 3 benchmark signal points are also provided. Normalisation factors are extracted for each of the control regions and applied to the MC of the process which is normalised in the region, their effect is included in the fitted signal region background prediction. No significant excesses above the predicted event yield are observed. The largest deviations are small excesses of the order 1σ in the first $S_{obj-based}$ bin of SRC and the first m_{Eff} -bin of SRA.

The yields in the CRs, VRs and SRs are summarised graphically in figure 8.19, all the observed data yields show excellent agreement with the predicted SM MC.

8.3 Bottom squark with multiple b-jets

	CRA_{1l}	$CRA_{1l\text{-}L}$	$CRA_{1l\text{-}M}$	$CRA_{1l\text{-}H}$	CRB_{1l}
Observed events	224	153	52	19	42
Fitted bkg events	224.10 ± 14.96	150.1 ± 11.6	53.9 ± 5.5	20.1 ± 3.0	41.97 ± 6.47
Fitted ttbar events	182.49 ± 16.56	124.2 ± 12.4	43.0 ± 5.9	15.3 ± 3.0	36.29 ± 6.51
Fitted Z events	0.27 ± 0.07	0.2 ± 0.1	0.0 ± 0.0	$0.0^{+0.0}_{-0.0}$	0.11 ± 0.06
Fitted st events	14.77 ± 2.10	8.2 ± 1.3	4.4 ± 0.7	2.2 ± 0.2	2.08 ± 0.17
Fitted ttZ events	5.13 ± 0.99	3.7 ± 0.7	1.1 ± 0.3	0.3 ± 0.1	0.56 ± 0.11
Fitted ttW events	2.15 ± 0.37	1.0 ± 0.2	0.8 ± 0.1	0.3 ± 0.1	0.44 ± 0.07
Fitted ttH events	12.20 ± 3.92	8.7 ± 2.8	2.8 ± 1.0	0.7 ± 0.2	1.41 ± 0.43
Fitted W events	5.88 ± 1.87	3.6 ± 1.1	1.2 ± 0.5	1.1 ± 0.6	0.85 ± 0.15
Fitted diboson events	1.22 ± 0.51	0.4 ± 0.2	0.5 ± 0.5	0.3 ± 0.1	0.23 ± 0.03

Table 8.28: Background-only fit results for the inclusive A and B-type CR performed using 140.5fb^{-1} , the post-fit uncertainty shows the total statistical and systematic uncertainty. The individual bins in m_{Eff} are also shown.

No significant excess above the SM expectation is observed. Therefore limits on the BSM contributions to the data and on the specific models considered are calculated, these are summarised in section 8.4.

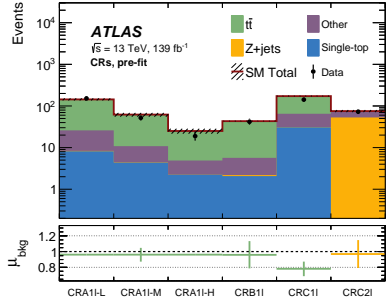
8 Searches for third generation squarks

Table 8.29: Background-only fit results for the A- and B-type regions (top table) and C-type regions (bottom table) performed using 139 fb^{-1} of data. The quoted uncertainties on the fitted SM background include both the statistical and systematic uncertainties.

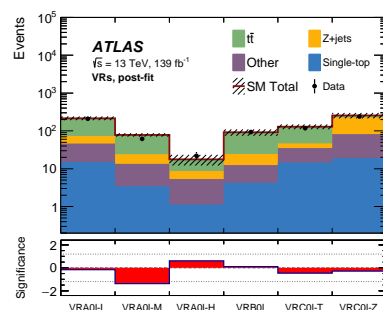
	SRA	SRA-L	SRA-M	SRA-H	SRB
Observed events	17	12	3	2	3
Fitted SM bkg events	17.1 ± 2.8	8.4 ± 1.7	5.7 ± 0.8	3.0 ± 1.5	3.3 ± 0.9
$t\bar{t}$	10.1 ± 2.5	4.7 ± 1.5	3.7 ± 0.6	1.7 ± 1.4	2.3 ± 0.8
Z+jets	2.6 ± 0.4	1.3 ± 0.2	0.9 ± 0.2	0.4 ± 0.1	0.3 ± 0.1
Single-top	1.4 ± 0.3	0.4 ± 0.1	0.3 ± 0.1	0.6 ± 0.2	0.5 ± 0.1
ttV	1.2 ± 0.3	0.7 ± 0.1	0.3 ± 0.1	0.1 ± 0.0	0.07 ± 0.02
$t\bar{t} + h$	1.1 ± 0.2	0.7 ± 0.1	0.3 ± 0.1	0.1 ± 0.0	0.13 ± 0.02
W+jets	0.4 ± 0.1	0.2 ± 0.1	0.1 ± 0.0	–	0.02 ± 0.01
Diboson	0.4 ± 0.1	0.3 ± 0.1	–	–	–
$m(\tilde{b}, \tilde{\chi}_2^0, \tilde{\chi}_1^0) = (1100, 330, 200)\text{ GeV}$	13.7 ± 0.3	0.7 ± 0.1	6.3 ± 0.2	6.6 ± 0.2	0.3 ± 0.1
$m(\tilde{b}, \tilde{\chi}_2^0, \tilde{\chi}_1^0) = (700, 680, 550)\text{ GeV}$	1.3 ± 0.6	0.2 ± 0.1	0.5 ± 0.4	0.6 ± 0.4	7.4 ± 1.2
$m(\tilde{b}, \tilde{\chi}_2^0, \tilde{\chi}_1^0) = (1200, 1150, 60)\text{ GeV}$	8.7 ± 0.2	1.4 ± 0.1	3.4 ± 0.1	3.8 ± 0.1	0.6 ± 0.1
	SRC	SRC22	SRC24	SRC26	SRC28
Observed events	47	28	12	4	3
Fitted SM bkg events	37.9 ± 6.2	21.2 ± 4.1	10.6 ± 2.3	3.7 ± 0.9	2.4 ± 0.6
$t\bar{t}$	5.4 ± 2.6	3.9 ± 2.3	1.1 ± 0.6	0.3 ± 0.3	0.1 ± 0.1
Z+jets	17.6 ± 4.7	8.8 ± 2.5	6.0 ± 1.8	1.7 ± 0.7	1.1 ± 0.4
Single-top	5.0 ± 1.5	2.7 ± 1.0	1.2 ± 0.3	0.7 ± 0.2	0.4 ± 0.1
ttV	4.3 ± 0.6	2.5 ± 0.4	1.1 ± 0.2	0.5 ± 0.1	0.2 ± 0.1
$t\bar{t} + h$	0.2 ± 0.0	0.2 ± 0.0	–	0.1 ± 0.0	0.0 ± 0.0
W+jets	3.5 ± 0.8	2.2 ± 0.5	0.6 ± 0.2	0.2 ± 0.1	0.4 ± 0.1
Diboson	1.8 ± 0.3	0.9 ± 0.2	0.6 ± 0.1	0.2 ± 0.0	0.1 ± 0.1
$m(\tilde{b}, \tilde{\chi}_2^0, \tilde{\chi}_1^0) = (1100, 330, 200)\text{ GeV}$	0.4 ± 0.1	0.3 ± 0.1	0.1 ± 0.0	0.03 ± 0.02	0.03 ± 0.01
$m(\tilde{b}, \tilde{\chi}_2^0, \tilde{\chi}_1^0) = (700, 680, 550)\text{ GeV}$	1.2 ± 0.5	0.5 ± 0.2	0.7 ± 0.4	–	–
$m(\tilde{b}, \tilde{\chi}_2^0, \tilde{\chi}_1^0) = (1200, 1150, 60)\text{ GeV}$	26.7 ± 0.3	6.3 ± 0.2	6.4 ± 0.2	5.8 ± 0.2	8.3 ± 0.2

8.4 Third generation SUSY limits

(a) Control region yields for all regions, the lower panel shows the background normalisation value extracted in the fit.



(b) Validation region yields for all regions, the lower panel shows the significance of any deviation of the data with respect to the prediction.



(c) Signal region yields for all regions, the lower panel shows the significance of any deviation of the data with respect to the prediction.

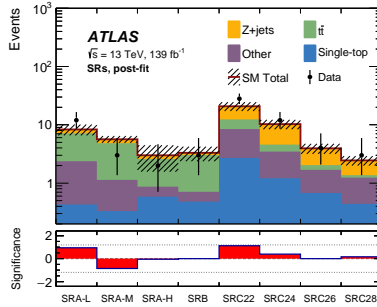


Figure 8.19: Summary of the yields for all regions in the background-only fit. The lower panel shows the most relevant information concerning the deviation between observed data and predicted SM yields in each region.

8.4 Third generation SUSY limits

The limits from the analysis described in sections 8.2 and 8.3 are summarised here for the model-dependent fits and the model-independent fits as described in section 7.1.2.

Model-Dependent Fit

Model-dependent fits were run considering all signal points shown in figure 8.13 for the multi b-jets analysis and the points in figure 8.3 and table 8.1 for the bbMeT analysis. For each separate fit, the signal point considered is included and a CLs value is calculated as described in section 7.1.2. Using the CLs values a 95% confidence level contour is determined by interpolating between the signal points. The limits for the bottom squark multi-b decay channel are shown for the DM130 and M60 grids in figure 8.20.

The limits for the bottom squark direct decay channel are shown in two different planes. Figure 8.21(b) shows the limit in the plane of $m_{\tilde{b}}^0$ vs $m_{\tilde{\chi}_1^0}$. 8.21(a) shows the limit in the plane of $m_{\tilde{b}}^0$ vs $\Delta m_{\tilde{b}, \tilde{\chi}_1^0}$ which highlights the gain in the compressed regions. Uncertainties on the cross-section of the signal

8 Searches for third generation squarks

process are calculated. In the bottom squark limit these are shown as $\pm 1\sigma$ lines around the resulting limit.

The dark matter limits show the maximum cross-section at 95% CLs in figure 8.22 for the scalar and pseudo-scalar mediator cases. In the dark matter limit the cross-section uncertainties are shown as a red band around the line at $\sigma/\sigma(g=1)$. Again the overlapping regions of sensitivity for the low-mass and high-mass targeted signal regions are used based on the best expected sensitivity to a given signal point.

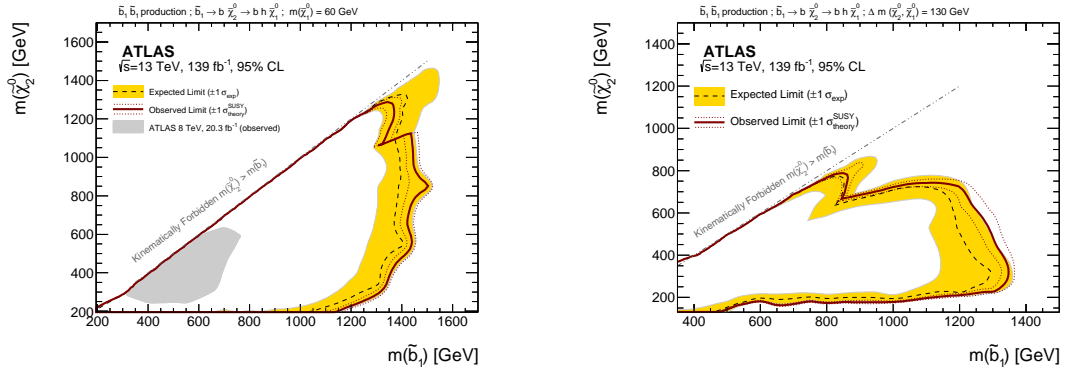


Figure 8.20: 95% confidence level exclusion contours for the M60 and DM130 signal hypothesis grids. In the regions where the sensitivity of the alternative signal regions, SRB and SRC, overlaps with SRA, the best expected (using SM MC prediction only) signal region is used to determine the CLs value for each point. Since the regions are not statistically independent, they cannot be combined.

The results presented here contribute considerably towards the overall limits proposed by ATLAS on sbottom pair production scenarios shown in figure 8.23. They also are competitive with the limits from the LHC's other general purpose detector, CMS, which are given for comparison in figure 8.24. The ATLAS results widen the targeted bottom squark channel beyond the direct decay into more complex decay chains. For the results targeting the same decay chain, the reach of the ATLAS and CMS analyses are equivalent.

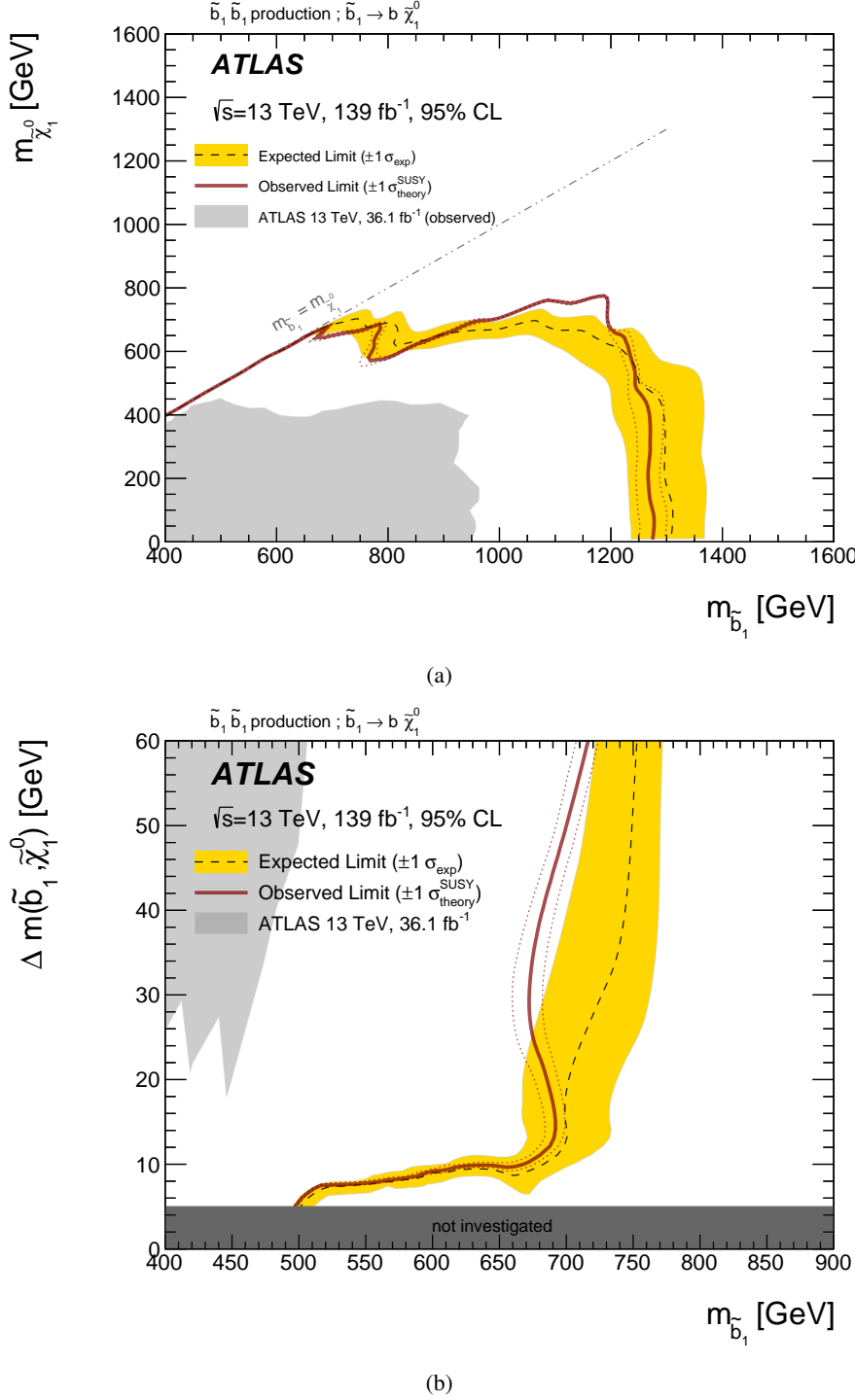


Figure 8.21: Exclusion limits at 95% CL on the masses of the \tilde{b} and $\tilde{\chi}_1^0$ displayed in the (a) $(m_{\tilde{b}}, m_{\tilde{\chi}_1^0})$ and (b) $(m_{\tilde{b}}, \Delta m_{\tilde{b}, \tilde{\chi}_1^0})$ planes. The dashed line and the shaded band are the expected limit and its $\pm 1\sigma$ uncertainty, respectively. The thick solid line is the observed limit for the central value of the signal cross-section. Regions excluded by previous analyses [97] are shaded in light grey, while the region with $\Delta m_{\tilde{b}, \tilde{\chi}_1^0} < 5 \text{ GeV}$, not investigated in this analysis, is shaded in dark grey.

8 Searches for third generation squarks

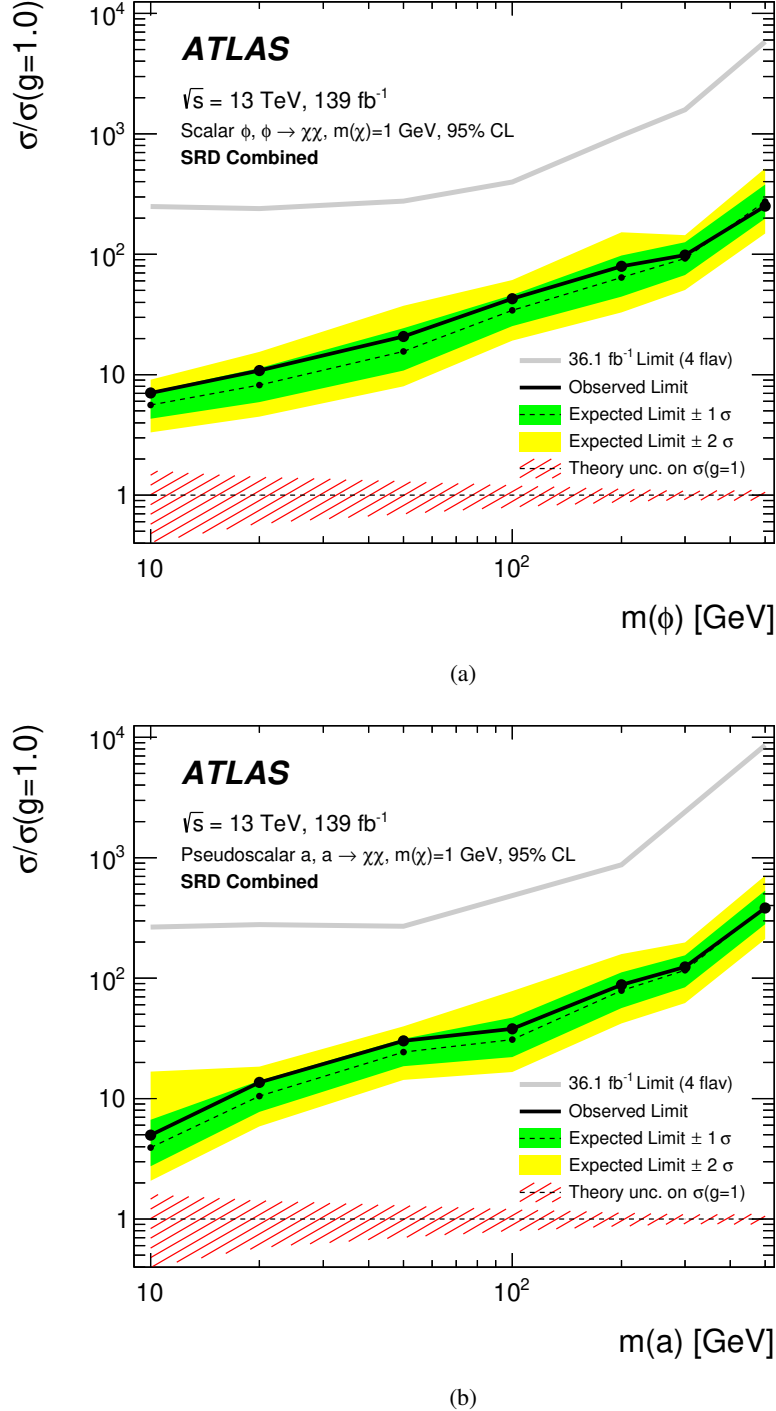


Figure 8.22: 95% CL limits on the cross-section for the models of dark matter production mediated by a (a) scalar or (b) pseudoscalar mediator. The dashed line and the shaded band are the expected limit and its $\pm 1\sigma$ and $\pm 2\sigma$ uncertainties, respectively. The thick solid line is the observed limit for the central value of the signal cross-section. The grey line shows the limit from previous results [98]. The hatched red band shows the uncertainty of the model cross-section.

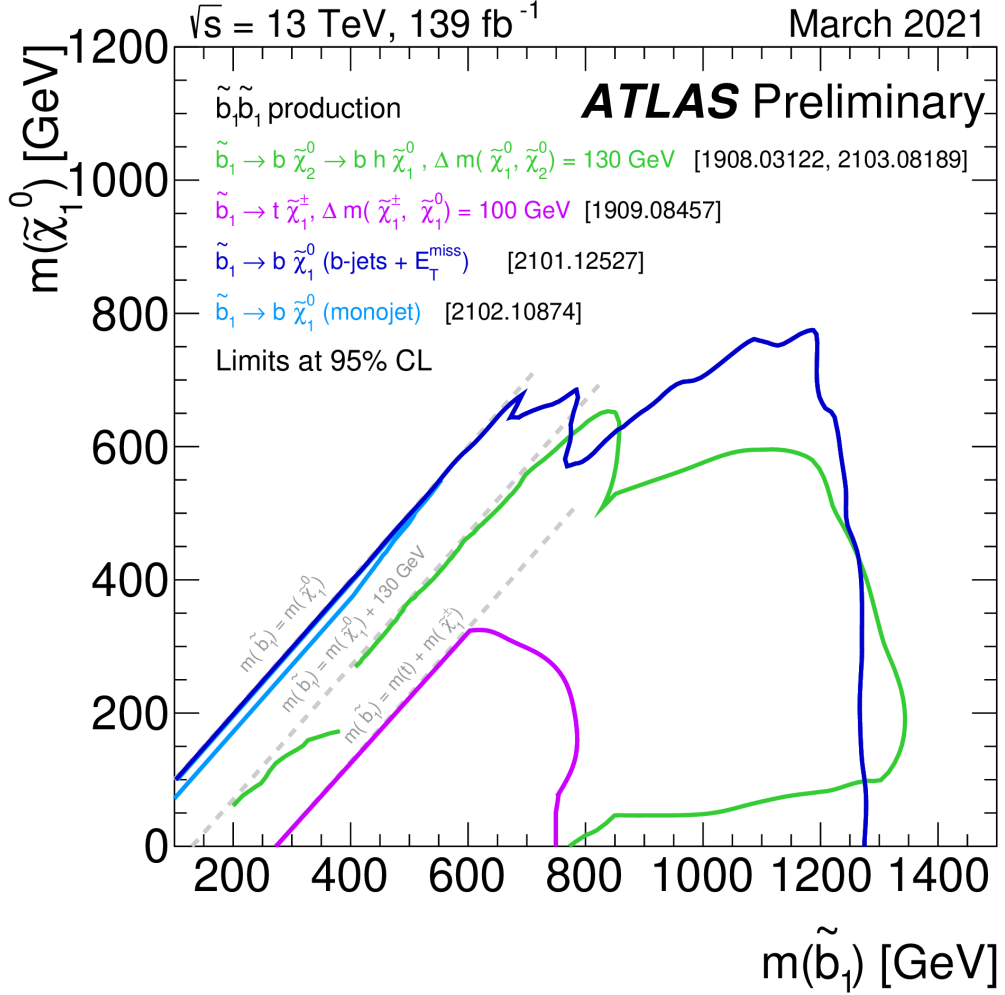


Figure 8.23: 95% CL limits on bottom squark pair production considering several final state scenarios analysed from data collected with the ATLAS detector. The results presented in this thesis are shown for the analysis described in section 8.3 by the dark blue line which is combined with a complimentary analysis that targets final states where the higgs decays to hadronic τ leptons [99]. The analysis described in section 8.2 is shown by the green line. Additional contributing results are shown for the case where the bottom squark decays via a top quark [100] by the purple line and for the mono-jet analysis by the light blue line [101].

8 Searches for third generation squarks

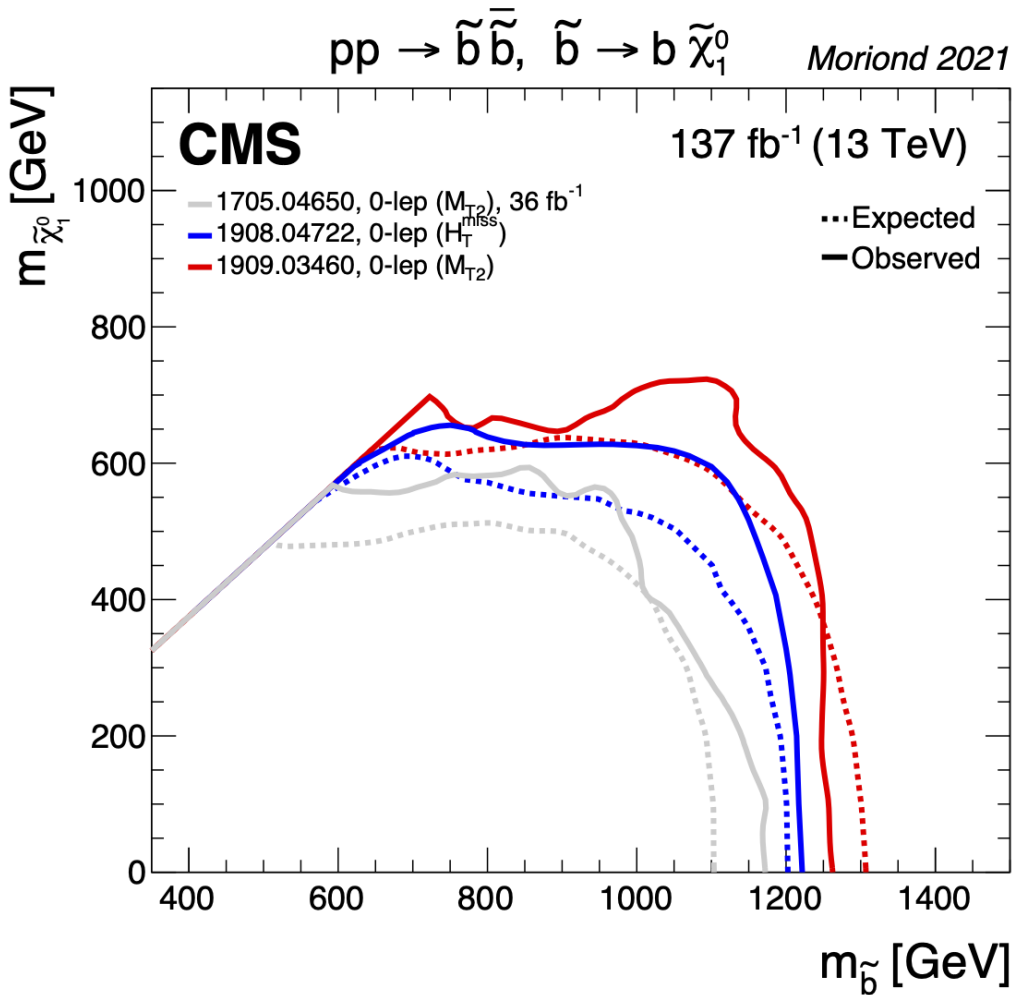


Figure 8.24: 95% CL limits on bottom squark pair production analysed from data collected by the CMS detector. The grey and red lines show results for Run 1 [102] and Run 2 [103] analyses studying the m_{T2} variable and blue line shows the Run 2 result studying the E_T^{miss} [104] variable.

8.4 Third generation SUSY limits

Model-Independent Fit

As described in section 7.1.2, this fit includes the control and signal regions but with no signal contribution included. In the multi- b analysis SRB is used as in the model-dependent fit, however SRA and SRC use the inclusive versions of the selections (gathering together all the bins in m_{Eff} and $\mathcal{S}_{obj-based}$). For the bbMeT analysis, the regions used are the discovery regions that are defined in the SR definition tables. 95% CL upper limits on possible signal cross-sections are derived for each SR, these are shown in table 8.30 and 8.31 respectively for the two analyses along with the confidence level for the null background-only hypothesis and discovery p -value for new BSM contributions.

Table 8.30: From left to right, observed 95% CL upper limits on the visible cross sections σ_{vis} , the observed (S_{obs}^{95}) and expected (S_{exp}^{95}) 95% CL upper limits on the number of signal events with $\pm 1\sigma$ excursions of the expectation, the CL of the background-only hypothesis, CL_B , the discovery p -value (p_0), truncated at 0.5, and the associated significance (in parentheses).

Signal channel	σ_{vis} [fb]	S_{obs}^{95}	S_{exp}^{95}	CL_B	$p_0 (Z)$
SRA	0.06	9.0	$10.1^{+4.7}_{-3.1}$	0.38	0.50 (0.00)
SRB	0.04	4.9	$5.1^{+2.8}_{-1.7}$	0.45	0.50 (0.00)
SRC	0.19	26.0	$20.8^{+7.0}_{-5.5}$	0.80	0.17 (0.97)

Table 8.31: Left to right: SM expectation from background-only fit for the model-independent regions, 95% CL upper limits on the visible cross-section ($\langle \epsilon \sigma \rangle_{obs}^{95}$), on the observed (S_{obs}^{95}) and expected (S_{exp}^{95}) number of signal events. The last two columns indicate the CL_B value, i.e. the confidence level observed for the background-only hypothesis, and the discovery p -value ($p(s = 0)$) capped at a value of 0.5.

Signal channel	Obs.	SM exp.	$\langle \epsilon \sigma \rangle_{obs}^{95}$ [fb]	S_{obs}^{95}	S_{exp}^{95}	CL_B	$p(s = 0) (Z)$
$SRA_{mct250i}$	552	555 ± 75	0.94	131	133^{+47}_{-35}	0.48	0.49 (0.03)
$SRA_{mct350i}$	104	120 ± 16	0.17	24	32^{+8}_{-9}	0.19	0.5 (0)
$SRA_{mct450i}$	23	27.1 ± 3.8	0.06	8.7	$12.3^{+5.5}_{-3.7}$	0.17	0.5 (0)
$SRA_{mct550i}$	7	10.4 ± 1.7	0.04	5.6	$8.1^{+3.9}_{-2.3}$	0.14	0.5 (0)
$SRA_{mct650i}$	8	5.6 ± 1.4	0.06	8.5	$6.7^{+3.4}_{-2.0}$	0.73	0.24 (0.72)
SRB	22	20.6 ± 4.6	0.11	15.3	$14.8^{+5.2}_{-3.2}$	0.54	0.40 (0.26)
$SRC - 2b$	58	44.4 ± 5.8	0.22	30.3	$20.7^{+8.1}_{-5.6}$	0.88	0.09 (1.33)
$SRC - 1b1v$	43	51 ± 10	0.13	17.6	$21.2^{+8.2}_{-5.8}$	0.28	0.5 (0)
$SRC - 0b1v$	151	148 ± 25	0.37	51	50^{+18}_{-13}	0.54	0.48 (0.2)
$SRD - low$	497	381 ± 76	1.8	250	155^{+65}_{-60}	0.91	0.07 (1.48)
$SRD - high$	320	242 ± 66	1.4	195	140^{+48}_{-44}	0.82	0.13 (1.13)

9 Searches for Electro-Weak SUSY

Although the production cross-sections for electroweak SUSY are low, the large dataset collected by the LHC and ATLAS searches enable us to gain sensitivity to many scenarios. In naturalness-motivated scenarios, if the electroweak superpartners are light they can provide an explanation for the g-2 discrepancy. For this reason, electroweak SUSY searches are a vital part of the research conducted with the ATLAS detector. This section describes the analysis of the pair production of the lightest chargino, $\tilde{\chi}_1^\pm$, along with the second-lightest neutralino, $\tilde{\chi}_2^0$.

9.1 Signal Model

If the sleptons are heavier than the electroweakinos then the $\tilde{\chi}_1^\pm$ can decay via $\tilde{\chi}_1^\pm \rightarrow W\tilde{\chi}_1^0$ and the $\tilde{\chi}_2^0$ can decay via $\tilde{\chi}_2^0 \rightarrow h\tilde{\chi}_1^0$. As discussed in section 2.2.6, in the MSSM when the mass-splitting between the chargino and lightest neutralino is large enough, the decay via the higgs becomes the dominant decay. The Feynman graph for this process is shown in figure 9.1. Many final states provide sensitivity to this signal using the Higgs as a handle, here we focus on leptonic decays of the $W \rightarrow l\nu$ where l is an electron or muon and ν is an electron or muon neutrino, and the Higgs decays to b-quarks $h \rightarrow b\bar{b}$ which exploits the largest branching fraction of any Higgs decay. The model is a simplified model and adheres to the same assumptions described in section 8.1.

The resulting final state contains 2 b -jets from the Higgs decay, a single lepton from the W decay and large missing transverse momentum largely from the $\tilde{\chi}_1^0$ pair with a smaller component from the neutrino. The masses of the sparticles are the free parameters of the model although the $\tilde{\chi}_2^0$ and $\tilde{\chi}_1^\pm$ are considered mass degenerate. The phase-space is spanned by $m_{\tilde{\chi}_1^\pm/\tilde{\chi}_2^0}$ and $m_{\tilde{\chi}_1^0}$ with the constraint that the mass difference between them is such that, $\Delta m(\tilde{\chi}_1^\pm/\tilde{\chi}_2^0, \tilde{\chi}_1^0) > 130$ GeV, to allow an on-shell higgs intermediate.

The analysis strategy for targeting this model is split into two parts: firstly an approach based on exploiting selections and binned fits in the mass-scale variables is described. The aim of this first analysis is to gain sensitivity to a broad coverage of signal mass hypotheses. This is referred to as the *selection-based* analysis. Secondly, an approach targeting lower E_T^{miss} using ML techniques is described. The ML approach aims to recover sensitivity in highly compressed scenarios where the mass difference $\Delta m(\tilde{\chi}_1^\pm/\tilde{\chi}_2^0, \tilde{\chi}_1^0) \sim m(h)$ such that the process is just kinematically viable. This is referred to as the *ML* analysis.

The ML-based analysis is in the final stage of extracting the results, as a result the final conclusions are not presented here but instead the approach and predicted sensitivity are described. For this reason,

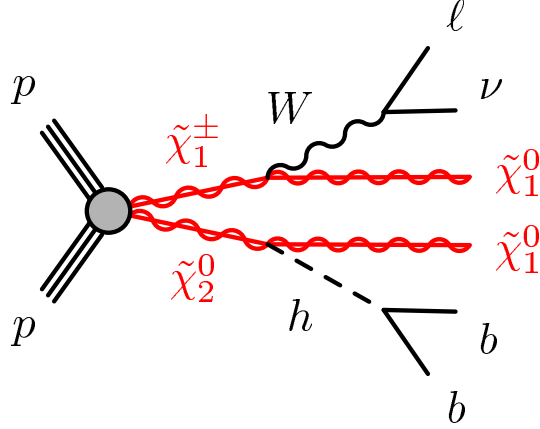


Figure 9.1: A diagram illustrating the signal scenario considered for the production of $\tilde{\chi}_1^\pm$ and a $\tilde{\chi}_2^0$ decaying via W and Higgs respectively.

the data yields in the signal regions are not shown. The work is however in a mature state and the presentation here will not differ to a large degree from the final result.

Personal contributions to the selection-based analysis outlined in section 9.2 include: developments towards the signal region selections and contributions towards the evaluation of systematic uncertainties.

Personal contributions towards the ML-based analysis outlined in selection 9.3 include: Development and validation of the analysis software for processing the data and MC simulation to extract analysis information, development of the ML approach and related software, training and deployment of the model and optimisation of selections for all regions considered and development and maintenance of the software for statistical analysis.

9.2 Selection-based Analysis

9.2.1 Event Selection

The data events are selected using E_T^{miss} triggers (with a required reconstructed E_T^{miss} greater than 240 GeV), exactly one lepton with $p_T > 7(6)$ GeV for electrons (muons), 2-3 jets with $p_T > 30$ GeV with exactly 2 b-tagged and the invariant mass of the b-jet pair to be in the window of 100-140 GeV, to target reconstruction of the Higgs mass. This selection forms the basis of the signal regions.

To gain sensitivity to the full phase-space of sparticle masses the selection is then subdivided into 3 regions targeting low, medium and high mass splittings. The differentiation between the signal mass splittings is with the m_T variable which tends to have higher values for higher $\Delta m(\tilde{\chi}_1^\pm/\tilde{\chi}_2^0, \tilde{\chi}_1^0)$. The sensitivity is gained by further splitting the signal regions by m_{CT} which is calculated using the 2-bjets

Observable	SR LM	SR MM	SR HM
N_{lep}	1	1	1
$N_{b\text{-jet}}$	2	2	2
m_{bb} GeV	[100–140]	[100–140]	[100–140]
N_{jet}	2 or 3	2 or 3	2 or 3
E_T^{miss} GeV	> 240	> 240	> 240
$m(\ell, b_1)$ GeV	–	–	> 120
m_T GeV (excl.)	[100 – 160]	[160 – 240]	[> 240]
	[180 – 230]	[180 – 230]	[180 – 230]
m_{CT} GeV (excl.)	[230 – 280] [> 280]	[230 – 280] [> 280]	[230 – 280] [> 280]
m_T GeV (disc.)	> 100	> 160	[> 240]
m_{CT} GeV (disc.)		> 180	

Table 9.1: Definition of 9 SRs, binned both in m_T and m_{CT} , resulting in a two-dimensional shape fit. The exclusion-specific selections for the model-dependent fit are denoted excl. The discovery region definitions are denoted disc.

as the visible objects producing 9 signal region bins. The signal regions are orthogonal to one another by the m_T requirements so that they can be simultaneously fit for greater coverage of the parameter space. Additionally the high-mass signal region benefits from a requirement on the invariant mass of the lepton and the leading b-jet. Table 9.1 outlines the selections. For the model-independent fit only single bin signal regions are used, taking the lower bound of the bins from the exclusive selection.

9.2.2 Background Estimation

The selections used in this analysis are similar to those from the previous Run 1 result [105]. The significant backgrounds from that result are the same as here: semi-leptonic $t\bar{t}$ is dominant with sub-dominant single top and W+jets production. The control regions are built to constrain these backgrounds through normalisation factors in the fit. The CRs use the same selections on the jets and leptons as the signal regions but are orthogonal due to an inverted m_{bb} window, they are made orthogonal to one another through the selections on m_T and m_{CT} . The $t\bar{t}$ CRs use the same m_T binning as the signal region, extracting three independent normalisation factors for each bin. The selections are summarised in table 9.2 where the jet and lepton selections are not shown.

As the control regions differ only in kinematics from the signal region selections, it is important to validate the extrapolation over m_{bb} and m_{CT} for the $t\bar{t}$ normalisation and m_T for single-top and W+jets. Validation regions are designed both inside the Higgs window of m_{bb} and outside to validate

9 Searches for Electro-Weak SUSY

Observable	CRW	CRST	CRT-LM	CRT-MM	CRT-HM
m_{bb} [GeV]	[50 – 90]	> 195		[50 – 140] $\parallel > 140$	
E_T^{miss} [GeV]	> 240	> 240		> 240	
$m(\ell, b_1)$ [GeV]	–	–	–	–	> 120
m_T [GeV]	[50 – 100]	< 100	[100 – 160]	[160 – 240]	[> 240]
m_{CT} [GeV]	> 180	> 180		< 180	

Table 9.2: Control region definitions. As preselections, 1 lepton, 2-3 jets and 2 b-jets are also required. The selection criteria that make the regions orthogonal are highlighted.

extrapolation over m_T and m_{CT} . They are binned in m_T (Low, Medium and High) as with the signal regions.

9.2.3 Systematic Uncertainties

Detector, statistical and modeling based systematics are used. For the backgrounds normalised in the control regions, the systematics affect the normalisation uncertainty and transfer factors to the signal regions and cancel considerably. The dominant modeling uncertainties come from parton shower uncertainties in $t\bar{t}$ evaluated using an alternative showering code, and single-top hard scatter uncertainties calculated using an alternative generator. As the single-top and $t\bar{t}$ samples are produced separately there is an interference effect that must be considered. The interference is either dealt with via a *diagram-subtraction* or *diagram-removal* procedure [106] neither of which models the data perfectly. The proper treatment requires an inclusive modeling of $W + b\bar{b}$ production but this MC is not yet available. Therefore a systematic is taken as a two-point variation between the two diagram procedures. The dominant detector-related effects come from jet energy scale and resolution uncertainties [107] and modeling of E_T^{miss} terms and pile-up. Sub-leading uncertainties related to the MC statistics in the signal regions also contribute.

9.2.4 Results

Background-only Fit

A background-only fit was performed where only the CRs are involved in the fit. The resulting yields for the signal regions for the background-only fit are shown in table 9.3, the CRs in 9.4. The yields are summarised in figure 9.2 including the breakdown for the exclusion SR bins, with the significance of deviation from the background-only hypothesis shown in the bottom panel. Good agreement is observed between the predicted and observed yields with a small excess observed in some of the signal regions of order 1.5σ . Though this was deemed not to be significant, it does impact the model-dependent limit, where the observed limit is below the expected.

As no significant deviation from the SM expected background yields were observed, limits on the models and the possible BSM contribution to the signal regions are shown in section 9.4.

9.2 Selection-based Analysis

SR-LM	Low m_{CT}	Medium m_{CT}	High m_{CT}
Observed	16	11	7
Expected	8.8 ± 2.8	11.3 ± 3.1	7.3 ± 1.5
$t\bar{t}$	4.4 ± 2.2	7.3 ± 2.5	4.6 ± 1.2
Single top	1.3 ± 1.1	$0.9^{+1.0}_{-0.9}$	0.6 ± 0.6
$W+jets$	2.0 ± 0.9	2.4 ± 1.3	1.1 ± 0.5
Di-/Multiboson	0.39 ± 0.13	$0.09^{+0.11}_{-0.09}$	0.18 ± 0.04
Others	0.81 ± 0.25	0.64 ± 0.15	0.77 ± 0.12
SR-MM	Low m_{CT}	Medium m_{CT}	High m_{CT}
Observed	4	7	2
Expected	4.6 ± 1.7	2.6 ± 1.3	1.4 ± 0.6
$t\bar{t}$	1.6 ± 0.9	0.8 ± 0.7	0.30 ± 0.24
Single top	1.6 ± 1.5	$1.0^{+1.1}_{-1.0}$	$0.15^{+0.19}_{-0.15}$
$W+jets$	0.6 ± 0.4	$0.3^{+0.4}_{-0.3}$	0.57 ± 0.26
Di-/Multiboson	0.09 ± 0.04	0.065 ± 0.028	0.14 ± 0.06
Others	0.69 ± 0.20	0.40 ± 0.13	0.24 ± 0.09
SR-HM	Low m_{CT}	Medium m_{CT}	High m_{CT}
Observed	6	5	3
Expected	4.1 ± 1.9	2.9 ± 1.3	1.1 ± 0.5
$t\bar{t}$	0.8 ± 0.4	0.36 ± 0.25	0.22 ± 0.15
Single top	$0.9^{+1.5}_{-0.9}$	0.9 ± 0.9	$0.16^{+0.26}_{-0.16}$
$W+jets$	1.9 ± 0.8	1.4 ± 0.8	0.45 ± 0.19
Di-/Multiboson	0.057 ± 0.025	0.075 ± 0.027	0.08 ± 0.04
Others	0.34 ± 0.09	0.19 ± 0.08	0.21 ± 0.08

Table 9.3: Background fit results for the exclusion SR regions. The errors shown are the statistical plus systematic uncertainties. Uncertainties in the fitted yields are symmetric by construction, except where the negative error is truncated at an event yield of zero.

9 Searches for Electro-Weak SUSY

CR channel	CRTL M	CRTMM	CRTHM	CRW	CRST
Observed events	657	491	641	144	155
Fitted bkg events	666 ± 25	480 ± 21	645 ± 26	143 ± 12	154 ± 15
Fitted ttbar events	560 ± 40	430 ± 33	550 ± 40	47 ± 9	59 ± 12
Fitted singletop events	60 ± 40	27 ± 23	33 ± 27	5 ± 4	57 ± 22
Fitted wjets events	34 ± 8	10.5 ± 2.8	44 ± 11	83 ± 16	23 ± 6
Fitted diboson events	4.3 ± 1.2	2.0 ± 0.5	2.8 ± 0.5	5.6 ± 1.0	2.8 ± 0.9
Fitted multiboson events	0.007 ± 0.005	0.0025 ± 0.0011	0.011 ± 0.004	0.0020 ± 0.0005	0.0041 ± 0.0013
Fitted vh events	0.096 ± 0.019	$0.011^{+0.012}_{-0.011}$	0.053 ± 0.012	1.21 ± 0.26	0.052 ± 0.011
Fitted Z+jets events	1.02 ± 0.21	0.31 ± 0.14	0.60 ± 0.14	0.94 ± 0.29	0.86 ± 0.19
Fitted $t\bar{t}$ V events	8.8 ± 1.2	9.8 ± 1.4	9.7 ± 1.4	0.20 ± 0.06	11.0 ± 1.5
Fitted tth events	0.63 ± 0.08	0.52 ± 0.07	0.66 ± 0.08	0.078 ± 0.023	0.45 ± 0.06

Table 9.4: Background fit results for the , TRM, TRH, WCR and STCR region(s), for an integrated luminosity of 140.5 fb^{-1} . The errors shown are the statistical plus systematic uncertainties. Uncertainties on the fitted yields are symmetric by construction, where the negative error is truncated when reaching to zero event yield.

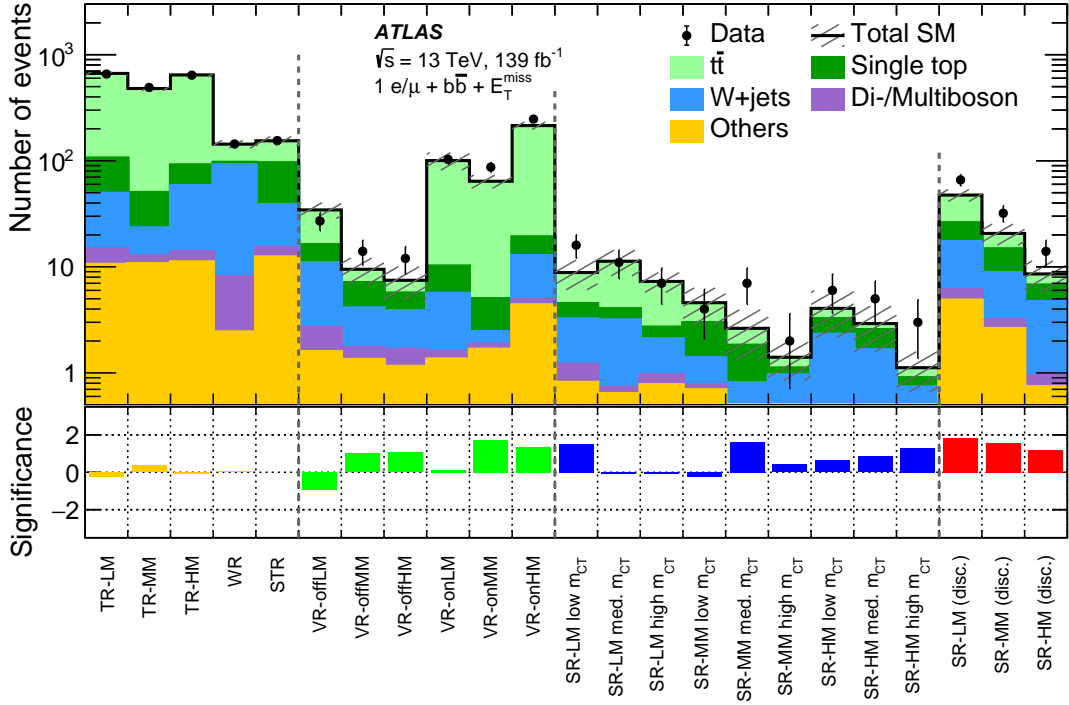


Figure 9.2: Comparison of the observed and expected event yields in control, validation, exclusion, and discovery signal regions. The bottom panel shows the significance of the differences between the observed and expected yields.

9.3 ML Analysis

9.3.1 Event Selection

The analysis in section 9.2 is the first result targeting this signal model and final state using the full Run 2 dataset and aims to give good coverage of the phase-space. The aim of the ML-based analysis is to compliment the selection-based result using more complex or dedicated techniques to improve the sensitivity in specific areas of phase-space.

This analysis targets the compressed scenarios where the mass splitting $\Delta m(\tilde{\chi}_1^\pm/\tilde{\chi}_2^0, \tilde{\chi}_1^0)$ is small but still kinematically viable for decay to Higgs - $\Delta m(\tilde{\chi}_1^\pm/\tilde{\chi}_2^0, \tilde{\chi}_1^0) \lesssim 200$ GeV. This area of phase-space is highly motivated as a natural solution to the g-2 anomaly but is difficult to gain sensitivity despite relatively large cross-sections for the signal points. The difficulty lies in the fact that the visible final state particles tend to have low momenta-reducing the efficiency of reconstruction. In addition, mass-scale related variables m_{CT} and m_T do not have the same extended tails which are relied upon for extracting sensitivity in the selection-based analysis, instead the kinematics are similar to the background SM processes.

Despite this, the signal still has some features that make it distinguishable from the SM backgrounds which lie in the correlations between variables. To extract these difference we use machine-learning classifier techniques to produce signal classification scores against the SM backgrounds which can then be used as a variable for extracting sensitivity. Similarly to section 8.2.1 gradient boosted decision trees using the algorithm XGBoost are implemented. The BDT development is similar to 8.2.1, the dominant SM background processes, $t\bar{t}$, single-top and W+jets are assigned categories, minor backgrounds are grouped into a 'other' category. Signal MC samples that satisfy the requirement $\Delta m(\tilde{\chi}_1^\pm/\tilde{\chi}_2^0, \tilde{\chi}_1^0) \leq 200$ GeV are grouped together to form the signal category, such that the BDT produces 5 output scores. A pre-selection is applied to all samples before training, in addition to the use of ML techniques, the trigger strategy is modified with respect to the selection-based analysis by switching to single-lepton triggers which have higher acceptance for the compressed signal points. To remove the contribution from multi-jet interactions where jets are mis-identified as leptons, a requirement on $S_{obj-based} > 5$ is applied. The pre-selection is given in table 9.5.

A similar training procedure is used as 8.2.1, the MC is split into 80%/20% train and validation samples, the model develops until the validation loss stops decreasing. The overtraining check using the KS-score described in 8.2.1 is also performed. The input variables to the BDT are summarised in table 9.6.

Before training, the modeling of the input variables are verified by comparing the input variable distributions of the SM backgrounds with data and also comparing the liner correlations (defined in equation 8.3) between the most important six variables used in the BDT in SM backgrounds and data. To understand the impact of the input variables on the BDT output, in order to determine the most important variables, the trained BDT is evaluated calculating SHAP scores [108] for each input variable and output classification, figure 9.3.

9 Searches for Electro-Weak SUSY

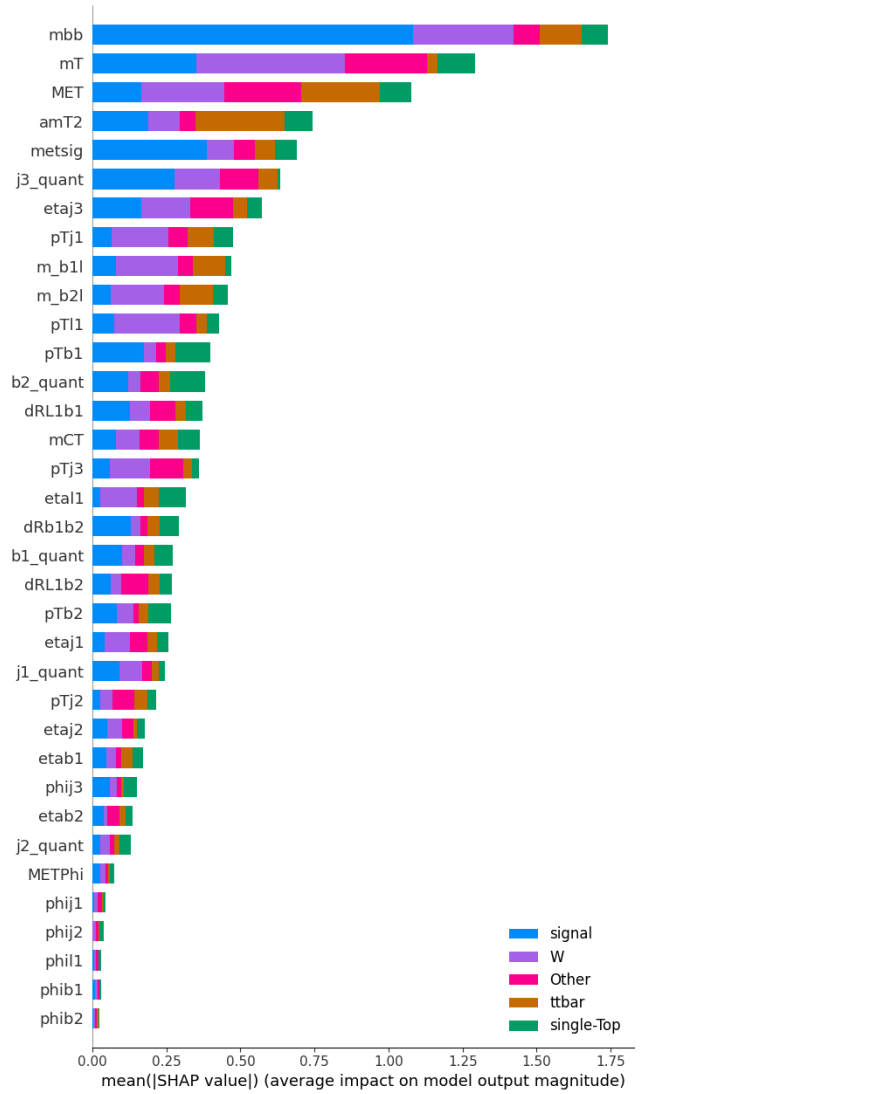


Figure 9.3: Feature importance of each of the most impactful variables used in the BDT broken down by class. The impact is based on the SHAP score which evaluates the effect of the model incorporating a variable vs not incorporating the variable, relative to other variables used [108].

Observable	pre-selection
N_{lep}	1
$N_{b\text{-jet}}$	≥ 2
m_{bb} [GeV]	[50–200]
N_{jet}	2 or 3
$E_{\text{T}}^{\text{miss}}$ [GeV]	> 50
$\mathcal{S}_{obj\text{-based}}$	> 5

Table 9.5: Definition of the pre-selection that is applied in the ML-based analysis used to select MC samples for training the BDT.

ML variable inputs
Object-level variables:
p_T^l, η^l, ϕ^l
$p_T^{b_1}, \eta^{b_1}, \phi^{b_1}$
$p_T^{b_2}, \eta^{b_2}, \phi^{b_2}$
$p_T^{j_3}, \eta^{j_3}, \phi^{j_3}$
$b_1^{quantile}, b_2^{quantile}$
$b_1^{j_1 quantile}, b_2^{j_2 quantile}, b_3^{j_3 quantile}$
Event-level variables:
m_{bb}
m_{CT}
m_T
$E_{\text{T}}^{\text{miss}}$
$\phi(E_{\text{T}}^{\text{miss}}) am_{\text{T2}}$
$\mathcal{S}_{obj\text{-based}}$
n_{Jets}
$\Delta R_{b_1, b_2}$
m_{b1l}
m_{b2l}
$\Delta R_{l, b_1}$
$\Delta R_{l, b_2}$

Table 9.6: The input variables for the XGBoost algorithm. Split into object-level and event-level variables.

Figure 9.3 shows some rather intuitive results for the dominant variables. The m_{bb} has the greatest impact in the signal output score as would be expected, with the m_T and $\mathcal{S}_{obj\text{-based}}$ also having a large impact. Of interest are the contributions from the b-tagging quantile and η of the third jet in the event. This is likely to be the correlation extracted between the $E_{\text{T}}^{\text{miss}}$ and the presence of an ISR jet.

The signal region is defined on top of the pre-selection by requiring high signal output score. The

9 Searches for Electro-Weak SUSY

final definition is developed using a grid search procedure to identify the requirements that yield the highest expected significance (equation 7.1) averaged across selected benchmark signal points in the target region. The variables optimised in the grid search are the $S_{obj-based}$, mCT and the signal score (w_{sig}) which is optimised as a binned variable-the number and range of bins is optimised. The resulting SR definition is given in table 9.7.

Variable	SR Wh
E_T^{miss}	$> 50 \text{ GeV}$
$N_{e/\mu}, p_T > 27 \text{ GeV}$	1
$N_{\text{jets}}, p_T > 30 \text{ GeV}$	2-3
$N_{b\text{jets}}, p_T > 30 \text{ GeV}$	2
m_{bb}	$\in [95, 140]$
$S_{obj-based}$	> 8
w_{Sig}	4 bins $\in [0.91, 0.928, 0.948, 0.964, 1]$

Table 9.7: Definition of the signal region targeting the $\tilde{\chi}_2^0 \tilde{\chi}_1^\pm \rightarrow Wh$ compressed signals

9.3.2 Background Estimation

The three dominant backgrounds considered in this analysis are expected to contribute relatively equally with single-top production the largest, then $t\bar{t}$ and $W + jets$. The strategy for estimating these dominant backgrounds is to build control regions at lower w_{sig} than the signal region using the output scores of the BDT for the relevant background category to increase the purity of the background targeted in the region. The optimisation of the control regions is to establish regions with sufficient data statistics at as high signal score as possible whilst maintaining good purity in the targeted background. The CRs are made orthogonal to one another by inverting selections on the different background scores, the definitions are summarised in table 9.8.

9.3.3 Systematic Uncertainties

Detector-based and modeling uncertainties are considered. The dominant detector-based uncertainties are those associated with jet energy resolution and jet energy scale. The dominant modeling uncertainties are those relating to the single-top $t\bar{t}$ interference schemes, with sub-leading uncertainties coming from the $t\bar{t}$ final state radiation (FSR) uncertainties. The $t\bar{t}$ FSR uncertainties come from uncertainties attributed to the tuning of the Pythia 8 [59] to data in Run 1 which are specifically associated with addition jet production [60].

Background-only Fit

The background-only fit was performed fitting the MC to the data in the control regions. The resulting yields for the SM background MC and data yields are summarised for the control and signal regions in tables 9.9 and 9.10. The yields are also shown in figure 9.4 where the bottom panel shows the significance of the deviation of data yields from the SM expectation.

9.3 ML Analysis

Variable	VR $t\bar{t}$	VR single-top	VR W+jets
E_T^{miss}		> 50GeV	
passTrig _{1lep}		✓	
$N_{e/\mu}, p_T > 27\text{GeV}$		1	
$N_{\text{jets}}, p_T > 30\text{GeV}$		2-3	
$N_{b\text{jets}}, p_T > 30\text{GeV}$		2	
$\mathcal{S}_{\text{obj-based}}$		> 5	
m_{bb}		$\in [50, 200]\text{GeV}$	
w_{Sig}	$\in [0.4, 0.9]$	$\in [0.2, 0.9]$	$\in [0.2, 0.9]$
$w_{t\bar{t}}$	> 0.4	-	-
$w_{\text{single-top}}$	< 0.2	> 0.2	< 0.2
w_W	< 0.4	-	> 0.4

Table 9.8: Definition of the control regions for estimating $t\bar{t}$, single-Top and W+jets dominant background processes. The selections in red highlight the selections that make the regions orthogonal to each other. The selections in blue highlight the selections that make the regions orthogonal to the control and signal regions.

table.results.yields channel	CRtt	CRst	CRW
Observed events	330	130	354
Fitted bkg events	330.03 ± 18.16	129.85 ± 11.30	353.98 ± 18.81
Fitted Z events	0.00 ± 0.00	$1.85^{+2.06}_{-1.85}$	6.08 ± 1.80
Fitted W events	$2.99^{+3.48}_{-2.99}$	$16.15^{+17.16}_{-16.15}$	279.72 ± 26.19
Fitted ttbar events	322.20 ± 19.06	43.75 ± 18.76	53.36 ± 20.71
Fitted st events	4.66 ± 4.08	66.14 ± 31.81	13.25 ± 6.36
Fitted diboson events	$0.00^{+0.01}_{-0.00}$	$0.04^{+0.20}_{-0.04}$	1.28 ± 0.94
Fitted Higgs events	0.00 ± 0.00	1.45 ± 0.20	0.00 ± 0.00
Fitted ttV events	$0.18^{+0.28}_{-0.18}$	0.47 ± 0.14	0.29 ± 0.10
MC exp. SM events	337.46 ± 57.00	147.52 ± 63.26	266.01 ± 32.60
MC exp. Z events	0.00 ± 0.00	$1.85^{+2.06}_{-1.85}$	6.08 ± 1.81
MC exp. W events	$1.99^{+2.17}_{-1.99}$	$10.75^{+12.15}_{-10.75}$	186.18 ± 14.65
MC exp. ttbar events	329.07 ± 57.22	44.69 ± 18.75	54.51 ± 23.06
MC exp. st events	6.21 ± 2.31	88.26 ± 65.34	17.68 ± 8.56
MC exp. diboson events	$0.00^{+0.01}_{-0.00}$	$0.04^{+0.20}_{-0.04}$	1.28 ± 0.94
MC exp. Higgs events	0.00 ± 0.00	1.45 ± 0.20	0.00 ± 0.00
MC exp. ttV events	$0.18^{+0.28}_{-0.18}$	0.47 ± 0.14	0.29 ± 0.10

Table 9.9: Post-fit yields for the SM background processes in the control regions from the background-only fit.

9 Searches for Electro-Weak SUSY

table.results.yields channel	SR_bin0	SR_bin1	SR_bin2	SR_optimised_mergeBin
Observed events	-1	-1	-1	-1
Fitted bkg events	7.3 ± 2.3	4.4 ± 1.8	3.2 ± 1.1	1.98 ± 0.89
Fitted Z events	$0.0^{+0.1}_{-0.0}$	$0.0^{+0.1}_{-0.0}$	0.0 ± 0.0	$0.02^{+0.06}_{-0.02}$
Fitted W events	2.0 ± 1.7	$0.6^{+1.1}_{-0.6}$	0.8 ± 0.5	0.88 ± 0.64
Fitted ttbar events	2.7 ± 1.3	2.1 ± 1.1	$0.9^{+0.9}_{-0.9}$	$0.33^{+0.69}_{-0.33}$
Fitted st events	2.5 ± 1.6	1.6 ± 0.8	1.4 ± 1.1	0.70 ± 0.43
Fitted diboson events	$0.0^{+0.0}_{-0.0}$	0.1 ± 0.0	0.0 ± 0.0	$0.00^{+0.01}_{-0.00}$
Fitted Higgs events	0.0 ± 0.0	0.0 ± 0.0	0.0 ± 0.0	0.00 ± 0.00
Fitted ttV events	0.1 ± 0.1	$0.1^{+0.1}_{-0.1}$	0.1 ± 0.1	0.05 ± 0.02
MC exp. SM events	7.53 ± 3.64	4.79 ± 2.52	3.39 ± 1.91	1.92 ± 1.29
MC exp. Z events	$0.04^{+0.06}_{-0.04}$	$0.04^{+0.07}_{-0.04}$	0.00 ± 0.02	$0.02^{+0.06}_{-0.02}$
MC exp. W events	1.33 ± 1.17	$0.42^{+0.73}_{-0.42}$	0.52 ± 0.39	0.58 ± 0.39
MC exp. ttbar events	2.75 ± 1.12	2.14 ± 1.10	$0.89^{+1.00}_{-0.89}$	$0.34^{+0.72}_{-0.34}$
MC exp. st events	$3.29^{+3.34}_{-3.29}$	2.08 ± 1.87	$1.90^{+1.97}_{-1.90}$	0.93 ± 0.93
MC exp. diboson events	$0.00^{+0.01}_{-0.00}$	0.06 ± 0.02	0.00 ± 0.01	$0.00^{+0.01}_{-0.00}$
MC exp. Higgs events	0.00 ± 0.00	0.00 ± 0.00	0.00 ± 0.00	0.00 ± 0.00
MC exp. ttV events	0.12 ± 0.08	$0.06^{+0.11}_{-0.06}$	0.08 ± 0.05	0.05 ± 0.02

Table 9.10: Post-fit yields for the SM background processes in the signal regions from the background-only fit.

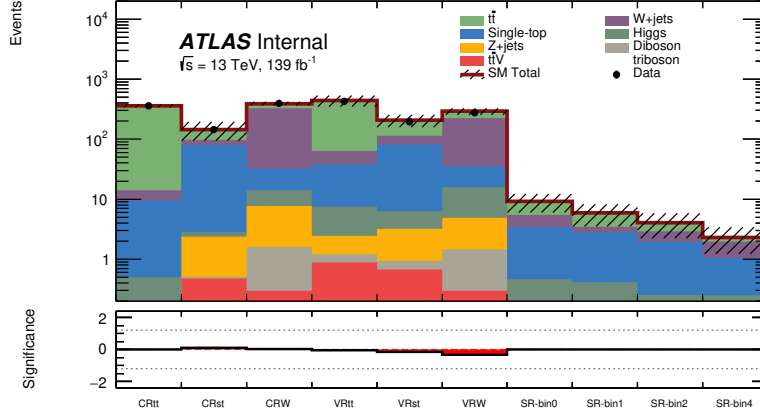


Figure 9.4: The pulls between the number of events observed and the total background expected after-fit in control, validation and signal regions. The lower panel shows the significance of the deviation. The data is not shown for the signal regions.

9.4 Electro-Weak SUSY Limits

Model-Dependent Fit

Model dependent fits were produced for each signal point considered, including the signal in the fit.

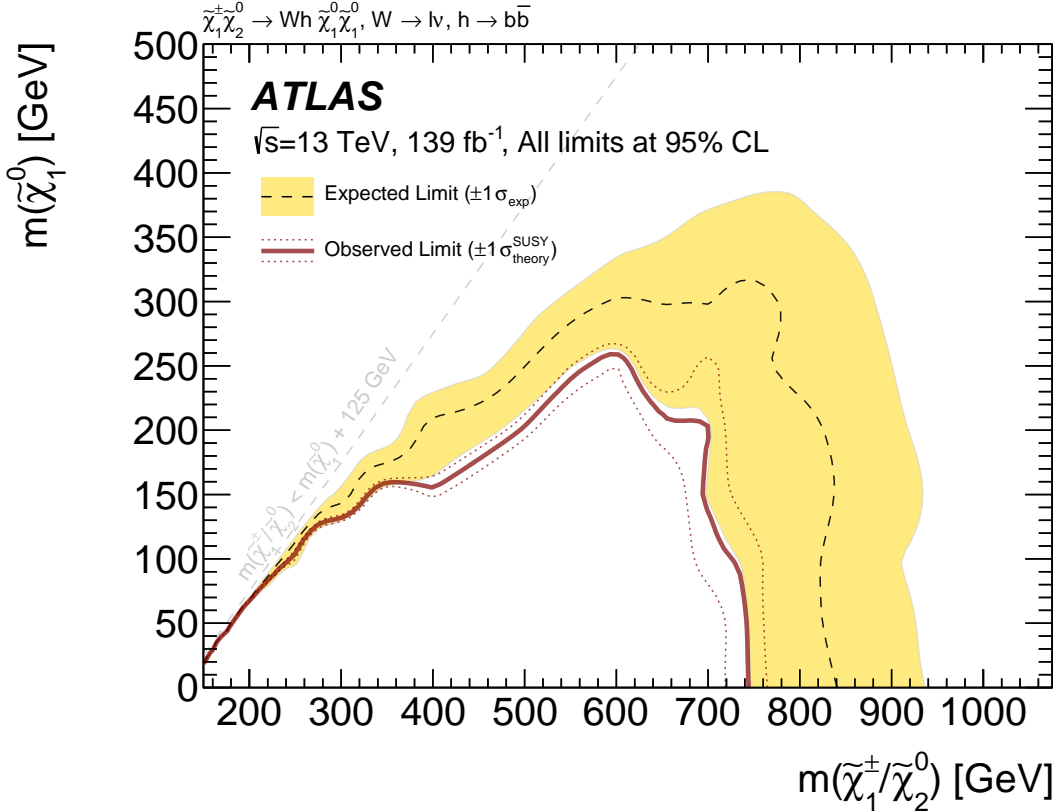


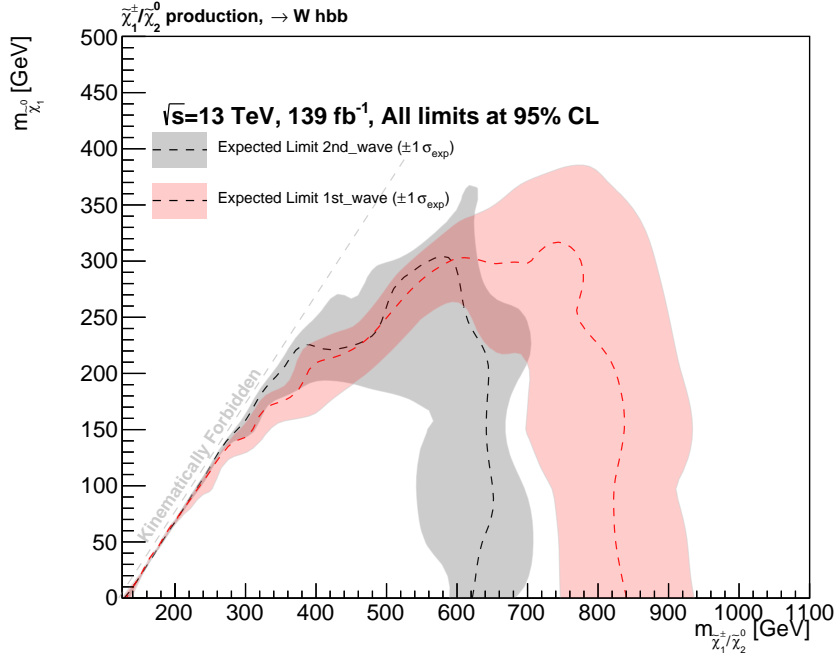
Figure 9.5: Model-dependent exclusion contour at 95% CLs. The observed limit is given by the solid line with the signal cross-section uncertainties shown by the dotted lines as indicated in the text. Expected limits are given by the dashed line.

CLs values are calculated for each point and a 95% CLs limit is derived by interpolating between points. For the cut and count analysis the limit is shown in figure 9.5. The same is done for the ML based analysis, however here the comparison between expected limits is shown between the cut-and-count and the ML approach highlighting the strengths of analysis in the compressed region, this is shown in figure 9.6.

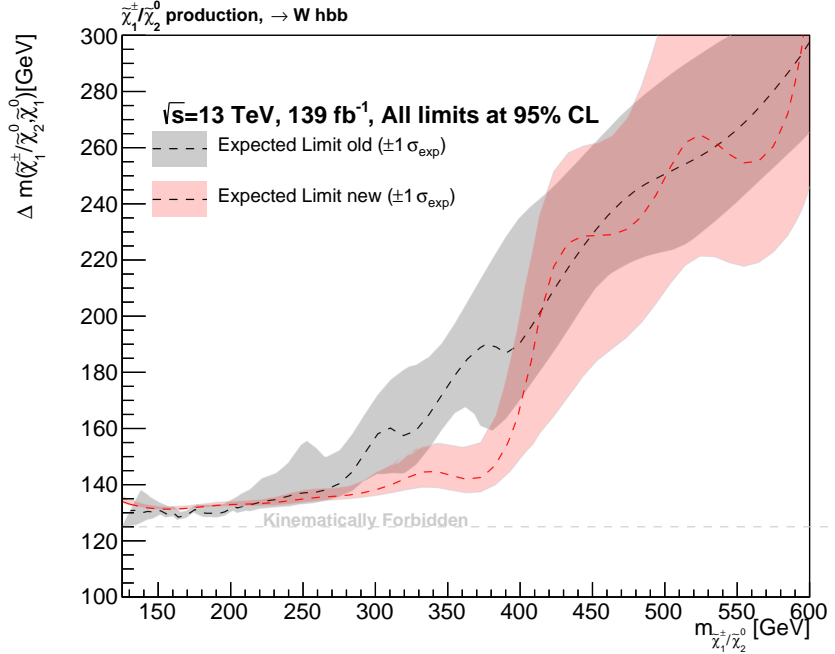
Due to the small excesses in the signal region bins of figure 9.2 the observed limit in figure 9.5 is around 1σ below the expected limit. This is particularly important in the compressed region where further developments of the analysis in the ML-based approach aim to provide more robust sensitivity to these mass scenarios.

The resulting limit from the selection-based analysis shown in figure 9.5 contributes greatly to the overall coverage of the search program for $\tilde{\chi}_1^\pm/\tilde{\chi}_2^0$ pair production decaying via the higgs at the LHC. The ATLAS and CMS summary limits are shown in figures 9.7 and 9.8.

9 Searches for Electro-Weak SUSY



(a) Expected limit in the standard view.



(b) Expected limit in the Δm view.

Figure 9.6: The expected exclusion limit for signals in the Wh analysis at 95% CLs. The limit includes all experimental and theoretical systematic uncertainties. 9.6(b) shows the limit in an alternate view with the mass difference $\Delta m(\tilde{\chi}_2^0, \tilde{\chi}_1^0)$ on the y-axis. In red the 1st wave expected limit is shown for comparison.

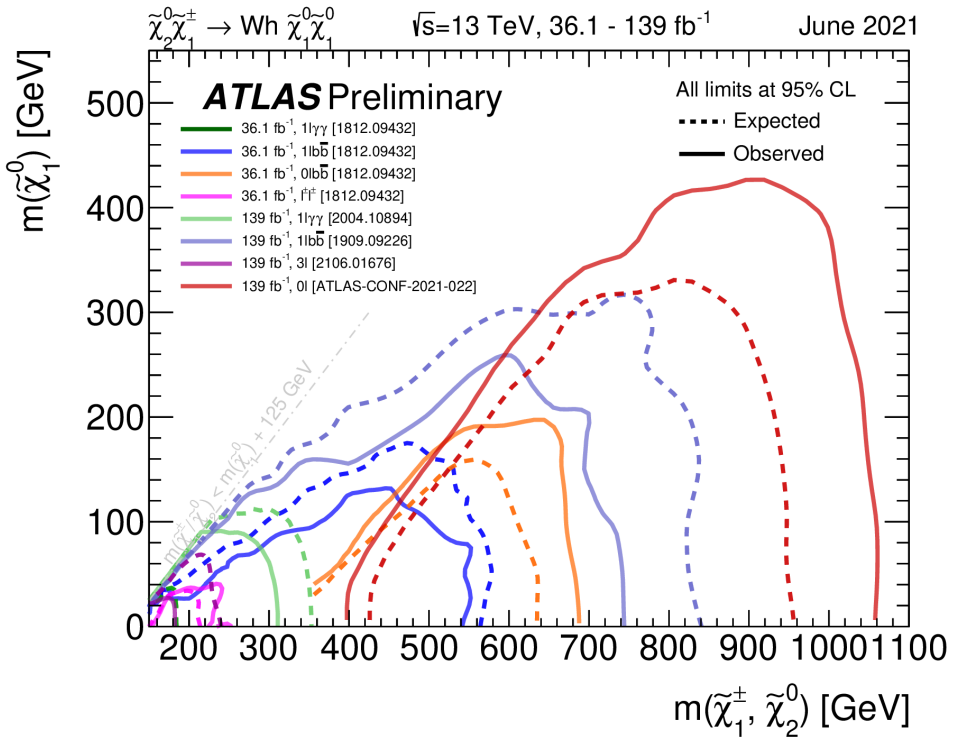


Figure 9.7: 95% CL limits on $\tilde{\chi}_1^\pm, \tilde{\chi}_2^0$ production decaying via a higgs, analysed from data collected by the ATLAS detector. The result from the analysis in section 9.2 is shown by the light blue. This result provides the strongest limit in the compressed region above $m_{\tilde{\chi}_1^\pm, \tilde{\chi}_2^0} = 250$ GeV. The previous run 1 result is shown by the blue line [109]. This is a selection-based approach with a simplified fit method compared with the run 2 analysis considering a shape fit in m_T . The public result that has the strongest limit in the compressed region is the analysis targeting higgs decays to photons, illustrating by the green line. The ML-based analyses described in section 9.3 will extend this sensitivity to higher $m_{\tilde{\chi}_1^\pm, \tilde{\chi}_2^0}$. The analysis targeting the all-hadronic final state, illustrated by the red line [] gives the strongest constraints towards high $m_{\tilde{\chi}_1^\pm, \tilde{\chi}_2^0}$.

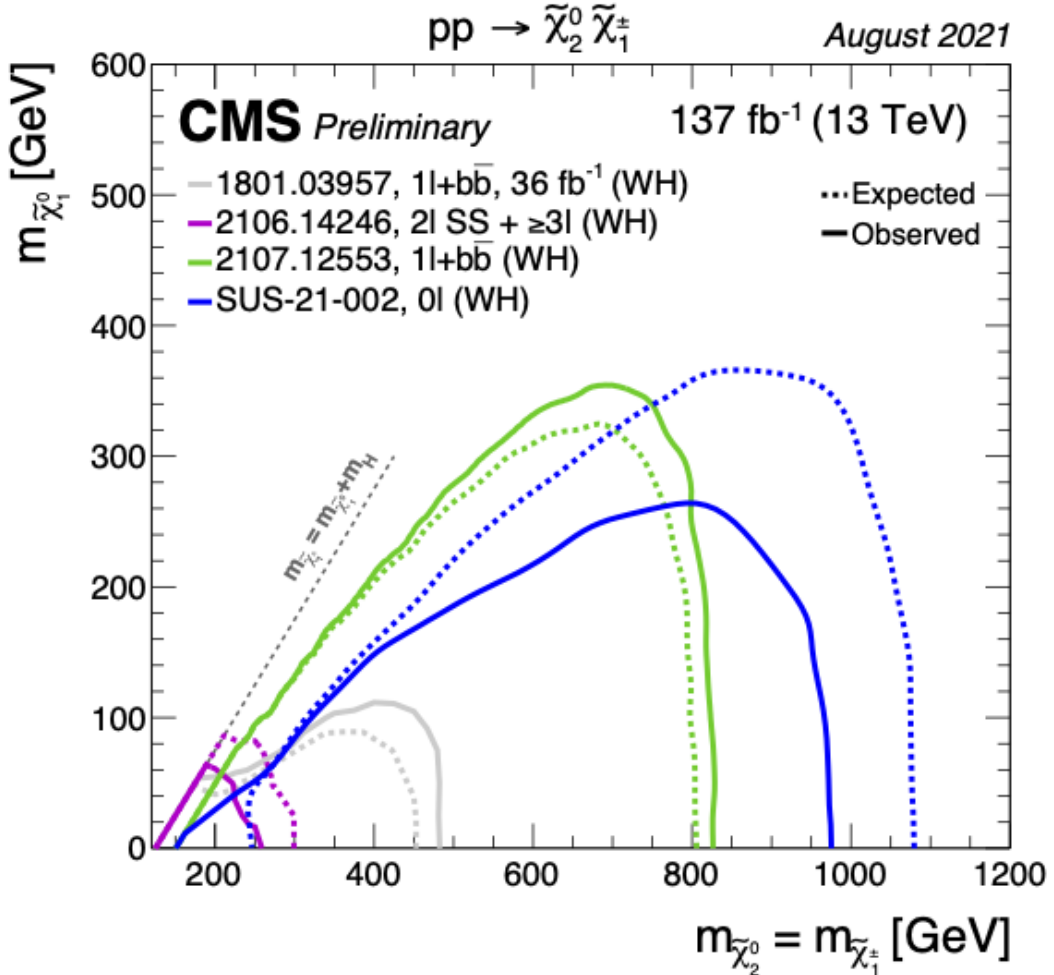


Figure 9.8: 95% CL limits on $\tilde{\chi}_1^\pm, \tilde{\chi}_2^0$ production decaying via a higgs, analysed from data collected by the CMS detector. The limits in grey line and green line target the same 1-lepton 2 b -jets final state described in this work for the run 1 and run 2 datasets respectively [110],[111]. The coverage of the CMS reach to these models is comparable with ATLAS with only reduced sensitivity to compressed scenarios, which is due in part to the reduced E_T^{miss} resolution compared with ATLAS. As with the ATLAS results, the strongest limit towards high $m_{\tilde{\chi}_1^\pm, \tilde{\chi}_2^0}$ is given by the all-hadronic final state shown by the blue line.

9.4 Electro-Weak SUSY Limits

Model-Independent Fit

For the cut-and-count analysis a model-independent fit was also performed. As described in section 7.1.2, this fit includes the control and signal regions but with no signal contribution included. The signal regions included in this fit are the discovery regions, denoted *disc.* in table 9.1. 95% CL upper limits on possible signal cross-sections are derived for each SR, these are shown in table 9.11 along with the confidence level for the null background-only hypothesis and discovery p-value for new BSM contributions.

Signal Region	$\langle\epsilon\sigma\rangle_{\text{obs}}^{95} [\text{fb}]$	S_{obs}^{95}	S_{exp}^{95}	CL_B	p_0	Z
SR-LM(disc.)	0.26	36.8	$20.0^{+8.0}_{-5.4}$	0.97	0.03	1.88
SR-MM(disc.)	0.18	24.8	$15.3^{+6.2}_{-4.6}$	0.94	0.06	1.54
SR-HM(disc.)	0.11	14.7	$9.7^{+3.3}_{-2.7}$	0.89	0.10	1.30

Table 9.11: Left to right: 95% CL upper limits on the visible cross-section ($\langle\epsilon\sigma\rangle_{\text{obs}}^{95}$) and on the number of signal events (S_{obs}^{95}). The third column (S_{exp}^{95}) shows the expected 95% CL upper limit (and its $\pm 1\sigma$ excursions) on the number of signal events if no BSM signal is present. The last three columns indicate the CL_B value, i.e. the confidence level observed for the background-only hypothesis, the discovery p -value (p_0) and the significance.

10 Searches for direct Dark Matter production

The process considered in this section derives from the 2HDM+a BSM scenario discussed in section 2.3.2 where the extended Higgs sector couples to dark matter through a pseudo-scalar mediator. The process considers the production of dark matter via the pseudo-scalar mediator in association with a top quark. The model here takes a simplified form, the masses of the additional bosons of the extended sector are set such that the mass of the CP-even heavy Higgs, H , and the charged higgses, H^\pm , are equal to the mass of the heavy CP-odd Higgs, A , greatly simplifying the number of free parameters. The lightest CP-even state, h is considered to be the SM Higgs and the mixing angle of the CP-odd states, α and the ratio of the Higgs VEVs, $\tan\beta$ are constrained such that $\sin(\beta - \alpha) = 1$ and h is de-coupled from the extended sector and is SM-like and the heavier neutral higgs, H , does not interact with the SM electroweak bosons. Additionally the mixing angle of the CP-odd states, θ , is fixed to $\sin\theta = \frac{1}{\sqrt{2}}$ which maximises the mixing between a and A .

Personal contributions to this work include: contributions towards development and validation of the analysis software for processing the data and MC, development of software for the evaluation of signal theoretical uncertainties and MC sample production.

10.1 Signal model

This analysis focusses on the channel which produces a final state with a single top quark and a W where the top quark decays to a b-quark and a W boson. The Feynman diagrams that contribute to the tW channel are shown in figure 10.1. This signature has not been studies previously at the LHC. The focus is on final states where one W decays leptonically which compliments a related analysis targeting di-leptonic final states [112] and encompasses DM simplified signatures produced in association with top pairs. The free parameters of the model are $\tan\beta$, m_{H^\pm} and m_a . To simplify the available phase-space, two grids are constructed, the first fixes $\tan\beta$ to 1 and scan over m_{H^\pm} and m_a . The second fixes $m_a = 250\text{GeV}$ and scans $\tan\beta$ and m_{H^\pm} . The final state signature contains a top quark decaying to a W -boson and a b-jet and another W -boson created in the hard scatter. One of the W -bosons decays leptonically and the other hadronically and the event has large missing transverse energy carried by the dark matter and neutrino.

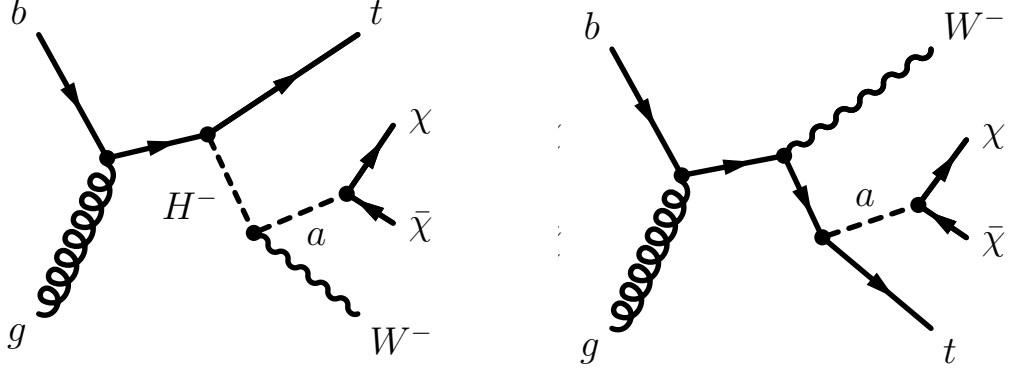


Figure 10.1: Feynman diagrams that contribute to the tW channel of dark matter production via the pseudo-scalar mediator a in the extended 2HDM+ a model.

10.2 Event Selection

The data events are triggered using the E_T^{miss} trigger, a requirement of reconstructed $E_T^{\text{miss}} > 250\text{GeV}$ is placed to ensure that the trigger is fully efficient. Exactly one lepton (electron or muon) with p_T greater than 30GeV is required. To reconstruct the hadronically decaying W events are required to have at least two jets with $p_T > 50\text{GeV}$ and a third jet with $p_T > 30\text{GeV}$. In addition at least one b-tagged jet with $p_T > 50\text{GeV}$, a second b-jet is allowed but the p_T must not exceed 50GeV which suppresses contributions from semi-leptonic $t\bar{t}$. The signal regions are optimised from this basic selection by optimising requirements on 3 key variables which are deemed the most sensitive discriminants between the signal and the dominant background processes: 3 mass related variables m_T - a key discriminant for $W+\text{jets}$ and semi-leptonic $t\bar{t}$, am_{T2} reduces di-leptonic $t\bar{t}$ in cases where one lepton is not reconstructed and $m_W^{\text{reclustered}}$ which is the invariant mass of jets identified as decay products of the W -boson. The re-clustering procedure is described in detail in [113], the jets in the event are anti- k_t large-radius jet parameter R of 3.0, the jet radius is then reduced to $R = \frac{2m_W}{p_T^{\text{jet}}}$, the jet with mass closest to m_W is the candidate its mass is used as $m_W^{\text{reclustered}}$. In order to gain sensitivity to many signal models in the model-dependent fit, the signal region is additionally binned in E_T^{miss} . The resulting regions are summarised in table 10.1.

10.3 Background Estimation

The dominant background contributions expected in the signal regions varies among the SR bins. $t\bar{t}$ contributes between 15% of the expected bin yield for the higher E_T^{miss} and 50% for the lower E_T^{miss} bins. $W+\text{jets}$ is the next most dominant contributing up to 40%. Dedicated control region are developed to normalise $t\bar{t}$ and $W+\text{jets}$ contributions. Sub-dominant backgrounds such as single-top, $t\bar{t} + V$ and di-boson backgrounds and other minor backgrounds are estimated entirely from MC. The $t\bar{t}$ control region, CR_{tt} , requires 2 b-jets, an inverted am_{T2} requirement with respect to the signal region

10.4 Systematic Uncertainties

Table 10.1: Summary of the signal region selections developed with the adaptive grid search algorithm and additional E_T^{miss} binning used in the model-dependent fit.

Variable	SR-bin1	SR-bin2	SR-bin3	SR-bin4	SR-bin5
$n_{\text{leptons}}(\text{baseline})$			≥ 1		
n_{leptons}			≥ 1		
$N_{b\text{-jets}}$			≥ 1		
N_{jets}			≥ 3		
$p_T(b_2)$ [GeV]			< 50		
$m_W^{\text{reclustered}}$ [GeV]			> 60		
m_T [GeV]			> 200		
am_{T2} [GeV]			> 220		
E_T^{miss} [GeV]	$\in [250, 300]$	$\in [300, 400]$	$\in [400, 500]$	$\in [500, 600]$	> 600

Cuts	CRW	VRW-1	VRW-2	CRtt	VRtt-1	VRtt-2
$n_{\text{leptons}}(\text{baseline})$	1				1	
n_{leptons}	1				1	
$N_{b\text{-jets}}$	1			≥ 2		1
N_{jets}	≥ 3				≥ 3	
$p_T(b_2)$ [GeV]	< 50			> 50		< 50
m_T [GeV]	$\in [40, 100]$		> 100		> 200	
$m_W^{\text{reclustered}}$ [GeV]	< 60	> 60	< 60	-		< 60
am_{T2} [GeV]		> 220		< 220		> 220

Table 10.2: The selection cuts defining the control and validation regions. The red highlighted selections indicate those that ensure orthogonality with the signal region.

and removed requirement on $m_W^{\text{reclustered}}$. The extrapolation over am_{T2} and $m_W^{\text{reclustered}}$ to the signal regions is validated with 2 validation regions which have either inverted am_{T2} or $m_W^{\text{reclustered}}$ requirements. The W control regions, CRW , requires m_T in the range $[40, 100]$ and $m_W^{\text{reclustered}} < 60$ GeV but otherwise identical selections to the signal region (excluding E_T^{miss} binning). CRW is also split into two dependent on the lepton charge to constrain W^+ and W^- independently. Again, two W validation regions are constructed, $VRW1$ using the CR selection on m_T but otherwise SR selections and $VRW2$ using the CR selection on $m_W^{\text{reclustered}}$ but otherwise SR selections. As in CRW the validation regions are also split by lepton charge. The selections are summarised in table 10.2.

10.4 Systematic Uncertainties

SM background modeling and detector related uncertainties are considered. The signal regions of the tW 1-lepton analysis are dominated by systematic uncertainties related to the modeling of

10 Searches for direct Dark Matter production

table.results.yields channel	tW1L_CRtt	tW1L_CRWp	tW1L_CRWm
Observed events	911	3143	1653
Fitted bkg events	907.41 ± 30.52	3135.45 ± 56.87	1665.08 ± 37.50
Fitted Top1L events	846.96 ± 34.11	748.75 ± 83.42	720.78 ± 86.33
Fitted SingleTop events	19.82 ± 11.53	276.59 ± 69.50	257.00 ± 70.15
Fitted Wjets events	3.18 ± 0.75	2005.00 ± 98.23	625.41 ± 42.11
Fitted Zjets events	$0.13^{+0.16}_{-0.13}$	6.63 ± 0.99	8.39 ± 1.29
Fitted Diboson events	0.87 ± 0.25	88.85 ± 15.55	46.05 ± 8.01
Fitted ttV events	31.01 ± 7.12	8.16 ± 2.69	5.96 ± 1.52
Fitted ttH events	4.37 ± 0.41	1.12 ± 0.17	1.17 ± 0.11
Fitted tWZ events	1.07 ± 0.29	0.36 ± 0.13	0.32 ± 0.11

Table 10.3: Results of the background only fit for the CRs. Statistical and experimental uncertainties are considered.

$t\bar{t}$ and single-top processes. These are the parton-shower and generator uncertainties for $t\bar{t}$ which are calculated using alternative MC programs for the two steps. The single-top dominant is the single-top/ $t\bar{t}$ interference uncertainty for diagram subtraction vs diagram reduction described in 9.2.3. The dominant detector based uncertainties come from the jet energy scale and resolution uncertainties and the b-tagging efficiency and mis-tagging. Uncertainties on the object resolutions are transferred to the E_T^{miss} term which also contributes somewhat to the overall uncertainty. The total systematic in the exclusion bins ranges from around 8% in the lower E_T^{miss} and around 18% in higher E_T^{miss} bins.

10.5 Results

Background-only Fit

The background-only fit is produced considering the null hypothesis of only SM contributions fitting the MC to data in the CR and extrapolating to the signal and validation regions. The resulting yields for the control and signal regions for the SM processes and data yields are summarised in tables 10.3 and 10.4.

Figure 10.2 shows the distributions of the key variables in the signal regions. 10.2(a) and 10.2(b) show the m_T and am_{T2} distributions with where the selection on m_T and am_{T2} are removed respectively and the arrows indicate the SR selection. No significant deviation from the SM prediction is observed, Although consistent small deviations of the order 1σ are observed in the first 4 bins of the signal regions which causes the observed limit to be weaker than the expected.

Model-Dependent Fit

As no significant deviations from the SM prediction are observed, model-dependent fits are run for

10.5 Results

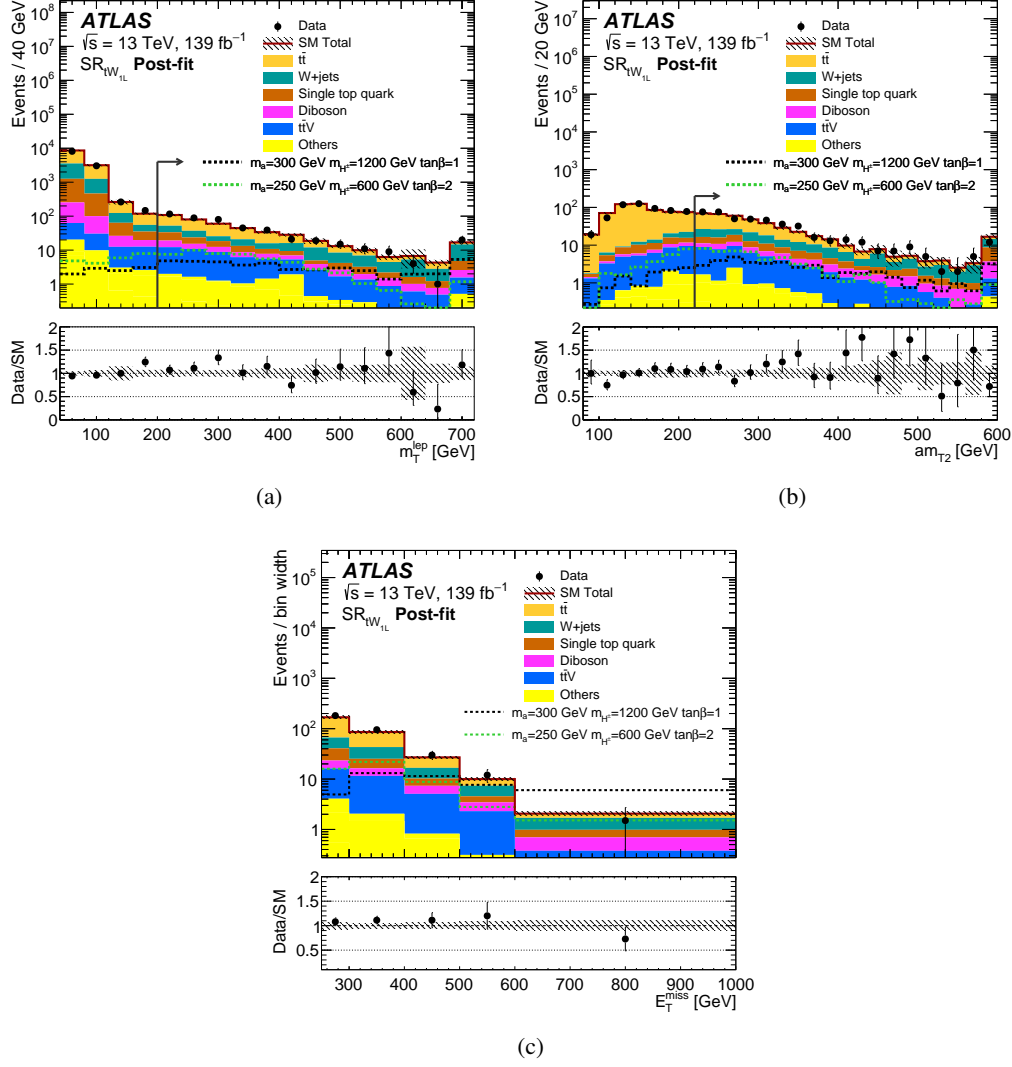


Figure 10.2: Distributions of m_T , am_{T2} and E_T^{miss} from the background-only fit. The SR requirement is indicated by the arrow. The expected distributions for representative scenarios with different m_a , m_{H^\pm} , and $\tan\beta$ are shown. The lower panels show the ratio of data to the background prediction.

10 Searches for direct Dark Matter production

Table 10.4: Background-only fit results for the tW_{1l} signal region. The backgrounds which contribute only a small amount (rare processes such as triboson, $t\bar{t} t\bar{t}$, $t\bar{t} WW$ and Higgs boson production processes, and non-prompt or misidentified leptons background) are grouped and labelled as ‘Others’. The quoted uncertainties of the fitted SM background include both the statistical and systematic uncertainties.

	SR^{Bin1}	SR^{Bin2}	SR^{Bin3}	SR^{Bin4}	SR^{Bin5}
Observed events	182	191	60	24	12
Fitted SM bkg events	169 ± 14	171 ± 13	55 ± 6	20.1 ± 2.8	15.6 ± 2.8
$t\bar{t}$	101 ± 12	84 ± 12	20 ± 5	5.1 ± 1.7	2.3 ± 1.5
Single top	16.3 ± 5.2	17.3 ± 5.2	5.4 ± 3.2	2.0 ± 1.8	$1.7^{+2.0}_{-1.7}$
$W+jets$	28 ± 4	37.0 ± 4.3	14.2 ± 2.4	6 ± 1	5.9 ± 1.1
$Z+jets$	2.0 ± 0.9	1.1 ± 0.7	0.3 ± 0.1	0.15 ± 0.04	0.15 ± 0.02
Diboson	7.2 ± 1.7	9.6 ± 2.0	4.6 ± 1.0	2.2 ± 0.5	2.7 ± 0.6
$t\bar{t} V$	12.3 ± 1.4	19.5 ± 3.5	8.7 ± 1.2	4.0 ± 0.7	2.5 ± 0.5
tWZ	1.7 ± 0.2	2.4 ± 0.5	1.17 ± 0.15	0.42 ± 0.09	0.39 ± 0.09
Others	0.6 ± 0.1	0.6 ± 0.1	0.17 ± 0.02	0.06 ± 0.02	0.03 ± 0.01

each mass hypothesis considered and CLs values calculated. As in the previous analyses, limits are constructed in the model hyper-parameter planes by interpolating between 95% CLs values at the produced points. The final limit is constructed as a statistical combination of the 1-lepton channel described here and the 2-lepton channel which complements it and is statistically independent due to the lepton requirements in all regions, figure 10.3.

Model-Independent Fit

For the model-independent fit, the exclusion signal regions are adapted by removing the upper bound on the E_T^{miss} binning such that the regions overlap. This forms 5 non-exclusive regions. A model-independent fit is conducted for each individual region and upper limits on the visible BSM cross-section at 95% CL ($\langle \in \sigma \rangle_{obs}^{95}$) and the expected and observed number of signal events. In addition the confidence level for the null (SM-only) hypothesis and association p-value are given in the final two columns.

10.5 Results

Table 10.5: The 95% CL upper limits on the visible cross section ($\langle\epsilon\sigma\rangle_{\text{obs}}^{95}$) and on the number of signal events (S_{obs}^{95}) for all SRs and analysis channels as detailed in the text. The fourth column (S_{exp}^{95}) shows the 95% CL upper limit on the number of signal events, given the expected number (and $\pm 1\sigma$ exclusions of the expectation) of background events. The last two columns indicate the CL_B value, i.e. the confidence level observed for the background-only hypothesis, and the discovery p -value ($p(s = 0)$). The associated significance is provided in parentheses.

Signal channel	$\langle\epsilon\sigma\rangle_{\text{obs}}^{95} [\text{fb}]$	S_{obs}^{95}	S_{exp}^{95}	CL_B	$p(s = 0) (Z)$
SR ²⁵⁰	0.72	100.6	67^{+33}_{-16}	0.85	0.12 (1.16)
SR ³⁰⁰	0.51	70.8	54 ± 16	0.85	0.15 (1.02)
SR ⁴⁰⁰	0.24	32.9	29^{+10}_{-6}	0.64	0.30 (0.52)
SR ⁵⁰⁰	0.14	18.9	19^{+8}_{-5}	0.52	0.45 (0.13)
SR ⁶⁰⁰	0.08	10.6	12^{+3}_{-4}	0.24	0.94 (-1.54)

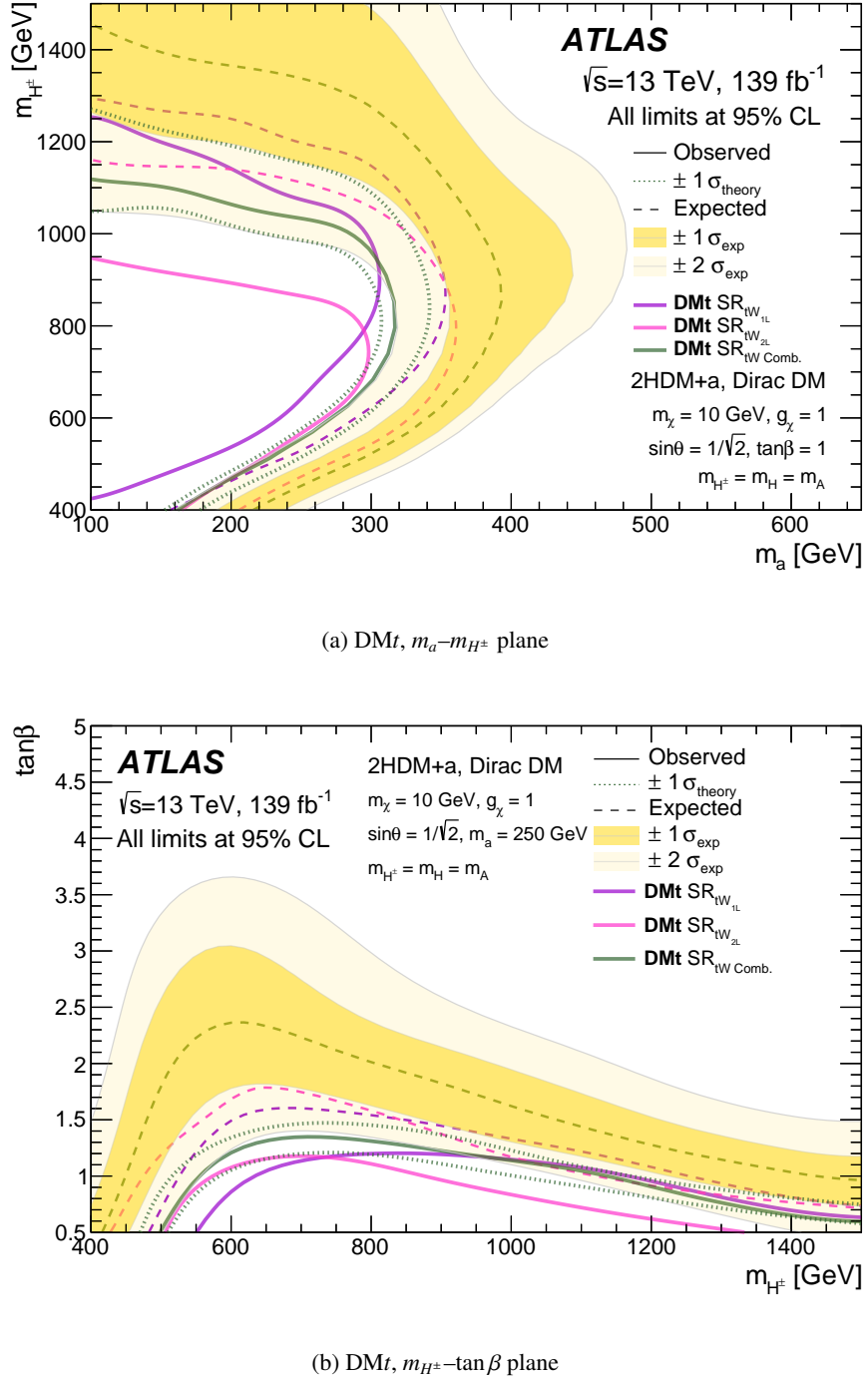


Figure 10.3: The expected and observed exclusion contours as a function of (m_a, m_{H^\pm}) (top) and $(m_{H^\pm}, \tan\beta)$ (bottom), assuming only DM_{tW} contributions, for the individual tW1L (purple line) and tW2L [112] (pink line) analysis channels, and for their statistical combination (green line). Experimental and theoretical systematic uncertainties, as described in Section 6, are applied to background and signal samples and illustrated by the ± 1 standard-deviation and ± 2 standard-deviation yellow bands and the green dotted contour lines, respectively, for the statistical combination.

11 Conclusion

This work presents analyses of 139fb^{-1} of proton-proton collision data at $\sqrt{s}=13\text{TeV}$ centre-of-mass energy collected by the ATLAS detector at the LHC between 2015 and 2018. The analyses target several BSM scenarios including third generation and electroweak SUSY and dark matter models, all of which are characterised by final states containing b-jets and missing transverse momentum. No significant excesses were found in the data selected by the analyses which would indicate the presence of new physics. Hence, the results are used to place stringent new limits on the possible phase-space and characteristics on new physics. The limits in this work extend the previous best limits to a large extent or provide brand new limits on uncovered BSM scenarios.

New limits on the bottom squark pair production are shown in section 8. The analysis excludes bottom squarks decaying directly to b-quarks in R-parity conserving models at 95% CLs for bottom squark masses up to 1270 GeV for massless $\tilde{\chi}_1^0$. The analysis has a special focus on compressed mass spectra using dedicated secondary vertex tagging and ML methods. Bottom squark masses up to 660 GeV for $\Delta m(\tilde{b}, \tilde{\chi}_1^0) = 10\text{ GeV}$ are excluded at 95% CLs. In addition, new complex decay chains for bottom squark pair production are explored where the \tilde{b} decays via an intermediate $\tilde{\chi}_2^0$ which then decays to the higgs boson and a $\tilde{\chi}_1^0$. In this scenario bottom squark masses up to 1.5 TeV are excluded for models with $m(\tilde{\chi}_1^0)$ fixed at 60 GeV, for models with $\Delta m(\tilde{b}, \tilde{\chi}_2^0)$ fixed at 130 GeV, bottom squark masses are excluded up to 1.3 TeV. Both analyses make significant improvements on the results based on Run1 data beyond the increased luminosity extrapolation.

Analyses targeting a model of electroweak SUSY with chargino-neutralino pair production decaying via the W and higgs bosons respectively are described in section 9. These analyses provide some of the strongest limits on chargino-neutralino pair production available at the current time and improve significantly on the Run1 result. Advanced ML methods are employed to extract sensitivity to difficult-to-reach areas of signal phase-space. The analysis excludes chargino-neutralino masses up to 740GeV for massless $\tilde{\chi}_1^0$. In compressed mass scenarios, which are well motivated by the recent confirmation of the g-2 discrepancy (section 2.1.6) models are expected to be excluded up to chargino-neutralino masses of $\sim 400\text{ GeV}$ for $\Delta m(\tilde{\chi}_1^\pm / \tilde{\chi}_2^0, \tilde{\chi}_1^0) = 130\text{ GeV}$.

Dark matter signals are explored both in simplified models and also motivated by the 2HDM+a framework. In the simplified DM models, final states with 2 b-jets are analysed. Cross-sections exceeding between 5 and 300 times the predicted rate for mediators with masses between 10 and 500 GeV are excluded for a dark matter mass of 1 GeV. In the 2HDM+a scenario, a new final state considering a single top quark and a W is analysed, which was thus far excluded from ATLAS searches. Models with dark matter mass of 10GeV and mediator coupling $g_\chi=1$ are excluded for

11 Conclusion

pseudo-scalar, a , masses below 200 GeV for all values of m_{H^\pm} in the range 400–1400 GeV and up to 330 GeV for m_{H^\pm} around 900 GeV. For $m_a = 250$ GeV, all values of m_{H^\pm} below 1.5 TeV are excluded for $\tan\beta$ below unity, and scenarios with $\tan\beta$ below 1.5 are excluded for masses of m_{H^\pm} around 800 GeV.

The LHC will begin run 3 of its data taking program which will further extend the dataset and thus the reach of the experiments towards new physics. The additional data provides new opportunities for discovering rare physics, particularly for electroweak SUSY. The development of modern analysis techniques particularly using machine-learning as here will enable the future data to be maximally exploited. There is promise for the discovery of new physics at the LHC by the end of run 3.

Acknowledgements

Appendix

A Understanding the Local Support Structures for the ATLAS High-Luminosity Upgrade

This appendix describes the production procedure for the stave and petal local support structures for the, barrel and end-cap structures for the ATLAS high-luminosity inner detector upgrade. The production procedure used currently is described in detail and notes are made on ways to improve current methods or to ensure consistency between support manufactures. The mass determination of the component substructures was measured throughout the stave production and the measurement results are given here, including determination of adhesive content. These measurements are compared with predicted values, differences between predicted and measured values are explored and the effect on the radiation length of the support structure is discussed.

A.1 Introduction

The local support structures are the backbone for the pixel and strip sensors that will operate in the upgraded ATLAS Inner Tracking Detector (ITK). The silicon sensors of the detector will be attached to the local support structures which sit in the detector's mechanical structure. In addition to giving a structural frame for the sensors to reside in, they also supply the cooling, grounding and electrical connections. The materials of the local supports are designed to incorporate these supply requirements. In addition, the supports must be both lightweight and highly rigid. When in operation, the particles measured by the detector will pass through the support structure. To maximise the ability of the detector to accurately track particles for particle identification and event reconstruction the support structure must have a minimal effect on the particles passing through them - a low radiation length as possible.

Therefore it is important to understand, in detail, the precise composition of the structures, and in addition, to verify that the production methods used afford that the local supports in the upgraded detector will adhere to expected tolerances in material composition. This understanding also aids modelling of the detector structure and the physics processes measured.

A.1.1 Materials within the Local Supports

The full structure of the local supports plus sensors and readouts is illustrated in figure A.1. The sections comprising the local support itself are those including and below-of the bus-tape layer. The bus-tape is made from polyamide polymer, with the electrical connections inside it made from copper strips and adhesive. The carbon-fibre face-sheet is constructed from layers of carbon fibre sheets

A Understanding the Local Support Structures for the ATLAS High-Luminosity Upgrade

which are pre-impregnated with cyanite ester resins.

The bus-tape and the carbon fibre face-sheet are attached together in the co-curing process. The central structure of the support is composed of sections of low density carbon-fibre honeycomb with a ring of higher density, thermally conducting carbon-fibre foam ('AllComp') surrounding a titanium cooling tube which provides the CO_2 circulation for the cooling system. The thermally conducting carbon-fibre foam completely surrounds the titanium cooling loop for effective heat dissipation. The carbon-fibre honeycomb is designed to be a low-density, lightweight structural material providing rigidity to the support. The central structure is surrounded along the edges by so-called close-outs, made from engineering plastics or carbon-fibre laminates.

The face-sheet is then replicated in reverse on the bottom side of the support to complete the sandwich structure.

Within the upgraded ITK for the ATLAS detector 2 types of supports are used;

- Stave supports, with simple rectangular geometries which will support the strip sensors on the barrel section of the ITK.
- Petal supports, supporting sensors on the end-caps of the ITK. These are required to have more complex wedge shape to allow for the difference in geometric coverage required.

Illustrations of the 2D stave and petal geometries and internal structure shapes are given in figure [A.2](#)

A.1 Introduction

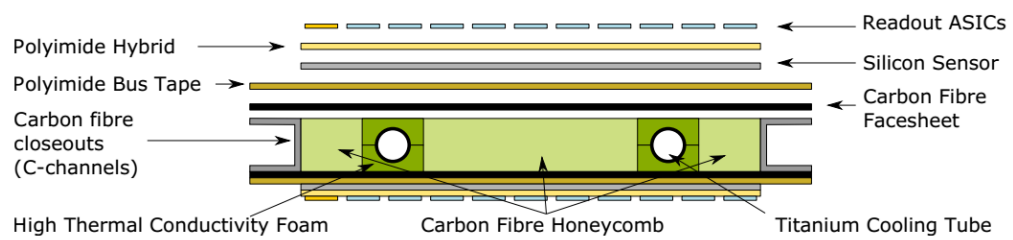
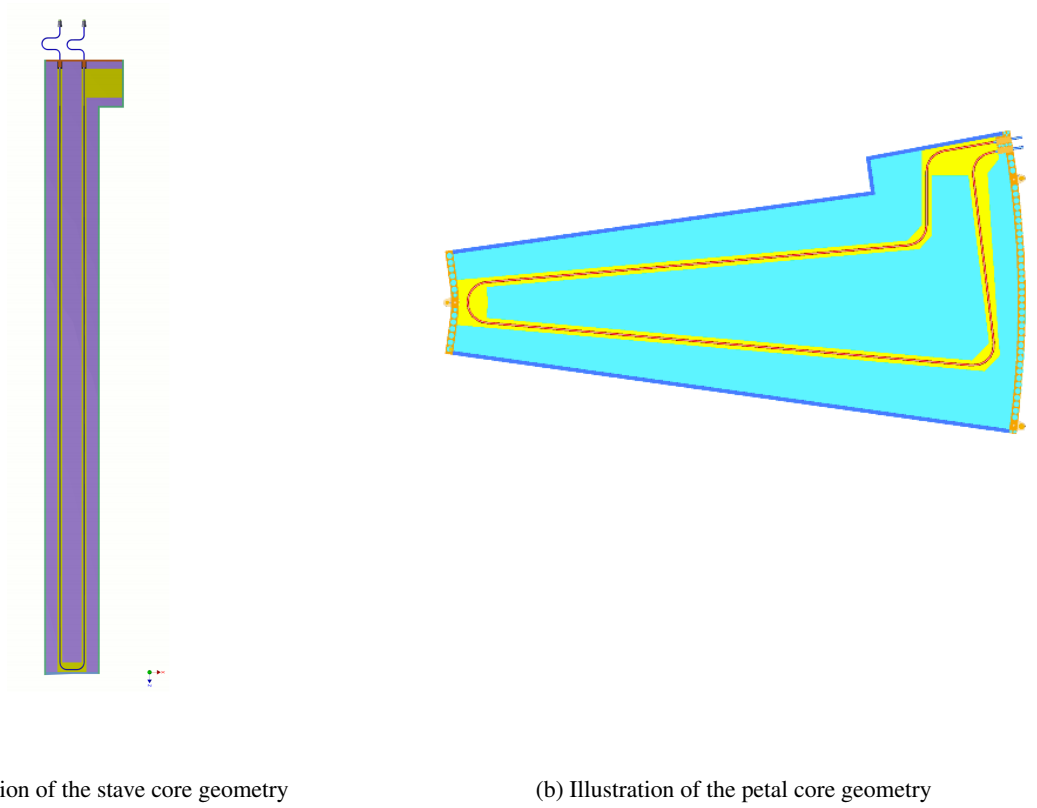


Figure A.1: Illustration of the internal structure of the local supports in staves and petals. Component materials are shown as a slice through the support.

A Understanding the Local Support Structures for the ATLAS High-Luminosity Upgrade



(a) Illustration of the stave core geometry

(b) Illustration of the petal core geometry

Figure A.2: Illustration of the differing geometries of the petal and stave support structures.

A.2 Stave Production

The stave manufacture procedure described here is that of the first full stave production at the University of Liverpool's facilities with the ITK stave design. As such, an examination of the manufacture processes was conducted regarding expected time constraints, production consistency, and overall ease of methods used with the intention of preparing the manufacture process for upcoming requirements.

The production is described in 8 steps. The mass of the stave components included in each step were measured as described in section [A.4](#) in order to determine the build up of adhesive used in each step. The step-by-step glue determination as it determines which steps can be addressed if the amount of glue is found to be too large.

Note the top and bottom face-sheets have already undergone co-curing before the assembly steps.

A.2.1 Step 0.1: Co-curing of face-sheets

The co-curing process is the method that combines the top and bottom bus-tapes with carbon fibre to form the top and bottom layers of the support. 3 layers of mono-directional carbon fibre sheets are arranged with fibre grains perpendicular to adjacent layers with the polyamide bus-tape on top, this is then placed into an autoclave at high-temperature and pressure such that the resin is pushed from inside the carbon fibre sheets and connects with adjacent sheets and the bus-tape thus securing the structure.

A.2.2 Step 0.2: Glue Mixing

The adhesive mixture used in this assembly is Hysol 9396 epoxy resin loaded with Boron Nitride powder. The mixture is 80:20 hysol resin:BN filler by weight and is mixed using a mixing machine at high revolutions to remove any bubbles.

A.2.3 Step 1: Gluing carbon foam blocks to lower face-sheet

The bottom face-sheet is placed bus-tape down onto a vacuum jig plate and aligned using pins (dowels) passing through reference holes drilled in the face sheet and jig. The vacuum jig plate is carbon-fibre topped jig with vacuum lines running within the jig connecting external vacuum lines to small suction holes that cover an area with size and shape of the face-sheet. This secures the face-sheet flat for the glueing steps as curvatures can arise in the face-sheet from the co-curing process.

Areas for glue placement are then taped out using 3 layers of kapton tape (flash breaker tape) to form a glue bath of depth 2.1mm. The tape lines are placed using a pre-made masking ruler, which gives positions relative to the reference dowel pins. Once all glue areas are taped out, the adhesive is mixed

A Understanding the Local Support Structures for the ATLAS High-Luminosity Upgrade

and smoothed into the tape bath using a flat edge and the tape is then removed. The taping and the resulting glue area can be seen in figure A.3.

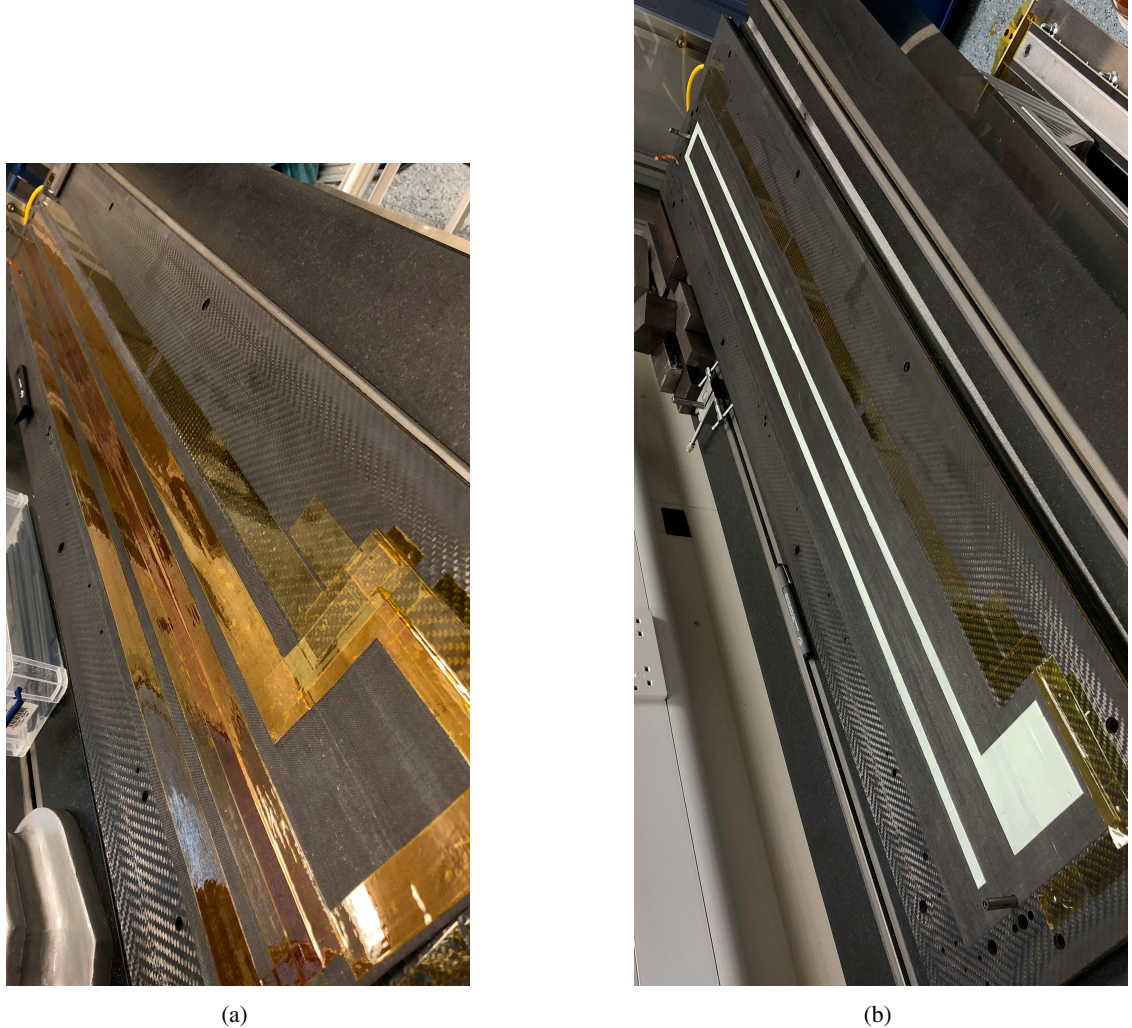


Figure A.3: Images of the glue area taping and resultant glued area on the bottom face-sheet from step 1 of the procedure.

The lower half of the carbon foam pieces are then fitted into another dedicated jig, the holding jig, along with the lower half PEEK close-outs. The foam sections and close-outs are held in the holding jig by screws which gently clamp the components in place. The entire jig is then flipped so the carbon foam pieces and the close-outs are facing down above the glued face-sheet. This jig again has position holes drilled into each end, the jig is placed into position arranging the holes onto the dowel pins which are sat in the vacuum jig. The pins holding the foam pieces are loosened to ensure proper contact with the face-sheet. The arrangement is weighed down and left for ≥ 24 hours to set.

Notes on Step 1

The taping procedure using 3 layers of on top of one another was in fact quite time-consuming, due the difficulty of accurately placing the tape repeatedly. This step could be sped-up if tape of thickness 2.1mm (bath depth) could be sourced, only one layer of tape would reduce time spent on this step.

An additional layer of tape is recommended to be placed onto the holding jig covering sections which will come into contact with the face-sheet and the edges which hold the foam and close-outs. This was done to avoid the situation where glue leaks and comes between the face-sheet and the holding jig. The holding jig sits on the arrangement for the full gluing time if this becomes attached this would cause damage when removed.

A.2.4 Step 2: Glueing cooling tube and upper foam blocks-UK method

After sufficient time is allowed for the glue to cure, the holding jig is removed. The lower foam blocks sitting on the face-sheet have a trough machined with depth equal to half the radius of the titanium cooling pipe. In the UK method, the adhesive is applied directly to the titanium pipe using a 2-piece gluing jig. The gluing jig comprises two pieces with troughs machined into them such that when clamped together they surround the titanium cooling tube. The troughs are at a depth such that they leave ~0.2mm gap around the cooling tube on one side of the jig and minimal gap on the other.

Glue is passed into the jig using a syringe via a hole in the top that connects to one side of the trough. The glue is pressed through at a constant rate and the jig is passed along the tube. This is repeated for both long edges of the cooling tube. As the glue jig will not fit onto the shorter edges or curved sections of the cooling tube, these sections are marked out and the trough itself is filled with adhesive, leaving sufficient space for the pipe. The tube is then placed into the trough of the lower foam blocks on the lower face-sheet. Glue is then also applied to top of the clean short section of the cooling pipe, again with the syringe. The upper foam blocks are then placed on-top of the glued cooling pipe, weights are applied and the setup is left for ≥24 hrs for the glue to set.

Cooling pipe glue coverage tests

During the application of the glue to the cooling pipe using the glue jig (UK method) we found that the adhesive coverage was uneven in places and that it was very dependent on the ability of the assembler to keep steady consistent motion of the jig. In addition the total amount of glue on the cooling tube is dependent on the precision of the width of the hole in the jig that it would pass through. As a result of these observations a test was conducted to understand how this coverage translated to contact with the foam blocks.

A length of cooling pipe was glued, with Boron Nitride loaded glue (the green colour making inspection easier) using the UK method as described above and placed into the carbon foam blocks and weighted down for 5 minutes. The upper foam block was then removed so the glue contact with

A Understanding the Local Support Structures for the ATLAS High-Luminosity Upgrade

the block could be inspected. This is illustrated in figure A.4 where we can see the contact with the carbon foam blocks is sparse. The alternative US method, which consists of filling the carbon foam troughs with glue directly, is expected to have better contact. As part of the motive of using the BN glue around the cooling pipe is to aid heat dissipation. This low contact is worth considering if staves produced with the UK method and US method are found to differ in thermal performance.

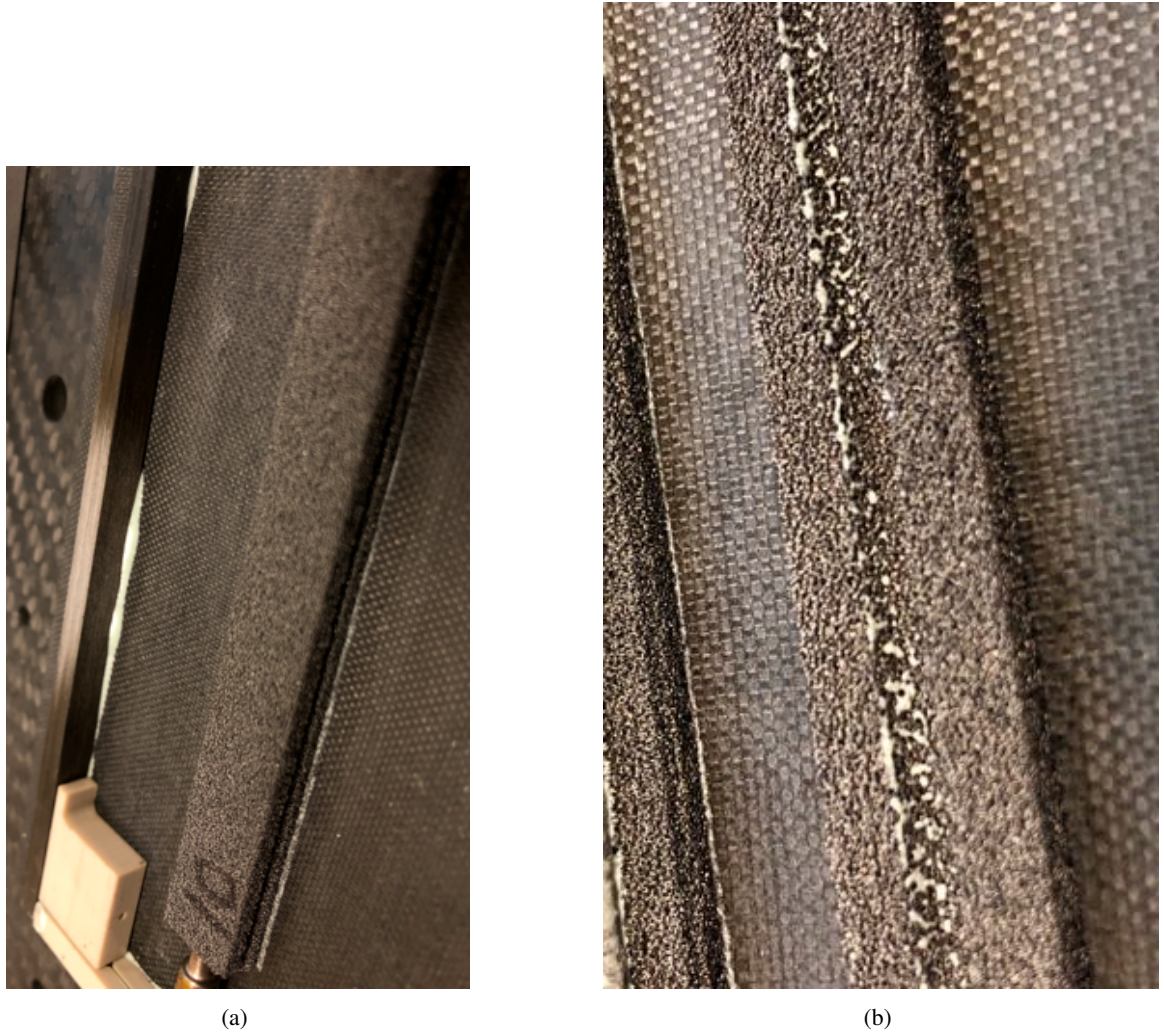


Figure A.4: Images of the glue contact with the carbon foam blocks.

Notes on step 2

- A full 'dry-fit' of the cooling tube with would be recommended in further iterations of the assembly procedure to ensure that fluctuations in the machining of the foam blocks or bends of the cooling pipe do not affect the gluing. These can be then be rectified before gluing any components.

- The UK gluing method can be cumbersome for one person. During this assembly a simple stand was constructed to hold the cooling pipe in place whilst the glue jig is arranged and the adhesive is applied. The stand gently clamps the cooling pipe at both ends and provides tension to reduce sag in the pipe. The use of the stand increases efficiency of the step and may make it easier to have consistent glue coverage on the cooling pipe.

A.2.5 Step 3: Gluing carbon-fibre c-channels

Carbon fibre c-channels are loaded into the dedicated jig. Glue is applied to the top surface of the c-channels held in the jig, with tape applied along the edges of the jig which will come into contact with the face-sheet when in position. The glue is applied to the c-channels using a syringe. The jig is then rotated so the glued c-channels are facing down onto the current assembly, aligned by fitting pre-machined holes onto the dowel pins, and weighted.

Notes on step 3

The current methodology places a thin line of glue along each of the c-channels. Because the contact between the c-channels and the face-sheet is flush and neither material is porous (like when working with carbon foam) any excess glue is pushed out from the edges of the c-channels. This can be seen in figure A.5. The excess glue is minimal in terms of mass but causes a problem when fitting the carbon honeycomb structure (step 4). The excess glue raises the surface that the honeycomb will be glued to at the edges along the c-channels. One can either remove the excess glue with a sharp edge once dry, though this is time consuming and risks damaging the face-sheet, or cut the honeycomb short of the glue edges when fitting. In order to avoid this issue, in future iterations one could limit the amount of glue on the using the same technique of building up a tape height along the edges of the jig and scraping away excess glue with a flat edge to leave a thin layer along the full length of the c-channel. This would avoid the leakage issue and gluing would be more consistent in this step.

A.2.6 Step 4: Gluing the carbon-fibre honeycomb

The internal areas of the assembly are measured and honeycomb pieces are cut to fit this area. The pieces are dry fit and numbered in their position. They are then removed and placed into a glue bath of depth 5.5mm (± 0.05 mm) and weighed down for 2 minutes. They are removed from the bath using a pair of tweezers and placed into relevant positions in the assembly. 2 sheets of rubber sheeting are laid on top of the honeycomb to avoid damaging the brittle edges and weights are placed on the rubber sheeting.

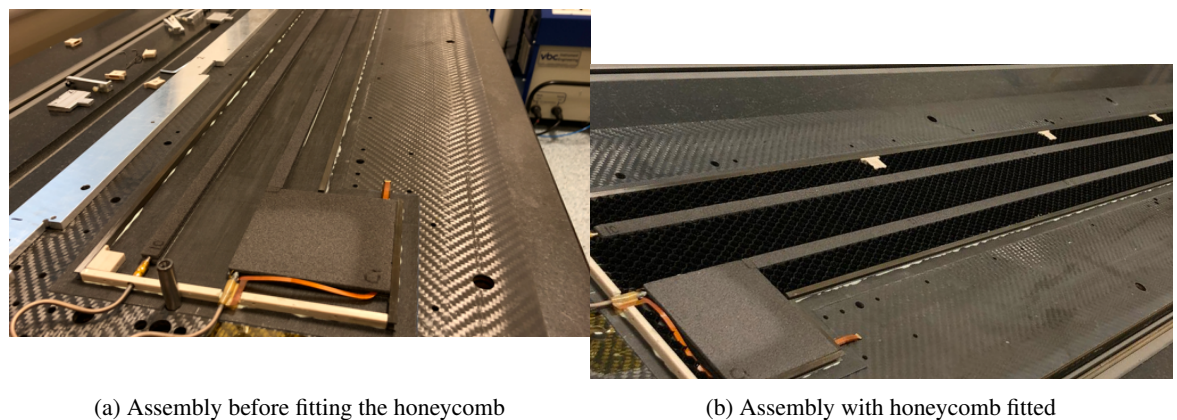
A.2.7 Step 5: Honeycomb grinding

The height of the honeycomb is larger than the height of the c-channels and carbon foam layers in the assembly. This is because there are non-negligible tolerances in the production of the honeycomb so the ordered height is such that it will not deviate below the height of the other layers in the assembly.

A Understanding the Local Support Structures for the ATLAS High-Luminosity Upgrade



Figure A.5: Image of the glue leaking from the c-channel-face-sheet contact after step 3.



A.2 Stave Production

As a result we need to remove the excess honeycomb, which can be seen in figure A.7. The proposal for the full production is to use a lathe to grind the honeycomb to the right height, however this was unavailable at the time of this assembly so an alternative method was used.

In the alternative method, fine-grain sand-papers were glued to lightweight metal blocks. These were rubbed gently over the honeycomb area with a small amount of downward pressure to reduce risk of snapping brittle edges. The grain of the sandpaper was reduced as the height came closer to that of the other assembly components. The assembly was cleaned using a vacuum after this process.

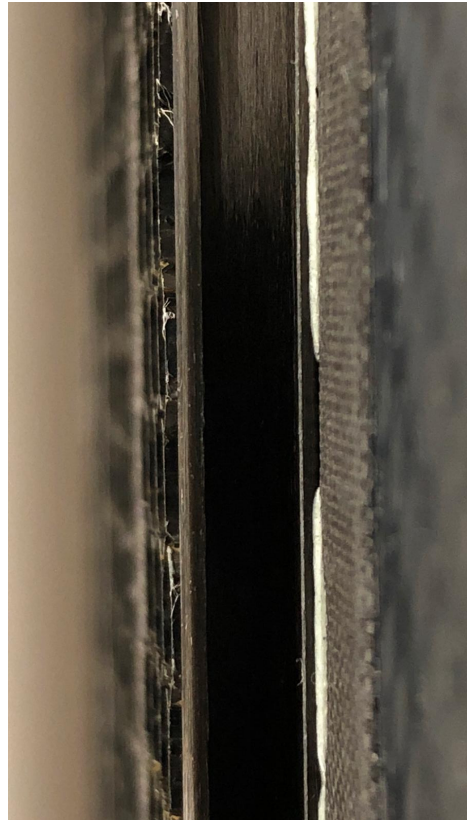


Figure A.7: Image of the excess honeycomb lying above the carbon fibre due to imprecision in the depth of the honeycomb manufacture.

Notes on step 5

The grinding method by hand appears to be successful in the process time, being similar to the time for the machined lathe method. It also provides greater control on the forces applied to the honeycomb to avoid damage. However the global flatness of the honeycomb is likely to be worse than with the machined method and would vary more between different rounds of stave assembly.

A.2.8 Step 6: Gluing the top face-sheet

The top face-sheet is placed onto a separate vacuum jig and the areas for the carbon foam blocks are mapped out using 3 layers of kapton tape as in step 1. The glue bath with 5mm depth, used in step 4, is mapped out with the negative of the area on the face-sheet, covering the areas of the carbon foam with kapton tape. The glue bath is filled with glue and scraped to the correct height with a flat edge. The area mapped out on the face sheet is filled with glue and scraped to the correct height as in step 1. The full lower assembly is placed into the glue bath, using the positioning dowels now placed in the jig of the glue bath and held for 2 minutes. The lower assembly is then lifted from the glue bath and placed onto the top face-sheet, again positioned in place by dowel pins. The full assembly is weighed down and left for the glue to cure for ~24 hours. After this time the weights are removed and sacrificial edges of the face sheets are removed.

Notes on step 6

After the sacrificial edges are removed in the last stage, some burrs are left. These can be removed using the same grinding process used to grind the honeycomb in step 5.

A.3 Petal Production

A.3.1 Step 0.1: Co-curing of face-sheets

The co-curing process is the method that combines the top and bottom bus-tapes with carbon fibre to form the top and bottom layers of the support. 3 layers of mono-directional carbon fibre sheets are arranged with fibre grains perpendicular to adjacent layers with the polyamide bus-tape on top, this is then placed into an autoclave at high-temperature and pressure such that the resin is pushed from inside the carbon fibre sheets and connects with adjacent sheets and the bus-tape thus securing the structure.

A.3.2 Step 0.2: Glue Mixing

The adhesive mixture used in this assembly is Hysol 9396 epoxy resin loaded with Graphite powder. The mixture is 80:20 hysol resin:Graphite filler by weight and is mixed using a mixing machine at high revolutions to remove any bubbles.

A.3.3 Step 1: Gluing of c-channels and closeouts to bottom face-sheet

The positions of the c-channels and close-out outlines are first drawn directly onto the face-sheet, with markings separating the individual pieces to be placed. Then the glue is mixed, proportions are added following the recipe above and the mixture is mixed in the high-speed mixer. The bottom face-sheet is placed onto the vacuum plate and the vacuum activated. The glue is then placed into a dispensary

A.3 Petal Production

machine which provides a consistent stream through a nozzle and the glue is dispensed with the use of the dispenser for one section of c-channel in a thin line along the centre of the piece outline. The relevant section is then placed onto glue and the process is repeated for all c-channels and close-outs. Under completion, all the glued sections are weighted and the arrangement is left for >24hrs for the glue to cure.

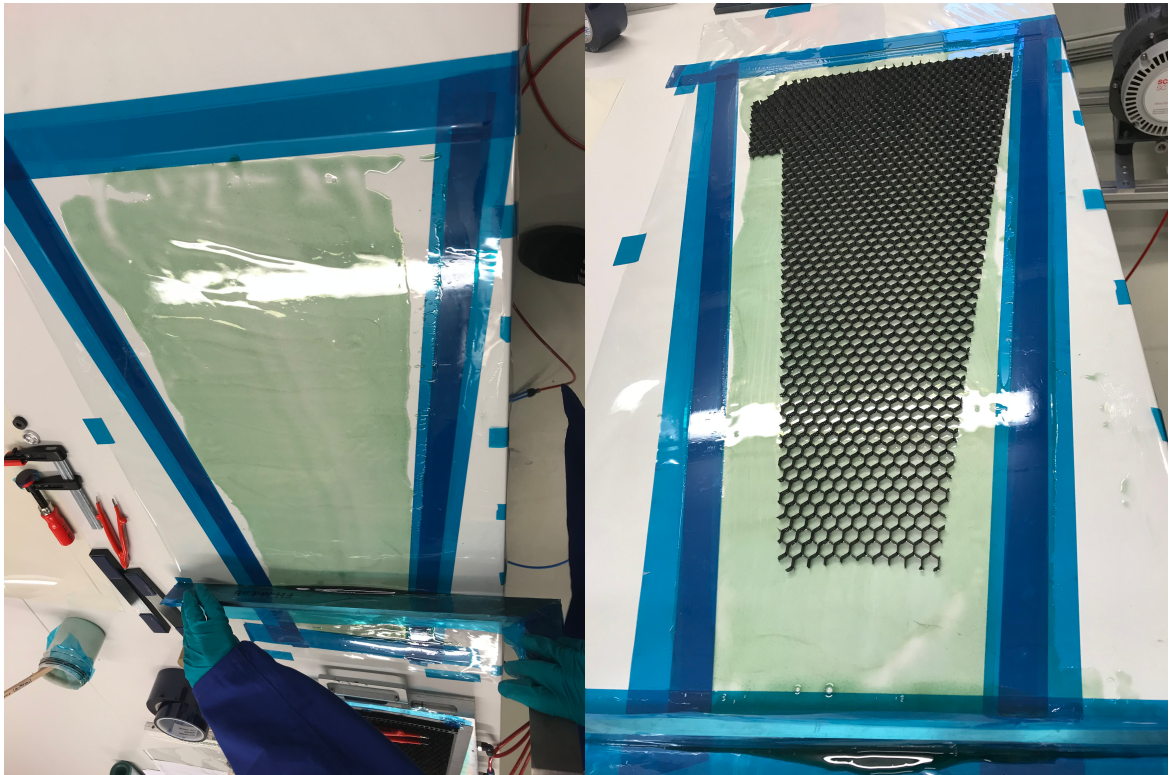


Figure A.8: Image of the bottom face-sheet after gluing c-channels and close-outs (stage 1).

A.3.4 Step 2: Gluing the honeycomb to the bottom face-sheet

A glue bath is first prepared by marking out an area onto plastic sheeting with 3 layers of kapton tape forming the edges of the bath to form a precise depth. The bath area is arranged to be just larger than the total area of honeycomb pieces to be glued. The glue is mixed and poured into the bath. A flat-edge is placed at the wide end of the bath with the side pressed against the tape and pulled smoothly over the glue towards the thin end to spread the glue evenly. This is repeated until the spread is even with complete coverage, excess glue is removed with the flat-edge. The honeycomb is pressed into the bath, some lateral movement is applied in order to build up a meniscus of glue within the cells of the honeycomb. Some weight is applied to the honeycomb for 2 minutes. The bottom face sheet is on the vacuum jig (it has remained in place since assembly of the c-channels and close-outs) and the vacuum is applied. The honeycomb is then removed from the bath using tweezers and placed into position on the face-sheet.

A Understanding the Local Support Structures for the ATLAS High-Luminosity Upgrade



(a) Laying the glue bath for the honeycomb insert

(b) Honeycomb structure in the glue bath



(c) Honeycomb structure in bath with weights

A.3.5 Step 3: Gluing the all-comp pieces and cooling pipe

Step 3.1: Lower all-comp gluing

The positions for the all-comp pieces are sketched onto the underside of the face-sheet, the face-sheet is again positioned on the vacuum jig and the vacuum activated. The glue is prepared as in step 1 and put into the dispensary machine. Glue is then applied to the sketched sections of the petal facing for the 3 all-comp pieces closest to the beam-line end of the petal. The glue is applied liberally, within the sketched lines, more so than with the c-channel gluing in step 1, to allow for absorption of glue into the porous all-comp and maintain a good coverage of the face-all-comp contact. The end-piece and the adjacent first long sections of the all-comp lower half are glued into position. These serve as a reference for subsequent pieces to be glued towards the middle of the facing. The process is repeated and the middle sections are glued and then the end distal to the beam pipe is glued in the same manner. Once glued into position the all-comp is weighed down and left for 24 hours.

Notes on Step 3.1

For future processes alignment could be improved by placing the cooling pipe into the cut-out of the lower all-comp sections as they are glued. This could help to avoid forcing the cooling pipe around subtle miss-alignments in the all-comp.

Step 3.2: Cooling pipe gluing

The glue is again prepared and put into the dispensary machine. A line of glue is placed into the cut-out for the pipe of the lower all-comp, again liberally to account for absorption. This is done for the full cut-out area. Meanwhile (or shortly after) the glue is applied to the cut-out of the loose upper-pieces of all-comp. The cooling pipe is then placed into the cut-out of the lower (glued to the face-sheet) all-comp blocks. To secure the cooling pipe into position, whilst working on securing the upper sections, small weights are applied onto the cooling pipe, these are then removed for sections of upper all-comp to be placed and then repositioned on top of the upper all-comp that has been placed to continue holding the pipe in place. Once all upper all-comp sections are in place additional weight is added and the arrangement is left for >24 hours for the glue to cure.

A.3.6 Step 4: Gluing the top face-sheet

The glue bath is again prepared with the same glue depth as previous steps. The full bottom arrangement,(face-sheet, honeycomb, all-comp, cooling pipe, close-outs) is secured onto the vacuum place. Dowel pins are placed through reference holes in the bottom face-sheet into matching holes on the vacuum plate. The vacuum is turned on, and a good seal is ensured but pushing down the loose edges of the face-sheet. The vacuum plate is then lifted and the arrangement is placed onto the glue bath with the inner structure (honeycomb, all-comp) into the glue. The structure is pressed in to assure

A Understanding the Local Support Structures for the ATLAS High-Luminosity Upgrade

good glue coverage, and left for around 2 mins. This allow meniscuses to form in the honeycomb areas. Meanwhile the top face-sheet is placed into another vacuum plate, mirrored with respect to the lower vacuum plate. Again a secure seal is ensured. The lower structure is then lifted from the glue bath and placed onto the lower face-sheet. The arrangement is aligned using the dowel pins currently in the lower vacuum plate which slide into holes in the opposing vacuum plate. Once aligned, the structure is pushed down to ensure complete contact between the glued components and the upper face-sheet. The setup is left for >24 hours for the glue to cure.

A.4 Mass determination in the Stave Production

A.4 Mass determination in the Stave Production

To establish the build up of mass during each stage in the stave construction, all assembly components were weighed separately before assembly, then the stave was weighed after each stage in the production process. The smaller pieces, such as the carbon foam blocks and the peek close-outs were weighed using standard, high-precision table-top scales. The larger components, such as the face-sheets and the c-channels are too long to be weighed accurately using these scales, the components will move on the weighing platform, any air movement around them will change the measurement.

A weighing environment was built to address these issues. Designed and built by David Sim at the University of Liverpool, it consists of a perspex box with a hinged door. 2 metres tall and around 50x50cm wide and deep so as to fit components of size up-to the full stave size. The top and bottom of the perspex box are aluminium plates. A hole of width ~2cm is drilled in the middle of the top aluminium plate. The scales used in this arrangement sit on top of the weighing box on the aluminium plate. The scales have a precision of 0.001g with a measurement range up to 1kg. The scales feature measurement via a hook in the undercarriage of the device which is then attached to a clamp. The components are weighed by clamping them in this arrangement.

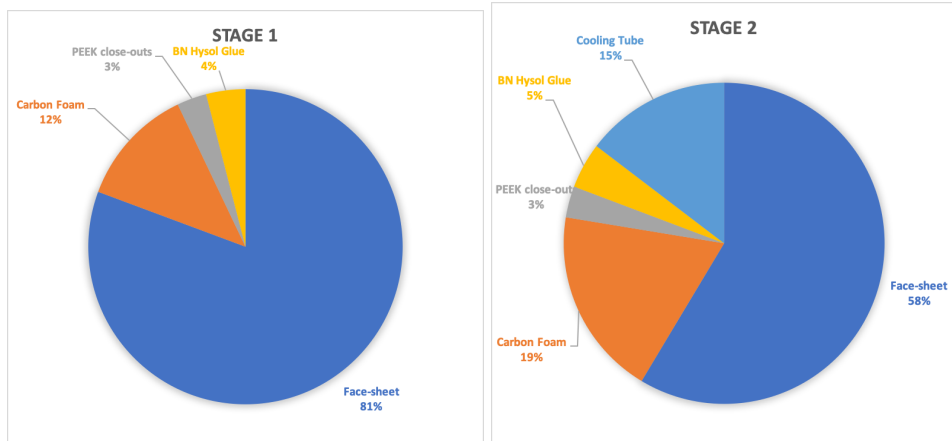
The build up of glue mass throughout the stages of production is summarised in table A.1

Production Stage	Glue mass (g ± 0.0005)	Glue contribution to total mass (%)
Stage 1	5.711	1.46
Stage 2	3.263	0.83
Stage 4	4.618	1.18
Stage 6	16.382	4.19

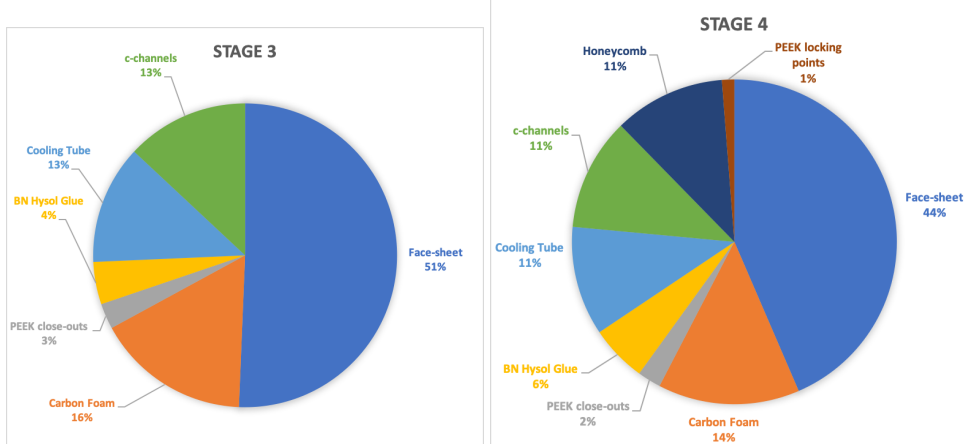
Table A.1: Measured glue contribution of the stave at each stage of production, by mass and as a percentage of the total stave mass.

Figures A.10 show the mass contribution coming from different sub-components of the structure through subsequent stages of building. Here the face-sheets are considered containing the bus-tape and carbon sheet co-cured.

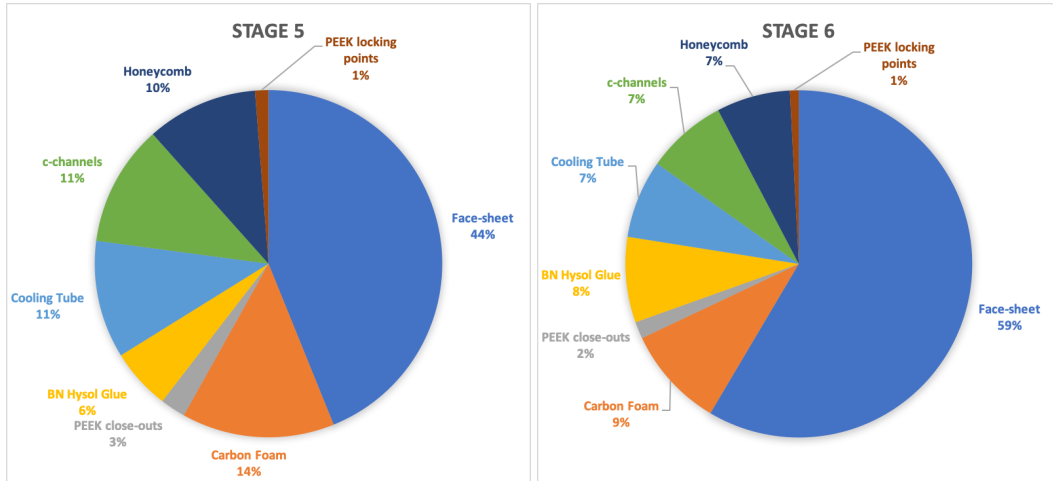
A Understanding the Local Support Structures for the ATLAS High-Luminosity Upgrade



(a) Mass contributions after stage 1 of assembly (b) Mass contributions after stage 2 of assembly



(c) Mass contributions after stage 3 of assembly (d) Mass contributions after stage 4 of assembly



(e) Mass contributions after stage 5 of assembly (f) Mass contributions after stage 6 of assembly

Figure A.10: Illustration of the mass contributions from sub-components within the stave at each stage.

A.5 Conclusion: Comparing production mass measurements with prediction.

A.5 Conclusion: Comparing production mass measurements with prediction.

Prior to construction of the petals and staves, the masses of the constituent components and glue content was estimated from the drawings. This estimation must use many assumptions which are difficult to estimate, for example estimating glue thicknesses. Using the information collected in the manufacture process described in this document we can attempt to validate or improve the assumptions made in the model of constituents within the petals and staves.

In this section, the differences between the predicted and measured masses of the constituents is explored and their effect on the predicted radiation length of the core is established.

The predicted masses of the sub-components in the stave core are calculated from the density of the material, either using the known value or calculating directly, and the volume of the material taken from design drawings. The sub-components are grouped into classes of the same material where possible. These can be compared directly with the measured component masses. There are some components which are constructed from different materials, in this case we calculate an density and radiation length for the component by summing the values for different materials of the component weighted by their relative abundances within the component (for example the bus-tape which contains polyamide with copper electrical line inserts).

With this information we calculate the radiation length contribution from each of the sub-components, the surface area of the stave core is normalised to the active sensor area, and the sub-component material width is thus calculated by dividing the sub-component volume by the active sensor area.

With this methodology we make several assumptions:

- The material density used in prediction calculations is accurate to within reasonable error.
- For the co-cured face-sheets, consisting of carbon-fibre face-sheets and bus-tape which we weigh combined, difference between predicted and measured mass are attributed to the bus-tape since carbon-fibre constituents are easier to predict.

Table A.2 shows the differences between the measured and predicted component masses, their contribution to the radiation length of the stave and the totals for each.

We find that the differences between the predicted and measured masses of the constituent components are small and there is only a small effect from these differences on the total radiation length of the core. However the measured glue content is much less than predicted. This difference is expected to be large between prediction and measurement, and shows that the base prediction was overly conservative. The result is that the total measured radiation length is smaller than predicted.

A Understanding the Local Support Structures for the ATLAS High-Luminosity Upgrade

Sub-component	Material	Predicted mass (g)	Measured mass (g)	Predicted %X0	Measured (Corrected)%X0
CF Face-sheet	K13C2U fibres + EX1515 Cyanate Ester (45 gsm, 43% Resin)	79.5	79.5	0.1281	0.1281
Bus-tape	Polyamide(61%), Copper(24%), Adhesive(15%)	92.12	149.44	0.0901	0.1640
All-comp CF foam	K9 Allcomp	35.89	36.980	0.0627	0.0646
Close-outs and Locking points	PEEK	11.11	9.3607	0.0197	0.0166
CF Honeycomb	YSH50A-75,fibers + EX-1515 cyanate Ester	29.15	26.901	0.0451	0.0417
Cooling Pipe	CP2,Titanium(92.7%) + Aluminium (Al ₂ O ₃)(7.3%)	11.79	11.506	0.0530	0.0513
CF c-channels	T300 CF+ Cyanate Ester	25.91	25.356	0.0436	0.0494
BN-loaded Glue	Hysol EA,9396 (80%) + Boron Nitride (20%)	88.24	31.179	0.1817	0.0161
Total		373.71g	374.218g	0.6240(%X0)	0.5772 (%X0)

Table A.2: The measured and predicted masses and radiation length percentages for the stave, calculations follow the aforementioned assumptions.

Bibliography

- [1] E. Noether, *Invariant Variation Problems*, Gott. Nachr. **1918** (1918) 235, arXiv: [physics/0503066](https://arxiv.org/abs/physics/0503066) (cit. on p. 3).
- [2] F. Hasert et al., *Search for elastic muon-neutrino electron scattering*, Physics Letters B **46** (1973) 121, ISSN: 0370-2693, URL: <https://www.sciencedirect.com/science/article/pii/0370269373904942> (cit. on p. 8).
- [3] G. Arnison et al., *Experimental observation of isolated large transverse energy electrons with associated missing energy at s=540 GeV*, Physics Letters B **122** (1983) 103, ISSN: 0370-2693, URL: <https://www.sciencedirect.com/science/article/pii/0370269383911772> (cit. on p. 11).
- [4] G. Arnison et al., *Experimental Observation of Lepton Pairs of Invariant Mass Around 95-GeV/c**2 at the CERN SPS Collider*, Phys. Lett. B **126** (1983) 398 (cit. on p. 11).
- [5] T. Schucker, *Higgs-mass predictions*, 2011, arXiv: [0708.3344 \[hep-ph\]](https://arxiv.org/abs/0708.3344) (cit. on p. 11).
- [6] S. Chatrchyan et al., *Observation of a new boson at a mass of 125 GeV with the CMS experiment at the LHC*, Physics Letters B **716** (2012) 30, ISSN: 0370-2693, URL: <http://dx.doi.org/10.1016/j.physletb.2012.08.021> (cit. on p. 11).
- [7] G. Aad et al., *Observation of a new particle in the search for the Standard Model Higgs boson with the ATLAS detector at the LHC*, Physics Letters B **716** (2012) 1, ISSN: 0370-2693, URL: <http://dx.doi.org/10.1016/j.physletb.2012.08.020> (cit. on p. 11).
- [8] L. Knox, *Determination of inflationary observables by cosmic microwave background anisotropy experiments*, Phys. Rev. D **52** (8 1995) 4307, URL: <https://link.aps.org/doi/10.1103/PhysRevD.52.4307> (cit. on p. 19).
- [9] K. Freese and W. H. Kinney, *Natural inflation: consistency with cosmic microwave background observations of Planck and BICEP2*, Journal of Cosmology and Astroparticle Physics **2015** (2015) 044, URL: <https://doi.org/10.1088/1475-7516/2015/03/044> (cit. on p. 19).
- [10] N. Aghanim et al., *Planck 2018 results*, Astronomy & Astrophysics **641** (2020) A6, ISSN: 1432-0746, URL: <http://dx.doi.org/10.1051/0004-6361/201833910> (cit. on pp. 20, 21).
- [11] M. Aker et al., *Improved Upper Limit on the Neutrino Mass from a Direct Kinematic Method by KATRIN*, Phys. Rev. Lett. **123** (22 2019) 221802, URL: <https://link.aps.org/doi/10.1103/PhysRevLett.123.221802> (cit. on p. 20).
- [12] D.-d. Wu, ‘A Brief Introduction to the Strong CP Problem’, vol. 52, 1991 (cit. on p. 20).
- [13] Y. Fukuda et al., *Solar Neutrino Data Covering Solar Cycle 22*, Phys. Rev. Lett. **77** (9 1996) 1683, URL: <https://link.aps.org/doi/10.1103/PhysRevLett.77.1683> (cit. on p. 21).

Bibliography

- [14] Y. Fukuda et al., *Measurements of the Solar Neutrino Flux from Super-Kamiokandes First 300 Days*, *Physical Review Letters* **81** (1998) 1158, ISSN: 1079-7114, URL: <http://dx.doi.org/10.1103/PhysRevLett.81.1158> (cit. on p. 21).
- [15] I. T. Lawson, *Solar neutrino results from the sudbury neutrino observatoryy*, *Nuclear Physics B - Proceedings Supplements* **110** (2002) 308, ISSN: 0920-5632, URL: <https://www.sciencedirect.com/science/article/pii/S0920563202014949> (cit. on p. 21).
- [16] A. D. Sakharov, *Violation of CP Invariance, C asymmetry, and baryon asymmetry of the universe*, *Pisma Zh. Eksp. Teor. Fiz.* **5** (1967) 32 (cit. on p. 22).
- [17] L. collaboration et al., *Test of lepton universality in beauty-quark decays*, 2021, arXiv: [2103.11769 \[hep-ex\]](https://arxiv.org/abs/2103.11769) (cit. on p. 23).
- [18] R. Aaij et al., *Test of lepton universality with B 0 K *0 + decays*, *Journal of High Energy Physics* **2017** (2017), ISSN: 1029-8479, URL: [http://dx.doi.org/10.1007/JHEP08\(2017\)055](http://dx.doi.org/10.1007/JHEP08(2017)055) (cit. on p. 23).
- [19] G. W. Bennett et al., *Final report of the E821 muon anomalous magnetic moment measurement at BNL*, *Physical Review D* **73** (2006), ISSN: 1550-2368, URL: <http://dx.doi.org/10.1103/PhysRevD.73.072003> (cit. on p. 23).
- [20] B. Abi et al., *Measurement of the Positive Muon Anomalous Magnetic Moment to 0.46 ppm*, *Phys. Rev. Lett.* **126** (14 2021) 141801, URL: <https://link.aps.org/doi/10.1103/PhysRevLett.126.141801> (cit. on p. 23).
- [21] T. Aoyama et al., *The anomalous magnetic moment of the muon in the Standard Model*, *Physics Reports* **887** (2020) 1, The anomalous magnetic moment of the muon in the Standard Model, ISSN: 0370-1573, URL: <https://www.sciencedirect.com/science/article/pii/S0370157320302556> (cit. on p. 23).
- [22] S. Coleman and J. Mandula, *All Possible Symmetries of the S Matrix*, *Physical Review* **159** (1967) 1251 (cit. on p. 25).
- [23] R. Haag, J. T. Lopuszaski and M. Sohnius, *All possible generators of supersymmetries of the S-matrix*, *Nuclear Physics B* **88** (1975) 257 (cit. on p. 25).
- [24] P. Nelson, *Naturalness in Theoretical Physics: Internal constraints on theories, especially the requirement of naturalness, play a pivotal role in physics*, *American Scientist* **73** (1985) 60, ISSN: 00030996, URL: <http://www.jstor.org/stable/27853063> (cit. on p. 28).
- [25] M. Papucci, J. T. Ruderman and A. Weiler, *Natural SUSY endures*, *Journal of High Energy Physics* **2012** (2012), ISSN: 1029-8479, URL: [http://dx.doi.org/10.1007/JHEP09\(2012\)035](http://dx.doi.org/10.1007/JHEP09(2012)035) (cit. on pp. 32, 33).
- [26] L. J. Hall, D. Pinner and J. T. Ruderman, *A natural SUSY Higgs near 125 GeV*, *Journal of High Energy Physics* **2012** (2012), ISSN: 1029-8479, URL: [http://dx.doi.org/10.1007/JHEP04\(2012\)131](http://dx.doi.org/10.1007/JHEP04(2012)131) (cit. on p. 32).
- [27] U. Ellwanger, C. Hugonie and A. M. Teixeira, *The Next-to-Minimal Supersymmetric Standard Model*, *Physics Reports* **496** (2010) 1, ISSN: 0370-1573, URL: <http://dx.doi.org/10.1016/j.physrep.2010.07.001> (cit. on p. 33).
- [28] P. Athron et al., *New physics explanations of a_μ in light of the FNAL muon $g - 2$ measurement*, 2021, arXiv: [2104.03691 \[hep-ph\]](https://arxiv.org/abs/2104.03691) (cit. on pp. 36, 37).

Bibliography

- [29] P. S. B. Dev, A. Mazumdar and S. Qutub, *Constraining non-thermal and thermal properties of Dark Matter*, *Frontiers in Physics* **2** (2014) 26, ISSN: 2296-424X, URL: <https://www.frontiersin.org/article/10.3389/fphy.2014.00026> (cit. on p. 38).
- [30] D. Abercrombie et al., *Dark Matter benchmark models for early LHC Run-2 Searches: Report of the ATLAS/CMS Dark Matter Forum*, *Phys. Dark Univ.* **27** (2020) 100371, ed. by A. Boveia, C. Doglioni, S. Lowette, S. Malik and S. Mrenna, arXiv: [1507.00966 \[hep-ex\]](https://arxiv.org/abs/1507.00966) (cit. on p. 38).
- [31] M. R. Buckley, D. Feld and D. Gonçalves, *Scalar simplified models for dark matter*, *Physical Review D* **91** (2015), ISSN: 1550-2368, URL: <http://dx.doi.org/10.1103/PhysRevD.91.015017> (cit. on p. 39).
- [32] M. Bauer, U. Haisch and F. Kahlhoefer, *Simplified dark matter models with two Higgs doublets: I. Pseudoscalar mediators*, *Journal of High Energy Physics* **2017** (2017), ISSN: 1029-8479, URL: [http://dx.doi.org/10.1007/JHEP05\(2017\)138](http://dx.doi.org/10.1007/JHEP05(2017)138) (cit. on p. 41).
- [33] A. Cherchiglia, D. Stöckinger and H. Stöckinger-Kim, *Muon g - 2 in the 2HDM: Maximum results and detailed phenomenology*, *Physical Review D* **98** (2017) (cit. on p. 41).
- [34] P. Pani and G. Polesello, *Dark matter production in association with a single top-quark at the LHC in a two-Higgs-doublet model with a pseudoscalar mediator*, *Physics of the Dark Universe* **21** (2018) 8, ISSN: 2212-6864, URL: <http://dx.doi.org/10.1016/j.dark.2018.04.006> (cit. on p. 41).
- [35] W. Herr and B. Muratori, *Concept of luminosity*, (2006), URL: <https://cds.cern.ch/record/941318> (cit. on p. 47).
- [36] G. F. Knoll, *Radiation detection and measurement / Glenn F. Knoll*, English, 2nd ed., Wiley New York, 1989 xix, 754 p. : ISBN: 0471815047 (cit. on p. 54).
- [37] B. Mindur, *ATLAS Transition Radiation Tracker (TRT): Straw tubes for tracking and particle identification at the Large Hadron Collider*, tech. rep., CERN, 2016, URL: <https://cds.cern.ch/record/2139567> (cit. on p. 55).
- [38] C. W. Fabjan and F. Gianotti, *Calorimetry for Particle Physics*, *Rev. Mod. Phys.* **75** (2003) 1243, URL: <https://cds.cern.ch/record/692252> (cit. on p. 56).
- [39] L. M. de Andrade Filho, J. Manoel de Seixas, R. Agostino Vittilo and B. Thomas Martin, *Three-dimensional event visualization for the ATLAS calorimeter*, *Computer Physics Communications* **183** (2012) 245, ISSN: 0010-4655, URL: <https://www.sciencedirect.com/science/article/pii/S0010465511003092> (cit. on p. 58).
- [40] F. Cavallari, *Performance of calorimeters at the LHC*, *Journal of Physics: Conference Series* **293** (2011) 012001, URL: <https://doi.org/10.1088/1742-6596/293/1/012001> (cit. on p. 57).
- [41] *ATLAS muon spectrometer: Technical design report*, (1997) (cit. on p. 59).
- [42] *Standard Model Summary Plots March 2021*, tech. rep., All figures including auxiliary figures are available at <https://atlas.web.cern.ch/Atlas/GROUPS/PHYSICS/PUBNOTES/ATL-PHYS-PUB-2021-005>: CERN, 2021, URL: [http://cds.cern.ch/record/2758261](https://cds.cern.ch/record/2758261) (cit. on p. 61).

Bibliography

- [43] M. Aaboud et al., *Measurement of the W-boson mass in pp collisions at $\sqrt{s}=7\text{TeV}$ with the ATLAS detector*, *The European Physical Journal C* **78** (2018), ISSN: 1434-6052, URL: <http://dx.doi.org/10.1140/epjc/s10052-017-5475-4> (cit. on p. 63).
- [44] Y. L. Dokshitzer, *Calculation of the Structure Functions for Deep Inelastic Scattering and e+e- Annihilation by Perturbation Theory in Quantum Chromodynamics.*, Sov. Phys. JETP **46** (1977) 641 (cit. on p. 64).
- [45] V. N. Gribov and L. N. Lipatov, *Deep inelastic e p scattering in perturbation theory*, Sov. J. Nucl. Phys. **15** (1972) 438 (cit. on p. 64).
- [46] G. Altarelli and G. Parisi, *Asymptotic freedom in parton language*, Nuclear Physics B **126** (1977) 298, ISSN: 0550-3213, URL: <https://www.sciencedirect.com/science/article/pii/0550321377903844> (cit. on p. 64).
- [47] E. Bothmann et al., *Event generation with Sherpa 2.2*, SciPost Physics **7** (2019), ISSN: 2542-4653, URL: <http://dx.doi.org/10.21468/SciPostPhys.7.3.034> (cit. on p. 67).
- [48] S. Agostinelli et al., *GEANT4—a simulation toolkit*, Nucl. Instrum. Meth. A **506** (2003) 250 (cit. on p. 66).
- [49] E. Bothmann et al., *Event generation with Sherpa 2.2*, SciPost Phys. **7** (2019) 034, arXiv: [1905.09127 \[hep-ph\]](https://arxiv.org/abs/1905.09127) (cit. on p. 68).
- [50] T. Gleisberg and S. Höche, *Comix, a new matrix element generator*, JHEP **12** (2008) 039, arXiv: [0808.3674 \[hep-ph\]](https://arxiv.org/abs/0808.3674) (cit. on p. 68).
- [51] F. Buccioni et al., *OpenLoops 2*, Eur. Phys. J. C **79** (2019) 866, arXiv: [1907.13071 \[hep-ph\]](https://arxiv.org/abs/1907.13071) (cit. on p. 68).
- [52] F. Cascioli, P. Maierhöfer and S. Pozzorini, *Scattering Amplitudes with Open Loops*, Phys. Rev. Lett. **108** (2012) 111601, arXiv: [1111.5206 \[hep-ph\]](https://arxiv.org/abs/1111.5206) (cit. on p. 68).
- [53] A. Denner, S. Dittmaier and L. Hofer, *COLLIER: A fortran-based complex one-loop library in extended regularizations*, Comput. Phys. Commun. **212** (2017) 220, arXiv: [1604.06792 \[hep-ph\]](https://arxiv.org/abs/1604.06792) (cit. on p. 68).
- [54] S. Schumann and F. Krauss, *A parton shower algorithm based on Catani–Seymour dipole factorisation*, JHEP **03** (2008) 038, arXiv: [0709.1027 \[hep-ph\]](https://arxiv.org/abs/0709.1027) (cit. on p. 68).
- [55] S. Höche, F. Krauss, M. Schönher and F. Siegert, *A critical appraisal of NLO+PS matching methods*, JHEP **09** (2012) 049, arXiv: [1111.1220 \[hep-ph\]](https://arxiv.org/abs/1111.1220) (cit. on p. 68).
- [56] S. Höche, F. Krauss, M. Schönher and F. Siegert, *QCD matrix elements + parton showers. The NLO case*, JHEP **04** (2013) 027, arXiv: [1207.5030 \[hep-ph\]](https://arxiv.org/abs/1207.5030) (cit. on p. 68).
- [57] S. Catani, F. Krauss, R. Kuhn and B. R. Webber, *QCD Matrix Elements + Parton Showers*, JHEP **11** (2001) 063, arXiv: [hep-ph/0109231](https://arxiv.org/abs/hep-ph/0109231) (cit. on p. 68).
- [58] S. Höche, F. Krauss, S. Schumann and F. Siegert, *QCD matrix elements and truncated showers*, JHEP **05** (2009) 053, arXiv: [0903.1219 \[hep-ph\]](https://arxiv.org/abs/0903.1219) (cit. on p. 68).
- [59] T. Sjöstrand et al., *An introduction to PYTHIA 8.2*, Comput. Phys. Commun. **191** (2015) 159, arXiv: [1410.3012 \[hep-ph\]](https://arxiv.org/abs/1410.3012) (cit. on pp. 68, 154).

Bibliography

- [60] ATLAS *Pythia 8 tunes to 7 TeV data*, tech. rep., All figures including auxiliary figures are available at <https://atlas.web.cern.ch/Atlas/GROUPS/PHYSICS/PUBNOTES/ATL-PHYS-PUB-2014-021>; CERN, 2014, URL: <https://cds.cern.ch/record/1966419> (cit. on pp. 68, 154).
- [61] R. D. Ball et al., *Parton distributions with LHC data*, Nucl. Phys. B **867** (2013) 244, arXiv: [1207.1303 \[hep-ph\]](https://arxiv.org/abs/1207.1303) (cit. on p. 68).
- [62] S. Frixione, P. Nason and G. Ridolfi, *A positive-weight next-to-leading-order Monte Carlo for heavy flavour hadroproduction*, JHEP **09** (2007) 126, arXiv: [0707.3088 \[hep-ph\]](https://arxiv.org/abs/0707.3088) (cit. on p. 68).
- [63] P. Nason, *A new method for combining NLO QCD with shower Monte Carlo algorithms*, JHEP **11** (2004) 040, arXiv: [hep-ph/0409146](https://arxiv.org/abs/hep-ph/0409146) (cit. on p. 68).
- [64] S. Frixione, P. Nason and C. Oleari, *Matching NLO QCD computations with parton shower simulations: the POWHEG method*, JHEP **11** (2007) 070, arXiv: [0709.2092 \[hep-ph\]](https://arxiv.org/abs/0709.2092) (cit. on p. 68).
- [65] S. Alioli, P. Nason, C. Oleari and E. Re, *A general framework for implementing NLO calculations in shower Monte Carlo programs: the POWHEG BOX*, JHEP **06** (2010) 043, arXiv: [1002.2581 \[hep-ph\]](https://arxiv.org/abs/1002.2581) (cit. on p. 68).
- [66] R. D. Ball et al., *Parton distributions for the LHC run II*, JHEP **04** (2015) 040, arXiv: [1410.8849 \[hep-ph\]](https://arxiv.org/abs/1410.8849) (cit. on p. 68).
- [67] J. Alwall et al., *The automated computation of tree-level and next-to-leading order differential cross sections, and their matching to parton shower simulations*, JHEP **07** (2014) 079, arXiv: [1405.0301 \[hep-ph\]](https://arxiv.org/abs/1405.0301) (cit. on p. 68).
- [68] J. Bellm et al., *Herwig 7.0/Herwig++ 3.0 release note*, Eur. Phys. J. C **76** (2016) 196, arXiv: [1512.01178 \[hep-ph\]](https://arxiv.org/abs/1512.01178) (cit. on p. 68).
- [69] L. Harland-Lang, A. Martin, P. Motylinski and R. Thorne, *Parton distributions in the LHC era: MMHT 2014 PDFs*, Eur. Phys. J. C **75** (2015) 204, arXiv: [1412.3989 \[hep-ph\]](https://arxiv.org/abs/1412.3989) (cit. on p. 68).
- [70] ATLAS Collaboration, *Performance of the ATLAS track reconstruction algorithms in dense environments in LHC Run 2*, Eur. Phys. J. C **77** (2017) 673, arXiv: [1704.07983 \[hep-ex\]](https://arxiv.org/abs/1704.07983) (cit. on p. 71).
- [71] M. Aaboud et al., *Jet reconstruction and performance using particle flow with the ATLAS Detector*, The European Physical Journal C **77** (2017), ISSN: 1434-6052, URL: <http://dx.doi.org/10.1140/epjc/s10052-017-5031-2> (cit. on pp. 73, 74).
- [72] *Optimisation of the ATLAS b-tagging performance for the 2016 LHC Run*, (2016) (cit. on p. 75).
- [73] *ATLAS b-jet identification performance and efficiency measurement with $t\bar{t}$ events in pp collisions at $\sqrt{s} = 13\text{TeV}$* , The European Physical Journal C **79** (2019), ISSN: 1434-6052, URL: <http://dx.doi.org/10.1140/epjc/s10052-019-7450-8> (cit. on p. 76).
- [74] ATLAS Collaboration, *Electron and photon performance measurements with the ATLAS detector using the 2015-2017 LHC proton–proton collision data*, (2019), arXiv: [1908.00005 \[hep-ex\]](https://arxiv.org/abs/1908.00005) (cit. on p. 77).

Bibliography

- [75] M. Aaboud et al., *Electron efficiency measurements with the ATLAS detector using 2012 LHC protonproton collision data*, *The European Physical Journal C* **77** (2017), ISSN: 1434-6052, URL: <http://dx.doi.org/10.1140/epjc/s10052-017-4756-2> (cit. on p. 77).
- [76] G. Aad et al., *Muon reconstruction and identification efficiency in ATLAS using the full Run 2 pp collision data set at $\sqrt{s} = 13$ TeV*, *Eur. Phys. J. C* **81** (2021) 578, arXiv: [2012.00578 \[hep-ex\]](https://arxiv.org/abs/2012.00578) (cit. on pp. 78, 82).
- [77] ATLAS Collaboration, *Performance of missing transverse momentum reconstruction in proton–proton collisions at $\sqrt{s} = 7$ TeV with ATLAS*, *Eur. Phys. J. C* **72** (2012) 1844, arXiv: [1108.5602 \[hep-ex\]](https://arxiv.org/abs/1108.5602) (cit. on p. 79).
- [78] M. Aaboud et al., *Jet energy scale measurements and their systematic uncertainties in proton-proton collisions at $\sqrt{s} = 13$ TeV with the ATLAS detector*, *Physical Review D* **96** (2017), ISSN: 2470-0029, URL: <http://dx.doi.org/10.1103/PhysRevD.96.072002> (cit. on p. 81).
- [79] G. Aad et al., *Jet energy resolution in proton-proton collisions at $\sqrt{s} = 7$ TeV recorded in 2010 with the ATLAS detector*, *The European Physical Journal C* **73** (2013), ISSN: 1434-6052, URL: <http://dx.doi.org/10.1140/epjc/s10052-013-2306-0> (cit. on p. 81).
- [80] ATLAS Collaboration, *Performance of electron and photon triggers in ATLAS during LHC Run 2*, (2019), arXiv: [1909.00761 \[hep-ex\]](https://arxiv.org/abs/1909.00761) (cit. on p. 82).
- [81] M. Aaboud et al., *Performance of missing transverse momentum reconstruction with the ATLAS detector using protonproton collisions at $\sqrt{s} = 13$ TeV s=13TeV*, *The European Physical Journal C* **78** (2018), ISSN: 1434-6052, URL: <http://dx.doi.org/10.1140/epjc/s10052-018-6288-9> (cit. on p. 82).
- [82] G. Avoni et al., *The new LUCID-2 detector for luminosity measurement and monitoring in ATLAS*, *Journal of Instrumentation* **13** (2018) P07017, URL: <https://doi.org/10.1088/1748-0221/13/07/p07017> (cit. on p. 82).
- [83] V. Cindro et al., *The ATLAS Beam Conditions Monitor*, *Journal of Instrumentation* **3** (2008) P02004, URL: <https://doi.org/10.1088/1748-0221/3/02/p02004> (cit. on p. 82).
- [84] ATLAS Collaboration, *Luminosity determination in pp collisions at $\sqrt{s} = 13$ TeV using the ATLAS detector at the LHC*, ATLAS-CONF-2019-021, 2019, URL: <https://cds.cern.ch/record/2677054> (cit. on p. 82).
- [85] *Formulae for Estimating Significance*, tech. rep., All figures including auxiliary figures are available at <https://atlas.web.cern.ch/Atlas/GROUPS/PHYSICS/PUBNOTES/ATL-PHYS-PUB-2020-025>: CERN, 2020, URL: [http://cds.cern.ch/record/2736148](https://cds.cern.ch/record/2736148) (cit. on p. 84).
- [86] M. Baak et al., *HistFitter software framework for statistical data analysis*, *The European Physical Journal C* **75** (2015), ISSN: 1434-6052, URL: <http://dx.doi.org/10.1140/epjc/s10052-015-3327-7> (cit. on p. 85).
- [87] K. Cranmer, *Practical Statistics for the LHC*, 2015, arXiv: [1503.07622 \[physics.data-an\]](https://arxiv.org/abs/1503.07622) (cit. on p. 86).
- [88] A. L. Read, *Presentation of search results: the CL_s technique*, *Journal of Physics G: Nuclear and Particle Physics*, From the workshop Advanced Statistical Techniques in Particle Physics **28** (2002) 2693, URL: <https://doi.org/10.1088/0954-3899/28/10/313> (cit. on p. 86).

Bibliography

- [89] C. Lester and D. Summers, *Measuring masses of semi-invisibly decaying particle pairs produced at hadron colliders*, Physics Letters B **463** (1999) 99, ISSN: 0370-2693, URL: [http://dx.doi.org/10.1016/S0370-2693\(99\)00945-4](http://dx.doi.org/10.1016/S0370-2693(99)00945-4) (cit. on p. 88).
- [90] T. Chen and C. Guestrin, *XGBoost*, Proceedings of the 22nd ACM SIGKDD International Conference on Knowledge Discovery and Data Mining (2016), URL: <http://dx.doi.org/10.1145/2939672.2939785> (cit. on pp. 89, 102).
- [91] H. Phan, ‘Audio Event Detection, Classification, and Beyond’, PhD thesis, 2017 (cit. on p. 91).
- [92] Dask Development Team, *Dask: Library for dynamic task scheduling*, 2016, URL: <https://dask.org> (cit. on p. 92).
- [93] ‘Kolmogorov–Smirnov Test’, *The Concise Encyclopedia of Statistics*, Springer New York, 2008 283, ISBN: 978-0-387-32833-1, URL: https://doi.org/10.1007/978-0-387-32833-1_214 (cit. on p. 93).
- [94] *Soft b-hadron tagging for compressed SUSY scenarios*, (2019) (cit. on p. 106).
- [95] G. Aad et al., *Measurements of the production cross-section for a Z boson in association with b-jets in proton-proton collisions at $\sqrt{s} = 13$ TeV with the ATLAS detector*, Journal of High Energy Physics **2020** (2020), ISSN: 1029-8479, URL: [http://dx.doi.org/10.1007/JHEP07\(2020\)044](http://dx.doi.org/10.1007/JHEP07(2020)044) (cit. on p. 112).
- [96] G. Busoni, A. D. Simone, T. Jacques, E. Morgante and A. Riotto, *Making the most of the relic density for dark matter searches at the LHC 14 TeV Run*, Journal of Cosmology and Astroparticle Physics **2015** (2015) 022, ISSN: 1475-7516, URL: <http://dx.doi.org/10.1088/1475-7516/2015/03/022> (cit. on p. 121).
- [97] M. Aaboud et al., *Search for supersymmetry in events with b-tagged jets and missing transverse momentum in pp collisions at $s = 13$ $\sqrt{s} = 13$ TeV with the ATLAS detector*, Journal of High Energy Physics **2017** (2017), ISSN: 1029-8479, URL: [http://dx.doi.org/10.1007/JHEP11\(2017\)195](http://dx.doi.org/10.1007/JHEP11(2017)195) (cit. on p. 139).
- [98] ATLAS Collaboration, *Search for dark matter produced in association with bottom or top quarks in $\sqrt{s} = 13$ TeV pp collisions with the ATLAS detector*, Eur. Phys. J. C **78** (2018) 18, arXiv: [1710.11412 \[hep-ex\]](https://arxiv.org/abs/1710.11412) (cit. on p. 140).
- [99] G. Aad et al., *Search for bottom-squark pair production in pp collision events at $\sqrt{s}=13$ TeV with hadronically decaying τ -leptons, b-jets, and missing transverse momentum using the ATLAS detector*, Physical Review D **104** (2021), ISSN: 2470-0029, URL: <http://dx.doi.org/10.1103/PhysRevD.104.032014> (cit. on p. 141).
- [100] G. Aad et al., *Search for squarks and gluinos in final states with same-sign leptons and jets using 139 fb $^{-1}$ of data collected with the ATLAS detector*, Journal of High Energy Physics **2020** (2020), ISSN: 1029-8479, URL: [http://dx.doi.org/10.1007/JHEP06\(2020\)046](http://dx.doi.org/10.1007/JHEP06(2020)046) (cit. on p. 141).
- [101] G. Aad et al., *Search for new phenomena in events with an energetic jet and missing transverse momentum in pp collisions at $\sqrt{s}=13$ TeV with the ATLAS detector*, Physical Review D **103** (2021), ISSN: 2470-0029, URL: <http://dx.doi.org/10.1103/PhysRevD.103.112006> (cit. on p. 141).

Bibliography

- [102] A. M. Sirunyan et al., *Search for new phenomena with the M_{T2} variable in the all-hadronic final state produced in protonproton collisions at $\sqrt{s} = 13\text{TeV}$* , *The European Physical Journal C* **77** (2017), ISSN: 1434-6052, URL: <http://dx.doi.org/10.1140/epjc/s10052-017-5267-x> (cit. on p. 142).
- [103] A. M. Sirunyan et al., *Searches for physics beyond the standard model with the M_{T2} variable in hadronic final states with and without disappearing tracks in protonproton collisions at $\sqrt{s} = 13\text{TeV}$* , *The European Physical Journal C* **80** (2020), ISSN: 1434-6052, URL: <http://dx.doi.org/10.1140/epjc/s10052-019-7493-x> (cit. on p. 142).
- [104] A. M. Sirunyan et al., *Search for supersymmetry in proton-proton collisions at 13 TeV in final states with jets and missing transverse momentum*, *Journal of High Energy Physics* **2019** (2019), ISSN: 1029-8479, URL: [http://dx.doi.org/10.1007/JHEP10\(2019\)244](http://dx.doi.org/10.1007/JHEP10(2019)244) (cit. on p. 142).
- [105] M. Aaboud et al., *Search for chargino and neutralino production in final states with a Higgs boson and missing transverse momentum at $\sqrt{s} = 13\text{TeV}$ with the ATLAS detector*, *Physical Review D* **100** (2019), ISSN: 2470-0029, URL: <http://dx.doi.org/10.1103/PhysRevD.100.012006> (cit. on p. 147).
- [106] E. Boos, V. Bunichev, L. Dudko, I. Myagkov and M. Perfilov, *Modeling of associated tW single top production including the interference with diagrams*, *EPJ Web Conf.* **158** (2017) 04003, ed. by P. Mandrik (cit. on p. 148).
- [107] G. Aad et al., *Jet energy scale and resolution measured in protonproton collisions at $\sqrt{s} = 13\text{TeV}$ with the ATLAS detector*, *Eur. Phys. J. C* **81** (2021) 689, arXiv: [2007.02645 \[hep-ex\]](https://arxiv.org/abs/2007.02645) (cit. on p. 148).
- [108] S. Lundberg and S.-I. Lee, *A Unified Approach to Interpreting Model Predictions*, 2017, arXiv: [1705.07874 \[cs.AI\]](https://arxiv.org/abs/1705.07874) (cit. on pp. 151, 152).
- [109] M. Aaboud et al., *Search for chargino and neutralino production in final states with a Higgs boson and missing transverse momentum at $\sqrt{s} = 13\text{TeV}$ with the ATLAS detector*, *Physical Review D* **100** (2019), ISSN: 2470-0029, URL: <http://dx.doi.org/10.1103/PhysRevD.100.012006> (cit. on p. 159).
- [110] A. M. Sirunyan et al., *Combined search for electroweak production of charginos and neutralinos in proton-proton collisions at $\sqrt{s}=13\text{TeV}$* , *Journal of High Energy Physics* **2018** (2018), ISSN: 1029-8479, URL: [http://dx.doi.org/10.1007/JHEP03\(2018\)160](http://dx.doi.org/10.1007/JHEP03(2018)160) (cit. on p. 160).
- [111] C. Collaboration, *Search for chargino-neutralino production in events with Higgs and W bosons using 137fb^{-1} of proton-proton collisions at $\sqrt{s} = 13\text{TeV}$* , 2021, arXiv: [2107.12553 \[hep-ex\]](https://arxiv.org/abs/2107.12553) (cit. on p. 160).
- [112] A. Collaboration, *Search for dark matter produced in association with a single top quark in $\sqrt{s} = 13\text{TeV}$ pp collisions with the ATLAS detector*, 2020, arXiv: [2011.09308 \[hep-ex\]](https://arxiv.org/abs/2011.09308) (cit. on pp. 163, 170).
- [113] M. Aaboud et al., *Search for top-squark pair production in final states with one lepton, jets, and missing transverse momentum using 36fb^{-1} of $s = 13\text{TeV}$ pp collision data with the ATLAS detector*, *Journal of High Energy Physics* **2018** (2018), ISSN: 1029-8479, URL: [http://dx.doi.org/10.1007/JHEP06\(2018\)108](http://dx.doi.org/10.1007/JHEP06(2018)108) (cit. on p. 164).

List of Figures

List of Tables